nagra.

Technical Report 12-01

The Long Term Geochemical Evolution of the Nearfield of the HLW Repository

November 2014

M.H. Bradbury, U. Berner, E. Curti,
W. Hummel, G. Kosakowski, T. Thoenen

Paul Scherrer Institut, Villigen PSI

National Cooperative
for the Disposal of
Radioactive Waste

Hardstrasse 73
CH-5430 Wettingen
Switzerland
Tel. +41 56 437 11 11

www.nagra.ch

nagra.

Technical Report 12-01

The Long Term Geochemical Evolution of the Nearfield of the HLW Repository

November 2014

M.H. Bradbury, U. Berner, E. Curti,
W. Hummel, G. Kosakowski, T. Thoenen

Paul Scherrer Institut, Villigen PSI

National Cooperative
for the Disposal of
Radioactive Waste

Hardstrasse 73
CH-5430 Wettingen
Switzerland
Tel. +41 56 437 11 11

www.nagra.ch

ISSN 1015-2636

Abstract

The work presented in this report focuses on the spatial and temporal evolution of the nearfield of the high level radioactive waste repository situated in the Opalinus Clay formation.

The major components of the nearfield of such a repository are spent fuel, vitrified high-level waste, canisters (assumed for the purposes of the present report to be made of carbon steel), compacted bentonite and a concrete liner. Over the one million year time period considered in safety analysis, these components will chemically interact with one another and potentially change their retention characteristics.

As a starting reference point the "initial" (unreacted) states of the Opalinus Clay, bentonite, concrete liner (mineralogies and water chemistries) and the canister are briefly described.

The main processes considered to influence the evolution of the repository in time and space, and which often operate over different time scales, are: interactions of the concrete tunnel liner with compacted bentonite and Opalinus Clay, temperature gradients caused by the heat generating high level waste, mineralogical changes to the compacted bentonite through interactions with the corrosion products of the iron canisters, and finally, the dissolution of the spent fuel and vitrified high-level waste. The consequences of these processes (as a function of time) on the long term barrier performance of the nearfield have been estimated, particularly with respect to radionuclide solubilities and the sorption, diffusion and swelling characteristics of the bentonite.

The main conclusions drawn are as follows: The alteration depth into the bentonite due to the interaction with the concrete liner (assumed to be 15 cm thick) is likely to be much less than 13 cm over a one million year time scale, with the main reaction products being clays (illite), hydroxides, carbonates, calcium silicate hydrates, and aluminosilicates. The swelling pressure and the sorption capacity of the bentonite in this region will be reduced, but not to zero.

Experimental findings and modelling studies indicate that any alterations due to the post closure temperature transients will not change the swelling and retention properties of the outer (more than) half of the bentonite which can be relied upon to fulfil its buffer function fully.

The dissolution of spent fuel and vitrified high-level waste are not expected to have any detrimental effects on the sorption properties or the swelling capacity of the bentonite. However, the potential influence of the release of boron from the vitrified high-level waste on complexation with highly charged radionuclides needs to be addressed.

Current studies indicate that the Fe^{2+} released by the corrosion of the steel canisters can lead to the alteration of montmorillonite at temperatures below 100 °C to form Fe-rich smectites or non-swelling clays and chlorites. Fe-rich smectites have similar properties to the Na-montmorillonite they replace. Hence, the near-field barrier function will not be significantly influenced with respect to sorption and swelling. However, if non-swelling clay minerals or chlorites are formed, then noticeable changes are expected, reducing the bentonite swelling capacity and sorption properties.

The release of iron from canister corrosion is a slow process. Estimates based on the corrosion rate indicate that the canister corrosion and the following conversion of montmorillonite needs between 100'000 and 200'000 years. The situation described here represents a "worst case" scenario. Other iron phases like magnetite or siderite are stable in this environment and decrease the availability of Fe^{2+} for Montmorillonite transformation. This suggests that significant quantities of bentonite will still be available up to one million years after closure of the repository.

Zusammenfassung

Der vorliegende Bericht befasst sich mit der räumlichen und zeitlichen Entwicklung des Nahfelds des geologischen Tiefenlagers für hochaktive radioaktive Abfälle im Opalinuston.

Die Hauptkomponenten des Nahfelds eines solchen Tiefenlagers sind verglaste hochaktive Abfälle aus der Wiederaufbereitung (HAA), abgebrannte Brennelemente (BE), Stahlbehälter, kompaktierter Bentonit sowie eine Spritzbetonverstärkung. Im Zeitraum von einer Million Jahren, der für die Sicherheitsanalysen relevant ist, werden sich diese Komponenten chemisch gegenseitig beeinflussen. Dadurch können sich deren Eigenschaften, welche die Radionuklidrückhaltung betreffen, verändern.

Als Ausgangspunkt wird der ursprüngliche Zustand der Stahlbehälter sowie die ursprüngliche Mineralogie und Porenwasserzusammensetzung von Opalinuston, Bentonit und ESDRED-Spritzbetonverstärkungen kurz beschrieben.

Die hauptsächlichen Prozesse, welche die räumliche und zeitliche Entwicklung eines Tiefenlagers beeinflussen und oft über verschiedene Zeitskalen operieren, sind: Wechselwirkungen zwischen Betonausbau und kompaktiertem Bentonit, Temperaturgradienten in der Umgebung der wärmegenerierenden hochaktiven Abfälle, mineralogische Änderungen des kompaktierten Bentonits aufgrund von Wechselwirkungen mit den Korrosionsprodukten der Stahlbehälter sowie die Auflösung der verglasten Abfälle und der abgebrannten Brennelemente. Die Auswirkungen dieser Prozesse als Funktion der Zeit auf die Langzeitsicherheit der Nahfeldbarrieren werden abgeschätzt, insbesondere im Zusammenhang mit der Löslichkeit von Radionukliden und den Sorptions-, Diffusions- und Quelleigenschaften des Bentonits.

Es konnten die folgenden Schlussfolgerungen gezogen werden: Die Dicke der Umwandlungsschicht des Bentonits als Folge der Wechselwirkung mit dem Betonausbau (angenommene Schichtdicke 15 cm) beträgt nach einer Million Jahren wahrscheinlich weit weniger als 13 cm. Die zu erwartenden Alterationsprodukte sind Tonminerale (Illit), Hydroxide, Carbonate, Calciumsilikathydrate und Alumosilikate. Quelldrücke und Sorptionskapazität des Bentonit werden in diesem Bereich reduziert sein, ohne aber auf null zurückzugehen.

Experimentelle Untersuchungen und Modellstudien weisen darauf hin, dass die Temperaturtransiente nach Verschluss nur zu geringen mineralogischen Veränderungen führen wird, wobei das Quell- und Rückhaltevermögen bei mehr als der äusseren Hälfte des Bentonits vollständig erhalten bleiben werden. Die Korrosion abgebrannter Brennelemente und verglaster Abfälle wird keine schädlichen Auswirkungen auf die Sorptions- und Quelleigenschaften des Bentonits haben. Allerdings ist der Einfluss von Bor aus der Auflösung des Glases sowie dessen Komplexbildung mit hochgeladenen Radionukliden zu prüfen.

Es gibt Hinweise darauf, dass Fe^{2+} aus der Korrosion der Stahlbehälter zu Umwandlungen im Montmorillonit führen kann. Bei Temperaturen unter 100 °C kann es zur Bildung von Fe-reichen Smectiten, nichtquellbaren Tonmineralen oder Chlorit kommen. Da Fe-reiche Smectite ähnliche Eigenschaften haben wie der ersetzte Na-Montmorillonit wird die Barrierenfunktion des Nahfelds in Bezug auf Sorption und Quellbarkeit in diesem Fall nur unwesentlich beeinflusst. Werden allerdings nichtquellbare Tonminerale oder Chlorit gebildet, so sind signifikante Änderungen zu erwarten, Quellbarkeit und Sorptionsvermögen werden vermindert.

Die Freisetzung des Eisens aus der Stahlkorrosion ist ein langsamer Prozess. Schätzungen auf der Basis der Korrosionsrate gehen von einem Zeitraum von 100'000 bis 200'000 Jahren für die vollständige Korrosion der Stahlkanister und die folgende Umwandlung des Montmorillonit aus. Diese Betrachtungen beschreiben aber ein "worst case" Szenarium. Andere Eisenphasen wie Magnetit oder Siderit sind in dieser Umgebung stabil und setzen die Verfügbarkeit von Fe^{2+} für die Umwandlung von Montmorillonit herab. Dies legt nahe, dass 1 Million Jahre nach Verschluss des Lagers immer noch erhebliche Mengen vom ursprünglichen Montmorillonit zur Verfügung stehen.

Résumé

Le travail présenté dans ce rapport se concentre sur l'évolution spatio-temporelle du champ proche d'un dépôt de stockage pour déchets de haute activité (DHA) situé dans les Argiles à Opalinus.

Le champ proche d'un tel site de stockage comprend principalement le combustible nucléaire irradié, les déchets vitrifiés, les conteneurs (pour les besoins de ce rapport, on considère qu'ils sont en acier au carbone), la bentonite compactée et un revêtement en béton projeté. Pendant la période d'un million d'années considérée dans les analyses de sureté, ces composants vont interagir chimiquement les uns avec les autres, ce qui pourra modifier leurs propriétés de rétention.

Pour commencer et comme point de référence, les Argiles à Opalinus, la bentonite, le revêtement en béton (minéralogies et chimies des eaux) ainsi que le conteneur en acier sont brièvement décrits dans leur état initial.

Les processus susceptibles d'influencer l'évolution du dépôt dans le temps et dans l'espace – et qui opèrent souvent à différentes échelles temporelles – sont: l'interaction du revêtement en béton avec la bentonite compactée et les Argiles à Opalinus, les gradients de température engendrés par la chaleur issue des déchets à haute activité, les changements minéralogiques induits dans la bentonite par les interactions avec les produits de corrosion des conteneurs en acier et finalement, la dissolution du combustible irradié et des déchets de haute activité vitrifiés. Les conséquences de ces processus, en fonction du temps, sur l'efficacité à long terme des barrières ouvragées ont été estimées, notamment au regard de la solubilité des radionucléides et des propriétés de sorption, de diffusion et de gonflement de la bentonite.

Les principales conclusions sont les suivantes: l'interaction avec le revêtement en béton (dont on suppose qu'il a une épaisseur de 15 cm) affectera la bentonite sur une profondeur bien inférieure à 13 cm sur une échelle de temps s'élevant à un million d'années, entrainant la production d'argiles, d'hydroxydes, de carbonates, de silicate de calcium hydraté et d'aluminosilicates. La pression de gonflement et la capacité de rétention en seront diminuées, mais demeureront supérieures à zéro.

Les résultats des études expérimentales et de modélisation suggèrent que les altérations provoquées par les transitoires thermiques en période de post-fermeture auront des répercussions sur les propriétés de gonflement et de rétention de la bentonite. Toutefois, ces processus n'affectent pas la moitié extérieure de l'épaisseur de bentonite et celle-ci pourra encore assumer pleinement son rôle de tampon.

On considère que les propriétés de sorption ainsi que la pression de gonflement de la bentonite ne seront pas altérées par la dissolution du combustible irradié et des déchets vitrifiés. Cependant, il sera nécessaire d'étudier les effets potentiels du bore, libéré par les déchets de haute activité vitrifiés, sur la complexation des cations à hautes charges.

Des études récentes suggèrent que le Fe^{2+} libéré lors de la corrosion des conteneurs en acier peut entrainer une altération de la montmorillonite à des températures inférieures à 100 °C, conduisant à la formation de smectites riches en Fe ou d'argiles non-gonflantes et de chlorites. Du fait que les smectites riches en Fe ont des propriétés similaires à la montmorillonite qu'elles remplacent, le processus n'aura pas de conséquences significatives sur les propriétés de rétention et de gonflement du champ proche, qui maintiendra sa fonction de barrière. En revanche, s'il y a

formation d'argiles non-gonflantes ou de chlorites, on doit s'attendre à des modifications significatives, avec une diminution de la pression de gonflement et de la capacité de sorption.

La libération de fer à partir des conteneurs corrodés est un processus lent. Des estimations basées sur les taux de corrosion indiquent que 100'000 à 200'000 ans seront nécessaires à une corrosion complète des conteneurs et à la transformation de la montmorillonite correspondante. La situation décrite ici constitue un scénario de type "worst case". D'autres phases ferrifères telles que la magnétite ou la sidérite sont stables dans ce type d'environnement et diminuent l'accessibilité de Fe^{2+} pour la transformation de la montmorillonite. Ceci signifie que des quantités considérables de bentonite seront encore disponibles un million d'années après la fermeture du dépôt de stockage.

Table of Contents

List of Tables

List of Figures

1 Introduction

In Switzerland, the Nuclear Energy Law requires that all types of radioactive waste be disposed of in deep geological repositories (KEG 2003). The Swiss Radioactive Waste Management Programme (Nagra 2008) foresees two types of deep geological repositories: a high-level waste repository (HLW repository[1]) for spent fuel (SF[2]), vitrified high-level waste (HLW) and long-lived intermediate-level waste (ILW), and a repository for low- and intermediate-level waste (L/ILW repository[3]).

In response to Stage 1 of the Swiss site selection plan, the so-called Sectoral Plan for Deep Geological Repositories ("SGT", BFE 2008), Nagra proposed six siting regions for the L/ILW repository, three of which are also suitable for the HLW repository. In each siting region for the HLW repository, the Opalinus Clay was proposed as the host rock formation.

In Stage 2 of the Sectoral Plan at least two sites for each repository type will be selected, based, in part, on the outcomes of so-called provisional safety analyses. For these sites, further, more extensive site-specific investigations will be performed in Stage 3, the aim of which is to identify a site for each repository type.

Thus, the Radioactive Waste Management Programme in Switzerland is moving towards the realization phase for deep geological repositories. Previously, the rather generic studies and approaches were sufficient for the needs and aims of the programme. However, now, potential siting regions and host rocks have been identified and the need is to carry out studies orientated towards site-specific conditions taking into account potential changes occurring in time and space. The emphasis is on providing information and data which are relevant to the "real systems", whether this be the far-field host rock or the near-field components. This also means that a new level of quality in the treatment of the wide variety of processes involved needs to be introduced. The components may interact with one another over time, changing mineralogies, porosities and physico-chemical characteristics.

This report focuses on the nearfield of the HLW repository. The safety assessments for the HLW waste repository are carried out for a period of one million years and during this period the repository will evolve in time and space. In order to obtain as realistic a picture as possible of this evolution the main processes operating over the different time scales have to be identified. The results of these processes and their safety relevant consequences have to be assessed and considered in the safety assessments. Specifically, the effects of these processes on radionuclide solubilities in the nearfield and on the sorption, diffusion and swelling characteristics of the bentonite have to be assessed. The main processes which may have implications for the long term barrier performance of the nearfield of the HLW repository are the interaction of the low pH concrete liner with the Opalinus Clay and bentonite, post closure temperature transients, the corrosion of the carbon steel canisters[4] and the interaction of the corrosion products with bentonite, and the dissolution of the spent fuel and the vitrified high-level waste. The types of interactions which may occur in the bentonite nearfield listed above are not new and have been considered in previous safety assessments (see for example, Nagra 2002a). In this report the aim is to try and look at the features and processes in a more detailed manner, identify the main effects, consider bounds for their influences on the barrier performance, look at the

---

1 German HAA-Lager

2 According to current legislation, spent fuel is classified as radioactive waste.

3 German SMA-Lager

4 Cu/steel canisters or copper coated steel canisters are alternative options being considered by Nagra.

potential cross interactions between the different processes and put the interactions in a time frame of up to one million years. The focus will be on mineralogical and water chemistry changes since these two factors have direct influences on radionuclide solubilities, sorption, diffusion and on swelling. The evolution of any water chemistry and/or mineralogical changes was taken into account in the development of sorption and solubility databases and solubility calculations for the provisional safety analyses for Stage 2 of the Sectoral Plan.

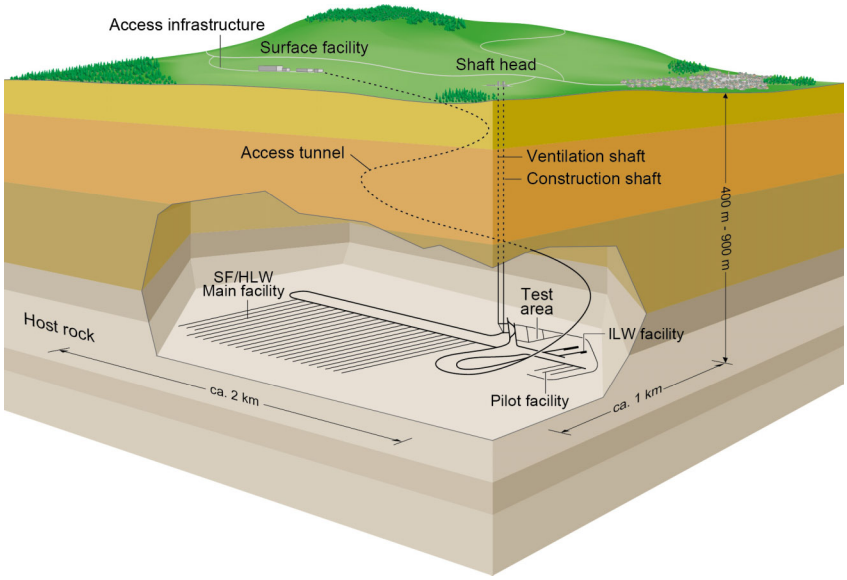

Fig. 1-1: Schematic representation of the proposed layout of a HLW radioactive waste repository.

2 Brief description of SF/HLW waste emplacement tunnels

The current proposal is to construct horizontal emplacement tunnels for SF and HLW waste canisters at the mid plane of an Opalinus Clay formation at a depth of circa 600 m. The Opalinus Clay in the geological siting regions considered has a thickness of about 100 m so that the radionuclide transport path to the rock formations above and below is generally of the order of 50 m. The ~ 800 m long emplacement tunnels have an inner diameter of ~ 2.5 m (2.8 m excavated diameter, with a low pH concrete liner thickness of ~ 0.15 m, see Fig. 2-1) and are separated from one another by ~ 40 m.

The spent fuel, contained in canisters 5.35 m long, ~ 1 m diameter with a wall thickness of 0.15 m, and the vitrified high level waste, contained in canisters ~ 3.25 m long, ~ 1 m diameter and a wall thickness of 0.15 m (Patel et al. 2012), are emplaced coaxially ~ 3 m apart within the system of parallel tunnels on a pedestal of highly compacted bentonite blocks (dry density ~ 1'750 kg m^3). The space is then back filled around the canisters with highly compacted bentonite pellets. The reference MX-80 bentonite has an emplacement dry density of 1'450 kg × m^{-3}, which at full saturation results in a swelling pressure of 3 – 4 MPa and a hydraulic conductivity of ~ 5 × 10^{-14} m s^{-1} (Karnland et al. 2007). At emplacement, the bentonite bedding blocks and bentonite pellets yield a combined dry density of ~ 1'500 kg m^{-3}. The characteristics of compacted MX-80 are given in Chapter 4.

The SF/HLW waste comes in two basic forms, as spent fuel (irradiated fuel rods) or as vitrified high level waste from reprocessing.

Irradiated fuel rods consist of stacks of cylindrical ceramic pellets of UO_2 (or a blend of UO_2 and PuO_2 (MOX)) in tubes of zirconium alloy cladding (Zircaloy) containing a wide variety of radionucides including fission products and activation products. A large number of fuel rods (100 to 200) form a fuel assembly. Some of the activation products, e.g. ^{14}C and ^{36}Cl, are in both the fuel pellets and structural materials (Zircaloy, and spacers and plates made from stainless steel and nickel alloys from fuel assemblies). Others, e.g. actinides, are present in the fuel only (see Chapter 9).

In vitrified high level waste, the highly radioactive liquid from reprocessing is evaporated, calcined and mixed at high temperatures with borosilicate glass forming additives to produce a homogeneous molten glass-matrix which is poured into stainless steel flasks and allowed to solidify before sealing by welding (see Chapter 8).

Concrete liners will be used to provide stable and safe conditions in the tunnels during the construction and operation phases, Fig. 2-1. The liners have no long-term safety function. Hence, they should not compromize any of the long-term safety functions of other repository components through interactions with them. In view of this, a "low pH concrete" is preferred (see Chapter 4) to minimize detrimental interactions with the bentonite and Opalinus Clay.

A longitudinal section and cross sections through an emplacement tunnel are shown in Fig. 2-1.

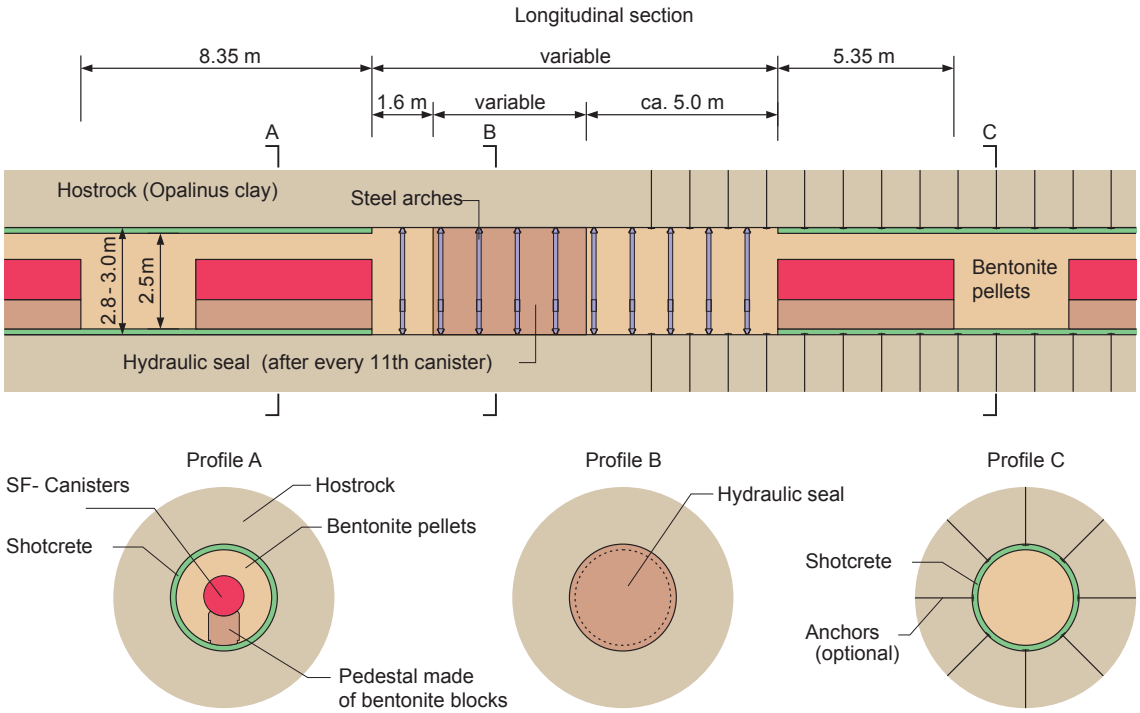

Fig. 2-1: Concept for the construction of the SF disposal galleries.

Vertical profiles through the SF disposal gallery at three different positions are illustrated (Nagra 2010, Fig. 5.2-2).

3 General overview of the evolution processes in a SF/HLW nearfield

Once the carbon steel canisters containing the high level waste or spent fuel have been emplaced, and the tunnels back filled and sealed, re-saturation of the initially "dry" compacted bentonite with the porewater from the Opalinus Clay formation will occur, and the components within the near field system and the adjacent host rock, will begin to interact with one another and evolve over many hundreds of thousands of years. With the exception of the chloride concentration, the Opalinus Clay and bentonite porewaters are chemically speaking very similar and consequently no negative consequences are expected through their interactions with one another.

The conditions in the compacted bentonite are initially aerobic, and may remain so for tens of years after closure. Because SF/HLW waste is heat generating, steep temperature gradients will form which hinder the saturation of the bentonite and may lead to mineral redistributions. The system gradually becomes anaerobic because of the consumption of entrapped oxygen, and the bentonite reaches saturation. Temperatures in the bentonite could remain above 50 °C for more than 1'000 years (see Chapter 6). The Opalinus Clay porewater saturating the bentonite must pass through the low pH concrete liner thus inducing steep chemical gradients in all three materials leading to dissolution/precipitation reactions. Such processes are likely to result in a reduction in transport rates across the two boundaries due to local clogging of the porosities on the bentonite and Opalinus Clay sides of the interfaces (see Chapter 5). The time scales involved are very uncertain. The reaction of anaerobic water with the steel produces iron corrosion products and hydrogen gas. Pressure build-up of hydrogen in the nearfield occurs since the accumulation rate is larger than the dissipation rate (Papafotiou & Senger 2014). In this context "pore blocking" and the resulting decrease in transport rates may become important issues. The carbon steel canisters are expected to maintain their integrity for at least 10'000 years, at which point radionuclides could be released. For the expected realistic corrosion rate of 1 μm/yr[5], iron in the breached canister would be present for in excess of 100'000 years. Over a period of ~ 100'000 years the corrosion products will have been in contact with the saturated compacted bentonite and interactions may have occurred leading to mineralogical changes in the bentonite. Various scenarios are possible, and their consequences need to be assessed. Once a canister is breached, the radioactive waste form (either spent fuel or vitrified high level waste) will be contacted by water under reducing conditions. It is anticipated that the conditions remain reducing even when radiolysis occurs. Under reducing conditions, the UO_2 (and PuO_2) pellets in the spent fuel have very low solubilities (see Chapter 9), and, because of the very low quantities of porewater present in the bentonite, the masses dissolved are likely to be exceedingly small. Radioactive and stable elements will be dissolving simultaneously from the waste, and thus both must be included in solubility considerations and sorption evaluations. In general, the influence of competitive sorption on transport rates is an issue and needs to be addressed (see for example Bradbury & Baeyens (2005), Pfingsten et al. (2011)). The fate of the released silica from glass corrosion must also be considered.

[5] The reference corrosion rates for Nagra's safety analyses have been reconsidered recently (Diomidis 2014). A statistical evaluation of experimental data resulted in a mean value of 0.43 μm/y. For the safety analyses, however, a higher reference value of 2 μm/y was selected. In this study, the earlier value of 1 μm/y was kept.

The aim of this report is to identify the main geochemical interaction processes occurring in a SF/HLW nearfield and their time-dependence, and to clarify how they might affect safety-functions (Nagra 2014a). In particular, the influence of these processes on, and their potential consequences for, radionuclide solubilities and transport characteristics (sorption, diffusion) of the compacted bentonite backfill and the adjacent host rock as time progresses has to be assessed.

4 "Initial states"

The main components in the nearfield of a SF/HLW repository are the waste package (carbon steel canister containing spent fuel or vitrified high level waste), the backfill material i.e. compacted MX-80 bentonite, a concrete liner in the emplacement tunnel and the adjacent host rock, Opalinus Clay. In order to make clear what the influences of the main evolution processes are, an "initial state" for the bentonite and the Opalinus Clay is defined in which no temporal changes have taken place. The source of the saturating water can only be the Opalinus Clay porewater, and because of the overwhelmingly greater buffering capacity of the host rock, this porewater will eventually condition the bentonite to be in equilibrium with it.

The procedure adopted is then to discuss the main processes occurring during the evolution of the near field geochemistry and consider their potential influences (see Chapters 5 to 9). The advantage of this methodology is that the factors influencing the evolution of the near field are described and their impact on safety functions is assessed separately so that the relative importance of each can be clearly seen i.e. how are the "initial state" conditions changed, and what are the implications of these changes. The potential interactions between the different components and processes and their influences on the barrier function of the MX-80 bentonite, with particular reference to swelling, radionuclide solubilities and sorption, are brought together in a final chapter.

4.1 "Initial states": MX-80 Bentonite and Opalinus Clay mineralogies

The "initial state" mineralogies of MX-80 bentonite and Opalinus Clay are given in Tab. 4-1 and 4-2, respectively. Tab. 4-3 summarizes their physico chemical and diffusion characteristics.

Tab. 4-1: "Initial state" MX-80 bentonite mineralogy.

(Müller-Vonmoos & Kahr 1983)

Minerals	**Wt. %**
Montmorillonite	75
Illite	--
Kaolinite	< 1
Calcite	0.7
Cristobalite	--
Gypsum	--
Muscovite	--
K-feldspar	5 – 8
Plagioclase	--
Pyrite	0.3
Siderite	0.7
*SiO_2	15.2
Tridymite	--

* Mainly quartz. According to Tab. 3 in Gailhanou et al. (2012), the total SiO_2 content in dehydrated MX-80 is 17.4 wt. % and consists of 60 % quartz, 27 % cristobalite and 14 % amorphous silica.

Tab. 4-2: "Initial state" Opalinus Clay reference mineralogy.

(Traber & Blaser 2013)

Minerals	**Wt. %**
Illite	24
Ill/Sm mixed layer	9
Smectite	0
Kaolinite	18
Chlorite	9
Chl/Sm mixed layer	0
SiO_2 (Quartz)	20
Calcite	13
K-feldspar	2
Plagioclase	0.9
Dolomite/ankerite	0.4
Siderite	4
Anhydrite	0
Gypsum	0
Pyrite	1

Tab. 4-3: Physio-chemical characteristics and diffusion coefficients for MX-80 bentonite and Opalinus Clay

(Berner et al. 2013, Kosakowski & Berner 2013)

	CEC ($meq\ kg^{-1}$)	**Bulk Dry Density** ($kg\ m^{-3}$)	**Total porosity**	**Anion porosity**
MX-80 Bentonite	*787	1'500	0.36	0.05
Opalinus Clay	**106	2'380	0.12	0.06

* Bradbury & Baeyens (2002)
** Nagra (2010)

Finally, for completeness, the structural formula of Na montmorillonite is presented. (Note that MX-80 is taken here as a "generic bentonite" since the actual bentonite which will be used in a few decades time is of course currently not known.) This structural formula of the montmorillonite fraction of MX-80 bentonite was investigated by Sauzéat et al. (2001) and was further refined by Tournassat et al. (2004) to yield the following structural unit cell formula for the Na-saturated form:

$$(Si_{3.98}\ Al_{0.02})(Al_{1.55}Fe^{3+}_{0.09}Fe^{2+}_{0.08}Mg_{0.28})\ O_{10}(OH)_2\ Na_{0.38}$$

4.2 Porewater chemistries

The Opalinus Clay porewater chemistries are given in Tab. 4-5 (Mäder 2009). In addition to the "initial state" case, two further compositions representing the band-width of partial pressures of carbon dioxide in the Opalinus Clay were calculated. The reference composition for the Opalinus Clay porewater was derived based on a large body of experimental data on aqueous extracts from an underground laboratory (Mt. Terri) or deep boreholes (Benken), combined with supplemental chemical constraints. For instance, the Ca and Mg concentrations were fixed by imposing calcite and dolomite saturation, respectively. Si, Fe(II) and S(-II) were constrained via quartz, siderite and pyrite saturation. Chloride concentrations were determined based on squeezed aqueous extracts and Na, K, Sr were controlled by measured occupancies in the exchangeable clay combined with selectivity coefficients. Finally, the carbonate system and pH were constrained by fixing the pCO_2 ($10^{-2.2}$ bar in the reference case) and applying charge balance. An overview of the assumptions and constraints can be found in Tab. 6-1 of Mäder (2009). To account for possible variations in salinity, a high-salinity water ("Mont Russelin") was defined in addition to the reference Opalinus Clay porewater (not shown in Tab. 4-4).

In order to perform reactive transport calculations including clay and cementitious materials, the Opalinus Clay porewater from Mäder (2009) had to be adapted. The modifications are described in Berner (2010) and are partly summarized in appendix A6. In essence, the modified model includes the additional equilibrium phases barite, kaolinite, illite and an ideal montmorillonite solid solution. This montmorillonite solid solution controls the cation exchange. Further, the modified model includes the elements Ba and Al. The resulting Opalinus Clay porewater is identical to that defined by Mäder (2009). The differences concern the number and nature of the constraints. The adapted Opalinus Clay porewater is constrained by ionic strength, the dominance of Na in solution, the SO_4/Cl-ratio in solution and the occupancies of exchangeable cations on the montmorillonite solid solution. The main difference to the model of Mäder (2009) is that the system pCO_2 becomes a calculated entity ($10^{-2.32}$ bar in the adapted model), in accordance with the requirements formulated in Pearson et al. (2011). The adapted model involves 90 % of the Opalinus Clay mass. The extended phase assembly produces enhanced robustness against parameter changes, and the consistency with thermodynamic models for concrete materials has been previously demonstrated (see Chapter 5).

The PSI/Nagra Chemical Thermodynamic Database 12/07 (Thoenen et al. 2014) is intended for use solely at 298.15 K (25 °C). ΔH, ΔCp and ΔS data necessary for calculations at different temperature are included for many but not all species and solids. Hence, fully consistent calculations at temperatures different from 25 °C are presently not possible. For individual questions at other temperatures the database is applicable, provided that the existing data gaps can be filled with reliable data. Concerning the solubility at elevated temperatures, some efforts have been undertaken (Thoenen et al. 2002) for a few selected safety relevant nuclides (Am, Pu, Np, U, Th, Tc), but the work has not yet been completed.

Tab. 4-4: "Initial state" and range of Opalinus Clay porewater chemistries, concentrations are given in mol L^{-1}.

(Mäder 2009)

	Opalinus Clay "Initial state"	**Opalinus Clay HIGH P-CO_2**	**Opalinus Clay LOW P-CO_2**
Temperature (°C)	25	25	25
pH log P-CO_2 (bar) Ionic strength (mol kg^{-1}) pe	7.203 -2.20 0.2299 -2.781	7.001 -1.80 0.231 -2.550	7.505 -2.80 0.229 -3.126
Dissolved constituents			
Na	1.644×10^{-1}	1.650×10^{-1}	1.638×10^{-1}
K	2.604×10^{-3}	2.616×10^{-3}	2.594×10^{-3}
Mg	9.625×10^{-3}	9.748×10^{-3}	9.519×10^{-3}
Ca	1.251×10^{-2}	1.268×10^{-2}	1.237×10^{-2}
Sr	2.106×10^{-4}	2.124×10^{-4}	2.091×10^{-4}
Ba	--	--	--
Al	--	--	--
Fe^{II}	5.24×10^{-5}	5.42×10^{-5}	5.09×10^{-5}
Fe^{III}	3.31×10^{-9}	1.73×10^{-9}	9.72×10^{-9}
Si	1.779×10^{-4}	1.78×10^{-4}	1.79×10^{-4}
Cl	1.600×10^{-1}	1.600×10^{-1}	1.600×10^{-1}
S^{IV}	2.472×10^{-2}	2.470×10^{-2}	2.474×10^{-2}
S^{-II}	1.24×10^{-8}	1.37×10^{-8}	1.16×10^{-8}
C^{IV}	2.506×10^{-3}	4.148×10^{-3}	1.214×10^{-3}

Saturated solids for Opalinus Clay: calcite, dolomite (ordered), quartz, siderite and pyrite.

Bentonite porewater compositions are given in Appendix C.

4.3 Low pH concrete liner

The mineral composition of the low pH concrete (ESDRED shotcrete) liner is given in Tab. 4-5 and the equilibrium water chemistry in Tab. 4-6.

The reactive transport calculations were performed using the adapted Opalinus Clay porewater, as mentioned in Section 4.2 and partly summarized in Appendix A6. Hence, the consistency with the porewater chemistry of the low-pH ESDRED concrete in dynamic calculations is ensured.

Tab. 4-5: Phase composition calculated for the low-pH ESDRED shotcrete.

(The total mass of 2'388.4 g includes 118.9 g of solution phase.) (Berner et al. 2013).

Phase	**Stoichiometry**	**Mass** [g]
Solid solution phases		
Jennite	$(SiO_2)(CaO)_{1.667}(H_2O)_{2.1}$	324.58
Tobermorite_II	$(SiO_2)(CaO)_{0.833}(H_2O)_{1.333}$	
Al-ettringite	$Ca_6Al_2(SO_4)_3(OH)_{12}(H_2O)_{26}$	38.88
Fe-ettringite	$Ca_6Fe_2(SO_4)_3(OH)_{12}(H_2O)_{26}$	
Hydrotalcite	$Mg_4Al_2(OH)_{14}(H_2O)_3$	11.31
Fe-hydrotalcite	$Mg_4Fe_2(OH)_{14}(H_2O)_3$	
Single phases		
Gibbsite	$Al(OH)_3$	1.45
Barite	$BaSO_4$	3.27
Calcite	$CaCO_3$	10.56
Hydro-magnetite	$Fe_3O_4(H_2O)_2$	0.005
Ferrihydrite	$Fe(OH)_3$	7.27
Illite	$K_{0.6}Mg_{0.25}Al_{2.3}Si_{3.5}O_{10}(OH)_2$	17.42
Celestite	$SrSO_4$	0.004
Inert (SiO_2)*)	SiO_2	1784.7

* The term "Inert (SiO2)" mainly includes non-reacting concrete aggregates. As the name suggests, this component does not undergo any chemical reaction in the calculations but was assigned the chemical and physical properties of quartz for keeping track of mass, volumes and necessary physical parameters.

Tab. 4-6: Low-pH ESDRED shotcrete: calculated equilibrium pore solution (Berner et al. 2013)

ESDRED low pH concrete	
pH	11.07
E_h	-180.7 mV
IS	0.150
Element	**Calculated pore water composition** (mmol/kg)
Al	0.12
Ba	2.2×10^{-4}
C	0.0168
Ca	5.39
Cl	124.3
Fe	3.9×10^{-5}
K	25.71
Mg	1.2×10^{-4}
Na	104.9
S	7.88
Si	0.353
Sr	0.41

Total porosity for ESDRED cement = 0.18

Cation and anion diffusion coefficient in ESDRED cement = 4.9×10^{-11} m^2s^{-1}

4.4 Carbon steel canister

For spent fuel the nominal dimensions of the carbon steel canister are 5.35 m long, 1.05 m outer diameter with a wall thickness of 0.14 m (body) to 0.18 m (lid), and for the vitrified high level waste, 3.23 m long, 0.72 m outer diameter and a wall thickness of 0.14 (body) to – 0.18 m (lid) (Patel et al. 2012).

For a 516 grade 70 carbon steel, the ASME standard composition is, dependent on grade:

Carbon:	0.27 – 0.31 wt. %
Manganese:	0.79 – 1.3 wt. %
Phosphorus:	0.035 wt. % max
Sulphur:	0.035 wt. % max
Silicon:	0.13 – 0.45 wt. %

5 Interaction of a low pH concrete tunnel liner with Opalinus Clay and bentonite

5.1 Introduction

A shotconcrete liner is required as a supporting structure in the SF/HLW emplacement tunnels for operational safety reasons (Nagra 2010, 2014a).

Given the sharp geochemical gradients between clay and shotcrete, the following effects in the nearfield due to the interactions at the interfaces between clay and liner can be expected:

- Dissolution of clay minerals (in bentonite, Opalinus Clay) which will locally affect the radionuclide sorption capacity.
- Changes in the cation exchange population will to a certain degree affect the swelling pressure of the bentonite.
- Changes in porosity due to precipitation/dissolution of minerals which will locally influence the transport properties (hydraulic conductivity, diffusivity).
- Changes of pH in the bentonite or Opalinus Clay will impact the radionuclide sorption and solubilities.

The central question is:

How much buffer and host rock material will be affected by the interactions due to chemical gradients in space and time?

Concretes and clay materials are chemically very different materials: Concretes are artificial materials produced from cement, aggregates (sand or gravel) and water. The initial ingredients in concrete are in thermodynamic disequilibrium which induces short term transformations that are responsible for the demanded material properties (handling, curing, strength). The initial porewater chemistry is dominated by high pH values (13 and above) due to the significant amounts of dissolved alkali hydroxides. In the long term, slow mineral transformations such as alkali-aggregate reactions will change the initial cement mineral assembly and lower the pH of the porewater.

Clay materials are natural materials that contain high amounts of swelling (montmorillonite) or non-swelling (illite, kaolinite) clay minerals. Porewaters typically have a near neutral pH. Porewater compositions are not solely determined by mineral equilibria. Cation exchange processes and surface complexation on the charged surfaces of clay minerals also have a strong impact.

Concrete – clay interactions are likely to be influenced by various chemical and transport processes (Fig. 5-1) and their interactions (Fig. 5-2). From a chemical point of view, mineral precipitation and dissolution kinetics, as well as ion exchange reactions, might alter the pore space with accompanying changes in material transport, flow and mechanical properties. In terms of transport, the saturation state, the water flow and the diffusion of solutes across the material interfaces, will strongly influence the extent and time-scale on which chemical processes occur. Even without a concrete liner, the bentonite and Opalinus Clay porewaters will not be in equilibrium in terms of salt content (ionic strength). Both compartments will equilibrate predominantly by diffusive transport through the concrete liner and induce chemical disequilibrium there. The temperature pulse originating from the spent fuel decay heat may also accelerate chemical transformations, change the stability of mineral phases in the cement

material and accelerate diffusive transport. Last but not least, mechanical processes such as tunnel convergence or the swelling of clay minerals, might also change the pore space and the associated transport parameters. Tunnel convergence is expected to induce (micro-) cracks at the interface (in the liner) which would enhance the transport of solutes and would override the effects of pore clogging due to mineral precipitation. The enhanced transport will accelerate mineral transformations at the interfaces and mineral precipitation might close the (micro-) cracks (pathways) again. A simple sketch showing many of these complex interdependencies is given in Fig. 5-2.

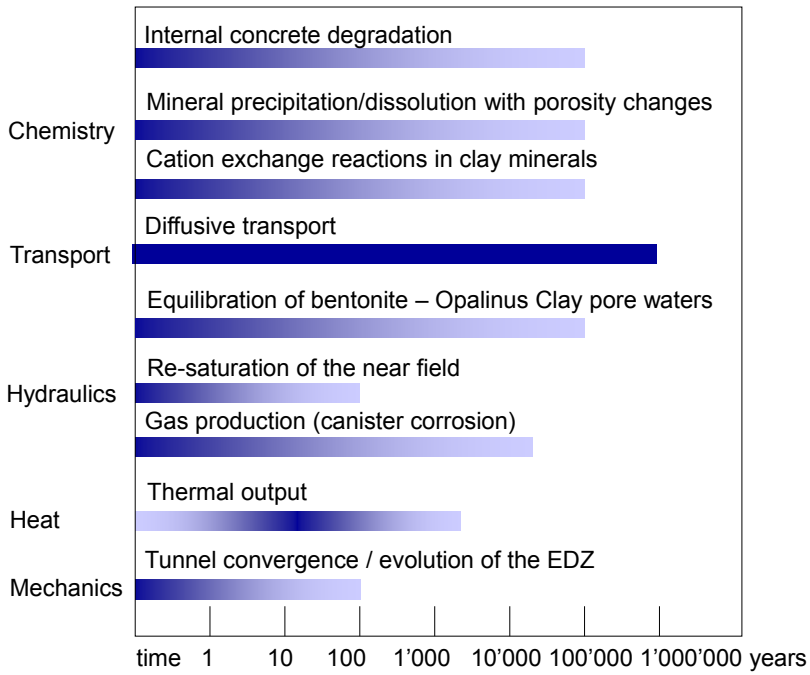

Fig. 5-1: Processes that might influence the evolution of a concrete liner and the interactions with surrounding barriers.

Interactions between processes are not considered. The colour intensity and the length of the bars are qualitative indications of the strength and the time frame of influence (Kosakowski et al. 2014).

Under saturated conditions, due to the very low permeability of bentonite and Opalinus Clay, fluid and solute transport are essentially dominated by diffusion. The long time scale of diffusive processes, which limit the rate of chemical changes, implies that such systems are not readily accessible in laboratory experiments. Consequently, the information from relevant natural analogues and the results from reactive transport calculations, in combination with simple mass balance calculations, are normally used to assess the extent of possible changes of the engineered and natural barriers on PA-relevant time scales. For some processes, and process couplings, there is little or no information in the literature. This includes the interactions of chemical and mechanical processes in the liner and the influence of elevated temperatures on the liner and its chemical evolution.

Information from literature reviews and mass balance calculations give some indication of the maximum possible changes of barrier materials, but cannot provide insight into the spatial and temporal evolution of the overall system, the specific influence of single processes (e.g. pore space changes), and on the feedback between different processes.

Reactive transport calculations specifically tailored to the bentonite, Opalinus Clay and concrete materials foreseen in the Swiss disposal design have been performed. Such reactive transport calculations allow a new qualitative view into the system evolution since different processes and couplings can be considered simultaneously (see Fig. 5-2). The current models are not yet able to consider all of the processes, and their predictive value is limited at the moment, but they represent an important step towards more realistic evaluations of real systems.

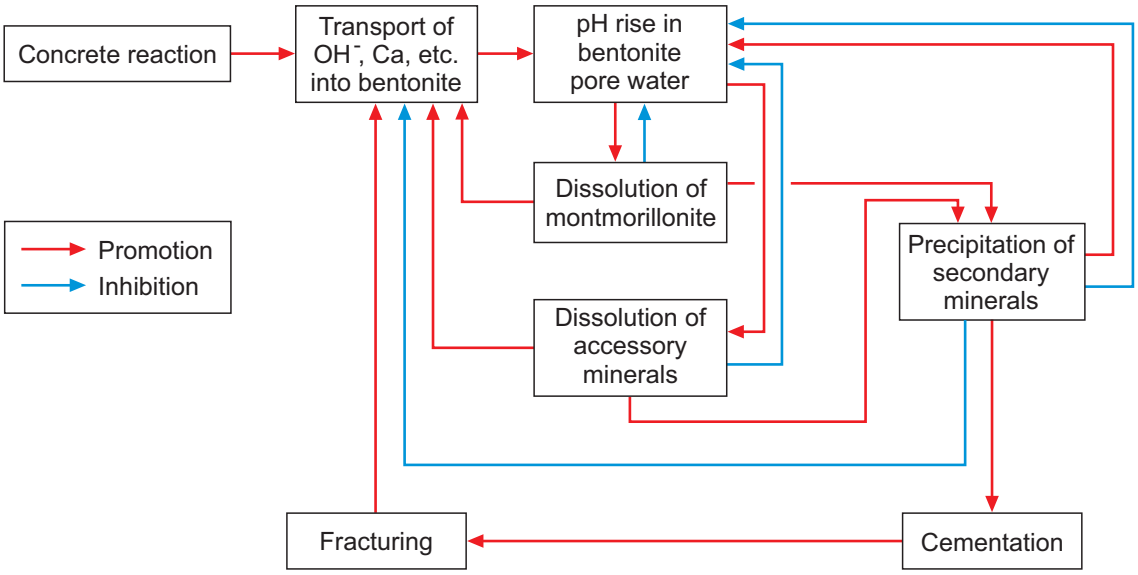

Fig. 5-2: Cement-bentonite interaction as a coupled non-linear system.
Savage et al. 2010a, after Metcalfe & Walker 2004

Setting up such coupled models in turn necessitates the refinement of geochemical models for cementitious (concrete) and clay materials and, particularly, the development of a consistent set of thermodynamic data valid for both types of materials simultaneously. For the liner materials a recent thermodynamic database CEMDATA07, based on the work of Matschei et al. (2007), was implemented to describe cement minerals in terms of solid solutions. Recently, an alternative database for cement materials was published (Blanc et al. 2010a, 2010b) which was not available at the time model calibrations were carried out. Since model calibrations simultaneously included thermodynamic data on concrete and clay components (montmorillonite), the decision was made to use the data from CEMDATA07. The development of the CEMDATA07 database used the same source data (Nagra/PSI TDB 01/01, Hummel et al. 2002) as was used in the present report. A full comparison of the two data sets and a benchmark exercise indicating potential differences in modelling results are not yet available. The chemical models by Blanc et al. (2010a, 2010b) do not yet include data for solid solutions, whereas the model calculations in the present report mainly rely on describing hydrated cement minerals in terms of solid solutions.

For clay materials, the reference PSI/Nagra Chemical Thermodynamic Database 12/07 (Thoenen et al. 2014) was supplemented with newly evaluated solid solution thermodynamic data on montmorillonite. The inclusion of smectites is discussed and was called for in a recent paper on Opalinus Clay porewater modelling (Pearson et al. 2011). Some first attempts in this direction have already been made by Gaucher et al. (2009) in modelling the Callovo-Oxfordian argillite. A more comprehensive and coherent database for clay minerals is now available (Blanc et al. 2012), but was not considered in the present work.

5.2 Summary of the existing literature on experimental data, natural analogues and reactive transport calculations on cement-clay interactions

Gaucher & Blanc (2006) give an overview of the publications on experiments, natural analogues and modelling related to cement/clay interactions. Based on their literature review they conclude that it is premature to make any definite conclusions on the consequences of an alkaline disturbance in a clay medium. They consider that the mineralogical consequences of an alkaline disturbance are fairly well-known, although the thermodynamics of the clays, zeolites and cement phases need to be improved. Large uncertainties remain in the fields of dissolution kinetics and mineral precipitation, especially for the dissolution kinetics of montmorillonites. Finally, they state that: "The simulations will become increasingly representative in so far as we are able to take into account a specific geometry, the complexity of the concrete and bentonite mineralogical systems; to incorporate the surface chemistry of the clays, zeolites and CSH phases; and to consider a mineralogical control of the pCO_2 and the evolution of the porosity."

Savage et al. (2002) modelled the alteration of bentonite by hyper alkaline fluids at a cement-bentonite interface in a diffusive transport environment. They found a maximum porosity increase of up to 80 – 90 % over a narrow 1 – 2 cm zone close to the cement -bentonite contact surface. All of their simulations (except one with alternative aqueous speciation data for Si) showed a total filling of the porosity a few centimeters beyond the interface into the bentonite after about 3'200 years.

Traber & Mäder (2006) performed a detailed reactive transport modelling study of the concrete/Opalinus Clay interface with an in-depth analysis of the evolution of reaction fronts and associated mineralogical and porosity changes. The model was, in part, calibrated with laboratory experiments. One specific long-term advection-diffusion experiment using a K-Na-Ca-OH synthetic cement water as input resulted in complete clogging after approximately one year (Adler 2001, Adler et al. 2001). While some mineral alteration could be determined, a reduction in porosity at the cm-scale could not be confirmed. It was inferred that the clogging process preferentially affects pore throats, and may not require substantial mass transfer. The overall features could be described with a reactive transport model (Adler 2001), and most of the kinetic constraints used by Traber and Mäder (2006) were based on this laboratory experiment and related work.

Trotignon et al. (2007) did numerical modelling on the durability of concrete engineered barriers in contact with mudrock (clay host rock). They believe that one key process is the "progressive localized cementation of the altered mudrock." Their results suggest that "a sharpening of the cementation front will occur, and lead to low cementation lengths in the mudrock (~ 0.2 m)."

Yang et al. (2008) presented a numerical model of coupled saturated/unsaturated water flow, heat transfer and multi-component reactive solute transport for the calculation of the geochemical evolution of a SF/HLW multi-barrier system. The model consists of a bentonite buffer having a thickness of 0.75 m, and a concrete liner of 0.2 m thickness in a clay formation. They found that the porosity decreased from 0.37 to 0.18 during the first 10'000 years in the clay near the concrete-clay interface. Their modelled minimum porosity in the concrete was 0.045 after 350'000 years. In their simulations the porosity was never blocked completely, which was attributed to the inclusion of cation exchange reactions and the exclusion of Na-montmorillonite dissolution.

Watson et al. (2007) modelled the interaction between low pH cements and bentonite. The extent of bentonite degradation was much less for low pH cement porewater than for Ordinary Portland Cement (OPC). In some of the cases investigated the authors observed complete blocking of the porosity within 1'000 years due to the precipitation of laumontite, whereas in other cases this was not the case. Watson et al. (2007) concluded that their model results depend very strongly on the geochemical setup: e.g., the use of solid-solution models for the CSH gels, uncertainties concerning the precise mechanism and the rate constant of montmorillonite dissolution at elevated pH, the role of dissolved Si and the consideration/selection of secondary minerals.

The group of De Windt and van der Lee at the Ecoles des Mines de Paris used the HYTEC code to model the evolution of clay-cement interfaces (De Windt et al. 2004a,b, De Windt et al. 2007, 2008, De Windt & Badreddine 2007). In De Windt et al. (2004b) they found that the precipitation of calcite or minerals with a high molar volume, such as CSH and zeolites, may lead to a significant decrease of the pore volume at the cement/claystone interface. They present a case where the porosity on the clay side of the interface is clogged within 2'500 years, but they conclude that "this result should be considered with care. The clogged area is relatively thin and may thus be mechanically fragile. The model assumes homogeneous precipitation within a representative elementary volume and complete sealing of the pore space. They claim that in reality clogging is more heterogeneously distributed and less perfect".

De Windt et al. (2008) performed numerical modelling in order to match the mineralogical and petrographical observations of a Tournemire site borehole, first sealed by concrete and then over-cored after 15 years of concrete/argillite interactions. They recognized that the inclusion of kinetic precipitation and dissolution rates was necessary to reproduce the mineralogical changes observed on the argillite site of the interface. They could qualitatively match the major mineralogical alterations, although there were still some differences between experiment and modelling in terms of the formation of single mineral phases.

A similar approach was presented by Arthur et al. (2006) in which they tried to do an experimental calibration of a reactive-transport model of buffer cementation in the framework of the Stripa and Äspö field tests (LOT). They successfully fitted the mineralogical evolution in the experiments, but could not reproduce the data on permeability/diffusivity/porosity changes measured in the experiments.

Based on short term experimental data on mineralogical transformations Fernández et al. (2009, 2010) modelled concrete interaction with a bentonite barrier and made long-term predictions on the behaviour of the interface. They calculated that total clogging occurred after 5'000 years. They found several sources of uncertainties in the system; kinetics of mineral dissolution/precipitation reactions are not known for many minerals, coupling between geochemical processes and thermo-hydro-mechanical properties is normally not considered, clay specific processes such as anion exclusion are also not included in such modelling studies. They found a fundamental lack of detailed knowledge on how the processes operate at the pore scale, and how such details could be up-scaled.

Marty et al. (2010) found strong indications for sealing at interfaces in numerical investigations of the alteration of a bentonite plug by iron corrosion and concrete interactions. Yang et al. (2008) reported investigations on a similar system and found incomplete clogging, which they attributed to the high initial porosity of the bentonite buffer.

Marty et al. (2009) investigated the influence of reaction kinetics and mesh refinement on the results from numerical modelling of concrete/clay interactions. They investigated an interface between concrete and the Callovo-Oxfordian argillite in a fully saturated diffusive transport regime. A major result of their study is summarized in Fig. 5-3. They define complete porosity clogging when the porosity reaches a value of 0.01. From Fig. 5-3 it becomes evident that calculated clogging times strongly depend on the spatial discretization of the model/interface domain. This can be easily explained by the fact that on the one hand the solute flux across the interface is independent of the discretization. On the other hand the absolute change of solid volume due to chemical reactions directly at the interface depends on the solute flux. As a smaller volume can be filled much faster for the same solute flux, the relative volume change (porosity) is directly linked to the spatial discretization. The introduction of kinetic limitations for geochemical reactions also influences the clogging times. If kinetics strongly controls the mineral precipitation/dissolution, the dependency of clogging times on spatial discretization is weakened. Marty et al. (2009) conclude that "in order for a simulation to be as representative as possible of temporal and spatial scales of cementation, the processes must be supported by more comparative data such as long term experimental investigations of natural analogues."

It should be noted that the findings of Marty et al. (2009) still represent the state of the art in this area of coupling chemistry with transport. In order to become predictive it is absolutely necessary to parameterize or calibrate the computer models using relevant experimental data.

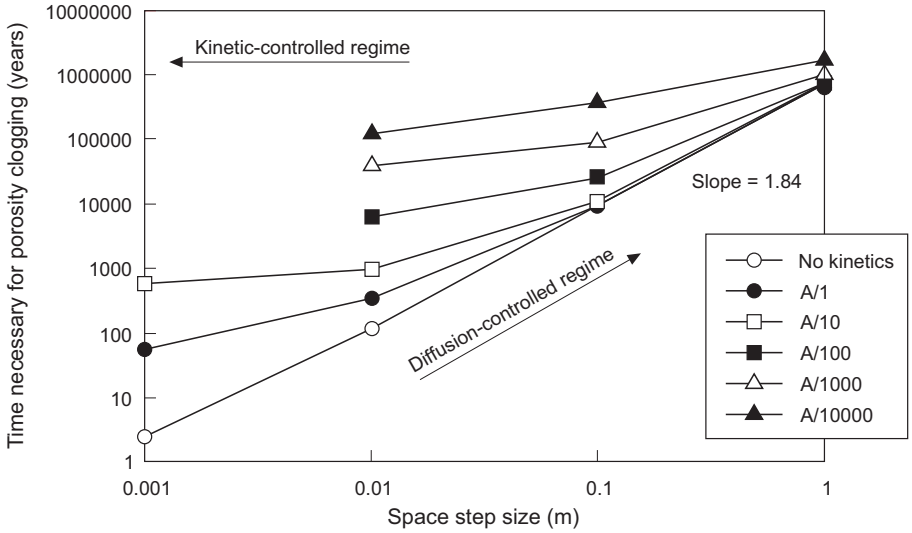

Fig. 5-3: Variation in the time necessary for porosity clogging as a function of both the spatial discretization and the reaction rate from Marty et al. (2009).

"A" denotes the specific reactive surface area which is changed to simulate varying reaction kinetics. A/1 denotes the fastest and A/10000 denotes the slowest reaction.

5.2.1 Influence of saturation

Studies on the influence of water saturation on cement/clay interface reactions are scarce. Tinseau et al. (2006) performed a mineralogical characterization and mass-balance calculations of the Tournemire argillite after in situ interaction with concretes in a geometrical setting where one side of the concrete is exposed to air. They differentiate between dry and wet contacts and

conclude that no significant modifications of the argillite are observed after 125 years at low water saturations, except for pyrite dissolution and gypsum precipitation. In the presence of water, precipitation of gypsum, recrystallization of mixed-layer clays, neoformation of zeolites and K-feldspars overgrowth are observed[6]. At the concrete/argillite interface dolomite neoformation and leaching of chloride and kaolinite occur. The processes are enhanced with contact time, low flow rate and the nature of the concrete.

A review on the changes of hydrological properties of aquifer media due to chemical reactions was done by Saripalli et al. (2001). Based on a literature review they give recommendations for future research. Some topics relevant to the evolution of cement/clay interfaces are: changes in the specific solid (mineral)-water contact area as a function of the degree of water saturation and the effect of the water saturation itself on the diagenetic processes (including precipitation and dissolution).

Simulations of reactive transport in partially saturated media have been done for example, by Burnol et al. (2006, 2007), Gherardi et al. (2007), Molins & Mayer (2007), Xu (2004), Xu et al. (2006), and Wellman et al. (2008).

Burnol et al. (2006, 2007) simulated the interactions at a concrete/clay interface and investigated the influence of temperature, unsaturated conditions and porosity variations. They calculated an occlusion of the porosity close to the interface, but did not report any details on this finding.

Gherardi et al. (2007) numerically modelled the self-limiting and self-enhancing caprock alteration induced by CO_2 storage in a depleted gas reservoir using a reactive transport code. Although this system is not identical to a clay/cement interface, the behaviour in terms of porosity changes has some similarities. They found that *"when a free CO_2-dominated phase migrates into the caprock through pre-existing fractures, or through zones with high initial porosity acting as preferential flow paths for reservoir fluids, low pH values are predicted, accompanied by significant calcite dissolution and porosity enhancement. In contrast, when fluid-rock interactions occur under fully liquid-saturated conditions and a diffusion-controlled regime, the pH will be buffered at higher values, and some calcite precipitation is predicted which leads to further sealing of the storage reservoir".*

5.2.2 Experimental data and natural analogues

An exhaustive overview on the available experimental and natural analogue data on cement/clay interactions is given by Gaucher & Blanc (2006). Another extensive overview of experimental data is given in Metcalfe & Walker (2004). There are many data on the mineralogical evolution of such interfaces available, also from newer studies (Cuevas et al. 2006, Yamaguchi et al. 2007). A recent overview of experimental data, specifically including natural analogues, is given by Savage (2009, 2011). Quantitative experiments that can be used to "calibrate" numerical models in terms of the evolution of porosity are missing. In addition, data on porosity-permeability and porosity – diffusivity relationships under different water saturations are needed.

Jougnot & Revil (2007) presented data on the saturation dependence of the diffusion coefficient of ions in the Callovo-Oxfordian argillite. Such data can be used to define a modified Archie's relation for a specific material.

A natural analogue for the alteration of clays by high-pH solutions was found near Maqarin (northern Jordan). A very detailed description of the site can be found in Smellie (1998). At the Maqarin site hyper alkaline waters originating from naturally formed clinkers, similar to cement

[6] A critical analysis of their results shows that K-feldspars overgrowth can not be observed with the experimental methods used in this study (Gaucher, personal communication).

waters with a high pH, circulated through fractures in a clayey biomicrite. The fracture walls showed dissolution and precipitation of different minerals, whereas within the fractures different opening/closing episodes may have taken place exhibiting complex mineralogical sequences. In the extended summary of Smellie (1998), it is stated that the evidence from Maqarin shows:

- that sequences of minerals predicted by thermodynamic and coupled modelling are similar to those observed in hyper alkaline alteration zones
- that the rock matrix may be accessible to the diffusion of aqueous species even during the phase of on-going wallrock alteration
- and that narrow aperture fractures will probably be self-sealing

Although the investigated system is not purely diffusion controlled, the above findings are indications that clogging at clay/cement interfaces is possible over long times. The sealing processes in the fracture porosity and within the adjacent rock matrix have also been explored by reactive transport modelling using a dual porosity approach, both in general (Steefel & Lichtner 1994) and specifically for Maqarin (Steefel & Lichtner (1998).

Recently, a new natural analogue for the interactions of hyper alkaline waters with bentonites was investigated by Arcilla et al. (2007) and Alexander et al. (2008). At the current state of these investigations no data on clogging processes or porosity changes are available.

A study by Savage et al. (2010b) on the alteration of clay under mildly alkaline conditions (pH 9-10) at Searles Lake (California, US) yielded no indications of porosity blocking.

Gaboreau et al. (2011) characterized quantitatively the porosity at a cement – clay-rock interface at the Tournemire Underground Laboratory after 15 years of interaction and could, for the first time, verify porosity clogging. They could show that the perturbations (in terms of mineralogical and porosity changes) were limited to 3.5 cm and 1.5 – 2 cm from the interface in cement and clay rock, respectively. The concrete and clay rock were not homogeneous and contained a fissure network. Alterations were observable near the material interface and near the fissures. The porosity in the concrete increased due to portlandite dissolution, whereas the porosity in the clay rock was strongly reduced, which the authors attributed mainly to precipitation of C-(A)-S-H phases. The corresponding mineralogical data were published in Techer et al. (2012).

A similar study was conducted at the Andra Meuse/Haute Marne Underground Research Laboratory for two cement based materials/claystone interfaces after 4 to 5 years contact time (Gaboreau et al. 2012). The observed mineralogical and porosity alterations were restricted to a zone of less than 1 cm around the interface. For the two samples the porosity evolution in the cement material is quite different, increase of porosity in one case and decrease in the other. The authors attribute this to the differences in the composition of the cement materials, the interface geometry, the hydrodynamic conditions (full water saturation vs. partial water saturation, advection vs. diffusion) and spatial heterogeneities at the host rock formation scale.

5.2.3 Summary/conclusions of literature reviews

The conclusions of our literature research on possible effects of cement-clay interactions are very similar to those by Savage et al. (2010a). We repeat here the conclusion by Savage et al. (2010a):

- The interaction of cement/concrete with groundwater will lead to leaching in accord with a sequence of decreasing solubility of cement minerals with time (e.g. Berner 1992).
- The diffusive transport of solutes across a cement-clay interface leads to sharp gradients in pH (and pCO_2). Such sharp gradients may lead to rapid precipitation of carbonates, hydroxides and CSH phases, resulting in decreased porosity (e.g. Watson et al. 2009).
- The exchange of Na^+ in MX-80 bentonite by K^+ and Ca^{2+} from cement leads to a decrease in montmorillonite swelling pressure. These cation exchange reactions advance in front of dissolution-precipitation reactions (e.g. Fernández et al. 2009).
- Fast protonation-deprotonation reactions at clay edge sites can typically neutralize 55 moles of hydroxyl ions per cubic metre of MX-80 bentonite (at 2'000 kg m^{-3} water-saturated compaction density).
- Montmorillonite and other minerals present, such as quartz, feldspars, pyrite, and gypsum, are slowly dissolved at high pH. Such reactions consume hydroxyl ions and slow down the progress of the high pH front. Multiple reaction fronts form and propagate due to different dissolution and precipitation rates, with later fronts overriding those formed earlier. The overall evolution thus forms a complex porosity structure, with porosity changes within both the concrete and clay. The net change in porosity across the entire alteration zone may be small.
- Secondary minerals such as clays, hydroxides, carbonates, calcium silicate hydrates, and aluminosilicates such as zeolites and feldspars (e.g. Savage et al. 2007) are formed in a zonal fashion. C(A)SH, illite, feldspars, and the more aluminous zeolites are preferable formed at higher pH, i.e. in regions close to the interface, and the more siliceous zeolites form at lower pH, i.e. in regions further away from the interface
- The effects of the short period of increased temperatures on the liner and mechanical-chemical couplings and interactions are not well explored.

In the computer modelling studies by, for example, Fernández et al. (2009, 2010), Kosakowski et al. (2009), Marty et al. (2009), Watson et al. (2009), De Windt, et al. (2001) the cement/clay interactions are treated as non-linear systems with complex interplay between fluid and solute transport, mineral precipitation and dissolution reactions, ion exchange and consecutive changes of physical properties (porosity, hydraulic conductivity, diffusivity). These studies provide insight into coupling processes and system evolution, but largely lack predictive capabilities.

Nearly all of the above mentioned studies considered an OPC type cement, or similar, and investigated the interaction with bentonite or argillaceous rocks. To the best of our knowledge no studies exist which have investigated the interaction between the specific materials in the Swiss repository design: MX-80 bentonite, low-pH concrete (ESDRED) and Opalinus Clay.

5.3 Mass balance calculations

Bentonite buffer

Savage et al. (2010a) made some simple mass balance calculations in order to estimate the maximum amount of montmorillonite that could be dissolved due to the in-diffusion of hyper alkaline solution from the liner. They used the following reaction for the dissolution of montmorillonite at pH > 10

$$Na_{0.33}Mg_{0.33}Al_{1.67}Si_4O_{10}(OH)_2 + 4.68\ OH^- \Rightarrow$$

$$0.33Na^+ + 0.33\ Mg^{2+} + 1.67\ Al(OH)_4^- + 4\ HSiO_3^- \quad (5.1)$$

and assumed that this is the only OH^- consuming reaction. Taking into account that 1 kg of low pH concrete contains 1.69 mol of OH^-, that the molar mass of montmorillonite is 0.367 kg mol^{-1}, and that a 1 meter long tunnel segment contains 2'875 kg of low pH concrete and 1'218 kg of montmorillonite, they found that 432 kg of bentonite (~ 380 kg of montmorillonite) could be destroyed by this reaction. This amount represents about 8 wt. % of the total bentonite around the canister in a 1 m long tunnel segment. According to Section 4.1 of Savage et al. (2010a) this corresponds to an alteration thickness of 0.13 m for the given initial conditions (no tunnel convergence).

Opalinus Clay

For Opalinus Clay it has been reported by Savage et al. (2010a)[7] that 1 m^3 of Opalinus Clay can buffer the total hydroxide inventory of about 4 m^3 of typical OPC concrete. This translates into 0.12 m^3 and an alteration distance of 0.04 m of Opalinus Clay for a 1 m long tunnel segment with a low-pH liner (no tunnel convergence).

5.4 Reactive transport calculations

Mass balance calculations can be very useful and the method of choice when no other possibilities are available. They yield quantitative results, demonstrating to what extent chemical reactions may proceed. Reactive transport calculations allow the impact of single processes and the inter-relation of processes to be studied and can follow features and events in time and space. Nevertheless simplifications are necessary; this study utilizes an equilibrium chemistry approach in a fully water saturated system at 25 °C and 1 bar. The calculations which have been carried out are described in detail in Berner et al. (2013) and the thermodynamic setup in Berner et al. (2013) and Kosakowski & Berner (2013). Only a summary of the results is presented in this section. (The basic setup is given in Appendix 1.)

This section therefore summarizes the results of two reactive transport calculation cases that investigate the degradation of a concrete liner in contact with bentonite backfill and Opalinus Clay host rock. Both cases are identical in terms of geometry, boundary and initial conditions. In Case 1 the feedback from chemistry, porosity changes and transport is fully considered, whereas in Case 2 the porosity and the transport parameters (diffusivity, permeability), as well as the volume of the fluid phase, are assumed to be constant.

---

[7] Based on Sections 8.4.4 and 8.4.5 of European Comission (2005).

Case 1 is more realistic since the reduction of porosity induced by the precipitation of secondary minerals slows down the transport at the interfaces. In Case 2, the transport is assumed to continue at constant rates (constant porosity), even if the volume of the precipitates exceeds the physically available pore space. Case 2 is more conservative. It violates, to a certain extent, volume constraints, and provides an accelerated system evolution. It yields a qualitative answer as to which direction a system would evolve if the transport continued (e.g. due to cracking at interfaces induced by tunnel convergence). However, the temporal mineral evolution is no longer synchronized with the simulation time. In addition, mineral fronts are sharpened since much larger amounts of minerals can be accumulated over time.

From the large amount of information that can be extracted from the reactive transport calculation runs, we focused on:

- the temporal and spatial evolution of the porosity near the interfaces
- the temporal evolution of the mineral assemblage at the interfaces and the extent of mineral alterations
- the extent of the pH plume

5.4.1 The evolution of the mineralogical composition near the interface

Spatial mineralogical profiles are given in Fig. 5-4 to 5-8. The mineralogical evolution for both calculation cases can be summarized as follows:

In the Opalinus Clay the changes are restricted to a zone of a few centimeters thickness. Quartz reactions were not kinetically controlled, therefore quartz is partly dissolved, together with calcite, pyrite, illite and kaolinite. The clay phases are replaced by Na-montmorillonite. The volumetric changes indicate a strong tendency for clogging at the interface between the low pH shotcrete and the Opalinus Clay. The porosity reduction strongly decreases the mass flux over the interface and effectively stops any mineralogical evolution in the calculation Case 1.

The evolution of the concrete liner is similar at both interfaces. Starting from the inner interface, the ettringite and CSH phases are dissolved and a sequence of minerals precipitates: hydrotalcite, gypsum, phillipsite, clay minerals (montmorillonite) and calcite. The sequence of disappearance of cement phases is in general agreement with the changes in phase composition observed during concrete leaching (e.g. Taylor 1997). Phillipsite is formed as an intermediate phase in the middle of the shotcrete domain after 10'000 years and until 20'000 years. After the complete disappearance (dissolution) of the CSH-phase, first gypsum, and then hydrotalcite, are replaced by calcite and clays. The mineral alterations are more pronounced and faster near the Opalinus Clay boundary. The concrete degradation rate is strongly reduced once the interfaces clog. Only for the Case 2 calculation, where the mass flux over the interfaces is not altered, a complete degradation of the concrete is reached (after more than 50'000 years).

A zone with clear mineral alterations extends up to 10 cm into the bentonite when assuming full porosity feedback (Case 1). This zone is not expected to expand further since the mass flux over the interface is minimal due to porosity clogging. In Case 2 the mass flux over the interface continues even if the volume of precipitates exceeds the physically available volume. Therefore, the alteration distance is more than 20 cm at the end of the simulation run (~ 52'900 years). The progress of the alteration front will slow down with time since the concrete is already completely degraded at this time and the initially steep chemical gradients are strongly reduced. (It should be noted that the time scales given here are relative, and not absolute and are only roughly comparable.)

Mineralogical alterations in the bentonite in terms of volumetric changes are small. Close to the interface, within the first few centimeters, montmorillonite is dissolved and quartz, calcite and hydrotalcite are precipitated. The composition of the montmorillonite phase is changing slightly on a decimeter scale. The Na-montmorillonite content is reduced towards the concrete liner by a few percent and replaced by Ca-, Mg- and K-montmorillonite. The volumetric changes lead to a decrease in porosity, indicating a tendency to clog the interface.

In both model cases the overall dissolution of montmorillonite is very small. In the Opalinus Clay, no net dissolution of the clay minerals is observed. In the bentonite compartment the accumulated dissolution of montmorillonite is small and corresponds to less than a 1 cm dissolution distance at the end of the simulation for Case 2 where a constant porosity is assumed. For Case 1 in the shotcrete layer, and for Case 2 in the clay materials near the shotcrete, a re-precipitation of montmorillonite is observed. Taking into account the further degradation of the concrete, with an associated drop in pH (see Section 5.4.3), it is not expected that significantly more montmorillonite will be dissolved at later simulation times.

In summary, the mineralogical changes and their spatial extension are comparable to those described in Savage et al. (2010a). The dissolution of montmorillonite is much less than estimated by Savage using the very conservative mass balance approach and without considering any transport constraints.

Mineralogical profiles for Case 1

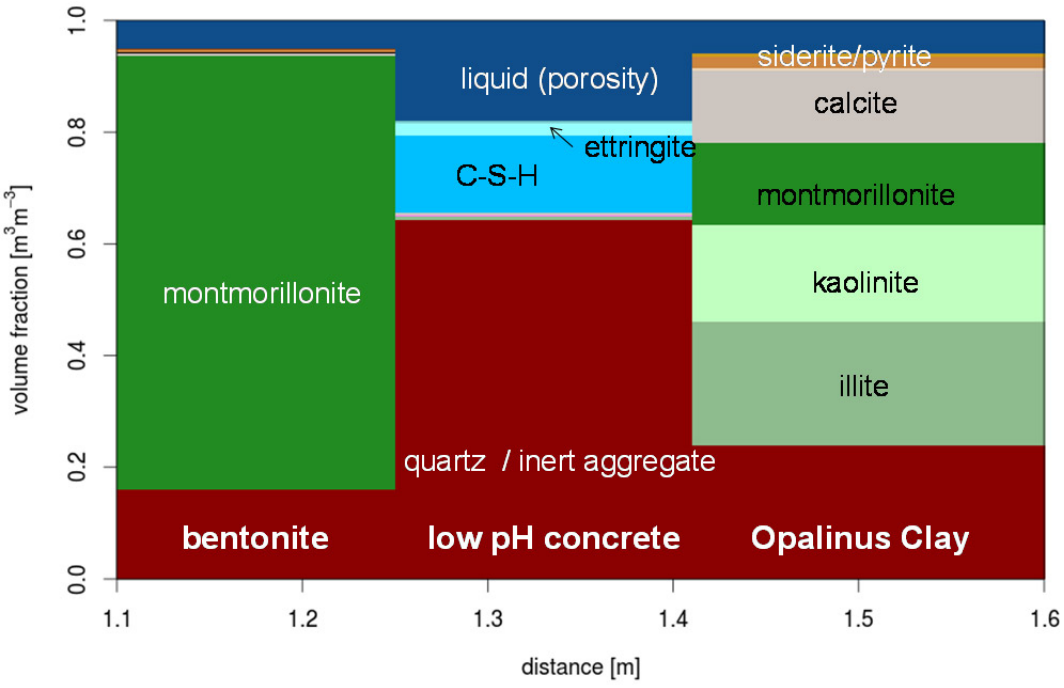

Fig. 5-4: Initial mineralogical profile across the low pH concrete liner and the adjacent bentonite and Opalinus Clay.

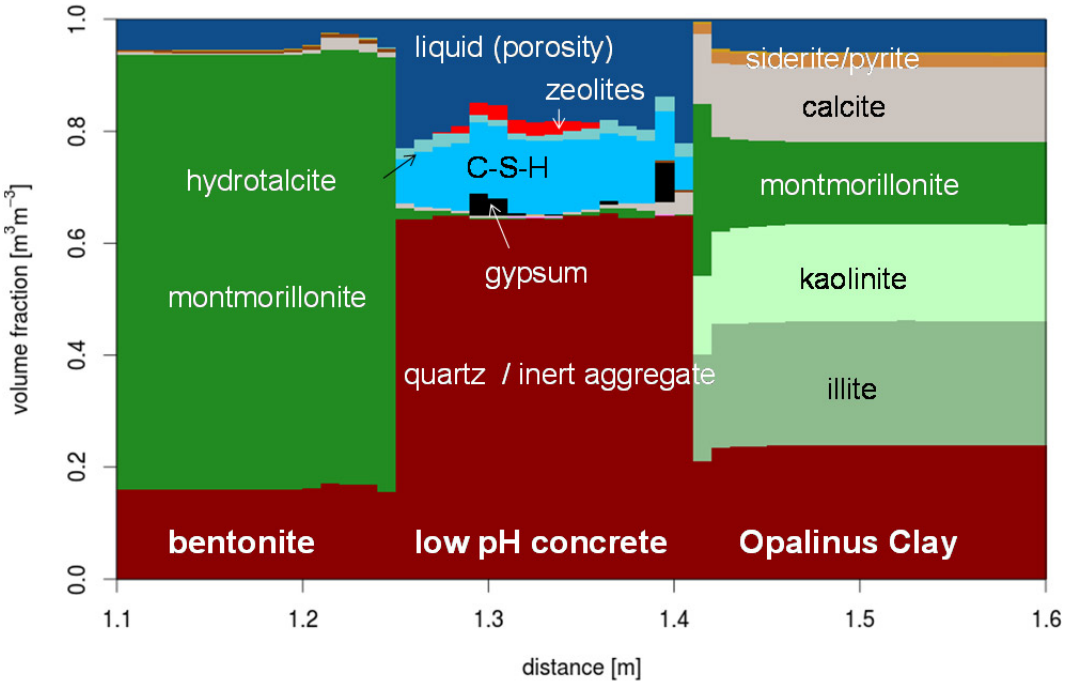

Fig. 5-5: Mineralogical profile across the low pH concrete liner layer after about 10'000 years considering full (porosity) feedback on transport.

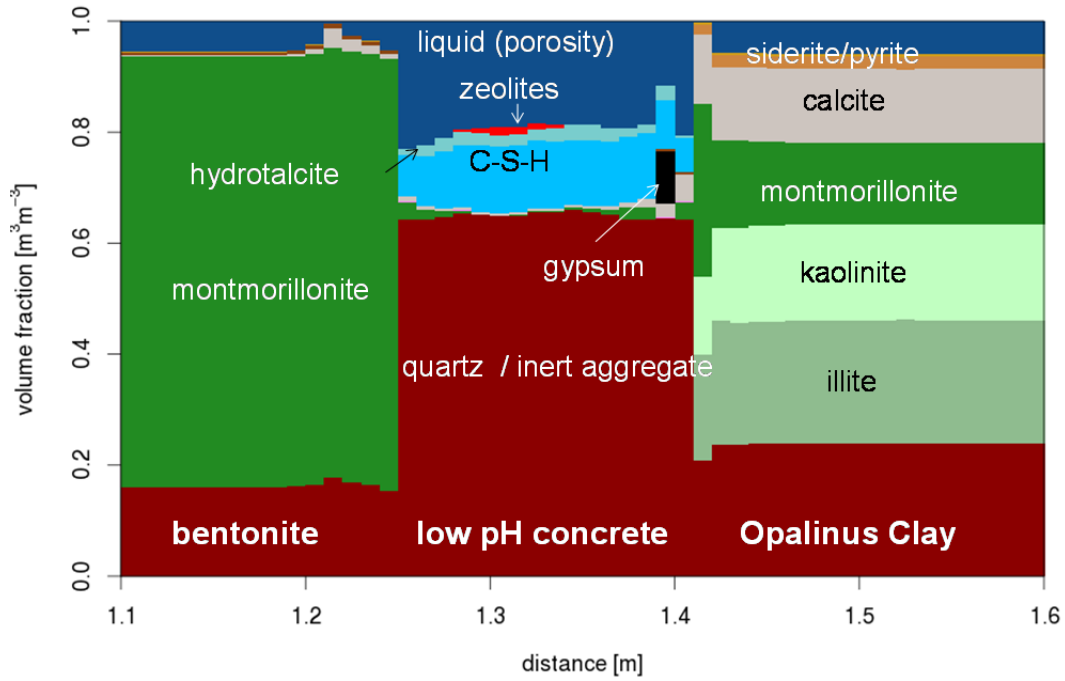

Fig. 5-6: Mineralogical profile across the low pH concrete liner layer after 30'800 years considering full (porosity) feedback on transport.

Mineralogical profiles for Case 2

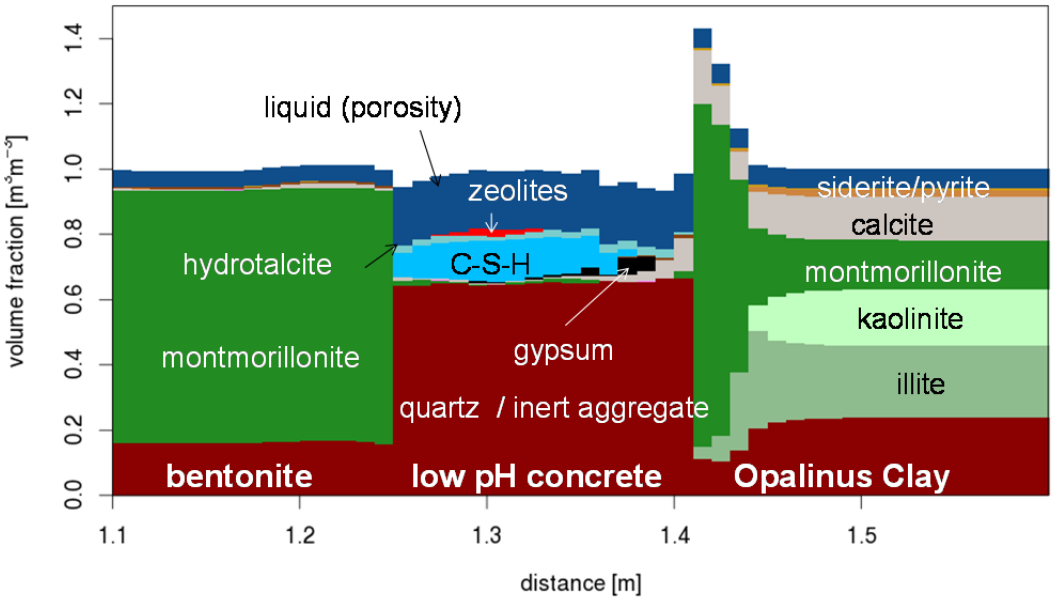

Fig. 5-7: Profile of the mineral assemblage near the low pH concrete interface for constant transport parameters after ~ 10'000 years (Case 2 porosity changes not fed back to transport parameters).

Note that volume may exceed 100 % under given assumptions.

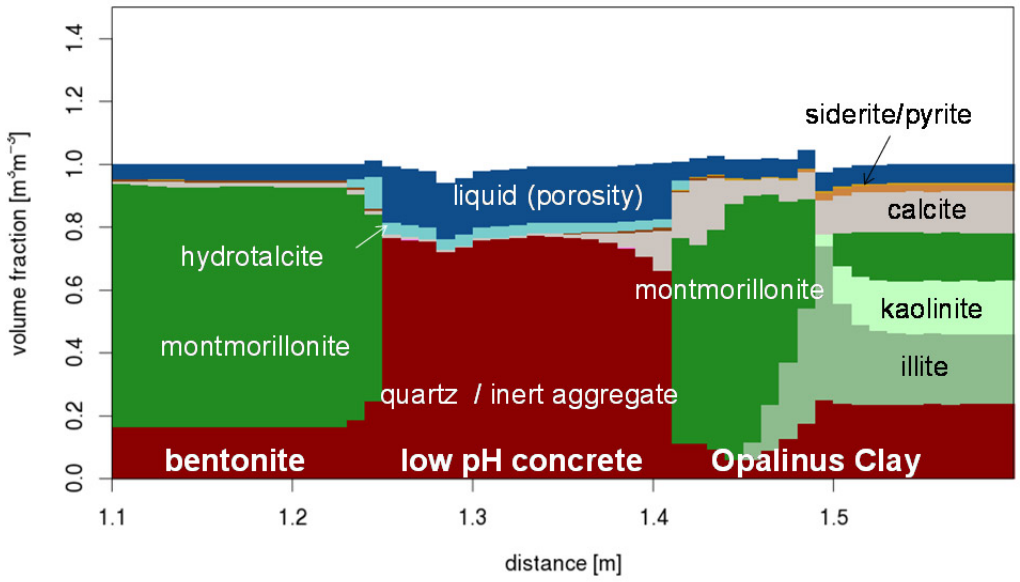

Fig. 5-8: Mineralogical profile for constant transport parameters after ~ 56'500 years.

5.4.2 Evolution of the porosity

Fig. 5-9 shows the porosity profiles over the interface for the Case 1 calculation considering full chemical feedback. The interface between the concrete liner and the Opalinus Clay shows a strong tendency to clog after a few thousand years. At the concrete liner-bentonite interface the porosity reduction is much less and evolves more slowly. Note that, when the open porosity is fully clogged, the interlayer space is not accessible.

The tendency for clogging is also visible in Figs. 5.7 and 5.8 for Case 2, where constant transport parameters were assumed. The volume of the solid phases on the outer and inner concrete liner boundary exceeds the maximum available volume of 1 m^3. It should be noted that for the case of constant transport parameters the total volume of mineral phases at the bentonite/ concrete interface only minimally exceeds the total available volume within 50'000 years.

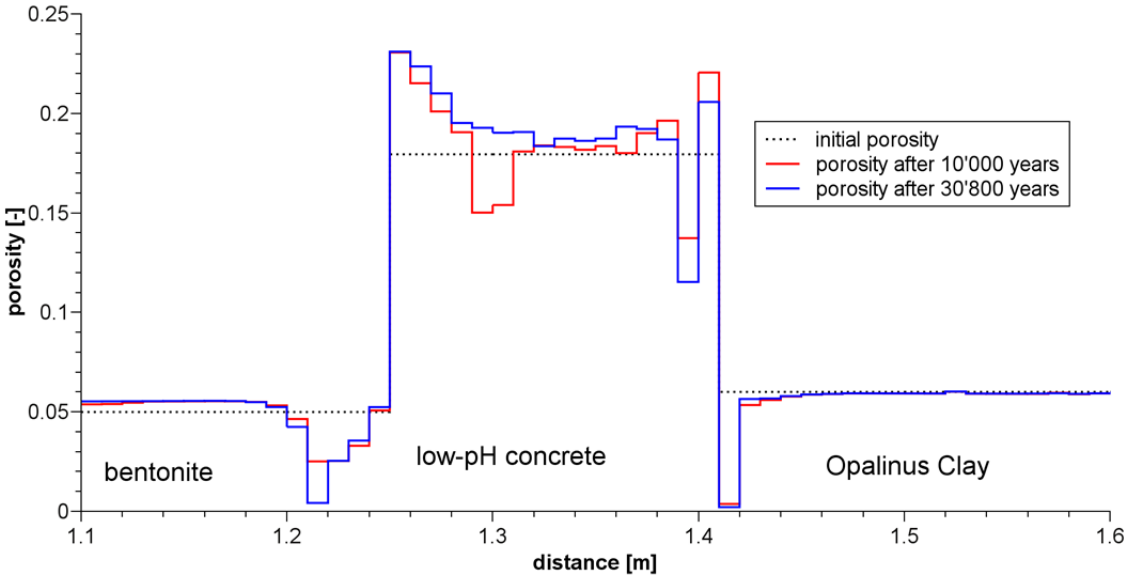

Fig. 5-9: Porosity evolution initially, after ~ 10'000 years and after ~ 30'800 years for Case 1 (with porosity feedback).

5.4.3 Evolution of the pH

The profiles for Cases 1 and 2 in Fig. 5-10 show a very limited propagation (centimeter range) of the pH plume into the Opalinus Clay. The propagation into the bentonite is more pronounced, and produces a significant pH increase in the first 0.1 m.

The pH in the concrete decreases in accordance with the concrete degradation. The pH soon drops to a value near 10.2, once the initial concrete porewater is equilibrated with the bentonite and Opalinus Clay porewaters (see Case 1 after 30'800 years). In Case 1 the pH profile will not change further in time because the clogging of the interfaces separates the three different compartments (bentonite, liner, Opalinus Clay) from each other. Except for compartment-internal re-equilibration, no further changes take place.

Calculations with no porosity feedback (Case 2) allow the long term evolution of the system to be evaluated, although the simulation times are not completely synchronous with real times.

After the dissolution of the CSH phase, and in the presence of hydrotalcite, the pH is ~ 9. The pH is further reduced to about 8 when hydrotalcite is dissolved and clay minerals start precipitating (compare Fig. 5-7 and 5-8).

It is not to be expected that a zone of elevated pH > 9 will extend much further after long times. After hydrotalcite is dissolved, the pH in the concrete liner and in the adjacent clay materials will reach values near 8. This will have no detrimental effects on the sorption properties of montmorillonite. (The mechanisms of interactions between cement minerals and concrete aggregates, possible time scales and mineral phase assemblages are discussed in detail in Kosakowski et al. (2014)).

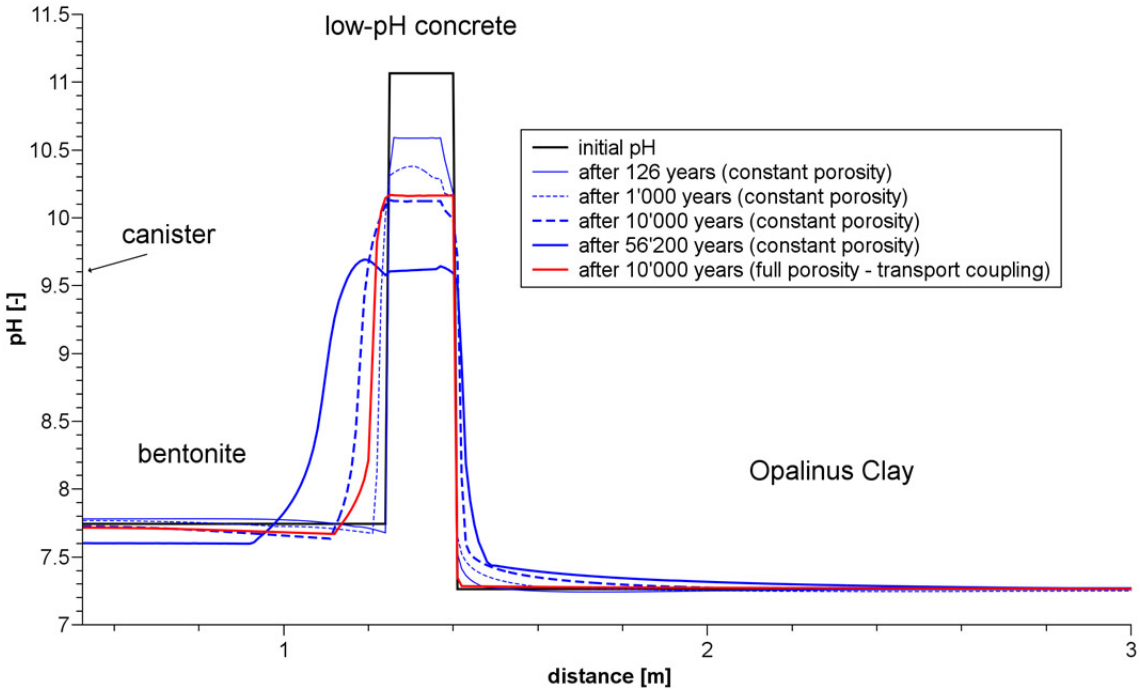

Fig. 5-10: pH profile initially, after 10'000 years for the case of porosity coupling and up to 56'200 years for the case without porosity changes.

For the case of porosity coupling no further changes in the pH are expected. Without porosity coupling the degradation of the concrete liner will decrease the pH in the concrete liner and in the adjacent clay materials to values near pH 8 in the long term.

5.4.4 Evolution of the pore water chemistries

In bentonite and Opalinus Clay porewaters Na and Cl are the major solutes making up the ionic strength. Cl is not involved in any mineral reactions, except in surface complexation reactions for preserving the charge neutrality of the solution. Na is involved in cation exchange reactions (Na-montmorillonite or Na-phillipsite) and may also participate in surface complexation reactions. Due to the diffusive exchange over the interfaces, the bentonite porewater composition will equilibrate with the Opalinus Clay porewater in the long term.

For Case 1 calculations (assuming porosity feedback) Fig. 5-11 shows the initial concentrations and concentrations after 100, 1'000, 10'000 and 30'800 years for Na and Cl. The initially high Cl

concentrations in the bentonite quickly drop to the concentration level in the Opalinus Clay porewaters. Na concentrations in bentonite equilibrate slower because cation exchange reactions reduce the mobility of Na, although identical effective diffusion coefficients are used throughout the simulations. After 10'000 years concentrations do not change significantly any further because mass transport across the clogged interfaces is minimal.

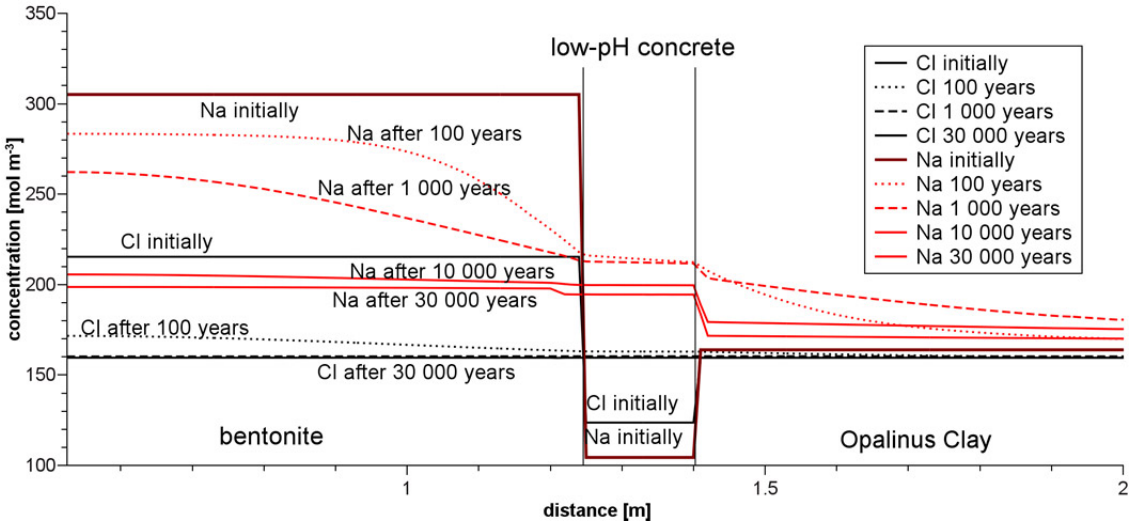

Fig. 5-11: NaCl concentration evolution in the vicinity of the concrete layer for Case 1.

Changes in pore water composition induce changes in the cation occupancy of clay minerals. In the bentonite compartment, Na and Mg in the montmorillonite phase are partially replaced by Ca and K (Berner et al. 2013). This transformation might influence the bentonite swelling pressure near the interface (Savage et al. 2010a).

5.5 Summary of the system evolution

The detailed evaluations provided in Section 5.4 show broad agreement with the summary from the literature in Section 5.2.3, in particular with the estimates and reviews in Savage et al. (2010a). This general agreement concerns:

- the type of geochemical reactions
- the spatial extent of mineralogical changes and the set of secondary phases formed
- the changes of porosity due to mineral precipitation and dissolution in both clay and cement media
- the cation exchange and occupancies on montmorillonite
- and acid-base reactions and corresponding buffer capacities

2-D Calculations for the specific materials foreseen for the Swiss high level waste repository provide information on the extent of pH changes, on the sequence and extent of mineral phase transformations, and on porosity changes. For the combination of MX-80 bentonite, low-pH concrete (ESDRED) and Opalinus Clay we found:

- The thickness of the zone containing significant mineralogical alterations is, at the maximum, a few tens of centimeters thick in both the bentonite and the Opalinus Clay adjacent to the liner. The extent of the mineral alteration zone in the Opalinus Clay is greater than in the bentonite when a constant porosity is assumed. Based on mass balance considerations Savage et al. (2010a) found maximum alteration thicknesses of 0.13 m in the Opalinus Clay and 0.04 m in the bentonite. In both domains the total amount of dissolved clay minerals is very small at the end of our simulations, despite the fact that chemical gradients are still present. However, it is not expected that significantly more clay minerals will disappear at later times. It is more likely that re-precipitation of clay type minerals occurs.
- Near both interfaces, bentonite – concrete liner and concrete liner – Opalinus Clay, the precipitation of minerals causes a reduction in the porosity. The effect is more pronounced and faster at the concrete liner – Opalinus Clay interface.
- The simulations reveal that significant pH-changes (i.e. pH > 9) in bentonite and Opalinus Clay are limited to small zones of less than 10 centimeters thick when the simulations were terminated. It is not anticipated that the zone of elevated pH will extend much further at longer times. After about 100'000 years the pH in the concrete liner and in the adjacent media will be ~ 8.
- The principal mineralogical alterations in the bentonite close to the concrete liner are the precipitation of calcite and hydrotalcite, and the replacement of the [Na,Mg]-montmorillonite by a [Ca,K]-montmorillonite.
- In the Opalinus Clay the situation is more complex, and two alteration regions are observed. Very close to the interface, kaolinite and illite are transformed into montmorillonite[8]. Depending on the coordinates in space and time, quartz, calcite and pyrite may dissolve, but partial neo-formation of calcite and illite is also possible. These findings are compatible with the view expressed in Savage et al. (2010a), i.e. "Multiple reaction fronts form and propagate due to different dissolution and precipitation rates, with later fronts overriding those formed earlier."
- Within the concrete liner zone, the (complete) degradation of the low C/S-ratio CSH phases is predicted, accompanied by the precipitation of hydrotalcite, phillipsite[9], clay minerals (illite, montmorillonite)[1], gypsum and calcite.

8 The neo-formation of montmorillonite under such conditions is a question which still needs to be resolved. Here, montmorillonite has to be regarded as a substitute for smectite like phases.

9 In our simulations phillippsite acts as a proxy for zeolithic phases in general.

5.6 Conceptual uncertainties

This section discusses uncertainties with respect to a reference setup that are caused by the choice of the conceptual model, simplifications and the non-consideration of processes and couplings between processes. We do not discuss the consequences of uncertainties (and heterogeneities) in material and transport parameters which would require computing resources which are far beyond those currently available to us, nor are parameter variations considered.

It is not yet possible to link any time scales for geochemical changes directly to the mass balance calculations in Nagra (2002a) and Savage et al. (2010a). In principle, our reactive transport calculations provide such a link, but the temporal evolution of interfaces is highly affected by an uncertain temporal and spatial evolution of the pore space. Currently, missing experimental data and conceptual difficulties make it impossible to incorporate pore scale processes in the continuum scale models, and thus to connect the model results with real time scales. However, the comparison of different scenarios is possible if the same spatial discretizations and kinetic parametrizations are used.

If we consider full coupling of mineral alterations and porosity, a clogging interface will separate the two domains in terms of mass transport and the system evolution stops. The two compartments will re-equilibrate close to the original composition in the long term. We are aware of the fact that the clogged regions could re-open through several mechanical processes (see Section 5.1) or that an effective separation of the compartments by clogging could be prevented by spatial material heterogeneities.

For simplicity and comparison reasons we therefore calculated scenarios where the coupling between mineral precipitation/dissolution and porosity changes is disabled. This specific assumption results in a constant mass transport over the interface. For the investigated cement/clay interfaces, where generally a strong decrease of porosity at the interface is observed, such a constant diffusive flux over the interface accelerates the evolution of the system and defines a kind of fastest possible evolution.

In our calculations (and similarly in the review of Savage et al. (2010a)) not all processes that might affect the evolution of porosity or the general geochemical evolution of the nearfield could be considered.

The coupling between porosity changes and changes in swelling pressures due to cation exchange, as well as mechanical phenomena such as tunnel convergence or cracking, were not considered in the calculations. Mechanical processes might alter the pore space and induce corresponding changes in mass transport. For example, tunnel convergence may cause a fracturing of the concrete liner. Such fractures open short-term pathways for the fast transport of solutes between the different materials. Field tests such as the HPF experiment (Mäder et al. 2006) or the Maqarin natural analogue (Smellie 1998, Steefel & Lichtner 1998), indicate that in the long term the fractures will be filled with precipitates and mass transport over the interface will be hindered.

The modelling approach chosen does not differentiate between cationic and anionic porosity, and does not include changes in the hydration state of swelling clay minerals. Consequences of pore space clogging for radionuclide transport in the interlayer of clay minerals cannot be deduced from the model calculations.

After emplacing the waste canister and backfilling the tunnel with bentonite, the saturation of the system starts. Water is moving from the host rock through the concrete liner into the bentonite. Complete (re-)saturation of all parts of the repository may take a few thousand years (Section 7.4.1. in Nagra (2002b)).

The model calculations do not consider the dynamics of re-saturation. Calculations start by assuming a fully saturated near-field. A simple sequential batch model to quantify the effect of saturation through a concrete liner on the bentonite porewater showed that the porewater composition is not significantly altered compared to a reference case (without concrete liner).

Parallel to the saturation process, a temperature pulse, originating from the waste canisters, will increase the near-field temperature (Section 7.6 in Nagra (2002b) and Chapter 6 in this report). These calculations were conducted in the absence of concrete liners. In the (worst) case of MOX/UO_2 canisters, a temperature of 80 °C is reached at the bentonite-Opalinus Clay boundary after 10 years and the maximum temperature of 95 °C is reached after a few hundred years. Within one thousand years the temperature drops back to 80 °C. In this work temperature effects are not considered. All simulations were conducted at 25 °C.

There is no doubt that temperature increases of this extent will accelerate mass transport over the interface. González Sánchez et al. (2008) investigated temperature dependencies of diffusion coefficients in montmorillonite. Based on their findings an increase in diffusion coefficients by a factor of 4 – 5 would be expected for an increase in temperature from 25 °C to 80 °C.

The impact of such a temperature excursions on the concrete liner in terms of mineralogical changes, and the potential reversibility of such changes (i.e. when the temperature drops back to ambient conditions), are poorly known. Consistent and comprehensive thermodynamic data for elevated temperatures are rare. (Note that the very recent compilations of Blanc et al. (2010a, 2010b) were not evaluated in this work). Changes in the mineral assemblage of the concrete would be expected. In addition, solubilities and kinetic reaction rates of minerals are strongly temperature dependent. For example, the kinetically controlled dissolution of quartz is more than 1'000 times faster at 80 °C than at 25 °C (Palandri & Kharaka 2004). This could lead to enhanced internal degradation of the concrete liner. Other minerals, such as calcite, show a lower solubility at higher temperature which might lead to an increase in the precipitation of such phases in regions of increased temperature. The temperature accelerated mass transport due to saturation processes and temperature dependent diffusion also enhances the precipitation/ dissolution of minerals as well as the corresponding porosity changes. A fast porosity decrease at interfaces stops mass flux across the interface which in turn suppresses mineralogical changes due to mass transport.

6 The elevated temperature period

6.1 Evolution of temperature in the bentonite buffer

The decay heat from the SF/HLW waste will affect the temperature within the engineered barrier system (EBS) and the surrounding host rock. Temperature is intrinsically coupled to many other processes in the repository nearfield; thus understanding its evolution is important.

In Nagra's demonstration of disposal feasibility project (Entsorgungsnachweis), the evolution of temperature in the emplacement tunnels of a HLW repository after closure was assessed for the limiting cases of constant high and low water contents of bentonite (Johnson et al. 2002).

The temperature distribution within the EBS of the HLW and SF emplacement tunnels and in the surrounding host rock was calculated using a 3D finite-element model. For the case of low water content it was assumed that the bentonite had an initial moisture content of 2 wt. % at emplacement, corresponding to a thermal conductivity of 0.4 W m^{-1} K^{-1} (Papafotiou & Senger 2014) and a heat capacity of 1.2 MJ m^{-3} K^{-1}, and that these values would not change in time and space. For the case of high water content, saturated bentonite with a thermal conductivity of 1.35 W m^{-1} K^{-1} (Papafotiou & Senger 2014) and a heat capacity of 2.4 MJ m^{-3} K^{-1} was chosen, and again, these values were taken as being constant over time. Heat transport was assumed to occur entirely by conduction. The contribution from convection was expected to be negligible because of the low gas and hydraulic permeabilities of bentonite and Opalinus Clay. The generation of water vapour at temperatures above 100 °C was not considered in the model.

The time-dependent temperature distributions for UO_2/MOX canisters are shown in Figs. 6.1 and 6.2 (taken from Johnson et al. 2002). For the case of low water content in the bentonite, the peak temperature at the canister/bentonite interface (U1 in Fig. 6-1) reaches ~ 160 °C. Within 1'000 years, the temperature has decreased to ~ 95 °C. The temperature at the mid-bentonite position remains in the range 100 to 115 °C for about 500 years (U_2 in Fig. 6-1). For saturated bentonite, the peak temperature at the canister/bentonite interface (U1 in Fig. 6-2) is below 110 °C, and within 1'000 years, the temperature has decreased to ~ 90 °C. The temperature at the mid-bentonite position remains below 100 °C (U_2 in Fig. 6-2).

For HLW canisters, with approximately half the initial heat output of the SF canisters, a peak temperature of ~ 150 °C is reached within a few years after emplacement for dry bentonite, decreasing to ~ 80 °C within 100 years. For saturated bentonite, the peak temperature at the canister/ bentonite interface remains below 90 °C (Johnson et al. 2002).

A difference of more than 50 °C in peak temperatures was calculated for the limiting cases of constant low and high water contents in bentonite. The assumption of an initially already saturated bentonite leads to unrealistically low temperatures at the canister/bentonite interface. However, the other extreme assumption of a dry bentonite, without re-saturation and without water vapour convection, leads to over-conservative high peak temperatures.

Consequently, a more detailed modelling of the two-phase flow processes associated with the early post-closure period has been carried out (Senger & Ewing 2008).

In this study of thermal-hydraulic (TH) processes, the model distinguishes between the different buffer materials. The bentonite blocks beneath the canisters have a higher dry density and different swelling pressures than the bentonite pellets used to backfill the emplacement tunnel. The initial conditions of this modelling study assume a two-year operational period at atmospheric pressure in the EBS. The bentonite backfilling pellets had an initial water content of

2 wt. % and the bentonite blocks an initial water content of 50 wt. %. Thermal conductivities were assumed to vary linearly with the water content from 0.4 to 1.35 W m^{-1} K^{-1} for bentonite with 2 wt. % moisture content to fully saturated bentonite, respectively.

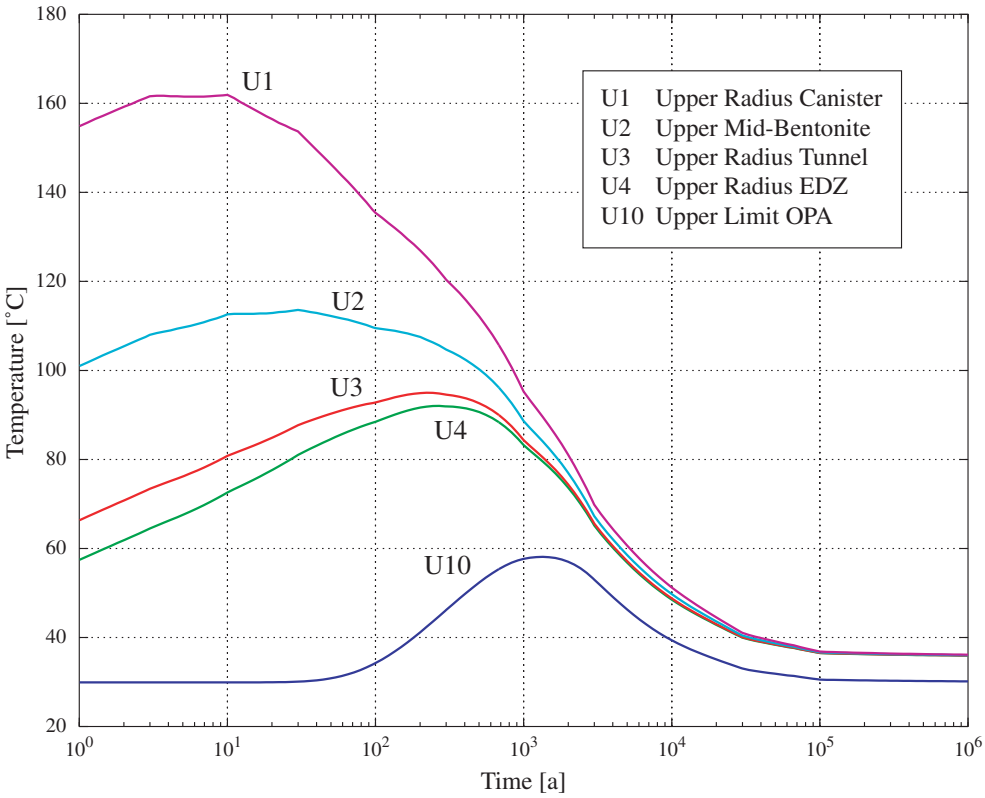

Fig. 6-1: Time-dependent temperature evolution in the vertical plane above the emplacement tunnels for canisters containing 4 PWR SF assemblies (3 UO_2 plus 1 MOX) for the case of low bentonite thermal conductivity (2 % moisture content).

The bentonite is assumed to have a thermal conductivity of 0.4 W m^{-1} K^{-1} and a heat capacity of 1.2 MJ m^{-3} K^{-1}. The initial ambient temperature is 38 °C. Canisters have a heat output of 1'490 W at the time of waste emplacement in the repository (Johnson et al. 2002).

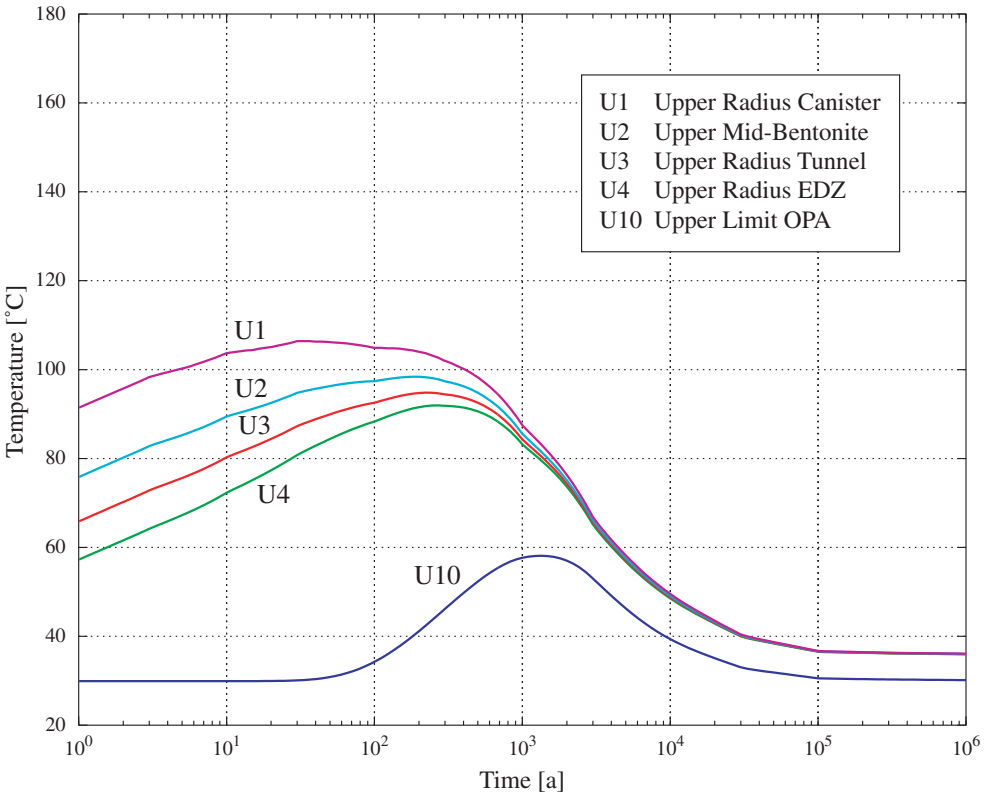

Fig. 6-2: Time-dependent temperature evolution in the vertical plane above the emplacement tunnels for UO_2/MOX canisters for the case of high bentonite thermal conductivity (saturated bentonite).

The bentonite is assumed to have a thermal conductivity of 1.35 W m^{-1} K^{-1} and a heat capacity of 2.4 MJ m^{-3} K^{-1} (Johnson et al. 2002).

Values for the heat generation from the waste canisters were taken from Johnson et al. (2002). As the canister with the highest heat output is the UO_2/MOX canister, calculations were performed only for this case. The numerical modelling of the expected TH conditions was performed using the multiphase flow simulator TOUGH2 (http://esd.lbl.gov/research/ projects/ tough/).

As shown in Fig. 6-3, and discussed in Senger & Ewing (2008), the temperature in the waste canister and adjacent bentonite rapidly increases after repository closure. The peak temperature of 132 °C is reached after about 4 years at the top of the UO_2/MOX canister (WP in Fig. 6-3). The bottom of the waste canister, which sits on top of the bentonite blocks, reaches only 115 °C. Essentially all of the bentonite pellets adjacent to the waste canister are then completely dry i.e. the initial low water content of the bentonite pellets evaporates as the temperature of the waste canister increases above 100 °C. This water evaporation starts water vapour convection processes. After 10 years the temperature has already slightly decreased (Fig. 6-3), and the saturation front advances into the bentonite pellets. After 20 years, most of the bentonite pellets become partially saturated, with liquid flow toward the canister. Between 60 and 80 years, the peak temperature declines to less than 100 °C (Fig. 6-3), and the bentonite becomes fully water saturated after 80 years. The temperature at the mid-bentonite position never exceeds 100 °C (Bent-cntr in Fig. 6-3).

A more recent sensitivity study on pressure and temperature evolution and gas production from Senger et al. (2014) supports these results.

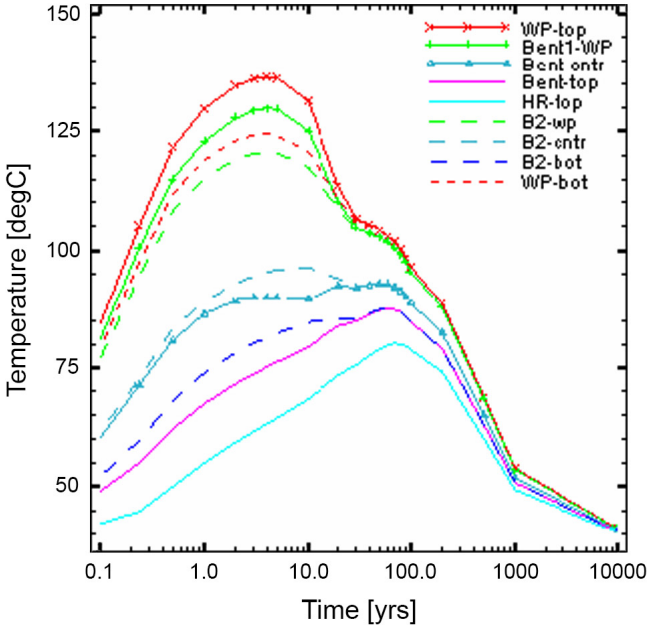

Fig. 6-3: Time-dependent temperature evolution in the vertical plane above (solid lines) and below (dashed lines) the UO_2/MOX canisters.

WP: canister hull, Bent1/B2-wp: bentonite next to WP, Bent/B2-cntr: in the centre of the bentonite, Bent/B2-top/bot: bentonite next to EDZ, HR-top: host rock (Senger & Ewing 2008).

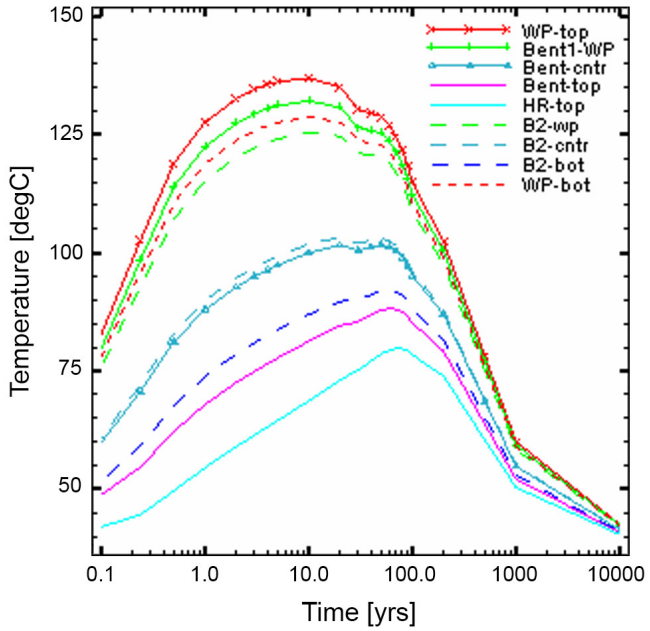

Fig. 6-4: Time-dependent temperature evolution in the vertical plane above (solid lines) and below (dashed lines) the UO_2/MOX canisters.

Heat transport by conduction only, i.e. no vapour diffusion or advection assumed in the model (Senger & Ewing 2008).

The initial rapid increase in temperature is common to both models. Also, the peak temperature of about 110 °C reached after 20 years for the fully saturated bentonite (Fig. 6-2), and the peak temperature of 115 °C, reached after 4 years for the 50 wt. % water content bentonite blocks (B2-wp in Fig. 6-3) are consistent. However, the significantly lower peak temperature at the top of canister surface as calculated by Senger & Ewing (2008) is due to the process of water evaporation included in their model. In the first years, the gas phase in the bentonite consists of as much as 25 % water vapour. In addition, the rapid decrease of temperatures as calculated by Senger & Ewing (2008) (100 °C after 80 years, Fig. 6-3) in contrast to Johnson et al. (2002) (100 °C after 800 years, Fig. 6-1, or 100 °C after 400 years, Fig. 6-2), is due to the consideration of unsaturated two-phase flow in the former model. This was demonstrated by model calculations in which heat transport by conduction only was considered i.e. no vapour diffusion or advection but still including time-dependent saturation with variable thermal conductivity (Fig. 6-4). In this case the temperature decreased slowly, reaching values below 100 °C only after ~ 300 years.

The model of Senger & Ewing (2008) is a purely thermal-hydraulic (TH) model. The chemical effects of water vapour at temperatures above 100 °C are thus not considered in this model. The absence of liquid water saturation could cause some modifications in the solubilities of gases (CO_2, H_2) and minerals and could increase the salinity of the porewater. To what extent these effects may change the system is unknown since suitable experiments and full TH(M)C models of this non-saturated system are not yet available.

6.2 Chemical stability of the montmorillonite buffer clay at elevated temperatures

6.2.1 Introduction

The transient elevated temperatures in the nearfield of a repository for spent fuel and high-level waste may cause conversion of montmorillonite, or more generally, smectite, and change the microstructure of the bentonite buffer material as indicated by several experiments.

The commonly assumed mineral reactions are smectite-to-illite conversions. One of these reactions is a solid-state one-to-one transformation where the T-O-T layers are conserved, and the reaction proceeds with a replacement of the tetrahedral Si^{4+} by Al^{3+}:

$$\text{Smectite} + Al^{3+} + K^{+} \rightarrow \text{Illite} + Si^{4+} \qquad (6.1)$$

The other conversion mechanism is one in which the destruction of the T-O-T layers provides the source of aluminium for the transformation, which thus consumes more smectite than it produces illite, and no external source of aluminium is required:

$$\text{Smectite} + K^{+} \rightarrow \text{Illite} + Si^{4+} \qquad (6.2)$$

No consensus has been reached as to which mechanism prevails in a repository. However, it is generally accepted that the rate of smectite-to-illite conversion is controlled by temperature and the availability of potassium.

In addition, according to equations (6.1) and (6.2), quartz, or more generally, crystalline or amorphous SiO_2 can precipitate and cement the stacks of montmorillonite together thereby

reducing the expandability and the ductility of the buffer. In the temperature range 0˚ to 350 °C the solubility of quartz and amorphous silica

$$SiO_2(s) + 2\ H_2O(l) \leftrightarrow Si(OH)_4(aq) \qquad (6.3)$$

increases with temperature and can be precisely calculated (Gunnarsson & Arnorsson 2000).

This process of "cementation" may also occur independently of the smectite-to-illite conversion due to dissolution and subsequent precipitation of amorphous silica, sulphates and carbonates in the zone of transient temperature gradients during the early post-closure period.

Calcite is present in bentonite, and the clay host rock imposes a high partial pressure of CO_2. An increase of temperature will modify the equilibria of calcite and other carbonate minerals. They become more stable and will precipitate. This can play a role in the cementation of the montmorillonite buffer clay not only in the zone of transient temperature gradients but also in the zone of highest temperature.

6.2.2 Experimental results

In their critical review Wersin et al. (2007a) discussed experimental results published up until 2005. They concluded that no significant changes of hydraulic and mechanical properties have been reported for bentonite materials exposed to temperatures below 120 °C under wet conditions. The data suggest that significant cementation and perhaps also illitization effects occur at 150 °C and beyond. Under dry conditions, bentonite is stable to higher temperatures – maybe as high as 350 °C. Wersin et al. (2007a) concluded that in order to verify their findings long-term experiments examining hydraulic, mechanical and mineralogical changes under realistic conditions at temperatures beyond 130 °C are required.

The experiments reported within the last five years are either long-term, but below 100 °C, or short-term batch experiments extending to higher temperatures or experiments carried out with fully saturated bentonite. The most relevant ones are briefly summarized in the following.

The aim of the FEBEX (Full-scale Engineered Barriers EXperiment) is to study the behaviour of components in the nearfield for a high-level radioactive waste repository in crystalline rock (ENRESA 2006). The project is based on the Spanish reference concept for disposal of radioactive waste in crystalline rock: The waste canisters are placed horizontally in drifts and surrounded by a clay barrier constructed from highly compacted bentonite blocks. An in situ test was performed in a gallery 70 m in length and 2.3 m in diameter excavated at the Grimsel test site. The heating system was made up of two heaters with dimensions and weights analogous to those of real canisters. The clay barrier was formed by blocks of compacted bentonite with about 50 % initial water saturation. The heating stage began in February 1997. A constant temperature of 100 °C was maintained at the heaters/bentonite interface. After five years of continuous heating, the heater next to the gallery was removed and the materials recovered (bentonite, metals, instrumentation, etc.) were analysed to investigate the different types of processes which had taken place. The second heater was left in place and it is planned to continue its operation until at least 2015. The average degree of saturation of all the bentonite extracted was 85 %. The mineralogical and geochemical characterization indicated that there had not been any major modifications to the bentonite during operation. The hydration of the bentonite in the blocks in contact with the granite caused the dissolution of the most soluble minerals (sulphates and carbonates), which were transported towards the inner part of the barrier. The occasional appearance of larger quantities of calcite and gypsum was reported (ENRESA 2006).

The main differences between crystalline and clay host rocks are generally that the granite porewaters are poor in carbonates and their CO_2 partial pressures are low. In fact, the Grimsel granite porewater is extremely poor in carbonates. In a clay rock formation, the carbonate contents of the porewater are high and the CO_2 partial pressures also. This means that an increase of temperature at the clay host rock / bentonite interface will cause a carbonaceous cementation at the interface and this cannot be observed in the case of a granite / bentonite interface.

In the Swedish repository concept for nuclear waste disposal (KBS-3 concept), the spent nuclear fuel will be contained in copper canisters surrounded by compacted bentonite. The decay heat from the fuel will increase the temperature in the repository which, combined with the uptake of groundwater, are expected to result in only minor mineralogical changes in the bentonite (SKB 2009).

A large-scale 5 year field experiment at Äspö Hard Rock Laboratory (HRL) with very dense MX-80 clay buffer surrounding a full-sized copper-lined KBS-3 canister in an 8 m deep, 1.75 m diameter deposition hole in granite was evaluated in 2007 with respect to the performance of the clay (Pusch et al. 2010). A filter had been placed at the walls of the hole in order to provide the clay with groundwater. The surface temperature of the canister was maintained at 85 °C for approximately 2 years and at a successively lower temperature later in the experiment. A sample taken from the proximity of the heater showed a hundred-fold increase in hydraulic conductivity. However, montmorillonite was still the dominating mineral phase (Pusch et al. 2010).

The ongoing LOT test series at the Äspö HRL is focused on the long term performance of the bentonite buffer, i.e. the conditions after water saturation, and on buffer related processes in a water-saturated bentonite buffer i.e. microbiology, cation transport, copper corrosion. In total, the LOT project includes seven test parcels. Three of them were exposed to standard KBS-3 conditions (maximum temperature below 100 °C) and four parcels to adverse conditions (maximum temperature below ~ 140 °C). Both the standard and the adverse test series included short term tests (1 to 2 years), medium term tests (> 5 years) and long term tests (> 10 years). The report (SKB 2009) concerns the A2 test parcel, which was a medium term test exposed to adverse conditions. The temperature at the copper tube surface was held constant at 130 °C. Due to the high thermal conductivity of the saturated bentonite blocks, a constant temperature of 100 °C was already measured at 6 cm distance from the copper tube surface (Fig. 4-3 in SKB 2009). The main results of the tests and post-mortem analyses were:

- redistribution of readily soluble accessory minerals in the bentonite, in particular $CaSO_4$
- increase in the cation exchange capacity of the bentonite in those parts exposed to high temperature
- no increase of hydraulic conductivity
- no formation of illite or any other typical montmorillonite alteration minerals

The Mock-Up-Cz experiment, performed by the Centre of Experimental Geotechnics (Czech Technical University, Prague), simulated the vertical placement of a canister with radioactive waste according to the Swedish KBS-3 system. Highly compacted blocks of clay comprizing of 75 % Ca montmorillonite, 10 % finely ground quartz and 5 % graphite powder were placed within an 80 cm diameter steel tube fitted with a filter to ensure the uniform wetting of the buffer, (Pusch et al. 2010). The system was subjected to thermal stress (up to 90 °C) and synthetic "granitic" water for a period of 3 years and 9 months. The process of illitization affected only 1 – 2 % of the original smectite and can thus be considered to have a very low effect on the physico-chemical properties. This small extent of smectite transformation was suggested to be due to the relatively short time of the experiment and also to the limited supply of potassium from the synthetic water used for hydration (Kolaříková et al. 2010).

The Heater Experiment (Göbel et al. 2006) at the Mont Terri Underground Research Laboratory consisted of a central vertical borehole, 30 cm diameter and 7.5 m deep, drilled into the floor of a niche in the shaly facies of the Opalinus Clay formation. Heat-producing waste was simulated by a heater element of 10 cm diameter, held at a constant surface temperature of 100 °C. The heater element was embedded in ring-shaped compacted bentonite blocks with an outer diameter of 30 cm. The heater was in operation from February 2002 for 18 months. Physico-chemical alterations in the geotechnical barrier by heat and hydration were weak. There was some cementation which could slightly affect THM characteristics such as porosity and thermal conductivity. The bentonite itself exhibited negligible modifications in its mineralogical characteristics. Saturation of the bentonite was not reached. The calculated saturation for all samples was slightly over 50 %.

In Korea smectite alteration tests were carried out in 0.5 M KCl solution at temperatures of 90, 140 and 200 °C, reaction times of 3, 7, 15, 28 and 50 days in batch experiments at 1g/20ml solid to liquid ratio (Lee et al. 2010). At 200 °C XRD data and dissolved silica concentrations indicated significant conversion of smectite to randomly interstratified illite – smectite layers. The fraction of expandable smectite layers and the CEC decreased by about 30 %. Sorption measurements for Cs and Ni with the samples heated to 200 °C in either 0.5 M KCl or demineralized water resulted in significantly lower K_d values of more than one order of magnitude for samples in 0.5 M KCl. However, in the latter case the pH dropped significantly, from 7.5 to 4.1 for the Cs experiments, and from 5.5 to 4.0 for the Ni experiments. Hence, the observed variation in K_d values might be due to the change in pH and/or other varying experimental conditions.

An older, long-term field experiment (4 years), was conducted in the Stripa mine with French kaolinite/smectite clay heated up to 170 °C in boreholes in granite (Pusch et al. 1992). After excavation of the clay core, Pusch et al. (1992) observed that the innermost centimetre-thick annulus had turned very dark due to the neoformation of trioctahedral smectite and stiff due to cementation by precipitated anhydrite and siliceous compounds. Effectively a claystone had been formed. The hydraulic conductivity of the claystone was about 1'000 times higher than that of the virgin clay due to the increased amount of interconnected void space and fissures. The rest of the clay core had undergone insignificant mineralogical and chemical changes but nevertheless there was evidence of rather strong cementation through the transport and precipitation of silica.

Similar cementation effects due to precipitation of silica have been observed in short-term laboratory experiments on strongly compressed MX-80 pellets (Pusch et al. 2003). The experiments comprized of the autoclave treatment of dry pellets for 30 days at 110 to 150 °C where distilled water was contained in cups placed on the free upper surface of the samples. Vapour treatment at 150 °C produces a clear decrease in swelling pressure which was ascribed to cementation by precipitation of silica released by the hot vapour. New experimental findings reported in Birgersson et al. (2014) where bentonite samples were treated with vapour indicate no differences in swelling capacity of the bentonite. They further conclude from a literature review on bentonite exposed to steam that: "There are consequently no significant results showing negative effects of steam on the passive uptake of water in bentonite, usually termed swelling capacity, and there are no indications that steam should change the physical properties of a bentonite buffer in a long-term perspective." The so called Couture effect (Couture 1985) could be explained by an experimental artefact.

6.3 Estimate of the influence of a shotcrete layer on the chemical stability of montmorillonite

The foreseen application of a shotcrete layer to the tunnel walls of the planned repository could potentially enhance the illitization process according to Eq. (6.1) or (6.2) by supplying additional potassium to the system. In the following a rough mass balance estimate is provided concerning this additional potassium source.

The following design of a (radial symmetric) repository tunnel for spent fuel is considered:

Canister radius 525 mm, bentonite radius 1250 mm, shotcrete radius 1400 mm, i.e. the thickness of the bentonite backfill is 725 mm and thickness of the shotcrete layer is 150 mm (Nagra 2010, Fig. 5.2-2). Then a shotcrete volume of 1 dm^3 corresponds to 3.24 dm^3 of bentonite.

1 dm^3 shotcrete made with ESDRED contains 0.0305 moles of potassium whereas 1 dm^3 of completely dry bentonite saturated via in-diffusing water vapour contains 3.56 moles of montmorillonite with a stoichiometry of $Na_{0.38}(Al_{1.55}Fe^{III}_{0.09}Fe^{II}_{0.08}Mg_{0.28})(Si_{3.98}Al_{0.02})O_{10}(OH)_2 \cdot 4.84H_2O$ (Berner et al. 2013)

Following Karnland & Birgersson (2006) we consider the following stoichiometry for the above mentioned aluminium conserving smectite-to-illite conversion, Eq. (6.2).

$$2\ Na_{0.38}(Al_{1.55}Fe^{III}_{0.09}Fe^{II}_{0.08}Mg_{0.28})(Si_{3.98}Al_{0.02})O_{10}(OH)_2 \cdot 4.84H_2O + 0.91\ K^+ \rightarrow$$

$$1.138\ K_{0.80}(Al_{1.98}Mg_{0.02})(Si_{3.22}Al_{0.78})O_{10}(OH)_2 + 4.296\ Si(OH)_4 +$$

$$0.18\ Fe(OH)_3 + 0.16\ Fe(OH)_2 + 0.537\ Mg(OH)^+ + 0.76\ Na^+ + 0.384\ OH^- + 1.06\ H_2O \qquad (6.4)$$

Thus, 0.0305 moles of potassium from 1 dm^3 ESDRED shotcrete could transform 0.067 moles of montmorillonite, or 0.6 % of the 11.52 moles of montmorillonite in the 3.24 dm^3 bentonite.

If we consider the potassium contents and volumes of HTS cements[10] or concretes with 20 % or 25 % final porosity (Berner 2009) the percentage of reacted montmorillonite varies between 0.3 % and 1.2 %.

In summary, these rough mass balance estimates show that the maximum additional supply of potassium from a 150 mm shotcrete layer has no significant influence on the illitization process of montmorillonite in the bentonite backfill.

[10] Sulphate resisting cement (Haute Teneur en Silice) Lafarge, France.

6.4 Summary

6.4.1 Long-term performance of the bentonite backfill

A number of large-scale experiments in underground rock laboratories, ranging from 18 months to 5 years, explored the temperature effects on bentonite at temperatures below 100 °C. These include the FEBEX experiment at the Grimsel test site (ENRESA 2006), the LOT experiment at Äspö (SKB 2009) and the Heater Experiment at Mont Terri (Göbel et al. 2006). As discussed in these reports, the major part of the bentonite backfill remained intact, and only small alterations of the mineralogical, chemical and mechanical properties were detected in these experiments.

Considering the review of Wersin et al. (2007a) and the experimental studies briefly summarized in this report, and also in agreement with the synthesis of relevant experimental data by Pusch et al. (2010), it is concluded that montmorillonite will remain the major clay mineral in a water saturated buffer system up to a temperature of about 130 °C.

According to the modelling study for the Swiss concept (Senger & Ewing 2008, Senger et al. 2014), the outer half of the bentonite backfill will most probably never experience temperatures above 100 °C and the maximum temperature at the canister surface is expected to reach about 130 °C.

The conclusion from these experimental and modelling studies is that the observed small alterations due to transient temperature excursions will not change the properties of the outer parts of the bentonite to such an extent that the buffer function is jeopardized.

6.4.2 Early post-closure period

In the first decades after tunnel closure steep temperature gradients, evaporation of water and complete drying of bentonite pellets close to the surface of the waste canisters, water vapour convection and suction of water toward the waste canister could promote several adverse effects.

The most prominent of these effects is the possible formation of dissolution/precipitation zones of amorphous silica, sulphates and perhaps also carbonates in the backfill close to the waste canisters. These dissolution/precipitation zones are accompanied by changes in porosity, and the possibility of clogged zones due to precipitation cannot be excluded a priori. Furthermore, the complete drying of bentonite pellets may lead to dry cracks and transient asymmetric volume changes of the backfill. This effect may have consequences for the mechanical properties of the backfill, but could also lead to cracking and re-opening of previously formed precipitation zones. These possible chemical and mechanical effects will in turn influence the hydrological and thermal evolution of the system.

None of the large-scale experiments reported so far provided any information about the evolution of an unsaturated bentonite system above 100 °C.

7 Interaction between iron and bentonite in the HLW repository

7.1 Introduction

The planned Swiss repository for the disposal of spent fuel (SF) and vitrified high-level waste (HLW) will contain considerable amounts of carbon steel and other iron containing materials. SF and HLW will be enclosed in steel canisters that will be placed on bentonite-block pedestals reinforced with steel structures in disposal tunnels whose walls may also be reinforced with steel anchors and steel nets. The void space around the canisters will be backfilled with granular bentonite. During the evolution of the repository, the steel canisters will eventually corrode and produce corrosion products (such as magnetite, green rust, and siderite) as well H_2 gas and dissolved Fe(II). Released Fe(II) may interact with bentonite, degrading its sealing and retention properties.

In the safety report for Project Opalinus Clay (Nagra 2002a), only a short paragraph was devoted to the interaction of Fe with bentonite:

"Magnetite will be formed on the steel canister surface as a product of the anoxic corrosion reaction. Under reducing conditions, magnetite may dissolve as Fe(II), which could favour formation of nontronite, a smectite with reduced swelling capacity, and other Fe-silicate phases (Grauer 1986). However, Müller-Vonmoos et al. (1991), in experiments performed at 80 °C over 6 months, found no evidence for Fe uptake by montmorillonite contacted with magnetite."

In the meantime, several experimental investigations on the interaction of corroding iron or steel with bentonite under anaerobic conditions have shown that montmorillonite may be converted into a number of different minerals, most of which have no or very little swelling capacity. Since the planned HLW repository has a large iron to bentonite mass ratio (see Appendix B2), it is reasonable to reconsider the interactions of corrosion-derived iron with bentonite and to assess their consequences. This is the purpose of this chapter.

Iron-bentonite interactions have recently been reviewed by Wersin et al. (2007b) and Johnson et al. (2008a) and the present chapter is largely based on these reviews, augmented by results from more recent literature.

In order to set the stage, it is useful to consider the evolution of temperature, oxygen content and relative humidity in the bentonite backfill surrounding SF- and HLW-canisters. After the emplacement of the canisters in the disposal tunnels, conditions in the bentonite backfill will be initially hot, aerobic and relatively dry. With time the canister surface will cool, oxygen will be consumed by reactions with the canister surface and the steel mesh stabilizing the tunnel walls and by the oxidation of pyrite in the bentonite, and the bentonite will saturate with infiltrating groundwater. Thus, conditions will gradually become cooler, anaerobic and saturated. Landolt et al. (2009) distinguished four phases for the conditions at the canister surface:

1. Aerobic dry Phase 1:
   The peak temperature of 120 -140 °C at the canister surface is reached after 5 – 10 years. Phase 1 ends when the canister surface is wetted with liquid water after 20 – 40 years.
2. Aerobic unsaturated Phase 2:
   The temperature decreases to values below about 100 °C. Phase 2 persists for 20 to 30 years until all oxygen is consumed.

3. Anaerobic unsaturated Phase 3:
   Corresponds to the period between the onset of anaerobic conditions and the full saturation of bentonite with infiltrating water and persists for about 50 years. Surface temperatures decrease to well below 100 °C.
4. Long-term anoxic Phase 4:
   Bentonite is fully saturated, the only oxidant remaining is water. Corrosion under these conditions produces hydrogen gas by reduction of protons and water. Surface temperatures continually decrease to ambient host rock temperatures of around 40 °C after some ten thousand years.

With respect to the long-term safety of the HLW repository, Phase 4 is by far the most important. Therefore the emphasis in this report will be put on the consequences of canister corrosion on bentonite under fully saturated anaerobic conditions at temperatures below about 100 °C.

7.2 Impact of iron released from corrosion on bentonite

The unaltered bentonite backfill has several physical and chemical properties that are safety relevant:

- High swelling pressure and swelling capacity
- Low hydraulic conductivity
- Favourable rheology
- High radionuclide sorption capacity

It is therefore important to know how, and to what extent, any alteration of the bentonite backfill may degrade these beneficial properties. Iron corrosion may lead to several alteration processes in the bentonite:

- Precipitation of discrete iron corrosion products:
  The dominant anaerobic iron corrosion product expected for nearly neutral to alkaline conditions is magnetite, Fe_3O_4. It has been shown to form in numerous experiments. At higher sulfide and carbonate concentrations the precipitation of Fe-sulfides or siderite, $FeCO_3$, can be expected. Green rust-type phases may also form, however, they appear to be metastable with respect to magnetite and siderite.
- Destabilization of montmorillonite and replacement by Fe-rich smectites or by non-swelling Fe-rich phyllosilicates:
  See below.
- Sorption competition of corrosion derived Fe(II) with radionuclides.
- Reduction of structural Fe^{3+} in smectites:
  Structural iron in the octahedral layer of smectites is more difficult to reduce than the iron in iron oxides and hydroxides because it is further away from surfaces which can be contacted with a reducing agent. The most commonly used and effective chemical reductant in the laboratory is dithionite, but iron can also be reduced by iron-reducing bacteria, where organic matter acts as an electron donor. The charge deficit caused by the reduction of Fe^{3+} to Fe^{2+} in smectites is compensated by the sorption of an exchangeable cation or by dehydroxylation of structural OH^-. The latter process plays an important role in the destabilization of montmorillonite into non-swelling Fe-rich phyllosilicates (see Section 7.3). The presence of Fe^{3+} in octahedral layers of smectites modestly reduces the swelling capacity, while the effect of Fe^{2+} in octahedral layers is more pronounced (Stucki 2006).

- H_2 gas as reducing agent:
  Nagra (2002a) considered H_2 gas released from iron corrosion as essentially inert, diffusing through the bentonite into the surrounding host rock without any chemical interactions. While it is possible to reduce structural Fe^{3+} with H_2 gas at temperatures above 300 °C, (see Stucki 2006 for references), it is not known whether H_2 released from iron corrosion will reduce structural iron under repository conditions at temperatures lower than 140 °C.

- An issue that has not received very much attention is the impact of canister corrosion on the overall water mass balance and the potential consequences on solute concentrations. Anaerobic corrosion of steel can consume considerable amounts of water. Therefore, the region adjacent to the external canister surface could become water depleted, leading to increased concentrations of soluble salts (mainly NaCl), so that the ionic strength would increase if this excess of dissolved salt were not transported away. The development of a high ionic strength porewater region at the canister-bentonite interface could have undesired consequences, e.g. an increased canister corrosion rate, modified bentonite swelling properties, and possibly also an increase in the solubility limits of radionuclides that form strong complexes with chloride. However, detrimental effects could mainly be ruled out up to an ionic strength of ca. 1 M NaCl (Cloet et al. 2014).
  The effects of water depletion due to canister corrosion are further discussed in Appendix B3.

7.3 Formation of Fe-rich phyllosilicates

7.3.1 Fe-rich clay minerals and phyllosilicates

Iron, both in its ferrous (Fe^{2+}) and ferric (Fe^{3+}) forms, is one of the main elements that make up the lattice of 1:1 and 2:1 clay minerals and other phyllosilicates (sheet silicates). Fe^{3+} substitutes for Al in dioctahedral positions and Fe^{2+} for Mg^{2+} in trioctahedral positions. Substitution of Fe^{3+} for Si in tetrahedral positions is less frequent and less extensive. Due to ion size restrictions, Fe^{2+} is not found in tetrahedral positions. Fe^{2+} is also common in the interlayer of smectites.

Among the 1:1 phyllosilicates (7Å-phases belonging to the kaolinite/serpentine group) the most important Fe-rich minerals are the following:

- Berthierine $(Fe^{2+}, Al, Fe^{3+}, Mg)_{2\text{-}3}(Si, Al)_2O_5(OH)_4$ is the most common of the Fe-rich 1:1 phyllosilicates and is mainly found in non-metamorphic marine sediments. The octahedral layer contains predominantly Fe^{2+}, with lesser amounts of Al^{3+}, and small amounts of Fe^{3+} and Mg^{2+} (Brindley 1982). In the past, berthierine was commonly called septechlorite, septechamosite, chamosite, 7Å-chamosite, or 7Å-chlorite (Hornibrook & Longstaffe 1996) and was often confounded with the Fe^{2+}-rich chlorite, which, to complicate matters, is today called chamosite. Berthierine is compositionally very similar to chamosite and is often seen as a low temperature precursor to chlorite, with which it forms mixed layers. Some authors consider berthierine and chamosite as polymorphs, e.g. Hillier & Velde (1992) and Jiang et al. (1992).

Odinite $(Fe^{3+}, Mg, Al, Fe^{2+})_{2.5}(Si,Al)_2O_5(OH)_4$ is a Fe^{3+}-rich, dioctahedral-trioctahedral 1:1 phyllosilicate which is formed in present-day tropical marine sediments. The octahedral layer contains mainly Fe^{3+}, Mg^{2+}, and Al^{3+}, with smaller amounts of Fe^{2+}. Odinite is susceptible to alteration to chlorite and probably does not survive in rocks older than from the Quaternary.

- Greenalite $(Fe^{2+}, Fe^{3+})_{2\text{-}3}(Si,Al)_2O_5(OH)_4$ is a rather uncommon Fe^{2+}-rich 1:1 phyllosilicate with a modulated structure (i.e. some of the tetrahedra in the tetrahedral layer are inverted).

The octahedral layer contains predominantly Fe^{2+}, with lesser amounts of Fe^{3+} and Mg^{2+}, and very small amounts of Al^{3+} and Mn^{2+} (Guggenheim & Eggleton 1988). Authigenic to diagenetic greenalite is found in banded iron formations and it also occurs as aqueous alteration product in meteorites (carbonaceous chondrites) formed during the earliest geological history of the solar system.

- Cronstedtite $(Fe^{2+}{}_2Fe^{3+})(SiFe^{3+})O_5(OH)_4$ is a rather uncommon Fe-rich 1:1 phyllosilicate with Fe^{2+} in the octahedral layer and Fe^{3+} divided between the octahedral and the tetrahedral layer to maintain charge balance. Cronstedtite occurs in ore veins as a low-temperature hydrothermal formation and, like greenalite, as an aqueous alteration product in carbonaceous chondrites.

Smectites contain far less iron than the minerals of the kaolinite/serpentine group just mentioned. The most iron-rich smectites are the following:

- Nontronite $(Ca_{0.5}, Na)_{0.3}Fe^{3+}{}_2(Si, Al)_4O_{10}(OH)_2 \cdot nH_2O$ is an Fe^{3+}-rich dioctahedral smectite that is found as a widespread authigenic mineral in recent marine sediments and as hydrothermal precipitates from hot brines discharged at oceanic rift zones. Nontronite also occurs as weathering product of ultramafic rocks and is found in sedimentary iron ore deposits (Güven 1988). The octahedral layer contains predominantly Fe^{3+} and the compositional range of solid solution is narrowly restricted around the Fe^{3+}-endmember (Güven 1988).
- Saponite $(Ca_{0.5}, Na)_{0.3}(Mg, Fe^{2+})_3(Si, Al)_4O_{10}(OH)_2 \cdot nH_2O$ is a ferromagnesian trioctahedral smectite. The octahedral sites are mainly occupied by Mg^{2+} and Fe^{2+}. A saponite with a composition very close to the ferrous endmember was found in recent sediments in the Red Sea and is believed to have precipitated from hot brines discharging at the ocean floor (Badaut et al. 1985). Fe^{2+}-rich saponite is rather unstable under atmospheric conditions and is immediately oxidized when removed from the original reducing environment (Güven 1988). Saponite is also hydrothermally deposited in mineralized veins and in vesicles in basalt.

Chlorites consist of 2:1 layers joined by octahedral hydroxide interlayers (they resemble smectites with additional octahedral layers replacing the interlayers). Most of the chlorites are trioctahedral and belong to the Mg^{2+}-Fe^{2+} series, for which there is a continuous solid solution. There is one iron-rich trioctahedral chlorite:

- Chamosite $(Fe^{2+}, Mg, Fe^{3+})_5Al(Si_3Al)O_{10}(OH)_8$ is found in sedimentary ironstones where it forms authigenically under reducing conditions in the presence of decomposing organic material. Chamosite often replaces berthierine with mixed-layer formation in transitional states. Besides the dominant Fe^{2+} and Mg^{2+}, the octahedral sites may also contain small amounts of Fe^{3+}.
- The most Fe-rich micas are glauconite and celadonite.
- Glauconite $(K, Na)(Fe^{3+}, Al, Mg, Fe^{+2})_2(Si, Al)_4O_{10}(OH)_2$ is a low-temperature dioctahedral mica that is diagenetically formed under reducing conditions at the interface between sediments and shallow seawater. It is an iron-rich illite-smectite mixed layer and is often composed entirely of illite layers (Thompson & Hower 1975). The octahedral sites are mainly occupied by Fe^{3+} and Mg^{2+}, with small amounts of Al^{3+} and Fe^{2+}. Glauconite is an alteration product of detrital biotite and other precursor minerals.
- Celadonite $K(Mg, Fe^{2+})(Fe^{3+}, Al)Si_4O_{10}(OH)_2$ is a low-grade metamorphic, dioctahedral mica that replaces ferromagnesian silicate minerals in altered intermediate to mafic volcanic rocks under zeolite facies conditions. Celadonite also occurs as amygdule fillings in basalts and andesites.

It is important to keep in mind that among all the minerals considered, only smectites and, to a much lesser extent, glauconite (depending on the amount of smectite in this mixed layer), have the capacity to swell.

7.3.2 Natural occurrence and stability range of Fe-rich phyllosilicates

Berthierine is mainly found as an early diagenetic phase formed under reducing conditions in marine oolitic ironstones or in sediments influenced by marine waters. There are also some non-marine occurrences: Mg-free berthierine was described by Toth & Fritz (1997) from a lateritic weathering profile where it was formed by alteration of detrital clay minerals (presumably kaolinite) and reduction of ferric minerals in an anoxic environment. Another non-marine occurrence was reported by Taylor (1990) from the terrestrial Wealden series where berthierine was formed by diagenetic alteration of iron oxyhydroxides and kaolinite under reducing conditions. Berthierine is often found to be replaced by chamosite, the iron-rich chlorite, which is compositionally very similar (Hughes 1989). During the transition from berthierine to chamosite these minerals form mixed layers (Ryan & Reynolds Jr. 1996 and Jiang et al. 1992), although structural observations suggest that in some cases such mixed layers can precipitate directly from solution (Hillier & Velde 1992). Ahn & Peacor (1985) have argued that berthierine is metastable with respect to chamosite. Based on the maximal burial depths of berthierine-bearing sediments, berthierine is preserved if diagenetic temperatures do not exceed about 70 °C (Hornibrook & Longstaffe 1996) to 100 °C (Aagard et al. 2000). Iijima & Matsumoto (1982) described berthierine from coal measures in Japan and deduced higher temperatures for the formation and transformation of berthierine. Burial depths indicate that the formation of berthierine from kaolinite and siderite takes place rather slowly at temperatures between 65 and 130 °C while the transformation to chamosite occurs at about 160 °C. While most authors consider berthierine as diagenetic precursor to chamosite, Jiang et al. (1992) have argued that the coexistence of berthierine and chamosite in a massive sulfide deposit can be interpreted as retrograde formation of berthierine from chamosite.

Odinite is typically formed in shallow estuarine environments under fluvial influence and modern occurrences of odinite are restricted to tropical and subtropical marine locations (Hornibrook & Longstaffe 1996). Odinite is the characteristic mineral of the so-called verdine facies, which is the result of the synsedimentary interaction between seawater and deposited sediments at depths between 5 and 60 m near an abundant source of iron (Odin 1990). According to Bailey (1988), the formation conditions of odinite are a normal marine salinity, a basic pH between 7.5 and 8.5, a temperature around 25 °C, an abundance of oxygen and a positive E_h above the sediment. In the Niger delta, according to Porrenga (1967), odinite is formed at shallow depths at temperatures between 25 and 27 °C (note that Porrenga (1967) uses the term chamosite for odinite). Lower temperatures appear to favour the formation of glauconite. Odinite is very susceptible to alteration (e.g. to chlorite) and all known odinite occurrences have formed within the last 12'000 years (Bailey 1988). Hugget & Hesselbo (2003) argued that odinite is possibly the most frequent precursor to berthierine. Since alteration of odinite requires the reduction of Fe^{3+} to Fe^{2+} and sediments enter a reducing environment at burial depths as little as about 1m, this would explain the absence of odinite in ancient sediments. Odin (1990) pointed out that individual clay minerals in the verdine facies represent small steps in a complex series of transformations. Odinite is formed first, soon followed by a reaction leading to other clay minerals such as ferric chlorite or pyrophyllitic clay. Since these secondary minerals are not known in ancient sediments, Odin (1990) suspected that another reaction takes place, possibly leading to the formation of ferric clays.

Greenalite and Cronstedtite are not very common. Apart from the terrestrial environments mentioned above, both can be found as aqueous alteration products of carbonaceous chondrites,

which are meteorites that have solar-like compositions and are derived from asteroids and possibly comets that did not experience planetary differentiation. Carbonaceous chondrites consist of submillimeter- to centimeter-sized components including chondrules, which were formed from molten or partially molten droplets in space before being accreted to the parent body, Ca-Al-rich inclusions, olivine aggregates, Fe-Ni metal, and a fine-grained matrix (Weisberg & McCoy 2006). According to Brearley (2006), aqueous alteration is perhaps the most widespread process that has affected primitive solar materials during the early geological evolution of the solar system. In carbonaceous chondrites, aqueous alteration is witnessed by the presence of numerous hydrous phases such as serpentines (including greenalite and cronstedtite), chlorite, montmorillonite, saponite, and vermiculite (Brearley 2006). The conditions of the aqueous alteration processes are poorly constrained since original fluids are rarely preserved. Isotope thermometry on carbonates in carbonaceous chondrites have indicated alteration temperatures between 20 and about 70 °C (Guo & Eiler 2007). According to Endress et al. (1996) these alterations must have started less than 20 million years after the time of formation of the oldest condensates of the solar nebula.

Chlorites have a wide compositional range and are generally formed at higher temperatures than other clay minerals (usually at temperatures above about 130 °C, see e.g. Cathelineau & Nieva 1985). In sandstones, the formation of chlorite can occur at depths corresponding to a temperature as low as about 90 °C (Aagard et al. 2000). Precursor minerals for chlorite are smectites, vermiculite, berthierine and odinite. The transformation from the precursors to chlorite often proceeds via the formation of mixed-layers. Based on observations of natural systems, Savage et al. (2010c) have argued that chlorite is likely the most stable alteration mineral of iron-bentonite interaction also at low temperatures, but that its formation is kinetically inhibited and proceeds in an Ostwald step rule sequence with magnetite, odinite, cronstedtite, and berthierine as transient precursor minerals. They used the following arguments (for references see (Savage et al. (2010c):

- Chlorite is the common Fe-silicate in ancient sandstones but is absent in sediments younger than about a million years. In contrast, odinite and cronstedtite are absent in sediments older than about a million years but they do occur in shallow and warm marine tropical sediments.
- Odinite specimens older than about a thousand years have greater proportions of interstratified 14 Å layers than younger ones suggesting that odinite is transformed into a more stable chlorite-like phase.
- Berthierine is a precursor phase to chlorite with which it often forms mixed layers. Berthierine itself often forms from odinite. The sequence odinite → berthierine → chlorite has been observed or inferred in several sandstone formations.
- Magnetite is rarely formed in the low temperature diagenesis of iron-rich sediments.

The formation of sedimentary chlorite, however, is not necessarily topologically tied to precursor minerals, since chlorite is often found as grain coating in the pore space of sandstones, as a result of precipitation from the pore solution (Curtis et al. 1985).

Fe-rich nontronite has been found to form by direct precipitation from the discharge of a hot brine at the bottom of the Red Sea (Atlantis II Deep geothermal system) at a temperature of 56 °C (Bischoff 1972). The structure of this Fe-rich smectite is characterized by Fe^{2+} and Fe^{3+} in the octahedral layer and by Si and Fe^{3+} in the tetrahedral layer, with a composition intermediate between a true dioctahedral ferric nontronite and a trioctahedral ferrous endmember, which Bischoff (1972) called hypothetical, but would correspond to a ferrous iron-rich saponite. Such a saponite close to the ideal ferrous endmember was reported by Badaut et al. (1985) from sedi-

ments of the Atlantis II Deep geothermal system. Since ferrous smectite is unstable under atmospheric conditions, characterization was fraught with technical challenges to ensure that Fe^{2+} is not oxidized. Ferrous iron-rich saponite was first reported by Kohyama et al. (1973) from clayey alteration zones of glassy rhyolitic tuffs.

7.3.3 Experimental data on smectite-iron interactions

During the last several years, numerous experimental studies have been published describing the interaction between corroding iron and bentonite or clay minerals under anoxic conditions. All these experiments have suffered from the fact that reaction rates are very low at temperatures below 100 °C, leading to only small mineralogical changes, so that alteration products are difficult to identify and analyze. In order to increase reaction rates, experiments were often performed at considerably higher temperatures or at very low solid/liquid ratios, which makes extrapolation to the relevant repository conditions rather difficult. While reaction rates are indeed increased at higher temperatures it is also true that these higher temperatures may be outside the stability range of low-temperature clay minerals, thus leading to reaction products irrelevant for low-temperature conditions.

Very often, iron and bentonite samples were powdered and mixed, leading to large reactive surface areas but completely changing the geometrical and textural relationships which influence the transport of reactants and products. Reaction products are often too fine-grained to be identified, making it impossible to allocate increased iron-contents measured in the bulk to individual mineral phases. Another experimental difficulty is that ferrous clay minerals are very easily oxidized, adding to the problems of characterizing reaction products. These difficulties notwithstanding, some useful information can be gained from such experiments.

A summary of experimental results is given in Tab. 7-1, and the corresponding experiments are discussed in Appendix B1. The main iron-corrosion product formed is magnetite, but green rust, amorphous $Fe(OH)_2$, hematite, goethite, lepidocrocite and possibly akagenite have also been reported. These iron-corrosion products form crusts directly on the corroding iron and are generally not visible in the altered bentonite (because they are either not present or too fine-grained to be detected with the available analytic tools). Siderite can be found in the corrosion crust, but is also formed in the alteration zone within the bentonite. Alteration zones in the bentonite are enriched in Fe, which is, in most cases, obvious from the change in colour. It is, however, often not possible to determine where the iron is actually located. An important example is Fe-rich smectite, which is one of the main alteration products formed. Fe^{2+} may be found in the octahedral layer, in the interlayer or possibly in iron-oxide coatings on external surfaces, but it is difficult to distinguish between these cases. In several experiments below 100 °C, there are indications that 7Å-phases such as berthierine, odinite, and cronstedtite were formed, however, their identification is often tentative. Chlorite was not found in experiments below 100 °C.

Based on the results of experiments by Guillaume (2002), Guillaume et al. (2003), Guillaume et al. (2004), Perronnet (2004), Lantenois et al. (2005), Wilson et al. (2006a), Charpentier et al. (2006), Perronnet et al. (2008), and themselves, Mosser-Ruck et al. (2010) tried to systematize the main mineralogical changes to be expected from iron-bentonite interaction under anoxic conditions. They identified three distinct mineralogical sequences as a function of temperature, pH, Fe/clay (Fe/C) and liquid/clay (L/C) ratios:

1 $T < 150$ °C, near-neutral pH, $L/C > 5$:
   $Fe/C > 0.5$: dioctahedral smectite → Fe-rich 7Å-phase (berthierine, odinite, cronstedtite)
   $Fe/C \approx 0.1$: dioctahedral smectite → Fe-rich dioctahedral smectite + Fe-rich trioctahedral smectite

2 T < 150 °C, alkaline pH (10-12), L/C > 5, Fe/C ≈ 0.1:
dioctahedral smectite → Fe-rich dioctahedral smectite (± palygorskite)

3 T ≈ 300 °C, Fe/C ≈ 0.1, L/C > 5:
near-neutral pH: dioctahedral smectite → Fe-rich saponite → trioctahedral chlorite + feldspar + zeolite
alkaline pH (10-12): dioctahedral smectite → Fe-rich vermiculite + mordenite

An important series of experiments affording some insight into the initial processes that may destabilize smectite in the presence of iron was presented by Lantenois et al. (2005). They examined the interaction between mixtures of Fe metal with various natural and synthetic smectites in pure water. Two types of saponite were used to represent trioctahedral smectites, the remaining smectite samples were dioctahedral, with one type of nontronite, one type of Fe-smectite, two types of montmorillonite, and four types of beidellite. For each experiment, 0.6 g of smectite powder and 0.6 g of iron powder were mixed and reacted with 30 ml of pure water under anoxic conditions at 80 °C for 45 days. In mildly acidic to neutral conditions (prepared by adding HCl) a significant proportion of iron was transformed to magnetite, while smectite was essentially unaffected, independent of the type of smectite present. An interesting point to note is that in this case smectite appears to have served as a catalyst, since iron was not transformed under the same conditions if smectite was absent. Under basic conditions di- and trioctahedral smectites showed contrasting reactivities: In experiments with trioctahedral smectite, both Fe and smectite appeared to be unreacted. In experiments with dioctahedral smectite, however, both Fe and smectite reacted to form magnetite and new Fe-rich 7Å-phyllosilicates with compositions compatible with odinite or cronstedtite. The extent of smectite transformation ranged from 20 to 50 wt. % for montmorillonite, and 40 to 70 wt. % for beidellite. 90 wt. % of Fe-smectite and 95 wt. % of nontronite were transformed.

Based on these results Lantenois et al. (2005) proposed a model for the initial smectite destabilization in the presence of iron. An important ingredient in this model is the assumption that in dioctahedral smectites the OH-groups situated at the apices of Fe^{3+}-containing octahedra are preferentially deprotonated and that protons are required for the oxidation of iron metal. Since protons are abundant in aqueous solution under acidic conditions, smectites are not deprotonated and remain unaltered during iron corrosion. At higher pH, however, the edge sites are essentially deprotonated and protons needed for iron oxidation can be obtained from deprotonation of the Fe^{3+}-OH groups. According to Lantenois et al. (2005) smectite destabilization leading to the transformation into Fe-rich phyllosilicates proceeds as follows:

1. Deprotonation of octahedral Fe^{+3}-OH groups, increasing the octahedral layer charge deficit.
2. Oxidation of iron metal to Fe^{2+} by interaction with released protons.
3. Sorption of Fe^{2+} cations on edge sites of smectite.
4. Oxidation of Fe^{2+} on edge sites to Fe^{3+} by reduction of structural Fe^{3+} to Fe^{2+}, again increasing the octahedral layer charge deficit.
5. Migration of Fe^{2+} cations into the interlayer to compensate for the increased charge deficit of the octahedral layer and further migration into ditrigonal cavities in the tetrahedral layer and finally into vacant sites in the octahedral layer. This leads to the formation of trioctahedral domains in the dioctahedral smectite, which is thought to be the main destabilizing factor. While the coexistence of di- and trioctahedral domains is very common in 1:1 phyllosilicates (e.g. in greenalite, berthierine, odinite, and cronstedtite), it is very limited in 2:1 phyllosilicates.

This conceptual model of the initial destabilization of dioctahedral smectites is compatible with the experimental observation by Lantenois et al. (2005) that trioctahedral smectites remain unaffected by iron corrosion, since they lack the structural Fe^{3+} required for easy deprotonation of octahedral OH-groups and also lack other cations that may be reduced in the octahedral layer. Finally, the octahedral layers in trioctahedral smectites are fully occupied, preventing the migration of Fe^{2+} into these layers.

Based on textural evidence from TEM studies of experimental reaction products, Lantenois et al. (2005) and Perronnet et al. (2008) came to the conclusion that the transformation from smectite to the Fe-rich 7Å-phases can be considered as a process that comprises at least three steps: The initial destabilization of smectite as described above leads to the formation of amorphous Si-Al-Fe gels which finally mature and crystallize into the Fe-rich 7Å-phases.

Tab. 7-1: Compilation of experimental data on anoxic interaction of iron with clay.
For a discussion of the experiments see Appendix B1.

Reference	Starting Solids	Aqueous Solution	Temperature [°C]	Duration d: days, w: weeks, m: months, y: years	Iron corrosion products	Neo-formed iron-rich minerals	Other neo-formed minerals	Comments
Müller-Vonmoos et al. 1991, Madsen 1998	Fe-powder + MX-80 or Montigel	hydrogen gas + water vapor	80	27 w	magnetite			
Müller-Vonmoos et al. 1991, Madsen 1998	magnetite-powder + MX-80 or Montigel	hydrogen gas + water vapor	80	29 w				
Oscarson & Heimann 1988	am. Fe(II)-silicate + bentonite	synthetic groundwater	23, 70	200 d				
Papillon et al. 2003	carbon steel sheets + FoCa7	natural granite groundwater	25	6 m	magnetite		calcite	
Papillon et al. 2003	carbon steel sheets + FoCa7	natural granite groundwater	80	8 m		siderite, 7 Å-phyllosilicate (berthierine?)	calcite	
Guillaume et al. 2004	magnetite-hematite powder + MX-80	low salinity NaCl-$CaCl_2$ sol.	80	1 m, 3 m, 9 m			quartz, K-feldspar, plagioclase	
Guillaume et al. 2004	magnetite-hematite powder + MX-80	low salinity NaCl-$CaCl_2$ sol.	300	1 m, 3 m, 9 m		saponite?	quartz, K-feldspar, plagioclase, zeolite	
Lantenois et al. 2005	Fe-powder + various di- and tri-octahedral smectites	mildly acidic to neutral solution	80	45 d	magnetite			
Lantenois et al. 2005	Fe-powder + various dioctahedral smectites	basic solution	80	45 d	magnetite	7 Å-phyllosilicate (odinite?, cronstedtite?)		
Lantenois et al. 2005	Fe-powder + various trioctahedral smectites	basic solution	80	45 d				
Charpentier et al. 2006	mixed Fe-magnetite powder + MX-80	alkaline solution	80, 150	3 m, 6 m, 9 m			transient palygorskite	
Charpentier et al. 2006	mixed Fe-magnetite powder + MX-80	alkaline solution	300	3 m, 6 m , 9 m		Fe-vermiculite, saponite	mordenite	
Wilson et al. 2006a	Fe-powder + Kunipia-F (+ calcite powder)	$FeCl_2$ solution	80, 150, 250	90 – 92 d	magnetite,	Fe-smectite	analcime	

Tab. 7-1: Continued

Reference	Starting Solids	Aqueous Solution	Temperature [°C]	Duration d: days, w: weeks, m: months, y: years	Iron corrosion products	Neo-formed iron-rich minerals	Other neo-formed minerals	Comments
Wilson et al. 2006a	Fe-, magnetite powder + Kunipia-F	NaCl solution	250	93 – 114 d	magnetite, hematite	Fe-smectite	analcime	
Carlson et al. 2007, Carlson et al. 2008	carbon steel wires + compacted MX-80	artificial NaCl-Na_2CO_3-groundwater	30, 50	829 d, 911 d	magnetite			
Carlson et al. 2007, Carlson et al. 2008	carbon steel and cast iron coupons + compacted MX-80	artificial NaCl-Na_2CO_3-groundwater	30, 50	900 d, 356 d	magnetite, hematite, goethite			
de Combarieu et al. 2007	Fe-powder or -foil + COX-powder	ultrapure water	90	6 m	magnetite	7 Å-phyllosilicate, Fe-chlorite?		
Ishidera et al. 2008	carbon steel coupon + compacted Kunipia F	artificial seawater	80	10 y	am. $Fe(OH)_2$, green rust (GR1), lepidocrocite			
Martin et al. 2008	low alloyed steel-rod + compacted MX-80	synthetic Bure-porewater	90	8 m	magnetite	siderite		
Schlegel et al. 2008	iron-rod in COX-block	synthetic Bure-porewater	90	8 m	magnetite	siderite, nontronite?, saponite?	stevensite?	
Schlegel et al. 2010	iron-rod in COX-block	synthetic Bure-porewater	90	4 m	magnetite	siderite, chukanovite, 7 Å-phyllosilicate		anodically activated corrosion
Perronnet et al. 2008	iron-powder + FoCA7-powder	Evian bottled water	80	45 d		SiAlFe-gels, 7 Å-phyllosilicate (greenalite?, odinite?)		oxic corrosion
Milodowski et al. 2009b	carbon steel wires and coupons + compacted MX-80	1M NaCl	50	99 – 198 d	magnetite, akaganeite ?	altered montmorillonite	aragonite	
Milodowski et al. 2009a	carbon steel wires and coupons + compacted MX-80	0.01M NaCl 1M NaCl "Allard"-water	30	571 – 687 d	magnetite	altered montmorillonite, Mg-Fe-rich aluminosilicate	aragonite	

7.3.4 Information from natural analogues

There are only a few natural analogue studies that provide information useful for iron-bentonite interactions in repository environments. The main problem is the scarcity of terrestrial native iron. There are two main types of occurrence, one related to the formation at high temperatures from basaltic magma and the other to the formation at low temperatures by alteration (serpentinization) of ultrabasic rocks (Hellmuth 1991a). Native iron was formed in basaltic magmas that were reduced through the contamination and assimilation of surrounding carbonaceous sediments. The most prominent example is Disko Island in the Tertiary volcanic province in Greenland where iron-bearing basalts cover an area of about 8'000 km^3. Within the basalt, native iron is finely distributed with inclusion sizes ranging from millimeters to meters (the largest block found had a mass of more than 20'000 kg). Another, albeit much smaller occurrence of native iron is found in the basalt of Bühl (near Kassel) in Germany. Native iron is formed at low temperatures in ultrabasic rocks as a result of the reaction with water (serpenttinization) along fractures. Additional minor occurrences of native iron are coal beds, and in two locations native iron was found in high-pressure metamorphic rocks (Haggerty & Toft 1985).

While terrestrial native iron has been studied as a natural analogue for the preservation and corrosion of iron (e.g. Hellmuth 1991b), it is obvious from the geological environment of these occurrences that they are hardly relevant for iron-bentonite interactions. Native iron is also found on earth in meteorites, e.g., in carbonaceous chondrites, where extra-terrestrial aqueous alteration led to the formation of numerous hydrous minerals such as serpentines (including greenalite and cronstedtite), chlorite, montmorillonite, saponite, and vermiculite. The coexistence of these minerals suggests their use as a natural analogue, since the conditions of alteration in terms of temperature (20 – 150 °C), redox (reducing) and ratio of solid to solution are close to those expected for the near-field of a repository (Jullien et al. 2005). Judging from a limited literature review, however, such chondrites have not yet been put to use for elucidating iron-bentonite interactions.

A "semi-natural" analogue was investigated by Kamei et al. (1999) in a bentonite mine in Japan where an arch-shaped iron-support of a gallery was in contact with wet Na-bentonite for about 2'000 days. The colour of the bentonite near the support had changed from pale grey to green. Bulk analyses of the altered bentonite showed a remarkable increase in iron (6.3 to 14.4 wt. % Fe_2O_3 versus 2.3 wt. % in the unaltered bentonite). Since the amount of the exchangeable cations Na^+, K^+, Ca^{2+}, and Mg^{2+} was significantly reduced in the altered bentonite (22 – 30 meq/100 g versus about 55 meq/100 g for the unaltered bentonite), and the CEC remained essentially unchanged, Kamei et al. (1999) assumed that Fe^{2+} released from iron corrosion was exchanged with the interlayer cations. XRD suggested that no Fe^{2+} had entered the octahedral layers.

Since there are apparently no natural analogues where native iron is in contact with bentonite, an alternative is to look at bentonite deposits that have been in contact with Fe-rich solutions. Fukushi et al. (2010) observed greenish veins in brecciated bentonite in the Kawasaki bentonite deposit in Japan that suggested the interaction of Fe-rich hydrothermal solutions with bentonite. A plethora of analytical methods (XRF, SEM, XRD, EPMA, STEM-EDS, and XANES) revealed that the clay minerals in the vein fillings are most likely Fe-K-rich and dioctahedral, compositionally compatible with glaucony, which is a mixed-layer mineral consisting of smectite and glauconite. Additional alteration minerals in the veins are pyrite and opal. Textural relationships show that pyrite and glaucony were probably formed simultaneously, while opal was precipitated in a later stage. Since pyrite can be formed from ambient to high temperatures, glaucony has been found to form at temperatures as low as about 40 °C and opal is not stable at more than about 100 °C where it is transformed into quartz, Fukushi et al. (2010) concluded that

the vein minerals had formed at temperatures below about 100 °C. Clay minerals from the altered bentonite adjacent to the veins were identified to be most likely dioctahedral Al-smectites containing Fe.

7.3.5 Information from archaeological analogues

There appear to be no archaeological analogues relevant to iron-bentonite interaction. While several studies were concerned with the corrosion of iron artefacts in anoxic soils, e.g., Neff et al. (2006), Saheb et al. (2008), Bellot-Gurlet et al. (2009), and Neff et al. (2010) and references therein, the emphasis was put into characterizing the influence of the anoxic soil environment on the corrosion behaviour of the artefacts. The influence of iron corrosion on the soils was not considered.

7.3.6 Information from modelling

Several authors have modelled the impact of iron corrosion on bentonite, and the models they used can be put into three broad categories:

1. Wilson et al. (2006b) used equilibrium thermodynamics to calculate the stability fields of minerals as a function of water composition.

4 De Combarieu et al. (2007) used reaction-path modeling based on kinetics and equilibrium thermodynamics to model the evolution of minerals as a function of time. In this local equilibrium approach, thermodynamically unstable minerals dissolve according to a kinetic rate-law, while the precipitation of minerals takes place at thermodynamic equilibrium.

5 The remaining studies by Montes-Hernandez et al. (2005a), Montes-Hernandez et al. (2005b), Bildsetein et al. (2006), Samper et al. (2008), Marty et al. (2010), and Savage et al. (2010c) used various types of reaction-transport models combining kinetics, equilibrium thermodynamics and diffusion.

A problem common to all these modelling studies is that there are very few reliable thermodynamic data for clay minerals in general and specifically for the potential Fe-rich secondary minerals, and most of the data had to be based on estimates. The same is true for the kinetic parameters, especially in the case of precipitation. This casts some doubts on the reliability and predictive capacity of modelling the interaction of iron corrosion with bentonite and the following modelling results have to be viewed with this very much in mind.

Wilson et al. (2006b) calculated the stability fields of Fe-rich phyllosilicates under chemical conditions representative for the interface between iron canisters and the bentonite backfill. They estimated thermodynamic data for various Fe-rich phyllosilicates (2:1 smectites: Fe(II)-beidellite, Fe(II)-montmorillonite, Fe(II)-nontronite, two types of Fe(II)-saponite; 1:1 serpentines: berthierine and greenalite) and calculated their stability fields and those of other phyllosilicates (various members of the following mineral groups: 1:1 smectite-group, 2:1 pyrophyllite/talc-group, 2:1 mica-group, and 2:1 chlorite group) in log-activity diagrams for the system Al_2O_3-FeO-Fe_2O_3-MgO-Na_2O-SiO_2-H_2O and subsystems at temperatures of 25, 80, and 250 °C. Other minerals considered were amorphous silica and quartz, hematite, and magnetite. In the subsystem Al_2O_3-FeO-MgO-Na_2O-SiO_2-H_2O the most stable phases are kaolinite, berthierine, Fe(II)-saponite, paragonite and analcime. If smectites are excluded from the models, they are replaced by berthierine and chamosite, and if berthierine is also excluded, it is replaced by chamosite and kaolinite. Near the saturation limit of magnetite, the most stable Fe(II)-phyllosilicates are Fe(II)-saponite and berthierine.

In order to interpret their corrosion experiments of iron in contact with Callovo-Oxfordian clay (see Appendix B1), de Combarieu et al. (2007) performed reaction-path calculations that gave information on the mineralogical evolution as a function of time. Starting from an initial model system containing 2 g of Callovo-Oxfordian clay (35 wt. % illite, 25 wt. % quartz, 17 wt. % calcite, 11.2 wt. % Ca-montmorillonite, 3.8 wt. % Na-montmorillonite, smaller amounts of dolomite, albite, K-feldspar, pyrite, and goethite) and 2 g of metallic iron in 10 ml of pure water, the irreversible reaction-path to equilibrium was calculated at 100 °C by dissolution of unstable primary minerals according to kinetic laws and the precipitation of secondary minerals according to equilibrium thermodynamics. Potential secondary Fe-rich phyllosilicates considered were greenalite, cronstedtite, berthierine, chamosite (Fe-chlorite), biotite, 2 types of nontronite and high- and low-Fe smectite. The simulation time was 200 days. Primary minerals that were dissolved in addition to metallic iron are quartz, dolomite, illite, and montmorillonite. After 200 days mainly greenalite, magnetite and chlorite were formed, with very small amounts of Ca-saponite.

Montes-Hernandez et al. (2005a) used a 1-D diffusive reaction-transport code to model the mineralogical changes of a 1 m thick zone of bentonite (saturated with pure water but not equilibrated with the minerals!) that was put in contact with a model water representing the pore solution of the Callovo-Oxfordian formation on one side and a 0.001-molal Fe(II)-solution on the other side. The temperature was set at 100 °C and the initial E_h was -200 mV. Dissolution of primary minerals in the bentonite (85 vol. % Na/Ca-montmorillonite, plus biotite, albite, microcline, quartz, calcite and pyrite) was kinetically controlled, while the precipitation of secondary minerals was assumed to be controlled by thermodynamic equilibrium (local equilibrium assumption). Potential secondary phyllosilicates considered were vermiculite, Fe-saponite, Fe-Mg-saponite, Na-montmorillonite, Ca-montmorillonite, Fe-chlorite and Mg-chlorite. Since the bentonite was assumed to be initially in disequilibrium with pure water in its porespace and also in disequilibrium with the adjacent groundwater and Fe-solution, the system was very reactive. The main mineralogical change observed after a maximal simulation time of 3320 years was the complete conversion of Na/Ca-montmorillonite to Ca-montmorillonite due to equilibration with the model groundwater. Formation of illite, saponites, chlorites and Na-montmorillonite was minimal.

Montes-Hernandez et al. (2005b) used the same setup as Montes-Hernandez et al. (2005a) but replaced the Fe-(II)-solution boundary with metallic iron. The corrosion rate of iron was assumed to be 5 μm/year at 100 °C. Potential secondary phyllosilicates considered were illite, vermiculite, various saponites, Na-, Ca-, Mg-, K-, and Fe-montmorillonites, greenalite, cronstedtite, 7Å-chamosite (corresponding to berthierine and not chlorite), chrysotile, as well as Fe- and Mg-chlorite. After 10'000 years of simulated diffusive transport and reaction, montmorillonite was completely consumed in the first 10 cm of the bentonite adjacent to the groundwater and converted mainly to illite and saponite. In addition, minor amounts of quartz, cristobalite, and anhydrite were formed. Mineralogical changes in the bentonite adjacent to the metallic iron were minor and characterized by the formation of small amounts of laumontite, magnetite and chlorite. As in the simulations by Montes-Hernandez et al. (2005a), the alteration of the bentonite was dominated by the diffusive equilibration with the model groundwater.

Bildstein et al. (2006) modelled 1-D diffusive reaction-transport in a fully saturated model system consisting of a 7 cm thick stainless-steel canister, an 80 cm thick bentonite barrier (consisting mainly of Na-montmorillonite and Ca-montmorillonite with small amounts of feldspars, calcite, chalcedony and pyrite) and 10 m of an argillite (consisting mainly of illite, quartz, calcite, Ca- and Na-montmorillonite and minor amounts of dolomite, K-feldspar, kaolinite, pyrite, and goethite). Calculations were performed at 50 °C with an iron corrosion rate of 4.3 μm/year. The simulation time was limited to 16'200 years (complete corrosion of 7 cm of steel).

In the bentonite and in the argillite, the primary clay minerals were destabilized and replaced by cronstedtite and berthierine (sometimes also called 7Å-chamosite by Bildstein et al. 2006). After a simulation time of 5'000 years the reaction front reached 4 m into the argillite, characterized by the complete dissolution of Ca- and Na-montmorillonite and partial dissolution of illite. These minerals were replaced mainly by cronstedtite, berthierine, low-Fe smectite, siderite and scolecite (a Ca-zeolite).

Samper et al. (2008) presented 1-D and 2-D reaction transport models for the simulation of canister corrosion, the interaction of corrosion products with bentonite and the long-term evolution of the porewater composition in the nearfield of a repository in fractured granite. Dissolution and precipitation of clay minerals was not allowed in these models.

Marty et al. (2010) modelled 1-D diffusive reaction-transport in a model system consisting of a 1 m section of bentonite bounded on one side by 10 cm of metallic iron and on the other side by an infinite reservoir of a model groundwater representative for the Callovo-Oxfordian. In order to simulate iron corrosion, a small section containing fluid was inserted between the iron and the bentonite. The bentonite consisted mainly of montmorillonite, with smaller amounts of quartz, biotite, feldspars, calcite and pyrite. The temperature was assumed to be 100 °C. Potential secondary Fe-rich phyllosilicates considered were vermiculite, berthierine (referred to as 7Å-chamosite by Marty et al. 2010), greenalite, cronstedtite, chlorite, nontronite, and three different types of saponite. The simulation time was 100'000 years. Three distinct zones could be distinguished in the altered bentonite. At the interface with the groundwater the alteration zone is characterized by complete transformation of montmorillonite into illite and the precipitation of quartz, Mg-Fe-saponite and vermiculite. In the alteration zone adjacent to the corroding iron, montmorillonite was completely replaced by Fe-chlorite, Fe-saponite, and magnetite. In addition, small amounts of berthierine, chrysotile and laumontite were formed. In the central zone, montmorillonite was only slightly transformed into illite and Mg-Fe-saponite. Although montmorillonite was completely consumed at the interfaces with the groundwater and with the corroding iron, more than 60 % of the initial montmorillonite remained intact after a simulation time of 100'000 years.

Savage et al. (2010c) have suggested that evidence from natural systems indicates that the sequence of alteration of clay formations by iron-rich fluids may proceed according to the Ostwald step rule. They used a kinetic modelling approach that considers homogenous or heterogeneous nucleation, precursor cannibalization, and Ostwald ripening for calculating the time evolution of the surface area of secondary minerals. The model system consisted of 70 cm bentonite, bounded by 10 cm of metallic iron on one side and of a granitic model groundwater on the other side. The initial bentonite contained 71 wt. % Na-montmorillonite, 18 wt. % Ca-montmorillonite 8 wt. % Mg-montmorillonite, 2 wt. % K-montmorillonite and 1 wt. % calcite and was saturated with a $NaCl$-Na_2CO_3-porewater at pH 10.4. The temperature was set at 25 °C. Potentially forming Fe-rich phyllosilicates considered were berthierine, cronstedtite and chlorite. Two kinetic models were investigated. In the first model, the kinetic parameters for secondary mineral growth were assumed to be independent of the surface area, while in the second model, the surface areas of magnetite, siderite, berthierine, cronstedtite, and chlorite were calculated by tracking crystal size distributions as functions of nucleation and Ostwald ripening. Chlorite was allowed to grow on berthierine, while berthierine was allowed to grow on cronstedtite. In the simulations with the first model, berthierine is the dominating Fe-mineral in the bentonite compartment next to the corroding iron, while siderite begins to appear in considerable quantities only after simulation times of 10'000 years. Due to the relatively high concentrations of calcium in the model groundwater, and to the release of magnesium from dissolving montmorillonite, significant amounts of dolomite are also formed. Further away from the corroding iron, berthierine continues to be formed as more iron diffuses into the bentonite. The

simulations with the second model show a different evolution of secondary minerals. Magnetite initially forms near the iron-bentonite interface and is replaced by cronstedtite which dominates between 0.4 and 500 years, while berthierine and dolomite are also present. After 500 years cronstedtite is replaced by berthierine. Chlorite begins to form on the surfaces of berthierine after 5'000 years. Compared to model one, there is less Fe-mineral precipitation further away from the corroding iron.

All of these modelling studies cover a large variation of modelling assumptions, specific geometry, initial mineralogy, chemical composition of porewaters, and choice of potential secondary minerals, which is clearly reflected in the diversity of the results with respect to the extent of montmorillonite destabilization and to the type of Fe-rich minerals that are formed. These cover the range from smectites (low-Fe smectite and saponite), non-swelling 7Å-minerals (greenalite, cronstedtite, and berthierine) to non-swelling chlorite and finally to magnetite and siderite. It is, however, very challenging to single out the parameters that lead to the formation of a specific Fe-rich secondary mineral.

It is worth mentioning that some simulations predict significant porosity changes. In the simulation by Bildstein et al. (2006), complete porosity clogging occurs after 5'000 years near the surface of the corroding canister, due to the precipitation of magnetite and cronstedtite and, to a lesser extent, of berthierine and siderite. 10 cm into the bentonite, the porosity is increased, due to the dissolution of montmorillonite. Porosity in the bentonite is also significantly reduced near the corroding iron in the simulation by Marty et al. (2010), caused by the massive precipitation of Fe-saponite. In the simulations by Savage et al. (2010c), the precipitation of dolomite and iron corrosion products lead to complete clogging of the porosity causing the simulation to end prematurely.

7.4 Extent of bentonite alteration

While several of the experiments discussed above have shown that montmorillonite may be destabilized by iron corrosion, the extent of this destabilization is not easy to assess since the reaction rates at the temperatures of interest are rather low. A simple mass balance approach was used by Wersin et al. (2007b) to estimate the maximum extent of conversion of montmorillonite to non-swelling iron-silicates due to the corrosion of the steel supercontainer for the KBS-3H disposal concept. Assuming that all of the iron from the corroded supercontainer is available for conversion (neglecting the amount of iron bound in corrosion reaction products such as magnetite etc.) they estimated that about 12 mol % of montmorillonite would be consumed if Fe-chlorite (chamosite) were to be formed, and about 30 mol % if berthierine were formed. While this would have significant effects on the swelling capacity of bentonite (especially in the case of berthierine) at least 70 % of the sorption capacity would be conserved.

A similar procedure can be applied to SF and HLW for the Swiss disposal concept (for details see Appendix B2). In the case of SF, 70 mol % of montmorillonite could be converted to chamosite and more than 100 mol % to berthierine. For HLW the corresponding numbers are 30 mol % for the conversion to chamosite and 80 mol % for the conversion to berthierine. From a mass balance point of view, these percentages are too large to be considered insignificant. They clearly show that the amount of iron present in the SF and HLW canisters has a large potential to reduce the amount of montmorillonite in bentonite and thus reduce the swelling and sorption capacity of bentonite.

The maximum extent of montmorillonite conversion to berthierine or chamosite as a function of time can be calculated by considering iron corrosion rates (for details of the calculations see Appendix B2). Results for an average corrosion rate of 1 μm per year[11] (Johnson & King 2003) are summarized in Fig. 7-1 and Tab. 7-2. After 10'000 years of SF-canister corrosion, 15 % of montmorillonite could be converted to berthierine and 6 % to chamosite. After 20'000 years, 29 % could be converted to berthierine and 11 % to chamosite. For the corrosion of HLW-canisters, the numbers are 8 % (10'000 years) and 15 % (20'000 years) for the conversion to berthierine, and 3 % (10'000 years) and 6 % for the conversion to chamosite.

SF-canisters are completely corroded after 155'000 years, leading to the complete conversion of montmorillonite to berthierine or to 70 % of montmorillonite converted to chamosite. HLW-canisters are completely corroded after 127'000 years with 80 % of montmorillonite converted to berthierine or 30 % converted to chamosite.

As there are several competing sinks for iron in the bentonite backfill, not all of the iron released during corrosion is expected to partake in the destabilization of montmorillonite and lead to the formation of phyllosilicate phases. The main competitor for iron is likely to be magnetite. Depending on the carbonate and sulfide content of the bentonite porewater, siderite and sulfide are also expected to form.

Tab. 7-2: Time evolution of canister corrosion and montmorillonite transformation for a corrosion rate of 1 μm per year based on simple mass balance considerations.

		SF BWR	**HLW**
Canister	Time needed for complete corrosion of canister	155'000 yr	127'000 yr
Berthierine	Time needed for transformation of montmorillonite	72'600 yr	127'000 yr
	Amount of montmorillonite transformed	100 %	78 %
	Amount of iron corroded	52 %	100 %
Chamosite	Time needed for transformation of montmorillonite	155'000 yr	127'000 yr
	Amount of montmorillonite transformed	72 %	29 %
	Amount of iron corroded	100 %	100 %

[11] The reference corrosion rates for Nagra's safety analyses have been reconsidered recently (Diomidis 2014). A statistical evaluation of experimental data resulted in a mean value of 0.43 μm/y. For the safety analyses, however, a higher reference value of 2 μm/y was selected. In this study, the earlier value of 1 μm/y was kept. The time evolution of Montmorillonite transformation (Tab. 7-2, Fig. 7-1) scales linearly.

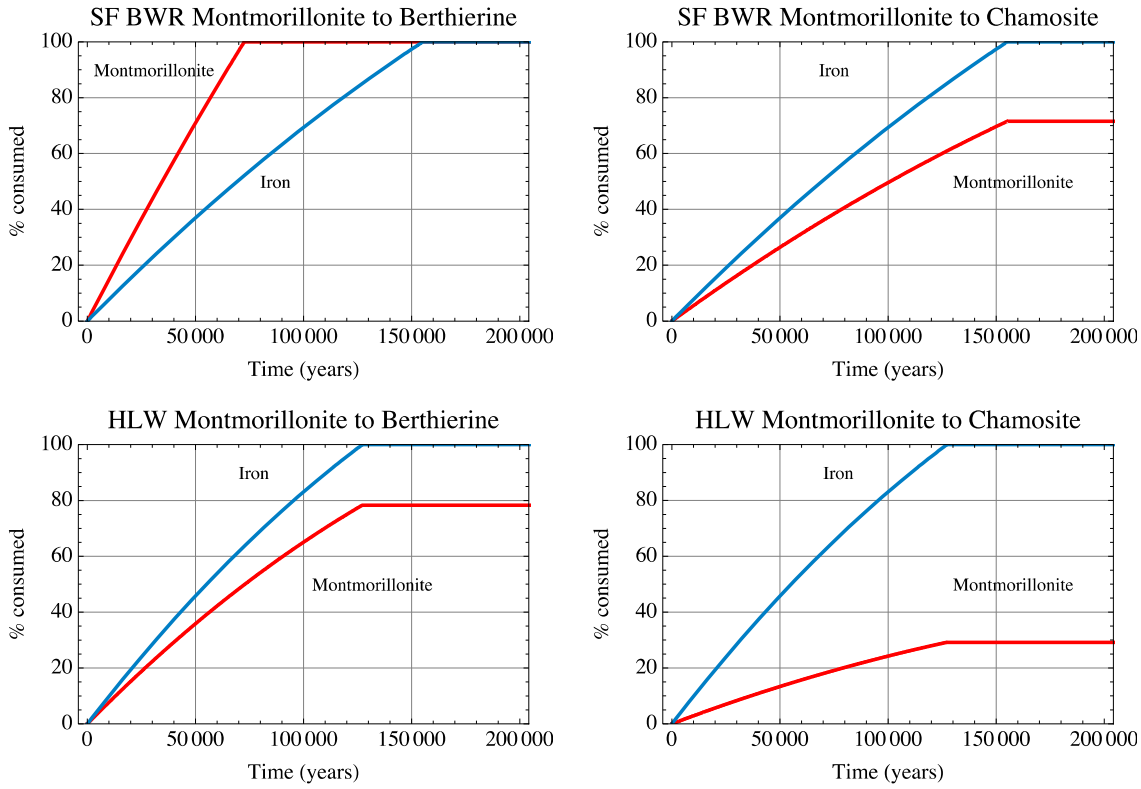

Fig. 7-1: Percentage of iron corroded and of montmorillonite converted as a function of time for a corrosion rate of 1 µm per year.

See Appendix B2.2 for details of calculation.

7.5 Summary

The interaction between iron, respectively, iron corrosion products, and bentonite in a reducing environment involves several processes, the details of which are not very well known. However, if iron corrosion can be prevented or significantly delayed then any influences on the bentonite properties could be prevented or seriously reduced. For this reason Nagra is considering alternative design options for the canisters such as Cu/steel canisters or copper coated steel canisters.

Sorption of Fe^{2+} released by the corrosion of iron on montmorillonite is the fastest process, and is governed by two main uptake mechanisms, namely, cation exchange and surface complexation. Fe^{2+} may compete for sorption with radionuclides of similar chemical characteristics (valence state and hydrolysis behaviour). Of greater significance is the potential destabilization and transformation of montmorillonite in the presence of iron, a process which is much slower and therefore much more difficult to investigate experimentally. The results of the reviewed experiments and modelling studies suggest that the destabilization and transformation of montmorillonite at temperatures below 100 °C may lead to the formation of two broad types of clay minerals: swelling or non-swelling. Swelling clay minerals found in experiments were Fe-rich smectites, in some cases tentatively identified as dioctahedral saponites, but the exact identification is often not possible due to difficulties in distinguishing between Fe^{2+} in interlayer or in octahedral sites. The non-swelling clay minerals found were in most cases 1:1 phyllosilicates belonging to the 7Å kaolinite/serpentinite group, such as berthierine. As in the case of the Fe-smectites, it is often not possible to distinguish between the different members of this group. The transformation of montmorillonite into Fe-rich 7Å minerals can be considered as a three

step process: The initial destabilization of montmorillonite leads to the formation of amorphous Si-Al-Fe gels which mature and crystallize into the Fe-rich 7Å-phases. Chlorite was not found in experiments below 100 °C. In the modelling studies, the secondary Fe-rich clay minerals formed at the expense of montmorillonite cover the range from smectites (low-Fe smectite and saponite), to non-swelling 7Å-minerals (greenalite, cronstedtite, and berthierine) and to non-swelling chlorite.

At the present state of knowledge, the extent of bentonite alteration due to iron corrosion, and the exact type of alteration products produced, cannot be predicted with any confidence. Simple mass balance constraints, however, indicate that enough iron is present in the SF-canisters so that about 70 % of montmorillonite could be converted to chamosite and more than 100 % to berthierine. For the HLW-canisters the corresponding numbers are at least 30 % for the conversion to chamosite and more than 80 % for the conversion to berthierine. Iron-bentonite interactions can therefore not be neglected on this basis. As there are several competing sinks for iron in the bentonite backfill, not all of the iron released during corrosion can be expected to destabilize montmorillonite. The main competitors for iron are likely to be magnetite and siderite. Depending on the sulfide content of the bentonite porewater, iron sulfides are also expected to form.

The maximum extent of montmorillonite conversion to berthierine or chamosite as a function of time can be calculated by considering iron corrosion rates. With an average corrosion rate of 1 μm per year and 10'000 years of SF-canister corrosion, about 15 % of montmorillonite could be converted to berthierine and 6 % to chamosite. After 20'000 years, 29 % could be converted to berthierine and 11 % to chamosite. For the corrosion of HLW-canisters, the numbers are 8 % (10'000 years) and 15 % (20'000 years) for the conversion to berthierine, and 3 % (10'000 years) and 6 % for the conversion to chamosite.

While these extents of montmorillonite alteration would probably not gravely affect the safety-relevant features of the bentonite backfill, it is perhaps useful to consider the extreme case of a complete transformation of montmorillonite to Fe-rich smectites, 7Å-minerals, or chlorite and to try and give a rough and qualitative assessment of its possible influence on the safety-relevant attributes of bentonite as defined in Leupin & Johnson (2013), see Tab. 7-3.

- Low hydraulic conductivity: If montmorillonite is replaced by Fe-smectites, the low hydraulic conductivity is probably not seriously affected. In the case of 7Å-minerals or chlorite, hydraulic conductivity is potentially increased by dehydration of interlayers and resulting layer collapse, but, on the other hand, may be decreased due to cementation by other minerals (e.g. quartz). In addition, 7Å-minerals and chlorite have no swelling capacity and therefore cracks in the buffer cannot close by self-sealing.
- Chemical retention of radionuclides: Fe-smectites: Little change in sorption capacity is to be expected, however, radionuclide retention may be reduced by sorption competition with Fe. 7Å-minerals: Little is known about the sorption properties of greenalite, cronstedtite, and berthierine. It is, however, reasonable to assume that they are comparable with serpentine. Since serpentine has a CEC of 1 meq/kg (Bradbury et al. 2010), the favourable cation exchange properties of montmorillonite are lost after the transformation to 7Å-minerals. Chlorite: According to Bradbury et al. (2010), the CEC of chlorite has been reported to be 50 or 100-400 meq/kg (the latter range is most probably too high), which is significantly smaller than the CEC of montmorillonite (787 meq/kg).

- Sufficient density: The density of a bentonite buffer must be high enough to ensure that the microporous structure provides an effective barrier for colloid transport. The transformation of montmorillonite to Fe-smectites will have little influence on the density of the buffer and therefore the transport of colloids will not be enhanced. The transformation of montmorillonite to 7Å-minerals or to chlorite, however, will change the pore structure, and this will be most likely detrimental to the buffer's capacity to prevent colloid transport.
- Sufficient swelling pressure: The swelling capacities of Fe-smectites are comparable to that of montmorillonite, therefore the swelling pressure will not change significantly after complete transformation of montmorillonite to Fe-smectites. The 7Å-minerals and chlorite have no swelling capacity, but the loss of swelling pressure is probably of little consequence, since significant conversion of montmorillonite is expected to take place long after mechanical equilibrium is attained.
- Mechanical support: The viscosity of the buffer material must be sufficiently high to prevent canister sinking. The viscosity is not expected to decrease after complete transformation of montmorillonite to Fe-smectite, and the same is probably true in the case of conversion to 7Å-minerals or chlorite.
- Sufficient gas transport capacity: If montmorillonite is completely transformed, most of the iron will be corroded, and gas transport is no longer a principal issue. During iron corrosion, however, some reactive-transport models suggest clogging of porosity around the canister, which would compromize the capacity of the buffer to transport corrosion gases.
- Minimize microbial corrosion: If montmorillonite is completely transformed, most of the iron will be corroded anyway. At that time, therefore, this safety attribute is no longer relevant.
- Resistance to mineral transformation: Mineral transformation is the subject of this chapter.
- Suitable heat conduction: Montmorillonite conversion will take place long after the thermal maximum has been attained, when the heat conduction properties are no longer of any importance.

In order to assess the potential influence on sorption of the complete transformation of montmorillonite to 7Å-minerals or to chlorite, a hypothetical porewater for transformed bentonite was defined, which is to serve as a rough guide. For details see Supplement 2.

Tab. 7-3: Estimated qualitative influence of complete replacement of montmorillonite by Fe-rich clay minerals on the safety-relevant properties of bentonite.

Safety-relevant attributes [1]	**Favours/contributes to** [1]	**Revised criteria buffer/ preferred values** [1]	**Montmorillonite replaced by Fe-smectites**	**Montmorillonite replaced by 7 Å-minerals**	**Montmorillonite replaced by chlorite**	**Comments**
Low hydraulic conductivity	Attenuation safety function of buffer, by ensuring diffusive transport	$K < 10^{-11}$ m s^{-1}	Little difference	Possible increase, no self-sealing	Possible increase, no self-sealing	Hydraulic conductivity is increased by dehydration of interlayers and resulting layer collapse, but may be decreased due to cementation by other minerals (e.g. quartz)
Chemical retention of radionuclides	Attenuation safety function of buffer, by retarding transport from the buffer	No quantitative criterion, strong sorption is favored	No change in sorption capacity, reduction of radionuclide retention by sorption competition	Reduction of sorption capacity, no interlayer for cation exchange	Reduction of sorption capacity, no interlayer for cation exchange	
Sufficient density	Attenuation safety function of buffer, by preventing colloid transport	$\rho s > 1'650$ kg m^{-3}	Little difference	uncertain	uncertain	The transformation to 7 Å-minerals or to chlorite is most likely detrimental to the buffers' capacity to prevent colloid transport. The adjacent Opalinus Clay diminishes colloid mobility.
Sufficient swelling pressure	Attenuation safety function of rock, by providing mechanical stabilization of rooms, and hence avoiding significant extension of EDZ	0.2 MPa $< Ps <$ minimum principal stress	Little difference	Probably not relevant	Probably not relevant	Although the 7 Å-minerals and chlorite do not swell, the potential loss of swelling pressure is probably of little consequence, since significant conversion of montmorillonite is expected to take place long after mechanical equilibrium is attained
Mechanical support	Safety function of canister, by ensuring it is surrounded by a protective layer of buffer (stress buffering)	Buffer must be sufficiently viscous to avoid canister sinking	No negative influence	No negative influence	No negative influence	Viscosity is not expected to decrease by these mineral transformations
Sufficient gas transport capacity	Attenuation safety function of buffer, by ensuring gas can migrate without compromising hydraulic barrier	No quantitative criterion; less than the minimum principal stress	No negative influence	Probably not relevant	Probably not relevant	If montmorillonite is completely transformed, most of the iron will be corroded anyway, and gas transport is no more a principal issue

Tab. 7-3: Continued

Safety-relevant attributes [1]	Favours/contributes to [1]	Revised criteria buffer/ preferred values [1]	Montmorillonite replaced by Fe-smectites	Montmorillonite replaced by 7 Å-minerals	Montmorillonite replaced by chlorite	Comments
Minimize microbial corrosion	Safety function of canister, by ensuring conditions favorable to slow corrosion	No quantitative criterion	Not relevant	Probably not relevant	Probably not relevant	A narrow disturbed zone near the canister could enable microbial activityat or near the interface and influence corrosion rate. Microbial activity, however, would be limited by the slow, diffusive supply of sulphate.
Resistance to mineral transformation	Longevity of other safety relevant attributes of buffer	No quantitative criterion				Mineral transformation is the subject of this chapter
Suitable heat conduction	Safety functions of buffer and rock, by ensuring favorable maximum temperature conditions	$0.4 < Tc < 2$ W m^{-1} K^{-1} (for a specific thermal heat load of 1'500 W)	Not relevant	Not relevant	Not relevant	Montmorillonite conversion takes place long after thermal maximum

[1] Source: Leupin & Johnson (2013)

8 Vitrified High Level Waste

8.1 Introduction

In Switzerland, a considerable fraction of high-level waste arising from the operation of nuclear power plants has been or is being reprocessed by AREVA (formerly COGEMA) and BNFL. The resulting borosilicate glass waste will be disposed of in the planned HLW repository in the Opalinus Clay. A major safety-relevant issue related to vitrified nuclear waste is its chemical degradation rate in aqueous media over repository-relevant timescales. Although experiments over such timescales (> 10^3 a) are obviously not possible, it is generally accepted that kinetic experiments conducted over a few years or decades can be used to infer long-term glass corrosion rates from which radionuclide release rates can be derived for performance assessments. In order to extrapolate data to repository-relevant time frames, glass corrosion experiments are routinely performed under special conditions aimed at accelerating the degradation process. For instance, advanced stages of glass corrosion can be simulated by increasing the specific surface area of the glass up to a factor of 500 by grinding to a fine-grained powder, or by carrying out the experiments at moderately increased temperatures (typically 90 °C) compared to those expected in geological repositories (~ 40 – 60 °C). The temperature increase is supposed to accelerate the corrosion process by approximately 1 – 2 orders of magnitude without modifying the relevant chemical reactions. In this chapter, the expected evolution of vitrified radioactive waste after canister failure is analysed and discussed, as well as possible deviations from the expected behaviour that could arise from known or yet unidentified "disturbance effects". As far as the glass corrosion kinetics are concerned, the analysis is based on the large pool of data available from both in-house experiments and the dedicated EU-projects carried out over the past decades (SOURCE-TERM, GLASTAB, NF-PRO). Complementary evidence from natural analogues is also used. The second part is devoted to possible chemical disturbances and their effects on the functionality and integrity of the near-field.

8.2 Glass corrosion kinetics

8.2.1 The empirical rate law

In pure water, borosilicate glasses corrode initially at rates of about 1 g m^{-2} d^{-1} (at 90 °C), which rapidly decrease as silica dissolved from the glass accumulates in the aqueous solution. The rate decrease has been shown to be inversely proportional to the silica concentration, leading to a well-known and widely applied empirical kinetic law (Grambow 1985, Grambow 1987, Curti et al. 1993, Vernaz & Dussossoy 1992). According to this model, a final, constant small corrosion rate (the residual rate) is reached when a limiting silica concentration, specific to each glass composition, is attained. The driving force maintaining this *residual rate* is supposed to be the small difference in free energy ("affinity") between the dissolving glass and the silica phase precipitating on the glass surface. Typical measured values of R_{sat} are between 10^{-4} and 10^{-3} g m^{-2} d^{-1} at 90 °C. Although popular, this model has repeatedly proven to be unsuitable or at least incomplete (Frugier et al. 2004) and there is now ample evidence that R_{sat} is not only determined by the silica concentration in the aqueous phase. Failure of the affinity model has emerged also from the analysis of the data gathered during the JSS-project and the more recent PSI long-term experiments (Curti 2003, Curti 2009).

8.2.2 The role of the gel layer on the long-term rate

Whereas all investigators agree that the major parameter controlling the initial stage of glass corrosion kinetics is the dissolved silica concentration, a long-standing debate persists on the mechanisms governing the long-term kinetics at high dissolved Si concentrations (~ 10^{-3} M at 90 °C). The PNL group in the U.S. favours the view that the primary factor controlling glass dissolution rates is always the Si concentration, therefore fully accepting the residual affinity model and applying it also in repository simulations (McGrail et al. 2001). On the other hand, the French group at CEA Marcoule (Gin et al. 2001) asserts that the reduction in glass corrosion rate observed at longer times is due to the protective properties of the amorphous gel layer formed on top of the fresh glass (passivating gel model). The thickness, composition and diffusion properties of such layer were found to depend on the amount of silica available and the chemical composition of the glass. According to this view, long-term rates cannot be predicted from thermodynamic principles only.

Cailleteau et al. (2008) showed that the "passivation power" of a gel depends on the concentration of network modifiers, such as Zr, in the pristine glass. Zr is sparingly soluble and is retained almost entirely in the gel layer. At high Zr concentrations, polymerization of the $(Si,Al)O_4$ tetrahedral units in the gel layer is inhibited by the high coordination number (CN = 8) of oxygen atoms around Zr^{4+}. This would result in a higher porosity of the gel layer and thus a higher diffusivity for dissolved species released from the glass. The consequence is a comparatively higher corrosion rate. Other investigations from the same group (Chave 2007, Thien 2010, Thien et al. 2010, Thien et al. 2012) indicate that other elements, such as Ca and Mg, may lead to the opposite effect, i.e. a decrease in corrosion rate when incorporated in the gel. These results indicate that the long-term glass corrosion kinetics largely depend on the properties of the gel layer.

8.2.3 The effect of clay on the glass corrosion kinetics

There is ample laboratory and field evidence that the corrosion of borosilicate glasses may be enhanced by the presence of clay (e.g. Godon 1988, Curti & Smith 1991, Curti et al. 1993, Lemmens 2001, Godon 2004, Godon et al. 2008) or Fe corrosion products such as magnetite (Bart et al. 1987). According to the current understanding, this effect is attributed to silica uptake by the mentioned materials, which is consistent with the "passivating gel model". If the silica released from the dissolving glass is actively removed by adsorption on the clay / iron oxide surfaces, or by precipitation of secondary silicates, the formation of a dense polymerized Si-rich layer on the glass surface is prevented, or at least delayed. The thickness of the gel layer will be smaller than in the absence of Si uptake, implying faster diffusion of dissolved species from and to the pristine glass surface. Consequently, glass corrosion will proceed at comparatively higher rates even at aqueous Si concentrations close to the saturation limit, C_{sat}, until the removal of Si stops, e.g. through saturation of the available sorption sites.

This interpretation is supported by the observation that the addition of fine-grained, easily soluble silica to the clay, e.g. in the form of opal or glass frit powder, completely blocks the catalysing effect of the clay. In such cases the measured corrosion rates are orders of magnitude lower and comparable to those measured in the absence of clay (Gin et al. 2001, Valcke 2007, Godon et al. 2008). The Si dissolved from the added silica rapidly saturates the sorption capacity of the clay. Therefore, the silica released from the corroding glass cannot be removed by sorption and is mostly retained in the gel layer, which acquires passivating properties by forming a polymerized network of silanol bonds.

In the framework of EURATOM programs, corrosion experiments with active SON68 type glass and other nuclear glasses were carried out in the HADES underground laboratory at Mol, Belgium (Kursten et al. 1997, Valcke 2007). Small polished glass wafers with total surface areas of a few cm^2 were mounted in special tubes drilled into the clay rock and put into direct contact with the Boom Clay or with compacted, almost water-saturated Ca bentonite, at temperatures varying between 16 °C and 170 °C and pHs from 6 to 9. At the end of the experiments (duration 1.3 – 7.5 years) the glass specimens were removed, gently washed and weighed to determine the normalized mass loss.

A compilation of results from *in-situ* experiments carried out with active SON68 glass in direct contact with Boom Clay is shown in Fig. 8-1, in comparison with the results of the PSI long-term laboratory experiments, carried out at 90 °C in pure water but without clay. The in-situ data from Kursten et al. (1997) indicate an average corrosion rate of 0.75 g m^{-2} d^{-1} at 90 °C over 7.5 years, a value close to the initial corrosion rate of SON68 glass in pure water. More recent in-situ experiments in the framework of the CORALUS project (Valcke 2007) indicate lower average rates, but still of the same order of magnitude. The average rates extracted from the data of Kursten et al. (1997) are at least 1'000 faster than the rates determined for SON68 glass in pure water. Moreover, in the in-situ experiments the corrosion rate does not appear to decrease over time (Tab. 8-1).

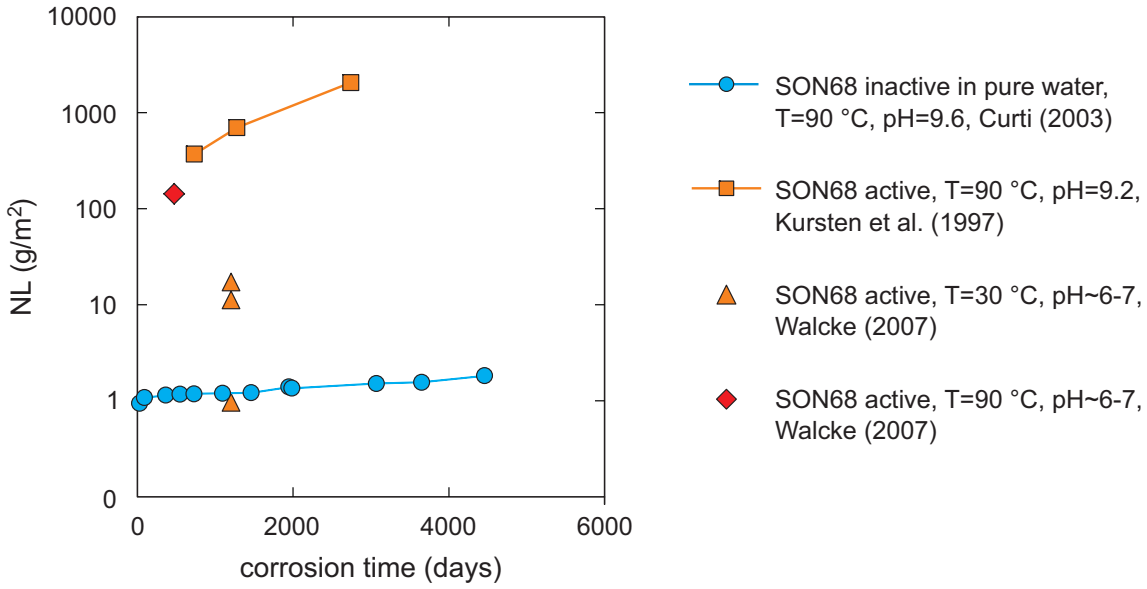

Fig. 8-1: Surface normalized glass mass losses from in-situ corrosion experiments in contact with Boom Clay, compared to the data obtained from the PSI long-term experiments.

As discussed above, the fast glass corrosion rates measured in contact with clay are usually explained by the uptake of silica by clay minerals. This mechanism was obviously not operating in the case of the PSI long-term experiments, where a fine-grained, high specific surface area glass powder was leached in pure water without addition of other materials. Under such circumstances, Si saturation in the aqueous solution is rapidly reached, and a dense passivating gel layer, mainly composed of amorphous silica, is formed, reducing the corrosion rate to very low values.

The presence of amorphous silica in MX-80 (Gailhanou et al. 2012), the reference bentonite backfill material in the Swiss HLW repository, may prevent such high corrosion rates via the two mentioned effects: (a) by decreasing the initial rate (the dissolved Si concentration at the start of corrosion would be closer to "silica saturation" than in the absence of amorphous silica); (b) by blocking the Si adsorption on the clay, thereby favouring the polymerization of silica in the gel layer.

Glass corrosion experiments carried out with AREVA glass in the context of the JSS project (Fig. 9 in Curti 2009) are consistent with this interpretation. Indeed, short-term glass dissolution is strongly enhanced in the presence of small amounts of MX-80 bentonite (1.67 g/L). Probably, in this case the amount of soluble silica in bentonite (2 wt. %) is not sufficient to increase significantly the dissolved Si concentration. Adding increasing amounts of MX-80 (up to 133 g/L) progressively reduces glass dissolution, until practically no difference is observed compared to glass corrosion in pure water (without any clay present). In this case, the dissolving amorphous silica is sufficient to both quickly saturate the sorption sites on the clay and to raise dissolved Si concentrations, so that the silica released through glass corrosion can be used to build a protecttive gel layer. The net effect is a reduced glass corrosion rate compared to the case of small amounts of added clay.

Tab. 8-1: Average corrosion rates in (g m^{-2} d^{-1}) determined from in-situ glass corrosion experiments with active SON68 glass in contact with Boom Clay, compared to the rates derived from the PSI long-term experiments with inactive SON68 in pure water.

T	**Time span**	**Kursten et al. (1997)**	**Valcke (2007)**	**Curti (2003)**
		In-situ exp. with Boom Clay		laboratory
90 °C	~ 0 – 2 a	5.1×10^{-1}	0.30	$\sim 2 \times 10^{-3}$
	~ 2 – 4 a	6.1×10^{-1}	--	1.3×10^{-4}
	~ 4 – 7.5 a	9.3×10^{-1}	--	1.3×10^{-4}
30 °C	~ 3 a	$8 \times 10^{-4} – 1.2 \times 10^{-2}$	--	--
16 °C	5 a	1.6×10^{-3}	--	--

It may be argued that the results of the Belgian experiments are more relevant for safety assessment purposes than laboratory experiments carried out in pure water. However, we point out that the described in-situ experiments cannot be considered to be representative of realistic disposal conditions. Indeed, there are fundamental differences between such experiments and the repository conditions expected in the planned Swiss HLW repository:

(a) *Physical separation between waste glass and clay* – in the repository, the waste glass will not be in direct contact with the clay, since the form will be physically separated from the bentonite buffer by a massive canister. In addition, the waste glass will be fractured, implying that most of the surfaces exposed to aqueous solution will be in the internal part of the waste form, which is physically separated from each material capable to enhance glass dissolution (iron corrosion products, clays). Experiments on a fractured ancient Roman glass body, buried in sea sediment during 1800 years, have shown that glass dissolution was less severe in the cracks of the internal part of the glass, compared to surfaces in direct contact with the sea sediment (Verney-Carron et al. 2008).

b) *Different glass surface to clay ratios* – In the Belgian in-situ experiments, small polished glass chips of a few cm^2 surface area were in direct contact with large masses of clay. This means that the clay imposes the chemical conditions (including pH) during the interaction with glass, and offers a large capacity for silica uptake. In the planned HLW repository, a relatively large volume of fractured glass (~ 0.15 m^3) will be physically separated from the bentonite buffer by a massive steel canister. After canister failure, porewater and possibly small amounts of wet bentonite will penetrate into the cracks separating the glass fragments, resulting in very low local clay/glass ratios. Since it has been demonstrated that the catalytic effect of clay is proportional to the clay mass to glass surface ratio (Godon et al. 2008, p. 88, Godon 2004, p. 258) it may be anticipated that the small amounts of clay in contact with the vitrified waste would be able to adsorb only a small fraction of the silica released from the glass during corrosion. Thus, residual rates will be reached in a very short time compared to the timescale of repository evolution. Indeed, a major finding of the JSS project was that the presence of small amounts bentonite during aqueous glass alteration had only a small and transitory catalytic effect (Werme et al. 1990, Curti 2009).

(c) *Time scale of the in-situ experiments is too short* – The corrosion time of 7.5 years in the Belgian in-situ experiments may not have been sufficient to reach silica saturation, due to the low glass surface/solution volume (*A/V*) ratio. In contrast, the high *A/V* ratios used in long-term laboratory glass leaching tests guarantees the rapid attainment of this condition, thereby simulating longer reaction times.

In conclusion, although there is no doubt that clay has the potential to considerably enhance glass corrosion rates, many uncertainties remain about the magnitude and time scale of such effects under repository conditions. The future challenge will be to devise experimental setups that really mimic representative deep repository conditions.

8.2.4 The effect of Fe alteration products

Alteration products resulting from the degradation of the steel canisters are generally considered to act in a similar way to clay, i.e. to enhance glass corrosion via removal of dissolved silica by sorption or precipitation of secondary silicates (Godon et al. 2008). Nevertheless, the experimental basis for this conclusion is rather weak, since only a few experimental investigations have been carried out to date. Most of the available data stem from the JSS project (Bart et al. 1987, Grambow 1987, Werme et al. 1990, Zwicky et al. 1989). Isolated studies were conducted by McVay and Buckwalter (1983) and Inagaki et al. (1996).

A summary of data obtained from the corrosion of AREVA type glasses in the presence of magnetite or goethite powder is shown in Fig. 8-2, in comparison with the results from experiments carried out in pure water (blue triangles). The data indicate that

(i) the addition of Fe oxides does indeed lead to increased glass corrosion

(ii) the total amount of corroded glass depends on the quantity and specific surface area of the added Fe corrosion product which is again consistent with the hypothesis that Si sorption drives the glass corrosion kinetics.

Nevertheless, a closer inspection indicates that this effect is probably transitory, since the slopes of all of the NL(B) data sets versus time (and therefore the glass corrosion rates) flatten out after 30 days corrosion time. Unfortunately, the experimental method used for the JSS experiments (preparation of separate samples for each single data point) prevented a sufficiently precise determination of the long-term rate, as is evident from the scatter of the data. Moreover, a corro-

sion time of 0.5 years is, in general, insufficient to reach the residual rate regime. Therefore, these results cannot be considered to be conclusive.

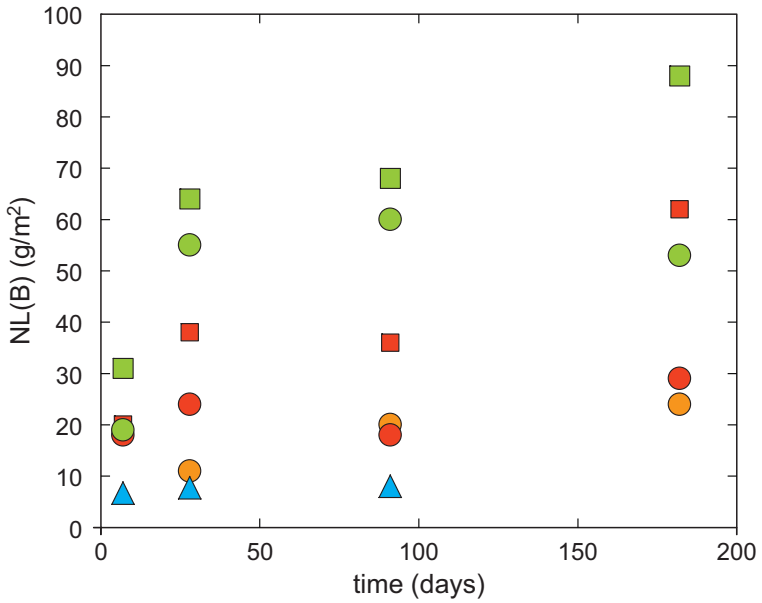

Fig. 8-2: Results of glass leaching experiments carried out with ABS118 (AREVA) glass at 90 °C and A/V=10 m^{-1} in pure water (blue triangles) and in the presence of different amounts of Fe corrosion products.

40 g/L commercial magnetite (orange circles); 4 and 40 g/L synthetic magnetite (red circles and squares, respectively); 4 and 40 g/L FeOOH (green circles and squares, respectively).

8.2.5 The effect of self-irradiation

Glass corrosion rates may be affected by radioactivity via at least three different mechanisms (Godon 2004): (a) structural damage induced by α,β self-irradiation; (b) decrease in pH and increase in E_h through water radiolysis; (c) modifications of the protective properties of the gel layer. Experimental evidence collected over the past decades consistently indicates that radiation damage and water radiolysis have no or only a short-term influence on glass corrosion kinetics. This conclusion is based on comparative experiments of radioactive glasses and the corresponding inactive simulations (Werme et al. 1990, Feng et al. 1993, Matzke 1997, see Godon 2004 for an overview).

Ideally, such experiments should be carried out using radioactive glasses doped with fast decaying α-emitters in order to simulate a cumulative internal dose comparable to that absorbed by vitrified nuclear waste after about ten thousand years. In many cases, no information is given on the actual dose accumulated before the start of the leaching experiments.

An exception to this rule was the investigation carried out by Matzke (1997) who carried out short-term (14 day) leaching tests at 150 °C using three ^{244}Cm-doped glasses (including SON68) with different cumulative doses. The results indicated that the amount of glass corroded remained unchanged, or was even reduced, with increasing alpha-dose. The maximum dose was 1.4×10^{25} α-decays/ m^3, corresponding to the dose accumulated in SF/HLW during $10^4 - 10^5$ years.

8.2.6 The combined effect of bentonite, Fe alteration products and self-irradiation

A major aim of the JSS study was to investigate the combined effects of self-irradiation and of the interaction with engineered barrier materials on glass corrosion kinetics. Representative data from the JSS project are presented in Fig. 8-3. The plot shows the normalized mass losses of boron from corrosion tests with active AREVA-type glass (JSSA, red data points) and its inactive counterpart (ABS118, green data points). One set of experiments (triangles) was carried out in pure water, whereas the other set was conducted under the same temperature and A/V conditions but in the presence of 33 g/L of magnetite powder and 133 g/L of MX80 bentonite (circles).

The results indicate similar corrosion kinetics for active and simulated (non-active) glass. After 1 year of corrosion time, the normalized mass losses of B, which represent the amount of glass dissolved during the corrosion process, can be considered to be identical for both glasses (within the rather poor reproducibility of the data, estimated to be about 20 %). These data also reveal that during the first months, about 3-4 times more glass was degraded in the presence of the magnetite/bentonite mixture compared to the tests in pure water. At later times, higher corrosion rates seem to persist for the tests with bentonite + magnetite, compared to the simple glass/water tests without additions, as indicated by the steeper slope of the corresponding curves. The average estimated rates for the time span 28-365 days (taking the ensemble of the data shown in Fig. 8-3) are 0.002 g m^{-2} day^{-1} in pure water and 0.007 g m^{-2} day^{-1} with addition of the magnetite/bentonite mixture. These results therefore indicate a significant increase in the glass corrosion rates when large amounts of engineered barrier materials are added. The corrosion time of 1 year was, however, insufficient to attain steady-state conditions.

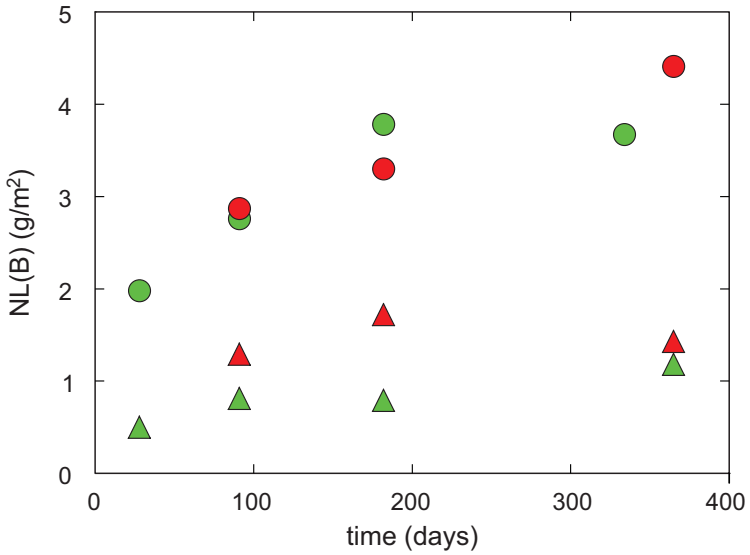

Fig. 8-3: Results of glass leaching experiments carried out at 90 °C and A/V = 1'100 m^{-1} with JSSA glass (red data points) and ABS118 glass (green data points), in pure water (triangles) and in the presence of a mixture of 33 g/L magnetite and 133 g/L MX-80 bentonite (circles).

8.2.7 Integrated tests (NF-PRO)

An attempt to investigate the combined effects of clay and iron corrosion products under conditions closely approaching those expected in a HLW repository was carried out in the context of the European NF-PRO project in the form of integrated laboratory tests (Minet et al. 2008). These "Joint Modular Integral Material Experiments" (JMIME) were carried out at 90 °C in two separate laboratories (SCK-CEN and CEA) for 2 years. The experimental setup consisted of a pressurized reactor cell filled with sequential layers of SON68 glass powder (0.0135 m^2/g, plus a single polished chip to allow for gravimetric mass loss measurements) magnetite powder (optional, 1.8 m^2/g), and compacted MX-80 bentonite (ρ_{dry}=1.4 g cm^{-3}). The reactor cell was connected to an inlet reservoir filled with pre-equilibrated bentonite porewater, which was pumped through the reactor at average flow rates varying between 1 and 5 mL/month. At the outlet, the percolating water from the glass layer was collected for the analysis of pH, B, Li, Si and other elements of interest.

The experiments carried out in the presence of MX-80 bentonite yielded almost constant corrosion rates of between ~ 0.007 and ~ 0.01 g m^{-2} d^{-1} (see Fig. 16 in Minet et al. 2008). These values are about two orders of magnitude smaller than the rates determined from the corresponding in-situ tests carried out in direct contact with Boom Clay (0.3 – 0.9 g m^{-2} d^{-1}, see Tab. 8-1) and ~ 3 – 5 times higher than the rate measured over the same time span (2 years) during the PSI long-term experiments in pure water (~ 0.002 g m^{-2} d^{-1}, see Tab. 8-1). In the JMIME tests including, in addition to bentonite, a magnetite powder layer between glass and bentonite, the amount of SON68 glass corroded was much higher than in the experiments with bentonite only (compare Fig. 8-14 and Fig. 8-15 in Minet et al. 2008). A corrosion rate of ~ 0.14 g m^{-2} d^{-1} was measured during the first 300 days, which then dropped to ~ 0.03 g m^{-2} d^{-1} during the second year. In the tests conducted with silica gel as an additive, much lower average corrosion rates were determined (0.004 – 0.013 g m^{-2} d^{-1}) as expected, confirming that pre-saturating the Si sorption capacity of the added materials effectively reduces their detrimental effect on glass corrosion kinetics.

A new aspect emerging from these experiments, directly related to the presence of compacted bentonite, was hydro-mechanical fracturing of the glass fragments. Electron backscattering images provided evidence of the formation of clay-filled cracks and fissures penetrating the glass grains. Such observations are relevant for the safety case, since they imply that, as a consequence of the swelling pressure, the exposed glass surface may increase and that bentonite may infiltrate in the waste form, providing direct contact between clay and glass. However, because the JMIME tests were conducted at hydraulic overpressures of 20-50 bars it cannot be excluded that the observed cracking and infiltration phenomena were artefacts.

In spite of the efforts made to closely reproduce repository conditions, the results from these tests are judged to be inconclusive due to operational problems (see pp. 11 – 12 in Minet et al. (2008)) and the fact that the duration of these experiments was insufficient to establish a constant residual rate.

8.2.8 The effect of temperature

A number of experiments were carried out in the framework of the JSS project to investigate the effect of temperature. In general, the initial glass corrosion rate was found to increase by about a factor of ten for each 30 °C increase in temperature. In tests carried out at high A/V ratios, corresponding to advanced stages of glass corrosion, similar though weaker temperature effects were observed. However, these data are not appropriate to determine the effect of temperature on long-term rates, because of the limited corrosion time and insufficient precision of the *NL(B)* data.

Considerable temperature dependence was also observed in the earlier mentioned Belgian field experiments (Fig. 8-1). A comparison of the data obtained by Kursten et al. (1997) and Valcke (2007) reveals that, after ~ 3 years corrosion in contact with Boom Clay, the amount of glass corroded at 30 °C was 1 – 2 orders of magnitude less compared to the experiment at 90 °C. This dependence is similar to that observed in laboratory experiments for the initial rate, suggesting that using 90 °C data when extrapolating glass corrosion rates for the safety case possibly leads to over-conservative values. Clearly, there is still a lack of long-term glass corrosion data for repository-relevant temperatures.

8.2.9 The effect of pH

The influence of pH on the degradation kinetics of borosilicate glasses (particularly on AREVA type glasses) is relatively well-known for the initial stages of aqueous corrosion. Initial corrosion rates have minimum values in the range pH 5-7 and increase both on the acidic and alkaline side (Advocat 1991). Whereas the increase at pH < 5 is of no environmental concern, the increase on the alkaline side is critical as soon as the glass comes in contact with alkaline cement porewaters. Under such conditions silica glasses are unstable and become soluble.

The dependence of the residual rate on pH is less known, but available data obtained at 90 °C with solutions buffered between pH 7 and pH 10 (the pH region relevant for glass corrosion in the HLW repository) indicate an insensitivity of the rate to pH (Godon 2004). This finding is consistent with the "passivation layer" model, after which the long-term rate is determined by the transport properties of the gel layer rather than by the chemistry of the leaching solution.

8.2.10 Information from natural and historical analogues

In spite of different glass composition and alteration conditions, natural volcanic glasses are the only materials available from which experimental information on the dissolution kinetics of vitrified nuclear waste on geological time scales can be obtained. Several attempts have been made in the past to estimate long-term corrosion rates of vitrified nuclear waste from naturally altered basalts, (Malow et al. 1984, Lutze et al. 1985, Luo et al. 1998, Crovisier et al. 2003) which are considered to be the closest natural analogues of nuclear waste glasses, owing to the similar SiO_2 and Al_2O_3 contents.

A necessary test to legitimize the use of volcanic glasses as natural analogues are laboratory experiments aimed at demonstrating that the aqueous corrosion of basalt proceeds via the same mechanisms and at rates comparable to borosilicate glasses. The detailed study by Techer et al. (2000) has confirmed both requirements. In particular, the dissolution rates of basaltic glasses measured in the laboratory were found to be comparable to those of SON68 (one of two reference glasses for the Swiss disposal program), and the dependence on dissolved silica was also observed. Moreover, a temperature dependence of the initial corrosion rate similar to that observed for nuclear waste glasses could be established, yielding an activation energy of 71 kJ mol^{-1}, comparable to the 82 kJ mol^{-1} determined for a BNFL glass (Werme et al. 1990). Such values point to $(Si,Al)O_4$ network dissolution as rate controlling corrosion mechanism.

Equally important is the issue as to whether the conditions under which volcanic glasses were altered are comparable to those of a deep geological repository. Most basalts were altered either in a submarine environment, i.e. in a relatively high-ionic strength (I ~ 0.7 M), $MgSO_4$-rich medium, or in dilute groundwaters under oxidizing (sub aerial) conditions. Moreover, the lower content of alkaline elements in basalts leads to lower pH-values (pH ~ 7-8) during the corrosion process compared to the nuclear waste borosilicate glasses. A final, and sometimes critical limi-

tation on the use of volcanic glasses to estimate corrosion rates on geological time scales, is the difficulty in obtaining reliable information on the duration of the interaction with water and on the physico-chemical conditions (temperature, solution composition, pH). Nevertheless, several attempts have been made to overcome these problems.

Grambow et al. (1986) estimated the rates of penetration of the corrosion front in basaltic glasses as a function of age (up to ~ 1 Ma) and time of exposure to aqueous solutions (seawater and ice melt-water). In all cases the temperatures were comparable to, or below, those expected in the repository nearfield (down to 0 °C in the case of ice meltwater). These authors subdivided the data in two groups:

(i) basalt samples dredged from the ocean floor and exposed to seawater over a time spans of up to 10'000 years, indicating alteration rates of 3 – 20 μm/1'000 years

(ii) basalt samples buried within clay-rich sediments, indicating alteration rates of 0.1-1 μm/1'000 years. The former group corroded under unfavourable conditions similar to the dynamic glass leaching experiments conducted to determine initial rates (i.e. flowing water with low or no dissolved Si), whereas the second group was supposed by the authors to represent Si saturated conditions in the presence of clay. Conversion of the penetration rates to the usual surface normalized rates using the formula:

$$R\ [\mathrm{g\ m^{-2}\ d^{-1}}] = \text{density of fresh glass } [\mathrm{g\ m^{-3}}] \times \text{penetration rate } [\mathrm{m\ d^{-1}}] \qquad (8.1)$$

led to average corrosion rates of 2.2×10^{-5} to 1.5×10^{-4} g m^{-2} d^{-1} for the dredged basalt samples and only ~ 10^{-7} to ~ 10^{-6} g m^{-2} d^{-1} for the second group. An extrapolation of the corrosion rates for dredged basalt samples from ~ 3 °C to 60 °C, assuming that the rate increases by a factor of ten for an increase in T of 30 °C, yielded rates of ~ 0.002 – 0.015 g m^{-2} d^{-1}.

The rates derived for basalts imbedded in clay-rich sediments (which were altered at higher, but unknown temperatures) are considerably smaller than the residual rates measured in any laboratory experiment. However, according to Luo et al. (1998) these values cannot be interpreted as kinetic rates because of possible interruptions in the water contact (e.g. due to sealing effects) and therefore should not be used for the safety case. Although this criticism may be justified, it must be realized that in geological systems – including a deep nuclear waste repository – sealing effects will probably play an important role anyway. Even if the data collected by Grambow et al. (1986) are very difficult to interpret quantitatively, and therefore not really usable for the purpose of safety assessment, their compilation suggests that the net average corrosion rate of vitrified waste (as opposed to the purely kinetic corrosion rate) may be very small in a deep geological repository.

Evidence in this direction was provided by a recent study on fractured blocks of Roman glass (Verney-Carron et al. 2008). This glass was altered during 1'800 years in clay-rich sea sediments and showed clear indications of differential leaching. The internal surfaces of the glass were found to be much less corroded than the external surfaces which had been in direct contact with the surrounding seafloor sediments. The lower extent of corrosion of the internal surfaces was attributed to the transport resistance provided by formation of secondary minerals in the cracks, which were partly sealed with alteration products.

8.2.11 Concluding remarks and recommended rates

The survey of kinetic data from field and laboratory experiments reveals that glass corrosion rates depend systematically on a number of physicochemical parameters (temperature, pH, solution and gel layer composition), on the interaction with engineered barrier materials and on the accessibility of the porewater to the glass surface. In particular, borosilicate glasses are found to corrode faster in contact with clay materials (bentonite) and Fe corrosion products (magnetite), at least on the timescale of laboratory and field experiments. An increase in temperature has a considerable catalytic effect during the initial stages of the corrosion process but seems to be less pronounced at later stages of corrosion, when the "residual rate" regime is approached. Current data consistently indicate that the corrosion rate of radioactive glasses is not significantly faster than the corrosion rate of corresponding inactive simulants, at least over an experimental time of 1 – 2 years.

In spite of the wealth of results produced by the JSS-project and other investigations, the available data are not sufficient to determine conclusively the effect of engineered barrier materials, temperature and self-irradiation on the residual corrosion rates at a level of confidence comparable to that achieved with the ongoing PSI experiments in pure water (Curti 2003, Curti et al. 2006). This is mainly a consequence of an experimental design leading to a poor accuracy in the determination of the residual corrosion rate. Also, the results from field experiments, and from recent integrated experiments in pressurized cells filled with compacted bentonite, must be viewed with caution since they do not reproduce faithfully the conditions of a deep repository. Nevertheless, the information gathered from natural and historical analogues is reassuring since it points to corrosion rates comparable to, or even slower than those derived from "long-term" laboratory experiments.

On the basis of the combined evidence from laboratory experiments and field studies, a set of recommended corrosion rates was derived for safety analysis calculations (Tab. 8-2). These rates reflect the current state of knowledge and may be subject to modification in future.

The reference values are based on the PSI long-term corrosion experiments. They are identical to those selected for the "Opalinus Clay Project" (Nagra 2002a) since there is no new experimental evidence that would justify any modification of these rates. For optimistic calculations, rates of one order of magnitude less than the reference values are recommended to account for the effects of temperature (50 – 60 °C instead of 90 °C in the corrosion experiments used to derive the reference rates) and of reduced porewater accessibility arising from cementation of the free space between the glass fragments. For pessimistic calculations, we rely on the results of Kursten et al. (1997) and Valcke (2007) for glass corrosion in contact with Boom Clay. A value midway between the data obtained at 30 °C and 90 °C was selected to comply with the expected repository temperatures.

Tab. 8-2: Recommended glass corrosion rates of the two reference glasses SON68 and MW for safety analysis calculations, given in (g m-2 d-1).

Glass	**Optimistic**	**Reference**	**Pessimistic**
Son68	2.0×10^{-5}	2.0×10^{-4}	0.1
Mw	1.5×10^{-4}	1.5×10^{-3}	0.1

8.3 System evolution in a realistic scenario

Following canister failure 10'000 years after emplacement or later, aqueous solution from the water-saturated bentonite will infiltrate, rapidly corrode the stainless steel flask (coquille) enclosing the vitrified waste and then permeate the exposed glass surfaces. Because of the thermal stress during post-production cooling, the glass will fragmented. The surface effectively exposed to aqueous attack will then be about 12.5 to 15 times larger than the area of the initial monolithic cylindrical block (Nagra 2002a, Tab. B3, p. B13).

When the melt is poured into the coquille, a free space of ~ 37 L is purposely left to prevent spillage of the molten glass and to accommodate differential thermal expansion. Under repository conditions, this open space will probably collapse due to the pressure exerted by the swelling of the saturated bentonite and the volume increase caused by the formation of iron corrosion products. The volume of free space into which porewater can penetrate will be very small, essentially limited to the interstitial volume between the glass fragments. Under such conditions, the glass surface to solution volume ratio (A/V) will be very high, favouring the rapid attainment of a residual glass corrosion rate ("saturation conditions").

On the other hand, infiltration of bentonite into interstitial spaces cannot be excluded. In this case at least part of the glass surface would be in direct contact with clay material, which would favour silica uptake and thus locally higher glass corrosion rates. In any case, the clay/glass mass ratio inside the canister would be small and thus the detrimental effect of Si sorption would be of short duration. This means that the glass itself, rather than the bentonite, will control the chemical conditions under which it is degraded. For instance, the pH of the porewater permeating the internal regions of the waste will probably be maintained between 9 and 10 (due to the dissolution of alkaline cations and the buffering by boric acid/borate), whereas in the external parts of the glass lower pH values would be imposed by the surrounding materials (Fe corrosion products and bentonite). After all the available sorption sites in the infiltrated bentonite are occupied, the silica concentration in the interstitial water would reach "saturation" level and the glass surfaces would then passivate, leading to small residual corrosion rates.

As glass degradation proceeds, secondary minerals will form. According to the evidence available from long-term corrosion tests and natural analogues, the major corrosion products will be clay minerals. BNFL glasses have been shown to produce Mg-rich smectites on reaction with CO_2-free pure water during 12 years, whereas the corrosion of AREVA type glasses produced a comparatively smaller amount of Ca-Zn clays (Curti et al. 2006, Curti et al. 2009) reflecting the initial composition of the glasses. Under repository conditions, formation of Ca-Fe carbonates is possible due to the presence of dissolved bicarbonate and Fe^{2+}. Verney-Carron (2008) showed that most of the cracks in a fractured Roman glass body buried in clay-rich submarine sediments during 1'800 years were partially or totally filled with a mixture of Mg-clay and Ca carbonates, leading to sealing-effects that reduced the extent of corrosion in the internal part of the glass block. There is also ample evidence that layers of corrosion products ("palagonite") form around basalt glass fragments altered in seawater.

Secondary phase precipitation and related "clogging" phenomena will undoubtedly also occur in an underground disposal system, although their effect on glass corrosion kinetics is difficult to quantify. The radionuclides released from the non-altered internal regions of the vitrified waste will therefore interact with a variety of secondary phases (clay minerals, molybdates, carbonates, LDH phases and Fe corrosion products) along their path towards the bentonite. Some of these phases have the potential of scavenging radionuclides via sorption or co-precipitation before they reach the bentonite. For instance, trivalent actinides (Am, Cm) and lanthanides have been shown to be retained in the octahedral sites of hectorite, a typical clay formed upon the corrosion of Li-bearing borosilicate glass (Pieper et al. 2006, Brandt et al. 2007). Trivalent ac-

tinides were also found to coprecipitate with Ca-molybdate (Bosbach et al. 2004). The formation of LDH-phases repeatedly observed in altered basalt glasses (Crovisier et al. 1986, Crovisier et al. 2003) could effectively retard the migration of anionic radionuclides such as ^{79}Se and ^{99}Tc. This aspect has been given little consideration up to date, mainly because of the difficulties involved in characterizing the glass corrosion products and their interaction with radionuclides. Such processes could greatly contribute to reducing calculated doses for critical nuclides.

The external part of the glass will probably be influenced by the presence of iron corrosion products, e.g. magnetite. As discussed earlier, experimental data indicate that glass corrosion is faster, at least temporarily, in the presence of iron oxides and that this effect is enhanced if the specific surface area of the iron phase is high. This effect is attributable to silica adsorption on the Fe oxide surface (Jordan et al. 2007).

8.4 Interaction of glass corrosion with the near-field

In the previous sections the effects of the near-field environment on the glass dissolution process were discussed. In this section, the focus is on the reverse issue, i.e. how does the glass dissolution process influence the chemical and physical properties of the surrounding near-field components (including the porewater).

8.4.1 Water radiolysis

This issue is more relevant for spent fuel and will be discussed in Chapter 9. There, we concluded that radiolytic oxidants will not play a role since they will be consumed by reaction with H_2(g) produced during the anaerobic corrosion of steel or because of the strongly decreased decay in the later stages of repository evolution. The alpha radiation field generated from the vitrified waste being always 1 – 2 orders of magnitude weaker than for SF, the same conclusion applies *a fortiori* also to vitrified waste, i.e. water radiolysis is not expected to have significant effects on redox conditions.

8.4.2 Release of soluble elements from the glass

During the degradation of vitrified waste a number of chemical elements will be released. Some of these are known to be effectively immobile and will precipitate almost completely *in situ* (e.g. Zr, Fe, lanthanides and actinides). These elements will not affect the properties of engineered barrier materials and are therefore not a concern for this chapter. Other elements (such as Na, B, Mo, Li) are soluble and not significantly retained in the gel layer. These elements tend to accumulate in the aqueous phase and will migrate by diffusion. They could therefore potentially modify the properties of bentonite porewater in terms of pH, ionic strength and ligand concentrations. This in turn could affect the solubility of radionuclides. A third category are semi-immobile, reactive elements occurring in high concentrations within the glass (Si, Al). These elements could diffuse out and re-precipitate, possibly modifying the chemical, mineralogical and rheological properties of the bentonite buffer. For instance, irreversible changes in ion exchange properties and mechanical strength of compacted bentonite were observed after thermally induced silicification of wet compacted bentonite (Pusch & Yong 2006).

The central question, whether such phenomena have the potential of damaging the overall safety function of the repository system, can be answered with the help of mass balance calculations. Tab. 8-3 presents a comparison of the elemental inventories in the glass, in the canister and in a

bentonite section corresponding to a single waste package. For the glass, the total initial inventory and the net released inventory, calculated using retention factors determined experimentally in Curti et al. (2006), are specified.

This simple comparison shows that silica migration into bentonite is not an issue since more than 95 % of the dissolved Si will re-precipitate in-situ in the gel layer or in alteration products. Only ~ 140 moles/canister (8.4 kg) could conceivably diffuse out and precipitate as SiO_2. Assuming that all the released Si will precipitate in the first 10 cm of the bentonite annulus (conservatively disregarding Si adsorption on clay and Fe corrosion products) this amount would correspond to less than 1 mg of SiO_2 precipitated per kg of bentonite. It can therefore be concluded that Si release from the glass will not induce significant changes in the chemical and physical properties of the bentonite buffer. Similar conclusions can be reached with regard to possible influences of Ca, Al and Na release.

Tab. 8-3: Total and released elemental inventory of MW glass compared to canister and bentonite inventories (in kmol/canister).

Only major elements are considered.

	MW glass			**Canister***	**Bentonite****
	Inventory	**% retained**	**Net release**		
Al	0.42	99.1	0.0038		184.39
B	1.94	0.0	1.94		--
C(in.)	--	--	--	0.59	8.44
Ca	0.0022	97.3	1×10^{-4}		19.75
Cl	--	--	--		1.12
Cr	0.022	80.3	0.004	32.3	
Fe	0.14	99.7	4×10^{-4}	107.46	
Li	1.03	18.6	0.84		
Mg	0.59	99.6	0.002		29.71
Mo	0.056	62.2	0.0211		
Na	1.06	42.0	0.61		41.52
Ni	0.015	99.7	4×10^{-5}	15.07	
Si	3.11	95.4	0.14	3.15	729.86

* A characteristic austenitic steel composition was assumed.
** Includes porewater inventory.

Soluble elements such as B, Mo and Li interact only weakly with solid phases and therefore may reach appreciable concentrations in the porewater. The sorption of B on smectites and illite is weak but nevertheless data are available. Measurements indicate consistently that B sorption reaches a maximum in the order of a few mmol/kg at pH 9-10 (Keren and Mezuman 1981, Goldberg 1997). Also Li has been reported to sorb on clay minerals (Pistiner and Henderson 2003) and may even be incorporated in the structure of smectites (Thien et al. 2010). B and Mo form anionic species such as MoO_4^{2-} and $BO(OH)_2^-$, which could act as ligands for actinides and

fission products. Li^+ may form strong complexes, e.g. with phosphate. In static leaching experiments, total concentrations as high as 0.05 M for B and 0.03 M for Li have been reached, whereas for Mo a maximum of $7x10^{-4}$ M was measured (Curti et al. 2006). Under repository conditions, out-diffusion will tend to reduce concentration levels. Simple steady-state diffusion calculations, following the model described in Curti & Tits (2005), indicate a maximum boron concentrations of about 10^{-4} M at the inner bentonite boundary for glass corroding at the reference rates specified in the "Opalinus Clay Project" (Nagra 2002a). This figure would increase at higher glass corrosion rates, e.g. about 10^{-2} M for an assumed corrosion rate of 0.1 g m^{-2} d^{-1}.

Presently available thermodynamic data on B, Li and Mo complexes are unfortunately very scarce, and not directly relevant for radionuclide speciation. To our knowledge there is currently no critical review of thermodynamic data for these elements, so that only a brief summary of the few published data available can be given here.

Tagirov et al. (2004) studied the formation of aluminate-borate complexes between 50 °C and 200 °C. They found that the solubility of Al-hydroxides increases by up to a factor of four as a function of boron concentration. This means that dissolved boron could, in principle, induce the dissolution of the kaolinite occurring as a minor mineral in bentonite, thereby causing an increase of the Al concentration in the aqueous phase. In principle, montmorillonite solubility could also increase due to the formation of Al-B complexes. However, such effects were detected only at very high B concentration (20 – 100 mM) and are therefore unlikely to occur under repository conditions.

Formation constants for the complexation of borate, $BO(OH)_2^-$, with several alkali and earth alkali metal ions (Na^+, Mg^{2+}, Ca^{2+}, Sr^{2+}, Ba^{2+}) are reported in Smith and Martell (1989). All $\log K^0_1$ constants lie between -0.2 and +1.8, indicating weak complexation. The $\log K^0_1$ for the complexation of borate with transition metals (Cu^{2+}, Cd^{2+},Zn^{2+}, Pb^{2+}), determined by Van den Berg (1984) using electrochemical methods, are somewhat larger (0.9-3.45). Formation constants for trivalent or tetravalent hard metal cations, which would be more representative to estimate the behaviour of trivalent and tetravalent actinides, have not been determined, with the notable exception of Fe^{3+}. For this metal, high formation constants were determined for the mono-borate and di-borate complexes by Elrod & Kester (1980) at 25 °C, pH 2 – 3 and I = 0.7 M ($\log K_1 = 7.2 \pm 0.1$, $\log \beta_2 = 13.5 \pm 0.2$).

Even if no reliable conclusion can be drawn here on the quality of the available published borate complexation data, the fact that they correlate fairly well with the corresponding silicate formation constants (Hummel et al. 2002) suggest that highly charged radionuclides (Am^{3+}, Cm^{3+}, Zr^{4+}, U^{4+}, $Pu^{3+/4+}$) will probably form stable borate complexes. Therefore, an impact on the solubility of radionuclides cannot be excluded on the basis of the current knowledge. For instance, assuming that Eu forms mono-borate and di-borate complexes of the same strength as the corresponding silicate species included in the PSI/Nagra Chemical Thermodynamic Database 12/07 (Thoenen et al. 2014) ($\log \beta^0_1 = 7.9 \pm 0.2$ and $\log \beta^0_2 = 12.8 \pm 0.4$), the potential effects on the solubility of crystalline $Eu(OH)_3$ in bentonite porewater can be estimated (Tab. 8-4). These scoping calculations indicate that Eu-borate complexes would be the major dissolved species, even at a relatively low total B concentration of 0.1 mM, which would lead to a doubling of the Eu solubility. The increase in $Eu(OH)_3$ solubility would be more than tenfold if total B concentrations exceed the mM level.

From this discussion, it is concluded that the issue of radionuclide complex formation with borate is still unresolved. A critical review of the available data is needed for a reliable evaluation of the effect of B on radionuclide solubility.

Tab. 8-4: $Eu(OH)_3$ solubility in bentonite porewater (mol/L) with and without consideration of Eu-borate complexes at pH = 7 .8 and I = 0.37 M.

$[B]_{tot}$	$[Eu]_{tot}$ with B-cplx.	$[Eu]_{tot}$ without B-cplx.	Relative increase
10^{-4}	4.8×10^{-7}	2.5×10^{-7}	1.9
10^{-3}	4.6×10^{-6}	2.5×10^{-7}	18.4
10^{-2}	1.0×10^{-5}	2.5×10^{-7}	40

Complex formation with lithium and molybdate ions is probably less of an issue due to the lower concentrations of these elements in the glass. Nevertheless, Li^+ is known to form strong phosphate complexes (this topic is discussed in Curti et al. 2006). The formation of analogous complexes with the oxy-anions of technetium and selenium is conceivable. Moreover, Li^+ is known to interact with smectite clays. As shown in several studies (Curti et al. 2006, Curti et al. 2009, Thien et al. 2010) a significant fraction of Li^+ dissolved from the glass is incorporated into secondary smectites formed during glass alteration. In principle, Li^+ diffusing out into the bentonite buffer could substitute in the octahedral cationic sites of montmorillonite, potentially changing its mineral properties (e.g. CEC).

8.4.3 Glass as a source of oxidants

A number of redox-sensitive elements, including safety-relevant radionuclides, may be present as oxidized species in the vitrified waste. For instance, chromium, cerium, iron and selenium occur predominantly as Cr(VI), Ce(IV), Fe(III) and Se(IV) in the MW reference glass (see Curti et al. 2006, Curti et al. 2013 for data on Ce and Se). Although, in principle, the anoxic conditions and high hydrogen concentrations in the near-field should provide the necessary thermodynamic driving force for reducing any oxidized species released from the waste, their reducibility under repository-relevant conditions needs to be demonstrated experimentally, particularly in the case of the frequently very sluggish multi-electron transfer reactions.

In a few cases such experimental tests have been successfully performed. For instance, micro-XRF data (Curti et al. 2013) have shown that dissolved Se(IV), is readily reduced and precipitated as insoluble Se(0) in contact with pyrite, a minor mineral occurring in bentonite and Opalinus Clay, under mildly reducing conditions (inert gas with trace O_2 present).

Fe(III) from the glass could conceivably precipitate on the surfaces of the glass fragments and delay the reductive precipitation of such radionuclides. However, it is evident from Tab. 8-3 that the amount of Fe(III) in the glass is negligible in comparison with the quantity of reduced iron from the canister. Therefore, the overall reducing capacity of the near-field system would not be compromized by interaction with Fe(III) released from vitrified waste.

8.4.4 Chemical gradients

When alkali-rich borosilicate glasses corrode in pure or dilute waters, the pH increases and stabilizes at ~ 9-10 due to the buffering capacity of the boric acid/borate system ($pK_a = 9.2$). In the corrosion experiments conducted at PSI with initially pure water (Curti 2003, Curti et al. 2006), a very stable pH of 9.5 ± 0.2 was measured over a time span of 12 years. According to recent calculations (Berner et al. 2013) bentonite porewater under repository conditions will probably have a pH in the range 7.2-7.9, i.e. about 2 pH units less than the pH arising from glass cor-

rosion. Therefore, significant pH gradients might be established between the porewater contacting the internal parts of the waste glass and the water permeating the canister and the bentonite.

Experimental data from laboratory and field corrosion tests clearly indicate that the presence of clay and/or Fe corrosion products such as magnetite tend to reduce the pH to values close to neutral (pH ~ 7-8, see Curti 2009). Taking into account the current knowledge, the effect of such a pH reduction on the glass corrosion kinetics and alteration would be negligible and even beneficial. For instance, initial glass corrosion rates have a minimum at pH ~ 7 and Si sorption on Fe oxides has a maximum at pH ~ 9 (Jordan et al. 2007), which implies that a pH reduction from 9-10 to ~ 7-8 would reduce both initial and residual corrosion rates.

It can thus be concluded that pH gradients between the glass and the rest of the near-field will probably not lead to increased glass corrosion rates. A pH plume extending far into the corroded canister and bentonite buffer is not likely due to the high buffering capacity of these materials.

The possibility of a gradient in oxidation potential (E_h) between canister hull and external bentonite region, related to concentration gradients of molecular hydrogen produced from the anaerobic corrosion of steel, is discussed in detail in Chapter 9.

8.5 Summary

About one third of the fuel used by Swiss nuclear power plants will be reprocessed to borosilicate glass in the AREVA (F) and BNFL (UK) reprocessing plants. The release of radionuclides from these glasses into aqueous solutions will be largely governed by their corrosion kinetics, which depends on a number of chemico-physical factors (pH, T, porewater composition) and by the interaction with surrounding engineered barrier materials (canister and bentonite buffer).

The initial rapid decrease in corrosion rate is related to the accumulation of silica released from the glass into the aqueous solution. Eventually, a residual rate 3 – 4 orders of magnitude below the initial rate in pure water is reached. Current data indicate that the residual rate is controlled by the diffusive properties of the gel layer formed on top of the dissolving glass surface, which acts as passivating layer. High silica content in the glass favours the polymerization of the gel layer, reduces silica polymerization and increases microporosity, leading to higher residual rates. Ca and Mg were found to have the opposite effect.

Many studies have shown that clay and iron corrosion products enhance the corrosion of nuclear waste glass, at least temporarily. This effect is ascribed to the uptake of silica by such materials, which prevents or delays the formation of a protective gel layer. Very high corrosion rates have been inferred from in-situ tests in the Boom Clay carried out over more than 7 years. However, such tests are not representative of the conditions expected in the planned Swiss HLW repository and probably overestimate realistic long-term rates. Recent laboratory experiments in pressurized cells filled with compacted bentonite indeed indicate a much weaker effect of the clay. It is concluded that the issue of the effect of clay and iron corrosion products on the long-term glass dissolution rate is still not completely resolved. In contrast, glass corrosion data from non-active and active glasses allow us to conclude that α,β self-irradiation has no significant influence on the glass corrosion kinetics.

Safety assessment calculations normally rely on glass corrosion data obtained at 90 °C. In principle, a temperature extrapolation to 40 – 60 °C would be desirable in order to obtain rates consistent with repository conditions. Experimental results indicate that initial glass corrosion rates would be reduced by 1 – 2 orders of magnitude, if such a temperature decrease is taken

into account. The available data are however not sufficient to perform an analogous extrapolation for long-term rates, although there are clear indications that also the residual rate decreases with temperature.

Evidence from natural and historical analogues is hard to interpret due to the difficulties in assessing the physical-chemical conditions as well as the effective duration of the aqueous corrosion process. However, the data obtained from the study of volcanic glasses and of a Roman glass buried in clay-rich sediments suggest smaller average corrosion rates than in controlled experiments, possibly because the open spaces between the glass fragments are progressively sealed with secondary minerals, thereby limiting the access of water.

On the base of the combined evidence from laboratory experiments and field studies, a set of recommended corrosion rates was derived for the safety case. For reference scenario calculations, the same rates used in the "Opalinus Clay" project are recommended (1.5×10^{-3} g m^{-2} d^{-1} for BNFL glass and 2.0×10^{-4} for AREVA glass). For optimistic calculations taking into account realistic temperatures and a reduced accessibility of water to the glass surface, corrosion rates lower by a factor of ten are recommended. Very high rates (0.1 g m^{-2} d^{-1} for both glass types) were proposed for a pessimistic scenario to account for the high uncertainties related to the detrimental effect of clay and iron corrosion products.

Due to the fragmentation of the glass block, the chemical characteristics of the porewater in direct contact with the internal glass surfaces will be controlled by the glass itself, implying a pH of ~ 9-10 and high borate concentrations. Therefore, significant chemical gradients could be established towards the bentonite buffer region. The formation of a mildly alkaline pH plume extending over a large fraction of the bentonite thickness appears unlikely due to the high pH buffering capacity of this material. However, high borate concentrations could well affect significant parts of the bentonite region. Borate may form strong complexes with highly charged, cationic radionuclides and thus increase their solubility limits. This issue cannot be presently resolved due to the lack of reliable complexation data. Other soluble elements originating from the glass which could lead to higher concentrations in the near-field and affect radionuclide speciation are Mo and Li.

Although some of the silica released from the glass could re-precipitate in the bentonite region, such effects are judged to be insignificant in view of mass balance considerations. Most of the Si, Al, Ca, Fe, Zn and Mg released from the glass will form secondary solids (mainly clay minerals), which are capable of retaining a number of critical radionuclides via adsorption or solid solution formation.

9 Spent fuel dissolution and related effects

9.1 Introduction

In Switzerland, approximately 1'140 t_{IHM}[12] of spent UO_2 fuel have been reprocessed to vitrified high-level waste (HLW) (Nagra 2014b). According to a 60 years operation scenario this will leave about 2'875 t_{IHM} of spent uranium oxide (UO_2) fuel and 139 t_{IHM} of mixed-oxide (MOX) fuel to be disposed of without reprocessing in a deep underground repository.

In order to make reliable predictions on radionuclide release and migration for the safety case, it is necessary to know the physicochemical properties and the dissolution kinetics of the spent fuel (SF) with sufficient degree of confidence. Moreover, potential secondary effects on the near-field environment, arising from the SF dissolution process, must be carefully evaluated.

The SF from nuclear power plants (NPPs) is a very heterogeneous material. The physico-chemical properties vary as a function of reactor type, burnup and even within a single rod, due to different irradiation and thermal conditions as a function of the vertical and radial position. Micro-cracking and chemical segregation effects may lead to heterogeneities even at the μm scale. Therefore, SF is, unlike vitrified waste, a compositionally and texturally non-uniform material with a wide range of properties that have to be examined in detail before any prediction on its behaviour during aqueous corrosion can be made.

Non-irradiated UO_2 pellets consist of pure ^{235}U enriched uranium oxide of rather uniform grain size (~ 10 μm), whereas MOX pellets are aggregates of $(U,Pu)O_2$ grains varying in texture and chemical composition. Significant chemical and physical changes affect the pellets shortly after, and during, in-reactor irradiation. The most important are (Ferry et al. 2004): (a) structural damage at the atomic scale induced by the high-energy (~ 200 MeV) fission fragments; (b) formation of restructured rim zones when the burnup exceeds ~ 40 GWd t^{-1}; (c) formation of nm-μm sized fission/He gas bubbles, (d) radial cracking induced by thermal stress during reactor irradiation (Frizon et al. 2009); (e) bulk chemical changes due to radioactive decay/ingrowth (fission products and their decay products, minor actinides); (f) segregation effects, e.g. migration of Cs and I out of the $U(Pu)O_2$ lattice towards grain boundaries and the fuel/cladding gap and possible re-precipitation as secondary phases.

According to Tab. XII in Ferry et al. (2004) UO_2 and MOX with a burnup of 60 GWd/t contain about 4 wt. % lanthanides, ~ 2 wt. % oxide precipitates, ~ 2 wt. % metallic precipitates and ~ 1 wt. % of volatile elements associated with fission gas bubbles. The actinide content (including the newly formed Th, Pa, Np, Am, Cm) decreases from 100 wt. % oxide at the start of irradiation to about 85 wt. % at the end of reactor operation.

Since chemical segregation processes taking place during reactor operation and dry storage have a major impact on radionuclide release during the aqueous corrosion of SF, these effects need to be addressed more specifically. One of the most important segregation processes is the migration of fission gases (mainly Xe and Kr), and He produced via alpha decay, towards grain boundaries and the fuel/cladding gap. The amount of released fission gas is found to correlate with the amount of easily soluble nuclides, the so-called "Instant Release Fraction" (IRF), which is enriched in the long-lived nuclides ^{129}I and ^{135}Cs. These nuclides may also react together to form secondary phases such as CsI, a very soluble salt that is readily dissolved on contact with water (Johnson & Shoesmith 1988). Cs may also segregate as an oxide and co-precipitate with Rb, Ba, Zr, Nb, Mo, Te. It is important to note that the release of volatile and soluble species

[12] Tons of initial heavy metal

from grain boundaries and the fuel-cladding gap depends on fuel type and reactor operation conditions. Specifically, fission gas release and IRF increase with fuel burnup and linear power rating.

Another typical segregation phenomenon in SF is the formation of micrometer-sized metallic particles, called ε-particles, where Mo, Tc, Ru, Rh, Pd, Ag, Sn, Sb and Te accumulate. In contrast, lanthanides and minor actinides tend to remain in the fuel matrix, possibly forming solid solutions with UO_2 or PuO_2.

9.2 Long-term ageing of SF in the absence of water

During intermediate storage, the chemical composition of SF evolves further due to the production of new elements from fast-decaying nuclides. Later, after emplacement in a geological repository, compositional changes and radiation damage progress more slowly since only long-lived nuclides remain. Nevertheless, on the scale of repository evolution these changes are still significant. Although the α-activity in MOX, as well as UO_2, SF will decrease by 4-5 orders of magnitude over 10^6 years (see Fig. 5-1 in Nagra 2005), the cumulative number of alpha decays will increase steadily with time. It is therefore important to establish the extent of radiation damage and related effects as a function of the cumulated dose.

A possible consequence of α-decay over geological timescales is the accumulation of irreversible structural damage in the $(U,Pu)O_2$ matrix. This process could potentially modify the lattice diffusivity of radionuclides and make them more leachable on contact with porewater. Ferry et al. (2005) estimated that radionuclide diffusion coefficients could increase to $\sim 10^{-25}$ m^2 s^{-1} due to the prolonged effect of alpha particles and fission fragments, which could lead to an upper limit for the IRF of about 5 % of the total radionuclides inventory in UO_2 fuel. Even higher percentages would be possible for MOX fuel (Johnson et al. 2005).

In addition to structural damage, α-decay continuously generates He which accumulates in proportion to the total dose. Helium produced by alpha-decay may form a separate gas phase or, by diffusing into pre-existing fission gas bubbles, increase their internal pressure. If a critical pressure exceeding the tensile strength of UO_2/PuO_2 is reached, micro-cracks would form, facilitating the migration of IRF radionuclides towards peripheral zones, and later on the penetration of porewater into the pellets (Frizon et al. 2009). According to recent model calculations, out-diffusion of He would prevent such critical pressures being reached, so that this potentially damaging mechanism can be ruled out (Ferry et al. 2008).

A further concern is the oxidation of SF during intermediate storage. Before emplacement in a geological repository, where reducing conditions will prevail, the SF assemblies will be stored on the surface for a period of several decades. Ferry et al. (2004) discuss air oxidation of SF in detail, but this issue is not considered to be relevant for the Swiss disposal program due to the careful handling of SF after discharge from the reactor. This includes double sealing of the SF dry storage casks and an inert gas filling (Johnson, personal communication).

In summary, spent fuel is a complex, highly heterogeneous and continuously evolving material. The degradation mechanisms in aqueous solutions will depend on fuel type and "age", as well as on irradiation conditions in the reactor. Therefore, a detailed knowledge of the material properties, and a good estimate of the canister breaching time, are essential prerequisites for making reliable predictions on the chemical evolution of SF and the release of radionuclides during aqueous corrosion.

9.3 Aqueous corrosion of canister and Zircaloy cladding

Aqueous corrosion, and eventually failure of the waste containment materials, is of concern because these processes define the time of earliest possible radionuclide release. In the case of direct disposal of SF, a thick metallic steel canister (with or without copper insert) and the Zircaloy cladding enclosing the fuel pellets must fail before SF can come in contact with aqueous solutions or a vapour-saturated gas phase. In this section we focus on the kinetic aspects relevant for the estimation of canister failure and corrosion times. The chemical interactions between corroding canister and SF/Zircaloy will be discussed later in this chapter (Section 9.5.2). The interactions between canister corrosion and bentonite are discussed in a separate chapter (Chapter 7).

After consumption of the residual oxygen introduced during the excavation of the repository tunnel system, the canister will corrode anaerobically, consuming water and producing magnetite as well as molecular hydrogen:

$$3\ Fe + 4\ H_2O(l) \Rightarrow Fe_3O_4\,(cr) + 4\ H_2(g) \qquad (9.1)$$

Anaerobic corrosion of carbon steel in systems containing compacted clay will proceed at rates of 1-2 μm a^{-1} (Patel et al. 2012), implying corrosion times in the order of 100'000 years for a 14-18 cm-thick canister. In a realistic scenario, mechanical failures are likely to occur before the canister is completely corroded, implying that iron and magnetite will coexist for a given time span during aqueous degradation of the SF. As shown later, the coexistence of metallic iron and magnetite in the canister puts tight constraints on the chemical and redox environment during the initial phase of waste degradation (see Section 9.5.2). The time frame for this initial period has been estimated to be between 10'000 years (earliest canister failure time) and 100'000 years after repository closure (Curti 2011a).

There is some uncertainty as to the nature of the iron corrosion products. In particular, it has been claimed that poorly crystalline, more soluble products ("hydromagnetite") could form instead of crystalline magnetite at the low temperatures prevailing under repository conditions. Nevertheless, there is clear evidence that coarse-grained crystalline magnetite can form as a product of steel corrosion even at the earth surface under atmospheric conditions, for instance as a corrosion product of steel bridges (Nasrazadani & Raman 1993).

There is a general consensus that the above reaction (Eq. 9.1), or similar ones, will produce large amounts of hydrogen (Carbol et al. 2009, Grambow et al. 2008, Shoesmith 2008) leading to the build-up of high gas pressures (10-100 bar) in the canister region (Nagra 2002a). The formation of H_2 during the anaerobic corrosion of iron has been amply documented in laboratory experiments (e.g. Schenk 1988, Smart et al. 2001). The rates and mechanisms of hydrogen transport through the engineered barrier system, and the possible consequences for the mechanical integrity of the near-field, are major issues currently under debate, but will not be addressed here because these issues are beyond the scope of this report. We will rather focus on the chemical reactivity of dissolved hydrogen towards SF under repository conditions.

Zircaloy corrosion occurs already during reactor operation on both sides of the cladding. Rates are very slow (Johnson et al. 2005), even at the high temperatures of reactor operation, due to the formation of a nm-thick passivation film at the base of a porous, 40-80 μm-thick alteration layer composed of zirconia (ZrO_2) developing on the external (waterside) cladding surface. A 5-15 μm thick ZrO_2 layer develops during reactor operation also at the inner side of the cladding (Minne et al. 2012). ZrO_2 has a very low sub-nanomolar solubility at near-neutral pH (Curti & Degueldre 2002, Brown et al. 2005). A recent TEM investigation on three different Zircaloy

cladding materials from Gösgen, examined after 3-5 irradiation cycles, showed that Zr oxidation is driven by in-diffusion of molecular oxygen during reactor operation (Abolhassani et al. 2010). Under water-saturated repository conditions, Zircaloy corrosion rates of less than 0.01 μm a^{-1} are predicted (Nagra 2002, p. 141). This figure is consistent with the experimental data of Kurashige et al. (1999) who derived rates of a few nm a^{-1} for Zircaloy corrosion in synthetic Na-Ca-Cl-HCO_3-SO_4 groundwater (pH 10.5 – 12.8, T = 30 °C or 45 °C).

Due to neutron activation of alloying elements and impurities present in the as-fabricated Zircaloy, the porous Zircaloy oxidized layers are enriched in ^{14}C, ^{36}Cl, ^{59}Ni and ^{63}Ni (Johnson & McGinnes 2002). The former two nuclides are soluble and expected to be rapidly released on contact with water, thus contributing to the IRF.

In spite of its favourable corrosion properties, Zircaloy cladding is not considered to be safety-relevant barrier in performance assessments due to the possible occurrence of through-wall perforations. Such failures are difficult to predict and may occur by a number of in-reactor and post-irradiation processes (Ferry et al. 2004). A major concern in this respect is the embrittlement of Zircaloy caused by Zr-hydride formation after adsorption of hydrogen during in-reactor irradiation (Choi 1997, Pierron et al. 2003). The loss of ductility is enhanced as the SF cools down after the end of reactor operation. However, according to current experience with intermediate storage, cladding failures prior to transport to the geological storage site are extremely rare with less than 1 in 10'000 rods leaking in wet storage (Johnson, personal communication). Since no data exist on failures occurring during geological storage, making predictions on frequency and timing of cladding failures is difficult and unreliable.

9.4 Aqueous corrosion of spent fuel

9.4.1 Definition of the source-terms

In practice, it is not possible to identify, distinguish and take into account all radionuclides sources and release mechanisms operating during the aqueous corrosion of the SF/Zircaloy package due to the heterogeneity of these materials. As mentioned previously (Section 9.1), a significant inventory fraction enriched in soluble nuclides will be rapidly dissolved on first contact with water, leading to the "Instant Release Fraction" (IRF) in the safety case. The IRF pulse will be followed by much slower long-term radionuclides release which is ascribed to the dissolution of the UO_2/PuO_2 crystalline lattice, generically called "matrix dissolution". For convenience, we follow here the same simplifying categorization, but at the same time we will present a differentiated view of the chemical processes responsible for the aqueous degradation of SF and radionuclides release to the repository near-field.

9.4.2 Early aqueous corrosion (instant release fraction)

As soon as bentonite porewater contacts fuel cladding and SF, readily accessible soluble radionuclides such as ^{135}Cs, ^{129}I, ^{36}Cl and ^{14}C will be mobilized, giving rise to a quasi-instantaneous activity pulse (Instant Release Fraction, shortly IRF). The IRF can be subdivided in contributions from nuclides segregated into the fuel-sheath gap (IRF_G) and at fuel grain boundaries (IRF_{GB}).

The experimental distinction between the two contributions is not easy to make as it depends on the type of sample used and on leaching time. The release from grain-boundaries is delayed with respect to release from the gap region, since time is needed for water to penetrate along intergranual channels and for the dissolved radionuclides to diffuse out. Leaching of intact cladded

pellet will give access to both contributions, provided radionuclide release is monitored during a sufficient long time span (weeks to months). A significant contribution to IRF_G (mainly ^{14}C) is thought to originate from the porous zirconia layers produced during reactor operation through oxidation of Zircaloy (Johnson et al. 2005). In contrast leaching of fuel fragments or powder previously separated from the cladding will yield predominantly the grain-boundary release contribution.

Due to the scarcity of SF leaching data, correlations with in-reactor operational parameters such as fission gas release (FGR)[13] or linear power rating (LPR)[14] are used as a guide to extrapolate IRF values for safety assessments (Johnson & Shoesmith 1988, pp. 647 – 648, Johnson et al. 2005). For instance, IRF data of Cs and I isotopes frequently correlate linearly with FGR. For PWRs operated with UO_2 to burnups < 40 GWd t^{-1}, FGR values usually do not exceed 2-3 % (Johnson et al. 2005, Johnson 2014), although higher values may occur with other reactor types. At higher burnup, FGR values increase to ~ 3-20 % depending on reactor operating conditions.

Johnson et al. (2005, 2008b, 2012) and Johnson (2014) reviewed leaching data for UO_2 and MOX spent fuel, from which IRF estimates were derived. The data indicate ^{135}Cs, ^{36}Cl, ^{14}C and ^{129}I to be the dominant radionuclides in the IRF, with contributions generally increasing with burnup (except for ^{14}C). The data of Johnson et al. (2012) indicate fuel fractional releases of about 1/3 the measured FGR-values for ^{137}Cs, and about equal or slightly less than the FGR for ^{129}I. The data also show dependence on the LPR. Among the studied samples the Gösgen fuel, which was subject to higher LPR compared to fuel from the other reactors, had by far the highest FGR and ^{129}I, ^{137}Cs fractional releases at comparable burnups.

It has been argued that an additional contribution to the IRF may be related to the development of fine-grained porous fuel structures at the periphery of high burnup UO_2 fuels ("rim zone", about 70-140 μm thick). This region contains a large density of 0.5-3 μm-sized fission gas bubbles (Dehaudt 2000) and is thus possibly enriched with Cs and I isotopes. However, detailed studies showed that most bubbles are closed, implying that the largest fission gas fraction and the associated volatile radionuclides are trapped within the pellet (Goll et al. 2007) and thus not accessible to aqueous solutions. So far, leaching experiments did not provide any systematic evidence for preferential aqueous release of radionuclides from the rim (Johnson et al. 2012). More likely, high FGR values are related to high linear power ratings. The high radial thermal gradients within the pellets probably promote thermal diffusion of volatile species. This could explain the high FGR values observed for Gösgen UO_2 fuel.

The best current IRF(total) estimates for UO_2/MOX fuel from Swiss nuclear power plants are 2 – 16 % (FGR) , 5 – 48 % for ^{36}Cl, 6 – 20 % for ^{129}I, 6 – 13 % for ^{135}Cs, 10 % for ^{14}C, 1 % for ^{90}Sr, ^{107}Pd and ^{99}Tc, 0.2 % for ^{79}Se and 0.1 % for ^{126}Sn (see Tab. 5 in Johnson 2014). Among the listed IRFs, only the values for ^{129}I and ^{135}Cs are correlated to FGR. The high bounding value estimated for ^{36}Cl probably applies only to the high LPR Gösgen fuel. The estimate originates from data by Tait et al. (1997) on CANDU fuel (Johnson 2014), which operated (as Gösgen) at much higher power rating than in usual PWR and LWR reactors. High temperatures in the centre of the pellet tend to enhance thermal diffusion of light volatile nuclides as ^{36}Cl. IRF values for ^{79}Se, ^{90}Sr, ^{99}Tc and ^{107}Pd are much smaller and burnup-independent. They were not derived from leaching experiments, but represent upper limits based on estimates of the amounts segregated out of the UO_2 matrix as discrete phases. Generally, the aqueous concentrations measured in the short-term for these nuclides are below the detection limits.

---

[13] FGR: percentage of produced fission gas (mainly He, Kr, Xe) segregated into the void spaces of the rods and open fuel porosity

[14] LPR: thermal power (W/m) generated per unit length of fuel in radial direction

The above data allow constraints to be put on the IRF limits for non-aged UO_2 fuel up to ~ 75 GWd t^{-1} burnup. However, leaching experiments with "young" SF cannot account for the effects of structural damage induced by α,β self-irradiation during the long-term evolution in a geological repository. As previously mentioned, the accumulation of structural damage over the time preceding canister failure has the potential to enhance athermal diffusion of radionuclides in the SF pellets and eventually lead to increased IRF values. Although α-activities corresponding to $10^4 - 10^5$ year old SF are frequently simulated by doping UO_2/PuO_2 with fast-decaying α-isotopes (e.g. ^{233}U, ^{238}Pu) or through external ion irradiation, the additional effects of fission reactions occurring in a reactor cannot be simulated by such methods. This means that experimental results obtained from doped or implanted UO_2 may not necessarily be representtative and should be interpreted with caution. For instance, the experiments involving annealing of ^{37}Cl-implanted UO_2 by Pipon et al. (2007a, 2007b) indicate very fast diffusion of chlorine, but they apparently contradict the measurements on ^{36}Cl release on CANDU SF made by Tait et al. (1997). These authors found only partial release of the ^{36}Cl inventory (< 20 %) to the aqueous solution in spite of the much higher fuel temperatures and LPRs under which CANDU reactors are operated (compared to PWR and LWR reactors).

Possibly, the combined effect of fission fragments and α self-irradiation over times $\geq 10^4 - 10^5$ years can be better evaluated through theoretical calculations. Based on simple model calculations, Ferry et al. (2005) and Johnson et al. (2005) estimated that long-term α-irradiation could enhance lattice diffusivity by orders of magnitude. However, more advanced molecular dynamic calculations (Martin et al. 2009) indicate that the accumulation of structural damage over time should not significantly enhance athermal diffusion of radionuclides in the SF matrix, so that IRF values derived from "young" SF leaching data could be used in the safety case. This uncertainty is covered in safety analyses by using a conservative IRF/FGR ratio of 3 for ^{36}Cl (Johnson 2014).

9.4.3 Matrix dissolution

9.4.3.1 Relevant processes during matrix dissolution

Following the IRF "pulse", minor actinides and non-volatile fission products such as ^{90}Sr are released at a rate proportional to the dissolution kinetics of $(U,Pu)O_2$. Moreover, even after the early IRF pulse, most of the ^{135}Cs and ^{129}I initial inventories still reside within the SF matrix. Therefore, the determination of a reliable source term function for SF matrix dissolution is critical for safety assessment calculations, and consequently, a considerable effort has been put into experimental studies of the corrosion rates of UO_2 and MOX fuel.

To a first approximation, SF can be regarded as crystalline UO_2, with a significant fraction of PuO_2 in MOX. Since thermodynamically stable forms of UO_2 and PuO_2 exist at low temperatures, saturation equilibria with respect to both phases (or with a solid solution of both components) will eventually be established in a closed system, implying that limiting aqueous concentrations of U and Pu would be reached. Under such conditions, thermodynamic laws require that SF matrix dissolution would cease, at least macroscopically.

As discussed in detail below, this simple closed-system model is not appropriate since additionnal processes (out-diffusion, radiolytic oxidation and recrystallization) may play a role and potentially enhance SF dissolution in the repository. It is well-known that the oxidized (VI) forms of U and Pu are much more soluble than the reduced (III, IV) forms (Johnson & Shoesmith 1988, Guillamont et al. 2003). Therefore, under oxidizing conditions UO_2 and PuO_2 destabilize to more soluble oxides and appreciable concentration gradients would be established,

generating diffusive fluxes of U(VI) and Pu(V,VI) towards the geosphere. Under such conditions the SF matrix would dissolve continuously, releasing the radionuclide inventory at higher rates. Thus, the correct prediction of oxidation potentials at the SF/canister interface is critical for deriving reliable SF dissolution rates under repository conditions.

Although anoxic conditions are predicted to be established in the repository near-field due to the presence of large amounts of metallic iron, water radiolysis due to α-irradiation from the SF will produce reactive oxidizing species (mainly H_2O_2 and O_2) in a thin film (a few tens of μm) of porewater directly in contact with exposed fuel surfaces. This could increase the E_h locally and cause oxidation of U(IV) and Pu(IV) at the wetted SF surface, greatly enhancing SF dissolution. Radiolysis will also produce an equal amount of reducing species (H_2), which are however considered to be less reactive than radiolytic oxidants.

Oxidative SF dissolution via radiolysis is an electrochemical corrosion process driven by the difference between the oxidation potential of the $UO_2(cr)/UO_2^{2+}$ half-cell and the higher potential of the aqueous solution in direct contact with the solid. In other words, a permanent redox disequilibrium is assumed to be established between the fuel surface and the corroding aqueous solution; the solution E_h being determined by an excess of radiolytic oxidants (Shoesmith 2000, Shoesmith 2003). The production of radiolytic oxidants will depend on burnup, fuel type (MOX and high burnups will produce more) and SF age. It will decrease by orders of magnitude over geological time spans, according to the calculated activity evolution (see e.g. Nagra 2005, Fig. 5-1).

The basic reactions operating during radiolysis-driven oxidative dissolution of UO_2 are illustrated in Fig. 9-1. Reaction 1 ($2\ H_2O = H_2O_2 + H_2$) represents the primary production of radiolysis products, whereas Reaction 2 (net reaction: $H_2O_2 + UO_2(c) = 2\ OH^- + UO_2^{2+}(aq)$) is the oxidetive dissolution of UO_2 via reduction of radiolytic oxidants. This reaction proceeds either directly at the UO_2 surface (right side) or is catalytically mediated by the (Pd, Ru, Rh)-rich ε-particles (left side). Reaction 3 ($H_2 + UO_2^{2+}(aq) = UO_2(c) + 2\ H^+$) represents the reduction of dissolved UO_2^{2+} to $UO_2(c)$ via oxidation of dissolved H_2 at the surface of ε-particles, which in principle could exactly counterbalance the catalytic oxidation of UO_2 by H_2O_2. However, whereas H_2O_2 can efficiently oxidize UO_2 even without mediation by ε-particles, H_2 does not react directly with UO_2. Because the surface area of UO_2 greatly exceeds that of exposed ε-particles, it follows that a net excess of oxidants is produced by radiolysis (Trummer et al. 2009) and thus a high E_h will result in the solution contacting the SF. Reaction 3 can nevertheless become significant and completely inhibit oxidative UO_2 dissolution if larger amounts of H_2 are supplied by anaerobic corrosion of the canister (see Section 9.4.3.2). The anodic coupling of ε-particles to the UO_2 oxide and its role in protecting SF from oxidative dissolution are now well established (Shoesmith 2008).

These reactions will proceed only as long as the E_h of the solution in direct contact with SF differs from the equilibrium potential of the $UO_2(c)/UO_2^{2+}$ half-cell. As reducing conditions are progressively (re-)established, electron transfer reactions will cease, the dissolved U, Pu concentrations will decrease and the system will finally reach saturation equilibrium with UO_2/PuO_2, characterized by constant U, Pu concentrations at or below the nanomolar level (saturation).

As will be shown shortly, even after saturation is attained, U, Pu and the other radionuclides may continue to be released at very slow rates due to recrystallization or out-diffusion. Consequently, electrochemical (polarographic) measurements are not sufficient to define a source-term function for SF dissolution and must be complemented by direct corrosion measurements in which the cumulative release of U and Pu are monitored.

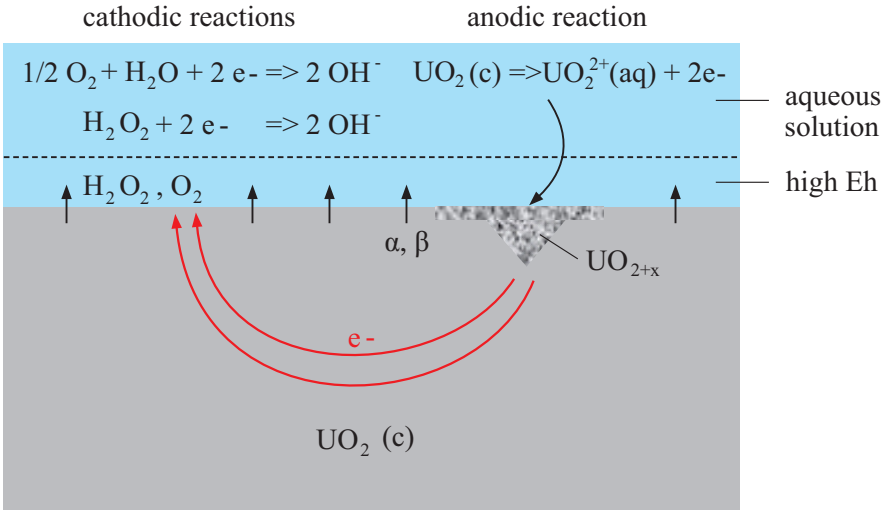

Fig. 9-1: Sketch showing the relevant chemical processes during corrosion of SF driven by the production of radiolytic products (simplified after Wu et al. 2014).

Radiolytic species are shown in red. The broken line shows the penetration depth of α-radiation in water.

Ollila (2007, 2008) investigated the corrosion of pure UO_2 in a closed, static system under anoxic (but H_2-free) conditions. The aqueous solution was spiked with ^{235}U so that it had initially a much higher $^{235}U/^{238}U$ isotopic ratio (10.4 %) than the solid with which it was in contact (2.8 %). By simultaneously monitoring the $^{235}U/^{238}U$ ratio and the U concentration in the aqueous solution, the total amount of UO_2 dissolved during each experiment was determined. The results show that UO_2 continued to dissolve slowly even after attaining a constant uranium saturation concentration. This indicates that a recrystallization mechanism was operating at (or very close to) thermodynamic equilibrium.

Recrystallization is a dissolution-reprecipitation process driven by the tendency of a solid to lower its Gibbs free energy even at saturation equilibrium with an aqueous solution. This may be achieved through grain-size coarsening (minimization of the surface energy) or by the incorporation of trace elements to form solid solutions (minimization of chemical potentials). A fine-grained solid will tend to dissolve and re-precipitate as a coarse-grained aggregate of well-shaped crystals in order to reduce the surface area contribution to the free energy. Alternatively, an initially pure solid may become unstable (dissolve) because the re-precipitating solid solution is more stable (less soluble). Recrystallization is frequently observed even at low temperatures in carbonate and sulfate minerals (Putnis & Putnis 2007, Putnis 2009, Curti et al. 2010).

The important implication of the results obtained by Ollila (2007, 2008) is that incompatible radionuclides (i.e. those that cannot be accommodated in the crystal lattice of UO_2, such as ^{135}Cs, ^{129}I, ^{79}Se) will continuously be released into solution during recrystallization and will not be incorporated in the re-precipitated UO_2 phase. In contrast, radionuclides such as Th and minor actinides (Am, Cm, Np) will probably form thermodynamically stable solid solutions in the newly formed UO_2 phase through a similar mechanism by which radium is incorporated in barite (Curti et al. 2010).

The extent to which recrystallization close to thermodynamic equilibrium may contribute to the overall migration of radionuclides towards the near-field will largely depend on redox conditions on the fuel surface. Because the solubility of U(IV)O_2 is several orders of magnitude

smaller than the solubility of U(VI) compounds, concentration gradients of dissolved elements – and therefore radionuclides out-diffusion rates – will be much smaller if reducing conditions are maintained on the surface of the fuel. In this case, the effect of recrystallization on radionuclide release will be negligible compared to the potential effect of oxidative dissolution.

9.4.3.2 Selected UO_2 dissolution data

Rondinella et al. (2001) investigated the dissolution of crystalline UO_2 in pure water at near-neutral pH, with and without ^{238}Pu doping, in order to simulate α-activities corresponding to different SF ages (up to > 10^6 years). Their experimental data indicated an increase of U aqueous concentrations with increasing alpha activity. The U concentrations measured for the high-activity sample (doped with 10 % ^{238}Pu to simulate SF just after reactor operation), were in the order of 10^{-7} M, i.e. about two orders of magnitude larger than the concentrations expected at equilibrium with UO_2. These results point to oxidative dissolution in spite of anoxic conditions during the experiments (N_2 purging) and can only be explained by assuming surface oxidation through radiolytic oxidants.

Carbol et al. (2005) carried out similar experiments in Na-K-Mg-Ca water with bicarbonate, chloride and sulphate as the major anions (I ~ 0.001 M, pH ~ 7.5). The solids used were ^{233}U-doped as well as ^{233}U-free UO_2. The doped sample simulated a SF age of about 3'000 years. As in the experiments of Rondinella et al. (2001), the U concentrations measured in the leaching solutions in contact with ^{233}U-doped UO_2 under anoxic (but H_2-free) conditions were about two orders of magnitude larger than those measured in the tests with the ^{233}U-free sample, confirming that water radiolysis has an oxidizing effect. A second set of experiments was carried out in inert gas atmosphere enriched with 6 % H_2 at 1 bar total pressure. Compared to the analogous tests conducted without H_2, the steady state U concentrations measured during leaching of the ^{233}U-doped samples were reduced by more than one order of magnitude (to less than 10^{-8} M). This is almost, but not quite, as low as the U concentrations measured for the ^{233}U-free UO_2 specimen. Thus, the presence of 6 % H_2 considerably reduced the oxidative dissolution of UO_2 having an α-activity corresponding to SF 3'000 years after the end of reactor operation, although a minor effect was still present.

The next logical step was to systematically increase the hydrogen partial pressure to simulate the conditions expected in a deep repository during canister corrosion. In these experiments a pure UO_2 pellet doped with 10 wt. % ^{233}U was leached in 10 mM NaCl ± 2 mM $NaHCO_3$ solution at pH 8.4. During the first 140 days, the hydrogen pressure was set to 16 bar (~ 0.01 M dissolved H_2), a value within the H_2-pressure range expected under repository conditions. Then the H_2-pressure was decreased stepwise to obtain progressively lower dissolved H_2 concentrations, down to a minimum of ~ 10^{-5} M. Under such conditions very low total U concentrations (~ 10^{-11} –10^{-10} M) were always measured, even at the lowest dissolved hydrogen concentration of ~ 10^{-5} M.

The results of Carbol et al. (2009) indicate that dissolved hydrogen, even at low concentrations, effectively suppresses the oxidative dissolution of UO_2 observed at sufficiently high α-activity under anoxic (but H_2-free) conditions. Because great care was taken to avoid contamination by external oxidants, it can be concluded from these results that the presence of H_2 at concentrations of ~ 10^{-5} M or higher indeed "neutralizes" the effect of radiolytic oxidants. It is now clear that the chemical activation of H_2 requires the mediation of a surface catalyst, which has been identified to be the platinoid-rich ε-particles (Trummer et al. 2009).

The leaching data obtained for non-doped or weakly doped UO_2 by Carbol et al. (2005) also indicate that the amount of radiolytic oxidants produced by aged SF (> 100'000 years) would be insufficient to induce oxidative dissolution. Therefore, beyond the critical time of ~ 100'000 years after emplacement, when steel corrosion will be more or less complete and H_2 production will have ceased, oxidative SF dissolution can be ruled out.

In summary, the results from the aforementioned investigations imply that SF is likely to remain immune to radiolytic oxidation at all times during the entire repository evolution. From this it follows that solubility-controlled dissolution, rather than electrochemical corrosion, will most probably be the rate-determining process governing SF degradation and radionuclide release after the IRF "pulse". The following two processes are considered to control radionuclide release from SF:

1. Out-diffusion of U, Pu towards the geosphere due to concentration gradients between the water in contact with SF and the geosphere may result in a slow but continuous dissolution of $U(Pu)O_2$. The driving force for the dissolution is the need to restore saturation equilibrium as U and Pu diffuse away. However, diffusion-driven dissolution of uranium will be negligible owing to the very low solubility of UO_2 under repository conditions (~ 10^{-8} – 10^{-10}M). Scoping calculations based on steady-state diffusion, and conservatively assuming zero concentration of U in the geosphere, indicate that diffusion-induced SF dissolution rates are of the order of 10^{-8} g m^{-2} d^{-1} or lower (Curti, unpublished calculations). Such rates are very small compared to chemical SF dissolution rates (Tab. 9-1).
2. Even in a system saturated with respect to UO_2, radionuclide release may continue due to recrystallization of the SF matrix. During this process, radionuclides released to solution which can hardly be accommodated in the UO_2 lattice (e.g. because of exceedingly large ionic radii) will not be incorporated in the reprecipitated UO_2 phase. Such radionuclides may nevertheless form separate secondary phases (see Section 9.5.2).

The previously mentioned experiments of Ollila (2007, 2008) proved that UO_2 dissolves even after saturation equilibrium is reached, pointing to recrystallization as the governing mechanism. In Fig. 9-2 examples of the data obtained from Ollila (2008) are presented, showing the cumulative U release from ^{233}U-free UO_2 as a function of reaction time. The data indicate that under anoxic conditions (N_2 + 1 ppm sulphide) UO_2 recrystallized at an appreciable rate, which did not decrease with reaction time. Addition of an iron strip nevertheless led to lower U concentrations (~ 10^{-9} M), indicating slower recrystallization rates.

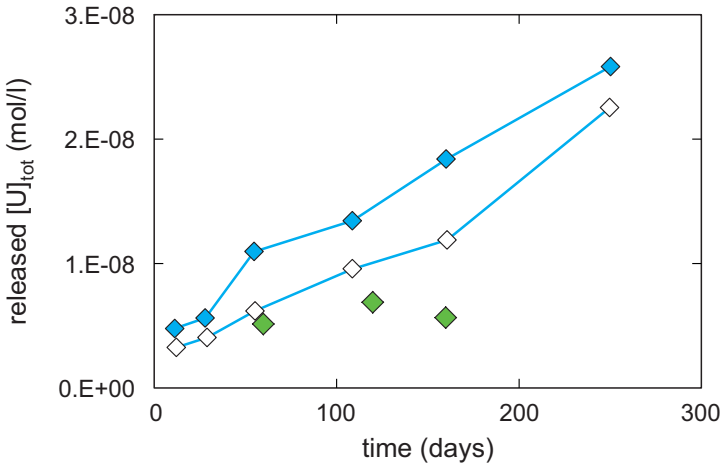

Fig. 9-2: Cumulative uranium release from UO_2 corroded in 0.01 M NaCl under anoxic conditions (Ollila 2008).

Blue and white diamonds denote the results of two separate experiments carried out in anoxic atmosphere but without iron present; green diamonds refer to an experiment with an additional strip of iron.

Tab. 9-1 summarizes the UO_2 matrix dissolution rates derived from Ollila's data in comparison with SF and UO_2 corrosion rates measured under oxidizing conditions and with dissolution rates of a typical borosilicate glass (R7T7, corresponding to the SON68 glass used as a reference for Swiss SF/HLW reprocessed in France). The data show that UO_2 recrystallization is by orders of magnitude slower than the dissolution of UO_2/SF under oxidizing conditions and of borosilicate glass.

Tab. 9-1: Range of UO_2 and SF matrix dissolution rates for (a) recrystallization in UO_2-saturated solutions under reducing conditions; (b) oxidative dissolution.

The data are compared with the range of dissolution rates for a typical borosilicate glass at 90 °C (c).

	Material	***R* [g m^{-2} d^{-1}]**	**Reference**
(a)	UO_2 non doped*	$8.7 \times 10^{-7} - 1.2 \times 10^{-5}$	Ollila (2008)
	UO_2 doped (5-10 % ^{233}U)**	$5.2 \times 10^{-7} - 2.6 \times 10^{-6}$	Ollila (2008)
(b)	UO_2 and SF***	About $10^{-4} - 10^{-1}$	Shoesmith et al. (1998) Ferry et al. (2004)
(c)	R7T7 borosilicate glass	About $10^{-4} - 10^{0}$	Vernaz et al. (2001)

* Calculated from linear regression analyses after digitizing graphical data
** Values as given in original reference (converted units)
*** Excluding biased data (see discussion in Shoesmith et al. 1998)

A further issue is the effect of clay minerals on the corrosion kinetics of SF. The dedicated experiments described in Cachoir et al. (2007) and Grambow et al. (2008) indicate that initially more U is dissolved from ^{233}U/^{238}Pu doped UO_2 in the presence of suspended clay compared to analogous experiments carried out without clay, independent of the application of H_2 overpressure (10 bar) or the addition of Fe additives. However, after a reaction time of approxi-

mately 100 days the corrosion rates decreased in both cases to vanishingly small values and became indistinguishable. These data therefore suggest that the detrimental effect of clay is transient and will not influence the corrosion resistance of the waste. Also it cannot be excluded that the initial phase of rapid dissolution was an artefact related to pre-existing surface oxidation of the UO_2 samples, as suggested by the high U concentrations (up to 10^{-4} M) measured in some experiments in spite of H_2(g) overpressure (see Fig. 9-5 in Cachoir et al. 2007). This view is corroborated by average UO_2 dissolution rates in the order of ~ 10^{-4} g m^{-2} d^{-1} over the first 110 days (Section 4.3 in Cachoir et al. 2007) which are two orders of magnitude higher than the rates inferred from Ollila's data (Tab. 9-1).

9.4.3.3 Concluding remarks on SF corrosion kinetics

In conclusion, the experimental evidence accumulated over the last years provides convincing evidence that molecular hydrogen produced through anaerobic steel corrosion will promptly react – via catalytic mediation by ε-particles – with radiolytic oxidants produced in a thin film of water in contact with the SF surface. This will suppress oxidative dissolution of spent fuel. Therefore, as long as sufficient hydrogen from anaerobic canister corrosion is available (time frame 10'000 to at least 100'000 years after emplacement), SF dissolution will be controlled by the low solubility of the U(Pu)O_2 matrix under very reducing conditions. After completion of the anaerobic canister corrosion process (~ 100'000 years after repository closure), hydrogen production will cease but alpha activity will have by then decreased below the threshold above which radiolysis-induced oxidative dissolution of SF occurs. Fast oxidative dissolution of SF is therefore unlikely at any time during the evolution of the HLW repository. It is argued that the relevant kinetic process determining radionuclide release from the SF matrix after the initial IRF pulse will be at all times slow recrystallization of UO_2, as indicated by the isotope dilution experiments of Ollila (2008). Inferred recrystallization rates will be very slow, i.e. several orders of magnitude below oxidative dissolution rates.

9.5 System evolution in a realistic scenario

9.5.1 Water ingress and SF dissolution kinetics

After canister failure (10'000 years after repository closure or later), aqueous solution penetrating from the water-saturated bentonite will reach the spent fuel assembly. As previously discussed (Section 9.3), it is not possible to make reliable predictions on the integrity of the cladding at that time, so that Zircaloy is not considered to have any safety barrier function. Probably only a few of the cladding envelopes will be defective at the time of repository closure, but one can argue that further Zircaloy embrittlement via adsorption of hydrogen produced during canister corrosion and the volumetric expansion induced by the formation of magnetite could easily lead to systematic mechanical failures of the cladding envelopes.

The porewater interacting with the SF surface will be enriched in molecular hydrogen, continuously generated by the corrosion of the intact parts of the metal canister. Taking into account the experimental results described in the preceding section, one must expect that hydrogen will promptly react with radiolytic oxidants, thereby protecting the fuel from oxidative dissolution. U and Pu concentrations will remain at very low levels (< 10^{-8} M) close to saturation equilibrium with crystalline UO_2 and PuO_2. The limiting processes governing radionuclide release are considered to be rapid release of the easily soluble and water accessible inventory fraction (IRF, mainly ^{129}I, ^{135}Cs, ^{36}Cl and ^{14}C) and later on recrystallization, with rates between ~ 0.5 and ~ 10 μg UO_2 m^{-2} d^{-1} as derived from isotopic exchange data. After canister corrosion is complete

(~ 100'000 years after repository closure) hydrogen will no longer be produced, suppressing any protective effect against SF oxidation. However, at that time the radiation field will have strongly declined. Current data indicate that the amounts of radiolytic oxidants produced will no longer be sufficient to activate oxidative SF dissolution.

9.5.2 Chemical evolution predicted from thermodynamic calculations

According to the scenario outlined in Section 9.5.1, the porewater penetrating into the failed containment will react simultaneously with spent fuel, Zircaloy cladding and the inner side of the canister, giving rise to a complex chemical system. In contrast to vitrified HLW waste, laboratory studies on SF mineral alteration are very scarce (e.g. Buck et al. 1997). Therefore, in order to make predictions on the porewater evolution and the secondary phases liable to form in this system, we had to resort to thermodynamic equilibrium calculations. These were carried out with the GEMS-PSI code (Karpov et al. 2001, Kulik 2002) using the recently revised version 12/07 (Thoenen et al. 2014) of the PSI-Nagra Chemical Thermodynamic Database 01/07 (Hummel et al. 2002).

The calculations simulate the reaction between bentonite porewater infiltrated into the canister hull and the surrounding solid materials (SF, Zircaloy and canister). Model calculations have been recently carried out to predict the chemical composition of bentonite porewaters under repository conditions. Berner & Kosakowski (2011) defined several variants based on different assumptions on the initial state of the bentonite and on the time evolution. For our calculations, we selected the porewater defined at the centre of the bentonite annulus at 10'000 years after waste emplacement. This water was assumed to react with specified amounts of the aforementioned solid materials, defined through the chemical inventories listed in Tab. 9-2.

Because the calculations aimed at reproducing the chemical conditions established in the first period after containment failure, partial corrosion of the canister was assumed by assigning 50 % of the Fe inventory to metallic iron and 50 % to magnetite (Fe_3O_4). The SF composition was defined using reference model inventories (Nagra 2013)[15] and included, besides the major components UO_2 and PuO_2, most safety-relevant radionuclides as well as stable Ba isotopes resulting from the decay of short-lived Cs nuclides. It was further assumed that sulphate and carbonate species present in the porewater were not reducible, in agreement with the well-known kinetic inhibition of such reactions in the absence of microbial activity (which was thus implicitly excluded in our model). Including such reactions would lead to alkaline solutions (pH= 11.6), pyrite formation and the production of methane (Curti 2011a).

In order to simulate an early stage of the chemical evolution after failure of the steel containment, the reaction of only a small fraction of the canister with the initial porewater was assumed. To make the calculations realistic, the reacting amounts of SF and Zircaloy were scaled (reduced) in proportion to the respective corrosion rates (Curti 2011a). Accordingly, thermodynamic equilibrium calculations simulate the reaction between 1 % of the scaled material inventory (Tab. 9-2) and 1 L of the bentonite porewater (BPW) reported by Berner et al. (2012). The major aims of these calculations were: (1) to estimate the chemical composition, pH and E_h of the porewater within the canister; (2) to identify potential secondary solids; (3) to calculate radionuclides solubility limits at the inner side of the canister and (4) to compare the obtained water composition with the initial bentonite porewater, in order to identify possible chemical gradients.

---

[15] The inventory given in MIRAM 12 (Nagra 2013) assumes an operational life-time of 50 years, while the later MIRAM 14 (Nagra 2014b) is based upon 60 years. Any differences between the two can be neglected for the thermodynamic calculations in this study.

The calculation (Tab. 9-3) yielded a porewater with pH, ionic strength, composition and a list of equilibrated solids very similar to those predicted for bentonite. However, significantly larger Fe(II) concentrations are predicted for the SF-Zircaloy-canister system (about 4 mM, i.e. more than two orders of magnitude larger than in the original BPW). The increased Fe concentration correlates with a reduced total carbonate content (15 μM vs. ~ 1 mM in BPW), following the constraint imposed by the assumed siderite-magnetite equilibrium. The increase in Fe concentration must be compensated by a reduction of the CO_3^{2-} concentration via siderite precipitation.

Tab. 9-2: Elemental inventories a single SF-Zircaloy-canister unit.
(See text for explanation.)

Material	**Element**	**Inventory** (mol/L)	**Scaled inventory** (mol/L)	**Scaling factor**
Steel canister*	C	2.474	2.474	1
	P	0.540	0.540	1
	Si	13.225	13.225	1
	Ni	63.287	63.287	1
	Fe**	451.225	451.225	1
Zircaloy	Zr	10.390	5.05×10^{-2}	4.9×10^{-3}
	Sn	0.122	5.94×10^{-4}	4.9×10^{-3}
Structural materials	Ca	3.21×10^{-3}	1.56×10^{-5}	4.9×10^{-3}
	Se	1.83×10^{-3}	8.91×10^{-6}	4.9×10^{-3}
	Sr	1.18×10^{-2}	5.72×10^{-5}	4.9×10^{-3}
	Pd	3.36×10^{-2}	1.63×10^{-4}	4.9×10^{-3}
	Eu	2.44×10^{-3}	1.19×10^{-5}	4.9×10^{-3}
Spent fuel	U	9.404	1.33×10^{-2}	1.4×10^{-3}
	Pu	2.407	3.39×10^{-3}	1.4×10^{-3}
	Ba***	6.93×10^{-2}	9.77×10^{-5}	1.4×10^{-3}
	Tc	2.42×10^{-2}	3.42×10^{-5}	1.4×10^{-3}
	Pd	6.98×10^{-3}	9.84×10^{-6}	1.4×10^{-3}
	I****	3.75×10^{-3}	5.29×10^{-6}	1.4×10^{-3}
	Cs****	7.88×10^{-3}	1.11×10^{-5}	1.4×10^{-3}
	Np	7.75×10^{-3}	1.09×10^{-5}	1.4×10^{-3}
	Am	1.79×10^{-3}	2.52×10^{-6}	1.4×10^{-3}
	Cm	5.71×10^{-5}	8.05×10^{-8}	1.4×10^{-3}
	O*****	324.289	300.700	--

* Simplified austenitic steel.
** Fe inventory calculated assuming of 50 %-50 %-mixture of steel and magnetite.
*** Ba inventory were determined from data given by Ferry et al. (2004).
**** I and Cs reduced to 90 % to account for the IRF.
***** Oxygen balanced from Fe_3O_4, UO_2 and PuO_2.

Tab. 9-3: Results of speciation calculations for the reaction between bentonite porewater and 1 % of the corrosion-rate normalized "SF-Zircaloy-canister" inventory.

	Original bentonite porewater	**Equilibrated after reaction with SF-Zircaloy-canister** (T = 25 °C, p = 1 bar)	
pH	7.79	7.53	
E_h(Volt)	-0.204	-0.445	
I(mol/kgw)	0.239	0.275	
Solutes	[mol/kgw]	[mol/kgw]	**Precipitated solids**, aqueous species**
Al	1.5×10^{-8}	1.6×10^{-8}	$Al(OH)_4^-$, $Al(OH)_3$(aq)
Am		2.7×10^{-8}	$AmHSiO_3^{2+}$, $AmSO_4^+$,Am^{3+}, $Am(SO_4)_2^-$
Ba	1.1×10^{-7}	1.1×10^{-7}	**(Ra,Ba)SO_4(s)**, Ba^{2+}, $BaSO_4$(aq)
C(inorg.)	9.0×10^{-4}	1.5×10^{-5}	HCO_3^-, $NaHCO_3$(aq), CO_2(aq), $CaHCO_3^+$
Ca	9.1×10^{-3}	9.9×10^{-3}	**gyp**, Ca^{2+}, $CaSO_4$(aq)
Cl	0.161	0.175	Cl^-
Cs		1.2×10^{-7}	Cs^+
Fe(II)	3.7×10^{-5}	4.35×10^{-3}	**mag, sid,** Fe^{2+}, $FeSO_4$(aq), $FeCl^+$
I		5.8×10^{-8}	I^-
K	1.22×10^{-3}	1.33×10^{-3}	K^+, KSO_4^-
Mg	5.15×10^{-3}	5.61×10^{-3}	Mg^{2+}, $MgSO_4$(aq)
Mo		$< 10^{-12}$	**tug**, MoO_4^2
Na	1.92×10^{-1}	2.09×10^{-1}	Na^+, $NaSO_4$(aq)
Ni		6.1×10^{-4}	**the**, Ni^{2+}, $NiHPO_4$(aq), $NiSO_4$(aq)
Np		4.0×10^{-10}	**NpO_2(am)**, $Np(OH)_4$(aq)
P		5.85×10^{-3}	HPO_4^{2-}, $H_2PO_4^-$
Pd		$< 10^{-12}$	**pal**
Pu		$< 10^{-12}$	**$PuPO_4$(s),** $PuSO_4^+$, $Pu(SO_4)_2^-$, Pu^{3+}, $Pu(OH)^{2+}$
Ra		2.0×10^{-10}	**(Ra,Ba)SO_4(s)**, $RaSO_4$(aq), Ra^{2+}, $RaCl^+$
S(VI)	3.01×10^{-2}	3.28×10^{-2}	SO_4^{2-}, $NaSO_4^-$, $CaSO_4$(aq), $MgSO_4$(aq)
Se		2.5×10^{-8}	**fse*** HSe^-
Si	1.82×10^{-4}	1.8×10^{-4}	**qtz,** $Si(OH)_4$(aq), $SiO(OH)_3^-$
Sn		1.7×10^{-8}	**cas,** $Sn(OH)_4$(aq), $SnO(OH)_3^-$
Sr	5.6×10^{-5}	6.2×10^{-5}	Sr^{2+}, $SrSO_4$(aq)
Tc		4.9×10^{-9}	**$TcO_2(H_2O)_{1.6}$**, $TcO(OH)_2$(aq)
U		3.5×10^{-9}	**UO_2(am,hyd),** $U(OH)_4$(aq)
Zr		6.5×10^{-10}	**bad** $ZrO(OH)_3^-$, $Zr(OH)_4$(aq)

gyp=gypsum=$CaSO_4$*$2H_2O$, **sid**=siderite=$FeCO_3$, **mag**=magnetite=Fe_3O_4, **tug**=tugarinovite=MoO_2, **the**=theophrastite=$Ni(OH)_2$, **pal**=palladium=Pd, **fse**=ferroselite=$FeSe_2$, **qtz**=quartz=SiO2(cr), **cas**=cassiterite=SnO_2, **bad**=baddeleyite=ZrO_2,

* The ferroselite solubility product was derived from Olin et al. (2005) and implemented in GEMS-PSI.
** Only major aqueous species contributing > 1 % and with conc. > 10-12 M are listed (in decreasing order)

Nickel is predicted to precipitate as pure $Ni(OH)_2$ (theophrastite) yielding a relatively high total aqueous concentration (~ 0.6 mM). However, since large inventories of stable Ni isotopes reside in the steel and other structural materials, the effective aqueous concentration of the safety-relevant radioisotope ^{59}Ni will be many orders of magnitude lower, due to isotope dilution.

The predicted concentrations of U and Pu are, as expected under reducing conditions, very low ($< 10^{-9}$ M) and are controlled by sparingly soluble phases, specifically UO_2(cr) and Pu(III)-phosphate.

Calculations were carried out also for a more advanced stage by simulating the reaction of BPW with 10 % of the scaled canister/Zircaloy/SF inventories (see Curti 2011a). The major effect was to enhance the consumption of water through the anaerobic corrosion of steel. This in turn resulted in a higher ionic strength and the earlier attainment of saturation limits. However, because the calculations refer to a closed system, they are not entirely realistic. After canister failure the open spaces inside the hull will remain at all times accessible to water infiltrating from the saturated bentonite. The net amount of water available will be determined by the competing rates of water consumption through steel corrosion and in-diffusion from the bentonite. Recent reactive transport calculations indicate that a steady state between corrosion-induced water consumption and water in-diffusion from bentonite is likely to be established (Senger et al. 2008), implying that there will be no local reduction in the amount of water. Nevertheless, a potential increase in porewater salinity cannot be excluded a priori even under such conditions. This issue is discussed in Appendix B3.

An additional limitation of the geochemical calculations is that surface adsorption reactions and the formation of solid solutions between specific radionuclides and major phases are neglected, with the single exception of Ra-barite formation. Both types of reaction cannot be included because the required thermodynamic and subsidiary data (e.g. specific surface areas, and properties of the solid solution phases involved) are currently not known. Moreover, all calculations were carried out at 25 °C and 1 bar, i.e. at *T* and *p* below those expected in a real repository, which is also a consequence of incomplete thermodynamic data. Whereas the effect of temperature is not considered to be critical, neglecting the high hydrogen pressures that can arise due to the anaerobic corrosion of steel may have a direct impact on radionuclide solubilities. For instance, the solubility limit of ^{93}Mo is predicted to be controlled by the following reaction:

$$MoO_2(s) + 2\ H_2O = MoO_4^{2-} + H_2(g) + 2\ H^+ \quad (9.2)$$

$$\log a(MoO_4^{2-}) = \log K_s - \log p(H_2) + 2\ pH \quad (9.3)$$

This implies that the solubility limit could be 1 – 2 orders of magnitude lower than predicted in our calculations at the expected hydrogen partial pressures (10-100 bar).

In spite of these shortcomings, the present geochemical calculations are useful for identifying "pure" solid phases that may potentially control the solubility limits of safety-relevant radionuclides, particularly those which are diluted by a large inventory of stable isotopes of the same element. For instance, the aqueous concentrations of Ni, Sn, Zr are likely to be limited by the precipitation of "pure" phases such as $Ni(OH)_2$ SnO_2 and ZrO_2 rather than solid solutions because of the abundance of these elements (predominantly present as stable isotopes) in the canister or in structural materials. The solubility limits of the safety-relevant radionuclides ^{59}Ni, ^{126}Sn and ^{90}Zr will be much lower than the corresponding elemental concentrations due to the dilution with stable isotopes.

Another key result is the prediction of Ra-barite solid solution formation as a result of the release of the Ba from SF. Precipitation of radiobarite is likely considering that Opalinus Clay porewater is already saturated with barite (Pearson et al. 2003) and that additional Ba resulting from the decay of short-lived Cs nuclides will be released from the waste itself. This precipitation reaction (Curti et al. 2010, Bosbach et al. 2010) reduces the aqueous concentration of radium to levels of ~ 10^{-10} M, below the concentrations expected if pure Ra sulphate were the solubility limiting phase.

9.5.3 Evidence from natural analogues

The secondary phases predicted by the geochemical calculations discussed above are to some extent consistent with evidence derived from natural analogue studies. At Poços de Caldas, the U(VI) dissolved in sulphate-rich groundwater was re-precipitated as "pitchblende" (hydrous UO_2) at the reducing side of the redox front, together with secondary pyrite (Waber et al. 1990). The formation of pyrite was explained by present-day populations of sulphate-reducing bacteria in the vicinity of the redox fronts (West et al. 1990). Apparently, no coffinite was formed in spite of the quite high Si concentrations in the present-day groundwaters (8 – 54 mg/L, see Tab. 3-4 in Chapman et al. 1990).

Coffinite (ideal formula: $USiO_4 \cdot nH_2O$, isostructural with zircon) should nevertheless be considered as a potential secondary U-phase under repository conditions. It is frequently found in the reduced zone of sedimentary U-deposits, e.g. in the Grants uranium district (New Mexico), where it occurs as a major U mineral in association with organic matter (Moench 1962, Deditius et al. 2008). Coffinite is prone to both homovalent and heterovalent substitutions and it may conceivably form solid solutions with a variety of radionuclides released during the aqueous corrosion of SF (Janeczek & Ewing 1992). Some doubts remain on the temperature stability field of this phase. Deditius et al. (2008) give a possible stability range of 80 – 140 °C, which would be above the temperature range expected in the Swiss HLW repository after canister failure (< 60 °C).

The best studied natural analogue for spent fuel under repository conditions is undoubtedly the "Cigar Lake" deposit. This 1.3 Ga old, massive uranium ore located in Northern Saskatchewan (Canada) was formed at the interface between precambrian graphite-rich metapelites and porous overlying sandstones. It mainly consists of uraninite, pitchblende and small amounts of coffinite, which – according to the collected geological evidence – formed by reductive precipitation of U(VI)-rich hydrothermal solutions percolating through the sandstones as they reacted with the graphite (Cramer & Smellie 1994, Smellie & Karlsson 1996). Intense hydrothermal activity altered the surrounding formations giving rise to Fe(III)-oxide bearing illitic clay layers surrounding the ore body.

Recently, Bruno & Spahiu (2014) analysed the geochemical information collected at the "Cigar Lake" and draw some important conclusions from the perspective of radioactive waste disposal. The most striking observation is that the uranium oxide ore remained essentially in its original reduced state in spite of a prolonged hydrothermal activity persisting for millions of years. No or little surface oxidation and no uranium remobilization were observed. At the same time, significant concentrations of dissolved hydrogen (about 8×10^{-4} M) were detected by chemical analyses of present-day ground water permeating the uranium ore. The U concentrations are in the order of 3×10^{-8} M to 1×10^{-7} M, indicating equilibrium with slightly oxidized UO_2.

Given the lack of U remobilization and of UO_2 oxidation, originally the Fe(III) minerals disseminated in the clay (haematite) were thought to have formed via reaction of Fe(II)-rich solu-

tions with radiolytic oxidants produced at the surface of the U minerals. This process would consume the radiolytic oxidants, thereby preventing the oxidation of UO_2. However, this model had to be discarded since calculations based on the available data and radiolysis rates (inferred from the H_2 production) always predicted a large excess of oxidants. The amounts of Fe(III) minerals observed are by far insufficient to explain the stability of the UO_2 ore body. Alternative models based on pyrite oxidation or a reduced effectiveness of alpha doses to water due to grain size effects[16] also predicted an excess of radiolytic oxidants.

Bruno & Spahiu (2014) propose that the lack of radiolytic oxidation observed at "Cigar Lake" can be explained by two factors:

(i) *Low efficiency of water radiolysis reactions at solid-water interfaces*: Reaction yields (G-values) used in radiolysis models are derived from experiments with direct irradiation of homogeneous aqueous solutions. Bruno & Spahiu (2014) argue that G-values are smaller when the solution is irradiated from a solid surface.

(ii) *Recombination reactions of radiolytic oxidants*: Laboratory experiments with ^{233}U-enriched UO_2, simulating the high dose rates typical of young SF, suggest that H_2 is non-reactive in the absence of ε-particles. Bruno & Spahiu (2014) argue that recombination reactions such as $H_2O_2 + H_2 \Rightarrow H_2O + OH^-$ may nevertheless take place at the UO_2 surface, but at such slow kinetic rates that they become manifest only at low α-dose rates typical of natural UO_2 ("Cigar Lake") or aged SF. At the high dose rates typical of non-aged SF, the above recombination reaction would be masked by the large excess of radiolytic oxidants.

9.5.4 Comparison of calculated radionuclides concentrations with experimental data and PA solubility limits

A comparison of calculated aqueous nuclide concentrations with selected experimental data and current PA solubility limits is shown in Tab. 9-4. It must be emphasized that experiments and calculations do not refer to uniform pH-E_h conditions. Moreover, our calculations refer to the SF-Zircaloy-canister system, whereas the solubility limits of Berner (2012) were adjusted to the bentonite environment. Therefore, differences among the various sets of data and results have to be expected.

In spite of these limitations, computed and experimental concentrations are fairly similar for most of the listed elements. Also, differences between solubility limits calculated for the bentonite environment and the SF-Zircaloy-canister system are limited. The 2 – 3 orders of magnitude difference in predicted U and Pu concentrations reflects differences in E_h buffering imposed in the two models. More surprising is the discrepancy in Mo concentrations. The concentration predicted in the SFZC calculation is at least six orders of magnitude below the concentrations predicted for the bentonite environment and those measured by Wegen et al. (2007), although in both calculations the solubility-limiting phase was MoO_2(s). This discrepancy is readily explained by the high sensitivity of MoO_2(s) to the oxidation potential (cf. Berner 2002). The E_h predicted after equilibration with the SF-Zircaloy-canister system is determined by the high hydrogen partial pressure and is thus considerably lower than for the original bentonite porewater; therefore a much lower aqueous Mo concentration results in the present calculation, in agreement with Eq. 9.3. Note that the E_h computed for the equilibration with the SF-Zircaloy-canister system is reasonably consistent with the electrochemical data of Carbol et al. (2005),

[16] Only a fraction of the alpha radiation produced within the uraninite/pitchblende grains would reach the water depending on particle size. In large particles, most of the alpha particles is absorbed by the solid.

who measured E_h-values in the range -0.4 to -0.1 V for UO_2 doped with ^{233}U corroding in 0.01 M NaCl in a N_2 - 8 % H_2 atmosphere.

Tab. 9-4: Radionuclide concentrations (mol/L) calculated for the SF-Zircaloy-canister system (SFZC) compared to solubility limits in bentonite porewater (Berner 2014) and to measured concentrations.

(a) 3 years static leaching experiments with UO_2 SF (50 GWd t_{IHM}^{-1}) in 5 molal NaCl brines under H_2 overpressure (Loida et al. 2005) ; (b) 146 day static experiments in deionized water (Ar, Ar-H_2 or H_2 atmosphere) by Wegen et al. (2007), (c) static leaching experiments in "Bentonite Granitic Groundwater", after Fig. 5.1.1-1 in Grambow et al. (2008), (d) static leaching in 0.01 M NaCl + 0.002 M $NaHCO_3$ up to 1 year.

	Solubility limits (Berner 2014)*** pH = 7.8 E_h = -0.204 I ~ 0. 239 m	**Model SFZC** (this work) pH = 7.6 E_h = -0.45 V I ~ 0. 4 m	**Exp. (a)** pH = 7.8 E_h: n.d. I ~ 5 m	**Exp. (b)** **** pH: n.d. E_h: n.d. I < 10^{-4} m	**Exp. (c)** **** pH: n.d. E_h: n.d. I : n.d.	**Exp. (d)** ****** pH: n.d. E_h: n.d. I ~ 0.01 m
Cs	Not limited	$10^{-7} – 10^{-6}$***	1×10^{-6}	n.d.	3×10^{-6}	$4 – 7 \times 10^{-8}$
Sr	$2 \times 10^{-6} – 6 \times 10^{-5}$	1.3×10^{-5}*	1×10^{-7}	n.d.	1×10^{-6}	$2 – 3 \times 10^{-9}$
U	$1 \times 10^{-8} – 3 \times 10^{-7}$	5×10^{-10}	2×10^{-8}	$0.2 – 5 \times 10^{-7}$	n.d.	$0.2 – 1 \times 10^{-9}$
Mo	7×10^{-6}	< 10^{-12}	n.d.	$2 – 7 \times 10^{-6}$	3×10^{-6}	$2 – 4 \times 10^{-8}$
Tc	$1 \times 10^{-9} – 5 \times 10^{-9}$	2×10^{-8}	2×10^{-8}	n.d.	n.d.	$0.3 – 2 \times 10^{-9}$
Np	$3 \times 10^{-11} – 1 \times 10^{-8}$	5×10^{-9}	5×10^{-10}	$0.03 – 4 \times 10^{-8}$	7×10^{-8}	$10^{-11} – 10^{-10}$
Pu	$4 \times 10^{-10} – 7 \times 10^{-10}$	< 1×10^{-12}	3×10^{-8}	$0.5 – 5 \times 10^{-9}$	6×10^{-8}	$0.5 – 5 \times 10^{-11}$
Am	$9 \times 10^{-9} – 3 \times 10^{-6}$	3×10^{-8}	2×10^{-9}	n.d.	2×10^{-8}	n.d.

* Values with asterisk denote concentrations below saturation.
** Since Cs solubility is not limited by any phase, two bounding values, corresponding to 1 % and 10 % of the inventory dissolved, are given.
*** Range defined by "lower guideline" and "recommended values" after Berner (2014).
**** A range is given encompassing the results of three distinct experiments.
***** Approximate values after ~ 100 days leaching time; n.d. = not determined or not reported.
****** Cs, Sr, Mo, Tc, Pu concentrations were derived indirectly from FIAP data given in source reference, by calculating nuclide inventories with WebKORIGEN (www.nucleonica.net) for the specified burnup (43 MWd/kgiHM), then normalizing to the solution volume (0.98 L) and mass of fuel (1.6 g) used in the leach tests.

9.6 Interaction of SF corrosion with the near-field

9.6.1 Preliminary remarks

In the former sections the focus was on how the near-field evolution may affect the SF dissolution process. In this section, the reverse issue is considered, i.e. how might the SF corrosion process modify the chemical and physical properties of the surrounding near-field components (including the porewater), once the aqueous corrosion of the waste package has started. Because of the close interconnections of the various system components with regard to the processes considered, this change of perspective is not possible without introducing some redundancy in the report.

9.6.2 Radiolysis

The issue of radiolysis has been discussed in detail in the preceding section in relation to possible undesirable oxidative effects on the fuel itself. Here, the main concern is the potential effect of water radiolysis on other components of the near-field. Whereas radiolysis by α and β particles is limited to a thin (a few ten μm-thick) layer of water in direct contact with the fuel surface (or its corrosion products), γ-radiation is more penetrating. However, most of the energy transfer in water (and therefore the production of radiolytic species) occurs only within a few cm distance from the γ-radiation source (Ferry et al. 2004, p. 204). In addition, γ-radiolysis produces mostly short-lived radicals that rapidly decay to redox-neutral species, mainly water. In anoxic water, molecular oxidants (H_2O_2) are not produced in detectable amounts (Ferry et al. 2004, p. 204). For these reasons, water radiolysis is not likely to affect the external components of the near-field system, notably the bentonite buffer. This conclusion can be extended to vitrified SF/HLW.

9.6.3 Release of soluble elements, chemical gradients and E_h constraints

Spent fuel and structural materials such as Zircaloy are composed of sparingly soluble elements. There are no readily soluble *major* elements (e.g. Na, B, Mo in vitrified HLW) which could be released in high concentrations into the bentonite buffer and affect its properties. Moreover, the speciation calculations discussed in the previous section indicate that the water in contact with the SF/Zircaloy/canister system will be similar to the bentonite porewater in terms of pH, ionic strength and composition. Strong chemical gradients between the porewater in contact with the corroding SF and the bentonite porewater are not predicted, with the notable exceptions of dissolved Fe and carbonate.

As mentioned previously (Section 9.5.2) the total carbonate and iron concentrations differ significantly in the two waters (Tab. 9-3). After equilibration with the SF/Zircaloy/canister system, the total carbonate concentration is predicted to drop from ~ 1 mM to 15 μM, whereas Fe increases from 37 μM to ~ 4 mM. In both waters the carbonate and Fe concentrations are interdependent since they are controlled by the siderite ($FeCO_3$) – magnetite (Fe_3O_4) equilibrium, according to the following E_h-pH dependent reaction:

$$3\ FeCO_3(s) + H_2O = Fe_3O_4(s) + 3\ CO_2(g) + 2\ H^+ + 2\ e^- \quad \log K^0(25\ °C) = -14.29 \qquad (9.4)$$

from which the following relation can be derived:

$$3 \log pCO_2 = 2\ pH + 2\ pe + \log K^0 \qquad (9.5)$$

Equation (9.5) has important thermodynamic implications. Because the bentonite porewater and the equilibrated SF-Zircaloy-canister water are buffered to very similar pH values, a decrease in carbonate concentration (and thus of pCO_2) must be compensated by a decrease in pe (E_h). At the same time, a reduction in carbonate concentration must be matched by an increase in dissolved Fe(II) concentration in order to maintain equilibrium with siderite.

In the adopted geochemical model, it is assumed that the canister steel will have only partially corroded at the time of canister failure, implying that SF corrosion will continue in the presence of an iron-magnetite mixture. Since iron is not thermodynamically stable in aqueous solutions (Garrels & Christ 1965, p. 179) it will be consumed under continuous production of hydrogen and water consumption until complete conversion to magnetite or similar Fe corrosion products. This irreversible reaction puts tight constraints on redox conditions during canister corrosion.

Specifically, the E_h of the porewater in contact with the corroding canister will be on or below the water stability line in an E_h-pH diagram until all of the iron is consumed according to reaction (9.1).

Following Garrels & Christ (1965), p. 174 – 178, interdependent equations relating E_h, pH and H_2 partial pressure can be derived for the lower water stability line (see Curti 2011a for more details). Fig. 9-3 shows graphical solutions of such equations at fixed pH. The E_h is plotted as a function of hydrogen partial pressure at the reference temperature of 50 °C for three different pH values, defining the expectable range under repository conditions. At the expected H_2 pressures (10 – 100 bar), very reducing conditions are predicted (E_h = -0.5 V to -0.75 V). Even at dissolved hydrogen concentrations as low as 10^{-8} M ($pH_2(g) \sim 10^{-5}$ bar) the conditions would remain very reducing ($E_h \sim$ -0.35 V to -0.5 V, well below the value predicted for bentonite porewater).

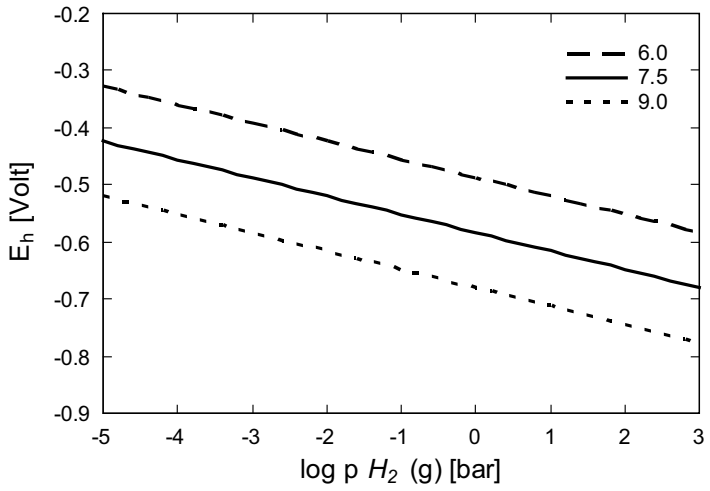

Fig. 9-3: E_h as a function of hydrogen partial pressure for 3 pH values (5, 7.5 and 9) at 50 °C at the water stability limit.

Such very reducing conditions will probably be localized in the region directly adjacent to the corroding canister and will last as long as metallic iron is present. After consumption of the iron in the canister, water will become thermodynamically stable, and the E_h raise above the lower water stability line.

During steel corrosion, hydrogen is merely a product of the irreversible corrosion reaction (9.1), not a reactant. The redox active species is metallic iron which provides the electrons required for the conversion of water to molecular hydrogen and magnetite. Therefore, the occasionally heard objection that such low E_h-values are not possible due to chemical inertness of $H_2(g)$ is not valid.

Another chemical effect of reactions at the SF-Zircaloy-canister interface which needs to be addressed is the potential increase in ionic strength due to the consumption of water during the anaerobic corrosion of steel. A local decrease in the degree of water saturation can be ruled out based on reactive transport calculations (Senger et al. 2008), which indicate that the consumed water will be readily replaced by in-diffusing bentonite porewater. However, an increase in water salinity as a result of water consumption cannot be excluded a priori. This issue is discussed in Appendix B3.

In conclusion, the only chemical effect that could potentially affect the near-field during the corrosion of the SF-Zircaloy-canister system is related to possible E_h-gradients between the bentonite and the waste package. There is no doubt that very low oxidation potentials will be triggered by the consumption of iron and water during canister corrosion. It is, however, not clear whether such low E_h conditions would be local (i.e. limited to the inner side of the canister), or would extend into the bentonite buffer. Such non-uniform redox conditions in the near-field system would imply significant opposite gradients in dissolved Fe(II) and carbonate concentrations. Fe(II) would tend to diffuse from the canister towards the bentonite, whereas carbonate species would move in the opposite direction. These arguments can be extended to the vitrified HLW system (Chapter 8) because the key underlying process (canister corrosion) is the same for both waste types.

9.7 Summary

The first part of this chapter dealt with the chemical and physical evolution of spent fuel prior to water ingress through the failed canister. During this dry phase, two processes could potentially modify the properties of spent fuel in such a way as to enhance its dissolution kinetics in a geological repository:

1. During reactor operation, mobile radionuclides associated with the fission gas, such as ^{135}Cs, ^{129}I, ^{14}C and ^{36}Cl, migrate from the core region of the fuel grains to grain boundaries and the fuel-cladding gap. On contact with water, this fraction is rapidly dissolved and mobilized (Instant Release Fraction, shortly IRF).

6 During dry ageing (at least 10'000 years after repository closure), structural damage to the UO_2 crystal lattice could arise from the intense α,β-radiation field. This could potentially enhance athermal lattice diffusion of radionuclides to grain boundaries, leading to higher IRF values compared to experiments with non-aged SF.

After canister breaching, porewater from the saturated bentonite will penetrate into the canister and start to corrode the spent fuel assembly. In spite of very low corrosion rates, the Zircaloy cladding will probably not act as a barrier because of mechanical failures, which may arise from the pressure exerted by the canister corrosion products (which have much higher molar volumes than steel), coupled with embrittlement induced by H_2 adsorption. As soon as the porewater contacts the spent fuel, the IRF inventory (mainly ^{14}C, ^{36}Cl, ^{129}I, ^{135}Cs) will be rapidly released. IRF figures are found to depend on fuel type, burnup and reactor operating conditions. Current estimates of total IRF values (sum of gap and grain-boundary contributions) for spent fuel from Swiss nuclear power plants are ~ 5-48 % for ^{36}Cl, ~ 6-20 % for ^{129}I, ~ 6-13 % for ^{135}Cs, ~ 10 % for ^{14}C, 1 % for ^{90}Sr, ^{107}Pd and ^{99}Tc, 0.2 % for ^{79}Se and 0.1 % for ^{126}Sn (Johnson 2014). Higher IRF-values in aged SF due to the accumulation of radiation damage over time (enhanced lattice diffusivity) are unlikely, but cannot be entirely excluded for light volatile nuclides (^{36}Cl, ^{14}C) based on current knowledge.

After mobilization of the IRF-inventory, the further release of radionuclides will be controlled by the dissolution rate of the UO_2/PuO_2 matrix. Recent experiments simulating a completely anoxic repository environment demonstrated that the oxidizing radicals produced through water radiolysis will be efficiently consumed by hydrogen produced during steel corrosion, thereby preventing fast oxidative dissolution of spent fuel. The hydrogen is activated by (Ru, Rh, Pd)-rich metallic nanoparticles present in the fuel (ε-particles), which act as catalysts. Based on the experimental and geological evidence, and an estimated timeframe for canister corrosion (10'000 to 100'000 years after repository closure), it is concluded that spent fuel will corrode at all times in a reducing environment. Under such conditions spent fuel dissolution rates are very

slow (~ 5×10^{-7} to ~ 1×10^{-5} g m^{-2} d^{-1}) and will be controlled in the long-term by the recrystallization of UO_2/PuO_2.

Thermodynamic calculations to predict the chemistry of porewater in equilibrium with spent fuel, Zircaloy and the corroding canister indicate a composition, pH and ionic strength very similar to those of the reacting bentonite porewater. Nevertheless, a considerably lower oxidation potential (E_h ~ -0.45 V or less compared with -0.20 mV in the bentonite porewater) is predicted as long as metallic iron and water are consumed through anaerobic corrosion of steel. Due to coupling with the siderite-magnetite equilibrium, this difference in oxidation potential could give rise to opposite concentration gradients of dissolved Fe(II) (enriched on the SF side) and carbonate (enriched on the bentonite side). The thermodynamic calculations also allowed us to identify secondary solids that could potentially limit the aqueous concentrations of safety-relevant radionuclides at the SF-Zircaloy-canister interface. Generally, the calculated radionuclide concentrations agree reasonably well with experimental data.

Based on recent reactive transport calculations it appears unlikely that the consumption of water induced by anaerobic steel corrosion could lead to water desaturation and a consequent increase in ionic strength.

10 Overall summary

Features and processes which could influence the long term evolution of the nearfield in the HLW repository have been described and discussed in the various chapters in this report i.e. low pH-cement liner, post closure temperature transients, iron corrosion/bentonite interactions, spent fuel corrosion and glass dissolution. The aim of this final chapter is to assess the overall influence of these different processes on the near-field barrier efficiency, especially with respect to radionuclide sorption and solubilities, and to see if there are any important cross interactions between the processes.

The concrete liner assumed to be present in the emplacement tunnels is a low pH variety with a pH of circa 11. Its foreseen thickness is only 15 cm compared with a corresponding thickness of about 75 cm for the compacted bentonite, dry density ~ 1'500 m^3 kg^{-1}. If the whole of the hydroxyl inventory in the concrete were to react with the bentonite, mass balance considerations yield an alteration depth of circa 13 cm. The montmorillonite is replaced by clays (illite), hydroxides, carbonates, calcium silicate hydrates, and aluminosilicates, such as zeolites and feldspars. The swelling pressure in this altered zone decreases and the sorption capacity is reduced, but not to zero (illite and zeolites show significant sorption). The sophisticated reactive transport calculations presented here indicate that the cement liner tends to react much more with the Opalinus Clay than with the bentonite. For this reason the altered bentonite zone is likely to be significantly less than 13 cm. Also, because the vertical extent of the Opalinus Clay is ~ 100 m, chemically disturbed zones of a few 10's of cm will have no noticeable influence on the barrier function.

What can be said is that the above mentioned reaction zone depth is the maximum thickness of bentonite that will be affected within 1 million years. Pore blocking will occur, but how fast and to what extent is uncertain, as is the relation between transport properties and porosity changes. The temperature at the nearfield/farfield interface, calculated without the cement liner, lies above 50 °C for circa 1'000 years with a broad peak of over 75 °C for more than 100 years. This could increase reaction rates but in reality, since equilibrium thermodynamics are assumed in the modelling, increased temperatures will have no influence on the conclusions drawn.

Regarding post emplacement temperature transients, the calculations of Senger & Ewing (2008), indicate that temperatures of above 100 °C may be expected for the inner half of the bentonite near to the canister during the first 60 – 80 years[17]. This portion of the bentonite will be unsaturated and experience a maximum temperature of ~ 130 °C. None of the results from large-scale experiments reported so far provided any information about the evolution of an unsaturated bentonite system above 100 °C (inner (less than) half of the bentonite). The sort of changes expected here are the possible formation of dissolution/precipitation zones of amorphous silica, sulphates and perhaps also carbonates close to the waste canisters. Accompanying changes in porosity are to be expected (possibility local clogging) and the potential formation of cracks. Such changes may influence the mechanical properties (swelling) and diffusion characteristics, but there is no evidence that significant changes occur in the montmorillonite component.

After ~ 80 years the bentonite becomes fully water saturated and the outer half of the bentonite never exceeds 100 °C. No significant changes in the bentonite are expected under saturated conditions at temperatures ≤ 120 °C, nor in unsaturated conditions at T < 100 °C.

[17] More recent work on this topic gave similar results (Senger et al. 2014).

The conclusion from experimental findings and modelling studies is that any small alterations due to transient temperature excursions will not change the properties of the outer (more than) half of the bentonite which can be relied upon to fulfil its buffer function fully with respect to swelling and sorption.

In general, the post emplacement temperature transient is not expected to have any important detrimental influence on the barrier function of the bentonite, particularly with respect to sorption. In this context the possibility of any significant illitization in the bentonite at the bentonite/ concrete liner interface is excluded on mass balance grounds. This is also consistent with the reactive transport calculations given in Chapter 5. For the unsaturated regions exposed to temperatures exceeding 100 °C, little reliable information exists.

Although the details of the interactions between iron corrosion products and bentonite in a reducing environment are poorly known, this is expected to have (potentially) the most important influence on the sorption and swelling characteristics of bentonite. There is experimental evidence to show that Fe^{2+} released by the corrosion of iron can lead to the destabilization and alteration of montmorillonite at temperatures below 100 °C to form 3 broad types of clay minerals: (a) Fe-rich smectites e.g. dioctahedral saponites, (b) 1:1 phyllosilicates belonging to the 7Å kaolinite/serpentinite group e.g. berthierine, and (c) non-swelling clays and chlorites e.g. chamosite. If the alteration of montmorillonite leads to Fe-rich smectites, then the near field barrier function will not be significantly influenced with respect to sorption and swelling because the Fe-smectites have similar properties to the Na-montmorillonite which they replace. However, if 7Å clay minerals or chlorites are formed, then noticeable changes are expected; i.e. a reduced swelling capacity and reduced sorption in the bentonite.

If an Fe corrosion rate of 1 micron per year is taken, and it is assumed that *all* of the Fe^{2+} released is used to form berthierine (7 Å clay minerals) or chamosite (chlorites) then after 20'000 years < 30 % of the montmorillonite is converted to berthierine or < 10 % to chamosite. Even under such an extreme and unlikely assumption, the extent of montmorillonite alteration will not seriously affect the safety-relevant features of the bentonite backfill during this time period.

Very conservative estimate indicate that it would take between 80'000 and 100'000 years to convert all of the montmorillonite to berthierine. The steel canisters assumed here[18] would take about 200'000 years to fully corrode, by which time 50 to 100 % of the montmorillonite would have been altered to chamosite. In all cases the degree of alteration depends on the ratio of the mass of steel to the mass of montmorillonite. Once the alteration has taken place, and/or all of the iron has been used, no further changes in the system up to 1 million years would be expected.

The situation described above represents a "worst case" scenario. The dominant anaerobic iron corrosion product expected for nearly neutral to alkaline conditions is magnetite, Fe_3O_4 (or Fe-sulfides or siderite at higher sulfide and carbonate concentrations respectively). Only part of the corroded iron will participate in the formation of Fe-smectites, or 7Å clay minerals or chlorites. What the relative fractions are, is unknown, and it is also unclear which alteration product or products is/are favoured. In addition, in order for alteration to take place, the diffusive transport of the Fe^{2+} produced by corrosion must take place, and this Fe^{2+} must react with montmorillonite. The kinetics involved here are also unknown.

Two further considerations indicate that the degree of transformation of montmorillonite could indeed be much less than the very conservative estimates given above. Siderite occurs in natural

[18] Cu/steel canisters or copper coated steel canisters are alternative options being considered by Nagra.

bentonite deposits as a secondary mineral, which implies that under equilibrium conditions Fe^{2+} is present in the porewater at a level corresponding to the saturation of this mineral under the prevailing conditions. The montmorillonite remains stable over geological time scales which means that the presence of Fe^{2+} in solution does not alone induce any transformations. Also, although the mechanism for the destabilization of montmorillonite by corroding iron under reducing conditions is not fully understood, the presence of native iron and electron transfer processes at the montmorillonite interface between sorbed Fe^{2+} and structural Fe^{3+} would appear to be necessary. Evidence of interactions have only been observed close to the iron source. The question is then "How far into the compacted bentonite is the presence of native iron still felt?" Indeed, the interactions between corroding iron and montmorillonite may just be a local phenomena.

In general, the corrosion of vitrified high level waste is not expected to have any detrimental effects on the bentonite. Glass dissolution rates of 1.5×10^{-3} g m^{-2} d^{-1} for BNFL glass and 2.0×10^{-4} for AREVA glass are expected, although these could be reduced by a factor of ten considering realistic temperatures and a reduced accessibility of water to the glass surface. However, the adverse effect of clay and iron corrosion products on the long-term glass dissolution rate is still not completely resolved.

Self-irradiation has no significant influence on the glass corrosion kinetics.

The formation of a mildly alkaline pH plume caused by the release of alkaline elements from the glass (Na, Li, K) appears to be unlikely due to the pH buffering capacity of canister corrosion products and bentonite, and most of the Si, Al, Ca, Fe, Zn and Mg released from the glass will form secondary solids (mainly clay minerals), which will add to the sorption potential of the buffer.

An unresolved issue is the effect of boron release, which could complex highly charged radionuclides. The thermodynamic data on borate complexation of radionuclides are scarce. At this point in time, their impact on radionuclide solubility is estimated on the basis of chemical analogy.

Spent fuel is likely to corrode at very slow rates ($\sim 5 \times 10^{-7}$ to $\sim 1 \times 10^{-5}$ g m^{-2} d^{-1}) at all times under reducing conditions, primarily due to the very low solubility of the UO_2 matrix. No adverse effects due to water radiolysis are expected because the radiolysis products will react with the hydrogen produced during the anaerobic corrosion of steel. As soon as the porewater comes in contact with the spent fuel, an "instant release fraction" inventory is assumed to be rapidly released. Thereafter radionuclide release rates will be determined by the fuel corrosion rate.

Other than this, borosilicate glass corrosion and the dissolution of the spent fuel are not expected to have any detrimental effects on the near field barrier functions.

All of the processes discussed in detail in this report have the potential to degrade the properties of the pristine bentonite. However, our current system understanding leads to the conclusion that the extent and rate of transformation of the montmorillonite means that enough of the bentonite will remain to fulfil the safety functions over the period of consideration.

11 References

Aagard, P., Jahren, J.S., Harstad, A.O., Nilsen, O. & Ramm, M. (2000): Formation of grain-coating chlorite in sandstones. Laboratory synthesized vs. natural occurrences. Clay Minerals, 35, 261 – 269.

Abolhassani, S., Bart, G. & Jakob, A. (2010): Examination of the chemical composition of irradiated zirconium based fuel claddings at the metal/oxide interface by TEM. J. Nucl. Mat. 399, 1 – 12.

Adler, M. (2001): Interaction of clay stone and hyperalkaline solutions at 30 °C: A combined experimental and modeling study. Dissertation, University of Bern.

Adler, M., Mäder, U.K. & Waber, H.N. (2001): Core infiltration experiment investigating high-pH alteration of low-permeability argillaceous rock at 30 °C, in Proceedings WRI-10 (10th International Symp. Water Rock Interaction, Villasimius, Italy), pp. 1299 – 1302, Balkema.

Advocat, Th. (1991): Les mécanismes de corrosion en phase aqueuse du verre nucléaire R7T7. Approche expérimentale. Essai de modélisation thermodynamique et cinétique. PhD thesis, Centre de Géochimie de la Surface (CNRS), Univ. Louis Pasteur, Strasbourg, 213 p.

Ahn, J.H. & Peacor, D.R. (1985): Transmission electron microscopic study of diagenetic chlorite in Gulf Coast argillaceous sediments. Clays and Clay Minerals, 33, 228 – 236.

Alexander, W., Arcilla, C., Kawamura, H. & McKinley, I. (2008): A new natural analogue study of the interaction of low-alkali cement leachates and the bentonite buffer of a radioactive waste repository, in Scientific Basis of Nuclear Waste Management XXXI, Vol. 1107, pp. 493 – 500, Materials Research Society.

Arcilla, C.A., Paguican, E., Ferrer, C., Alexander, W.R., McKinley, I.G. & Miyoshi, S. (2007): IPHAP: information on philippine bentonites, hyperalkaline waters and potential analogue sites, in Proceedings of international meeting, September 17 – 18, 2007, Lille France: Clays in natural & engineered barriers for radioactive waste confinement, pp. P/AP/13, 275 – 276, Andra, France.

Arthur, R., Wei, Z., Tianfu, X., Pruess, K. & Stromberg, B. (2006): Experimental Calibration of a Reactive-Transport Model of Buffer Cementation, Chinese Journal of Rock Mechanics and Engineering, 25(4), 741 – 749.

Badaut, D., Besson, G., Decarreau, A. & Rautureau, R. (1985): Occurrence of a ferrous, trioctahedral smectite in recent sediments of Atlantis II Deep, Red Sea. Clay Minerals, 20, 389 – 404.

Bailey, S.W. (1988): Odinite, a new dioctahedral-trioctahedral Fe3+-rich 1:1 clay mineral. Clay Minerals, 23, 237 – 247.

Bart, G., Zwicky, H.U., Aerne, E.T., Graber, Th., Z'Berg, D. & Tokiwai, M. (1987): Borosilicate glass corrosion in the presence of steel corrosion products. Mat. Res. Soc. Symp. Proc. Vol. 84, 459 – 470.

Bellot-Gurlet, L., Neff, D., Solenn, R., Monnier, J., Saheb, M. & Dillmann, P. (2009): Raman studies of corrosion layers formed on archaeological irons in various media. Journal of Nano Research, 8, 147 – 156.

Berner, U. (1992): Evolution of pore water chemistry during degradation of cement in a radioactive waste repository environment, Waste Management, 12(2-3), 201 – 219.

Berner, U. (2002): Project Opalinus Clay: Radionuclide concentration limits in the near-field of a repository for spent fuel and vitrified high-level waste, PSI-Report Nr. 02-22, Paul Scherrer Institut, Villigen, Switzerland, and Nagra Tech. Rep. NTB 02-10. Nagra, Wettingen, Switzerland.

Berner, U. (2009): Modelling hydrated HTS cement and its porewater. PSI Internal Report AN-44-09-10. Paul Scherrer Institut, Villigen, Switzerland.

Berner, U. (2010): Setting up bentonite pore water compositions. PSI Internal Report AN-44-10-04, Rev.1. Paul Scherrer Institut, Villigen, Switzerland

Berner, U. (2012): Solubility of radionuclides in a bentonite environment. PSI Internal Report TM-44-12-01. Paul Scherrer Institut, Villigen, Switzerland.

Berner, U. (2014): Solubility of radionuclides in a bentonite environment for provisional safety analyses for SGT-E2. Nagra Tech. Rep. NTB 14-06. Nagra, Wettingen, Switzerland.

Berner, U., Kulik, D.A. & Kosakowski, G. (2013): Geochemical impact of a low-pH cement liner on the nearfield of a repository for spent fuel and high-level radioactive waste. Phys. Chem. Earth, 64, 46 – 56.

Berner, U. & Kosakowski, G. (2011): Freigabe Bentonitporenwasser. PSI Internal Report AN-44-11-12. Paul Scherrer Institut, Villigen, Switzerland.

BFE (2008): Sachplan geologische Tiefenlager. Konzeptteil. Bundesamt für Energie BFE, Bern.

Bildstein, O., Trotignon, L., Perronnet, M. & Jullien, M. (2006): Modelling of iron-clay interactions in deep geological disposal conditions. Physics and Chemistry of the Earth, 31, 618 – 625.

Birgersson M., Karnland, O., Korkeakoski. P., Leupin, O., Mäder, U., Sellin, P. & Wersin, P. (2014): Montmorillonite stability under nearfield condtions. Nagra Tech. Rep. NTB 14-12, Nagra, Wettingen, Switzerland.

Bischoff, J.L. (1972): A ferroan nontronite from the Red Sea geothermal system. Clays and Clay Minerals, 20, 217 – 223.

Blanc, P., Bourbon, X., Lassin, A. & Gaucher, E.C. (2010a): Chemical model for cement-based materials: Thermodynamic data assessment for phases other than C-S-H, Cement and Concrete Research, 40(9), 1360 – 1374.

Blanc, P., Bourbon, X., Lassin, A. & Gaucher, E.C. (2010b): Chemical model for cement-based materials: Temperature dependence of thermodynamic functions for nanocrystalline and crystalline C–S–H phases, Cement and Concrete Research, 40(6), 851 – 866.

Blanc, P., Lassin, A., Piantone, P., Azaroual, M., Jacquemet, N., Fabbri, A. & Gaucher, E.C. (2012): Thermoddem: A geochemical database focused on low temperature water/rock interactions and waste materials, Applied Geochemistry, 27(10), 2107 – 2116.

Bosbach, D., Böttle, M. & Metz, V. (2010): Experimental study on Ra2+ uptake by barite (BaSO4). Technical Report TR-10-43. Swedish Nuclear Fuel and Waste Management Co (SKB), Stockholm, Sweden.

Bosbach, D., Rabung, T., Brandt, F. & Fanghänel, T. (2004): Trivalent actinide coprecipitation with powellite (CaMoO4): Secondary solid solution formation during SF/HLW borosilicate-glass dissolution. Radiochim. Acta 92, 639 – 643.

Bradbury, M.H. & Baeyens, B. (1995): A quantitative mechanistic description of Ni, Zn and Ca sorption on Na-montorillonite. Part III: Modelling. PSI Bericht 95-12, Paul Scherrer Institut, Villigen, Switzerland and Nagra Tech. Rep. NTB 95-06. Nagra, Wettingen, Switzerland.

Bradbury, M.H. & Baeyens, B. (1997): A mechanistic description of Ni and Zn sorption on Na-montmorillonite. Part II: modelling. J. Contam. Hydrol. 27, 223 – 248.

Bradbury, M.H. & Baeyens, B. (1998): A physico-chemical characterisation and geochemical modelling approach for determining porewater chemistries in argillaceous rocks. Geochim. Cosmochim. Acta 62, 783 – 795.

Bradbury, M.H. & Baeyens, B. (2002): Porewater chemistry in compacted re-saturated MX-80 bentonite: Physico-chemical characterisation and geochemical modelling, PSI Report 02-10. Paul Scherrer Institut, Villigen, Switzerland.

Bradbury, M.H. & Baeyens, B. (2005): Experimental measurements and modeling of sorption competition on montmorillonite. Geochimica et Cosmochimica Acta 69, 4187 – 4197.

Bradbury, M.H., Baeyens, B. & Thoenen, T. (2010): Sorption Data Bases for Generic Swiss Argillaceous Rock Systems. Nagra Tech. Rep. NTB 09-03. Nagra, Wettingen, Switzerland.

Brandt, H., Bosbach, D., Panak, P.J. & Fanghänel, T. (2007): Structural incorporation of Cm(III) in trioctahedral smectite hectorite: A time-resolved laser fluorescence spectroscopy (TRLFS) study. Geochim. Cosmochim. Acta 71,145 – 154.

Brearley, A.J. (2006): The action of water. In: Mc Sween Jr., H.Y. & Lauretta, D.S. (eds.): Meteorites and the early solar system II. The University of Arizona Press, Tucson, AZ, USA, 587 – 624.

Brindley, G.W. (1982): Chemical compositions of berthierine. Clays and Clay Minerals, 30, 153 – 155.

Brown, P.L., Curti, E. & Grambow, B. (2005): Chemical thermodynamics of zirconium. F.J. Mompean and J. Perrone (Eds.), Chemical Thermodynamics Vol. 8, NEA OECD, Elsevier, Amsterdam.

Bruno, J. & Spahiu, K. (2014): The long-term effect of hydrogen on the UO_2 spent fuel stability under anoxic conditions: Findings from the Cigar Lake Natural Analogue study. Applied Geochemistry, 49, 178 – 183.

Buck, E.C., Wronkiewicz, D.J., Finn, P.A. & Bates, J.K. (1997): A new uranyl oxide hydrate phase derived from spent fuel alteration, J. Nucl. Mat. 249, 70 – 76.

Burnol, A., Dupros, F., Spycher, N. & Xu, T. (2006): Simulation of the degradation of a concrete/clay interface: influence of temperature, unsaturated conditions and porosity variations, in Proceedings Tough Symposium 2006 May 15 – 17, Lawrence Berkeley National Laboratory, Berkeley, California.

Burnol, A., Dupros, F., Spycher, N., Xu, T., Blanc, P. & Gaucher, E. C. (2007): Simulation of the degradation of a concrete/clay interface: Influence of temperature, unsaturated conditions and porosity variations., in Proceedings of international meeting, September 17 – 18, 2007, Lille France: Clays in natural & engineered barriers for radioactive waste confinement. pp. P/AP/14, 277 – 278, Andra.

Cachoir, Ch., Lemmens, K. & Mennecart, Th. (2007): DELIVERABLE (D-N°:1.5.23) Final activity report for SCK•CEN (WP1.5) The effect of H2 on UO2 dissolution in the presence of engineered barrier clay. EU NF-PRO Project FI6W-CT-2003-02389. European Commission, Brussels, Belgium.

Cailleteau, C., Angeli, F., Devreux, F., Gin, S., Jestin, J., Jollivet, P. & Spalla, O. (2008): Insight into silicate – glass corrosion mechanisms. Nature Mater. 7, 978 – 983.

Carbol, P., Cobos-Sabate, J., Glatz, J.-P., Ronchi, C., Rondinella, V., Wegen, D.H., Wiss, T., Loida, A., Metz, V., Kienzler, B., Spahiu, K., Grambow, B., Quiñones, J., Martinez-Esparza Valiente, A. (2005): The effect of dissolved hydrogen on the dissolution of ^{233}U doped $UO_2(s)$, high burn-up spent fuel and MOX fuel. Technical Report TR-05-09. Swedish Nuclear Fuel and Waste Management Co (SKB), Stockholm, Sweden.

Carbol, P., Fors, P., Gouder, Th. & Spahiu, K. (2009): Hydrogen suppresses UO_2 corrosion, Geochim. Cosmochim. Acta 73, 4366 – 4375.

Carlson, L., Karnland, O., Olsson, S., Rance, A. & Smart, N. (2008): Experimental studies on the interactions between anaerobically corroding iron and bentonite. SKB Rapport R-08-28. SKB, Svensk Kärnbränslehantering AB, Stockholm, Sweden. 72 pp.

Carlson, L., Karnland, O., Oversby, V.M., Rance, A.P., Smart, N.R., Snellman, M., Vähänen, M. & Werme, L.O. (2007): Experimental studies of the interactions between anaerobically corroding iron and bentonite. Physics and Chemistry of the Earth, 32, 334 – 345.

Cathelineau, M. & Nieva, D. (1985): A chlorite solid solution geothermometer – The Los Azufres (Mexico) geothermal system. Contributions to Mineralogy and Petrology, 91, 235 – 244.

Chapman, N.A., McKinley, I.G., Shea, M.E., Smellie, J.A.T. (1990): The Poços de Caldas project: Summary and implications for radioactive waste management. Nagra Tech. Rep. NTB 90-33, Nagra, Wettingen, Switzerland and TR 90-24. Swedish Nuclear Fuel and Waste Management Co (SKB), Stockholm, Sweden.

Charpentier, D., Devineau, K., Mosser-Ruck, R., Cathelineau, M. & Villiéras, F. (2006): Bentonite-iron interactions under alkaline condition: An experimental approach. Applied Clay Science, 32, 1 – 13.

Chave, T. (2007): Etude des mécanismes d'altération par l'eau du verre R7T7 en milieu confiné. Ph.D. Thesis, Univ. Montpellier II, France.

Choi, Y. (1997): Formation of hydride in zircaloy-4 cladding tube. J. Mat. Sci. Lett. 16, 66 – 67.

Cloet, V., Schwyn, B., Baeyens B., Curti E., Diomidis N., Johnson L.H., Leupin, O.X., Mibus J., van Loon L.R. & Wieland E.: (2014): Einfluss der Salinität des Porenwassers der Wirtgesteine auf die Langzeitsicherheit der Tiefenlager. Nagra Working Report NAB 14-09. Nagra, Wettingen, Switzerland.

Couture, R.A (1985): Steam rapidly reduces the swelling capacity of bentonite. Nature 318, 50 – 52.

Cramer J. & Smellie J. (1994): Final report of the AECL/SKB Cigar Lake Analog Study. SKB Report 94-04. SKB, Stockholm, Sweden.

Crovisier, J.L., Advocat, T., Dussossoy, J.L. (2003): Nature and role of natural alteration gels formed on the surface of ancient volcanic glasses (Natural analogs of waste containment glasses). J. Nucl. Mat. 321, 91 – 109.

Crovisier, J.L., Fritz, B., Grambow, B., Eberhart, J.P. (1986): Dissolution of basaltic glass in seawater: experiments and thermodynamic modelling in: Scientific Basis for Nuclear Waste Management IX, Werme, L.O. ed., Mat. Res. Soc. Symp. Proc. Vol. 50, 273 – 280.

Cuevas, J., Vigil, R., Ram, S., Fern, R. & Leguey, S. (2006): The alkaline reaction of FEBEX bentonite: a contribution to the study of the performance of bentonite/concrete engineered barrier systems, Journal of Iberian Geology, 32(2), 151 – 174.

Curti, E. & Degueldre, C. (2002): Solubility and hydrolysis of Zr oxides: a review and supplemental data. Radiochim. Acta 90, 801 – 804.

Curti, E. & Smith, P.A. (1991): Enhancement of borosilicate glass dissolution by silica sorption and diffusion in compacted bentonite: a model study". In: Scientific Basis for Nuclear Waste Management XIV, Mat. Res. Soc. Proc. 212, pp. 31 – 39, Boston: Materials Research Society.

Curti, E. & Tits, J. (2005): Scoping calculations on Ba release from vitrified HLW waste and barite precipitation. PSI Internal Report AN-44-05-04. Paul Scherrer Institut, Villigen, Switzerland.

Curti, E. & Wersin, P. (2002): Assessment of Porewater Chemistry in the Bentonite Backfill for the Swiss SF/HLW Repository. Nagra Tech. Rep. NTB 02-09. Nagra, Wettingen, Switzerland.

Curti, E. (2003): Glass Dissolution parameters: Update for Entsorgungsnachweis. PSI-Report Nr. 03-18, Villigen, Switzerland and Nagra Tech. Rep. NTB 02-21. Nagra, Wettingen, Switzerland, pp. 46.

Curti, E. (2009): Status of European Glass Corrosion Science and Proposal for new long-term leaching Experiments, PSI Internal Report AN 44-09-12. Paul Scherrer Institut.

Curti, E. (2011a): Chemical Evolution of Spent Fuel and Zircaloy under Repository Conditions. PSI Technical Report, TM 44-11-03. Paul Scherrer Institut, Villigen, Switzerland.

Curti, E. (2011b): Comparison of Bentonite Pore Water calculations carried out with conventional and novel models. PSI Internal Report AN-44-11-18. Paul Scherrer Institut, Villigen. Switzerland.

Curti, E. (2012): Bentonite pore water compositions for safety assessment calculations ("Sectoral Plan"). PSI Internal Report AN-44-12-07. Paul Scherrer Institut, Villigen. Switzerland.

Curti, E., Aimoz, L. & Kitamura, A. (2013): Selenium uptake onto natural pyrite. J. Radioanal. Nucl. Chem. 295:1655 – 1665.

Curti, E., Crovisier, J.L., Morvan, G. & Karpoff, A.M. (2006): Long-term corrosion of two nuclear waste reference glasses (MW and SON68): A kinetic and mineral alteration study. Appl. Geochem. 21,1152 – 1168.

Curti, E., Dähn, R., Farges, F. & Vespa, M. (2009): Na, Mg, Ni and Cs distribution and speciation after long-term alteration of a simulated nuclear waste glass: A micro-XAS/XRF/XRD and wet chemical study. Geochim. Cosmochim. Acta 73, 2283 – 2298.

Curti, E., Fujiwara, K., Iijima, K., Tits, J., Cuesta, C., Kitamura, A., Glaus, M.A. & Müller, W. (2010): Radium uptake during barite recrystallization at 23 ± 2 °C as a function of solution composition: An experimental ^{133}Ba and ^{226}Ra tracer study. Geochim. Cosmochim. Acta 74, 3553 – 3570.

Curti, E., Godon, N. & Vernaz, E.Y. (1993): Enhancement of the glass corrosion in the presence of clay minerals: testing experimental results with an integrated glass dissolution model. In: Scientific Basis for Nuclear Waste Management XVI, Mat. Res. Soc. Proc. 294, 163 – 170, Boston: Materials Research Society.

Curtis, C.D., Hughes, C.R., Whiteman, J.A. & Whittle, C.K. (1985): Compositional variation within some sedimentary chlorites and some comments on their origin. Mineralogical Magazine, 49, 375 – 386.

De Combarieu, G., Barboux, P. & Minet, Y. (2007): Iron corrosion in Callovo-Oxfordian argillite: From experiments to thermodynamic/kinetic modelling. Physics and Chemistry of the Earth, 32, 346 – 358.

De Windt, L. & Badreddine, R. (2007): Modelling of long-term dynamic leaching tests applied to solidified/stabilised waste. Waste Management, 27(11), 1638 – 47.

De Windt, L., Badreddine, R. & Lagneau, V. (2007): Long-term reactive transport modelling of stabilized/solidified waste: from dynamic leaching tests to disposal scenarios., Journal of Hazardous Materials, 139(3), 529 – 36.

De Windt, L., Marsal, F., Tinseau, E. & Pellegrini, D. (2008): Reactive transport modeling of geochemical interactions at a concrete/argillite interface, Tournemire site (France), Physics and Chemistry of the Earth, Parts A/B/C, 33(Supplement 1), S295 – S305.

De Windt, L., Pellegrini D. & Van der Lee, J. (2004a): Coupled modeling of cement/claystone interactions and radionuclide migration, Journal of Contaminant Hydrology, 68(3-4), 165 – 182.

De Windt, L., Pellegrini, D. & Van der Lee, J. (2001): Reactive transport modeling of interaction processes between claystone and cement, 9 pp., (online) Available from: http://www.eurosafe-forum.org/files/semb3_6.pdf (Accessed 14 November 2011).

De Windt, L., Pellegrini, D. & Van der Lee, J. (2004b): Reactive transport modelling of a spent fuel repository in a stiff clay formation considering excavation damaged zones. Radiochimica Acta, 92, 9-11.

Deditius, A.P., Utsunomiya, S. & Ewing, R.C. (2008): The chemical stability of coffinite, $USiO_4 \cdot nH_2O$; $0 < n < 2$, associated with organic matter: A case study from Grants uranium region, New Mexico, USA, Chem. Geol. 251, 33 – 49.

Dehaudt, Ph. (2000): Le combustible nucléaire et son état physico-chimique à la sortie des réacteurs. Report CEA-R-5923. Commissariat à l'Energie Atomique (CEA), CEA/Grenoble, France.

Diomidis, N. (2014): Scientific basis for the production of gas due to corrosion in a deep geological repository. Nagra Working Report NAB 14-21. Nagra, Wettingen, Switzerland.

Dzombak, D.A. & Morel, F.M.M. (1990): Surface Complexation Modeling: Hydrous Ferric Oxide,Wiley-Interscience, New York.

Elrod, J.A. & Kester, D.R. (1980): Stability constants of iron(III) borate complexes. J. Sol. Chem. 9, 885 – 894.

Endress, M., Zinner, E. & Bischoff A. (1996): Early aqueous activity on primitive meteorite parent bodies. Nature, 379, 701 – 703.

ENRESA (2006): FEBEX Project. Final Report. Post-mortem bentonite analysis. Enresa publicación técnica 05-1/2006.

European Comission (2005): ECOCLAY II, Effects of cement on clay barrier performance – phase II. Final report, EUR 21921. European Commission, Brussels, Belgium.

Feng, X., Bates, J.K., Buck, E.C., Bradley, Ch.R. & Gong, M. (1993): Long-term comparison of dissolution behavior between fully radioactive and simulated nuclear waste glasses. Nucl. Technol. 104, 193 – 206.

Fernández, R., Cuevas, J. & Mäder, U. K. (2010): Modeling experimental results of diffusion of alkaline solutions through a compacted bentonite barrier, Cement and Concrete Research, 40(8), 1255 – 1264.

Fernández, R., Cuevas, J. & Mäder, U.K. (2009): Modelling concrete interaction with a bentonite barrier, European Journal of Mineralogy, 21(1), 177 – 191.

Ferry, C., Lovera, P., Poinssot, Ch. & Garcia, Ph. (2005): Enhanced diffusion under alpha self-irradiation in spent nuclear fuel: Theoretical approaches. J. Nucl. Mat. 346, 48 – 55.

Ferry, C., Piron, J. P., Poulesquen, A. & Poinssot, C. (2008): Radionuclides release from the spent fuel under disposal conditions: Re-evaluation of the Instant Release Fraction. Scientific Basis for Nuclear Waste Management XXXI 1107, 447 – 454.

Ferry, C., Poinssot, Ch. et al. (2004): Synthesis on the Spent Fuel Long Term Evolution. Commissariat a l'Energie Atomique (CEA), Technical Report R6084.

Flury, M. & Gimmi, T.F. (2002): Solute diffusion, in Methods of Soil Analysis, Part 4: Physical Methods, edited by J. H. Dane and G. C. Topp, pp. 1323 – 1351, Soil Science Society of America, Madison, Wisconsin, USA.

Frizon, F., Gin, S., Jegou, C. (2009): Mass transfer phenomena in nuclear waste packages. In: Wang, L. (Ed.), Advances in Transport Phenomena 2009. Springer, pp. 131 – 134.

Frugier, P., Gin, S. & Jegou, C. (2004): Affinity rate law failure to describe sodium borosilicate glass alteration kinetics. In: Scientific Basis for Nuclear Waste Management XXVII, Mat. Res. Soc. Proc. Vol. 807,127 – 132, Boston: Materials Research Society.

Fukushi, K., Sugiura, T., Morishita, T., Takahashi, Y., Hasebe, N. & Ito, H. (2010): Iron-bentonite interactions in the Kawasaki bentonite deposit, Zao area, Japan. Applied Geochemistry, 25, 1120 – 1132.

Gaboreau, S., Lerouge, C., Dewonck, S., Linard, Y., Bourbon, X., Fialips, C. I., Mazurier, A., Pret, D., Borschneck, D., Montouillout, V., Gaucher, E. C. & Claret F. (2012): In-situ interaction of cement paste and shotcrete with claystones in a deep disposal context, American Journal of Science, 312(3), 314 – 356.

Gaboreau, S., Prêt, D., Tinseau, E., Claret, F., Pellegrini, D. & Stammose, D. (2011): 15 years of in situ cement–argillite interaction from Tournemire URL: Characterisation of the multi-scale spatial heterogeneities of pore space evolution, Applied Geochemistry, 26(12), 2159 – 2171.

Gailhanou, H., Blanc, P., Rogez, J., Mikaelian, G., Kawaji, H., Olives, J., Amouric, M., Denoyel, R., Bourrelly, S., Montouillout, V., Vieillard, P., Fialips, C.I., Michau, N., Gaucher, E.C. (2012): Thermodynamic properties of illite, smectite and beidellite by calorimetric methods: Enthalpies of formation, heat capacities, entropies and Gibbs free energies of formation. Geochim. Cosmochim. Acta 89. 279 – 301.

Garrels, R.M. & Christ, C.M. (1965): Solutions, minerals and equilibria, Harpers' Geoscience Series. Harper and Row, New York, 450 p.

Gaucher, E.C. & Blanc, P. (2006): Cement/clay interactions – a review: experiments, natural analogues, and modeling., Waste Management, 26(7), 776-88.

Gaucher, E.C., Tournassat, C., Pearson, F.J., Blanc, P., Crouzet, C., Lerouge, C. & Altmann, S. (2009): A robust model for pore-water chemistry of clayrock, Geochimica et Cosmochimica Acta, 73(21), 6470 – 6487.

Gherardi, F., Xu, T. & Pruess, K. (2007): Numerical modeling of self-limiting and self-enhancing caprock alteration induced by CO_2 storage in a depleted gas reservoir, Chemical Geology, 244(1-2), 103 – 129.

Gin, S., Ribet, I. & Couillard, M. (2001): Role and properties of the gel formed during nuclear glass alteration: importance of gel formation conditions J. Nucl. Mater. 2001, 298, 1 – 10.

Glaus, M.A., Frick, S., Rosse, R., Van Loon, L.R. (2010): Comparative study of tracer diffusion of HTO, $^{22}Na^{+}$ and $^{36}Cl^{-}$ in compacted kaolinite, illite and montmorillonite. Geochim. Cosmochim. Acta 74(7): 1999 – 2010.

Göbel, I, Alheid, H.J., Jockwer, N., Mayor, J.C., García-Siñeriz, J.L., Alonso, E., Weber H., Ploetze, M., Klubertanz, G., Ammon, C. (2006): Heater Experiment: Rock and bentonite thermo-hydro-mechanical (THM) processes in the nearfield of a thermal source for development of deep underground high level radioactive waste repositories. Final report EUR 22586, Contract No: FIKW-CT-2001-00132. European Commission, Brussels, Belgium.

Godon, N. (1988): Effet des matériaux d'environnement sur l'altération du verre nucléaire R7T7 – influence des argiles. Ph. D. thesis, Univ. Orléans, France.

Godon, N. (2004): Dossier de référence sur le comportement à long terme des verres nucléaires. Rapport technique DTCD /2004/06, Commissariat à l'Energie Atomique, 282 p.

Godon, N., Gin, S., Minet, Y., Grambow, B., Lemmens, K. & Aertsen, M. (2008): Reference Report on the state of the art of glass properties and glass alteration during long term storage and under disposal conditions. NF-PRO project, Deliverable 1.1.1 of RTD component 1, European Commission (Contract F16W-CT-2003-02389), 144 p.

Goldberg, S. (1997): Reactions of boron with soils. Plant and Soil 193, 35 – 48.

Goll W., Hellwig Ch., Hoffmann P.B., Sauser, W., Spino J. and Walker C.T. (2007): UO_2 fuel behaviour at rod burn-ups up to 105 MWd/kgHM. Atw - International Journal for Nuclear Power, Vol. 52(2), 95 – 102.

González Sánchez, F., Van Loon, L., Gimmi, T., Jakob, A., Glaus, M. & Diamond, L. (2008): Self-diffusion of water and its dependence on temperature and ionic strength in highly compacted montmorillonite, illite and kaolinite, Applied Geochemistry, 23(12), 3840 – 3851.

Grambow, B. (1985): A general rate equation for nuclear waste glass corrosion. In: Scientific Basis for Nuclear Waste Management VIII, Mat. Res. Soc. Proc. 44, pp. 15 – 27, Boston: Materials Research Society.

Grambow, B. (1987): Nuclear Waste Glass Dissolution: Mechanisms, Model and Application – Report to JSS Project Phase IV. JSS Report 87-02. SKB, Stockholm, Sweden.

Grambow, B., Jercinovic, M.J., Ewing, R.C. & Byers, C.D. (1986): Weathered basalt glass: a natural analogue for the effects of reaction progress on nuclear waste glass alteration, Sci. Basis for Nuclear Waste Management IX, L.O. Werme, ed., Mat. Res. Soc. Symp. Vol. 50, 263 – 272.

Grambow, B., Lemmens, K. et al. (2008): Deliverable D1.6.3; Final Synthesis Report RTD Component 1: Dissolution and release from the waste matrix. EU NF-PRO Project, Contract Number: FI6W-CT-2003-02389. European Commission, Brussels, Belgium.

Grauer, R. (1986): Bentonite as a backfill material in the high-level waste repository: chemical aspects. Nagra Tech. Rep. NTB 86-12E. Nagra, Wettingen, Switzerland.

Guggenheim, S. & Eggleton, R.A. (1988): Crystal chemistry, classification, and identification of modulated layer silicates. In: Bailey, S.W. (ed.): Hydrous phyllosilicates (exclusive of micas). Reviews in Mineralogy, 19, Mineralogical Society of America, 675 – 725.

Guillamont, R., Fanghänel, Th., Neck, V., Fuger, J., Palmer, D.A., Grenthe, I. & Rand, M.H. (2003): Update on the Chemical Thermodynamics of Uranium, Neptunium, Plutonium, Americium and Technetium, Chemical Thermodynamics Vol. 5, F.J. Mompean et al., eds., OECD-NEA, Issy-les-Moulineaux, France.

Guillaume, D. (2002): Etude experimentale du système fer-smectite en présence de solution à 80 °C et 300 °C. Ph.D. Thesis, Université Henri Poincaré, Nancy 1, France, 211 pp.

Guillaume, D., Neaman, A., Cathelineau, M., Mosser-Ruck, R., Peiffert, C., Abdelmoula, M., Dubessy, J., Villiéras, F., Baronnet, A. & Michau, N. (2003): Experimental synthesis of chlorite from smectite at 300 °C in the presence of metallic Fe. Clay Minerals, 38, 281 – 302.

Guillaume, D., Neaman, A., Cathelineau, M., Mosser-Ruck, R., Peiffert, C., Abdelmoula, M., Dubessy, J., Villiéras, F. & Michau, N. (2004): Experimental study of the transformation of smectite at 80 and 300 °C in the presence of Fe-oxides. Clay Minerals, 39, 17 – 34.

Gunnarsson, I., Arnorsson, S. (2000): Amorphous silica solubility and the thermodynamic properties of H4SiO4 in the range of 0° to 350° C at Psat. Geochim. Cosmochim. Acta 64, 2295 – 2307.

Guo, W. & Eiler, J.M. (2007): Temperatures of aqueous alteration and evidence for methane generation on the parent bodies of the CM chondrites. Geochimica et Cosmochimica Acta, 71, 5565 – 5575.

Güven, N. (1988): Smectites. In: Bailey, S.W. (ed.): Hydrous phyllosilicates (exclusive of micas). Reviews in Mineralogy, 19, Mineralogical Society of America, 497 – 559.

Haggerty, S.E. & Toft, P.B. (1985): Native iron in the continental lower crust: Petrological and geophysical implications. Science, 229, 647 – 649.

Hellmuth, K.-H. (1991a): The existence of native iron – implications for nuclear waste management, Part I: Evidence from existing knowledge. Report STUK-B-VALO 67, Finnish Centre for Radiation and Nuclear Safety, Helsinki, Finland. 41 pp.

Hellmuth, K.-H. (1991b): The existence of native iron – implications for nuclear waste management, Part II: Evidence from investigation of samples of native iron. Report STUK-B-VALO 68, Finnish Centre for Radiation and Nuclear Safety, Helsinki, Finland. 71 pp.

Hillier, S. & Velde, B. (1992): Chlorite interstratified with a 7 Å mineral: An example from offshore Norway and possible implications for the interpretation of the composition of diagenetic chlorites. Clay Minerals, 27, 475 – 486.

Hornibrook, E.R.C. & Longstaffe, F.J. (1996): Berthierine from the Lower Cretaceous Clearwater Formation, Alberta, Canada. Clays and Clay Minerals, 44, 1 – 21.

Hugget, J.M. & Hesselbo, S.P. (2003): Low oxygen levels in earliest Triassic soils: Comment. Geology, 31, e20.

Hughes, C.R. (1989): The application of analytical transmission electron microscopy to the study of oolitic ironstones: a preliminary study. In: Young, J.P. & Taylor, W.E.G. (eds.): Phanerozoic Ironstones. Geological Society Special Publication, 46, 121 – 131.

Hummel, W., Berner, U., Curti, E., Pearson, Jr.,F.J. & Thoenen, T. (2002): Nagra/PSI Chemical Thermodynamic Data Base 01/01. Nagra Tech. Rep. NTB 02-16. Nagra, Wettingen, Switzerland and Universal Publishers/uPublish.com, Parkland, Florida, ISBN 1-58112-620-4, 565 p.

Iijima, A. & Matsumoto, R. (1982): Berthierine and chamosite in coal measures of Japan. Clays and Clay Minerals, 30, 264 – 274.

Inagaki, Y., Ogata, A., Furuya, H., Idemitsu, K., Banba, T. & Maeda, T. (1996): Effects of redox condition on waste glass corrosion in the presence of magnetite. In: Scientific Basis for Nuclear Waste Management XIX, W.M. Murphy and D.A. Knecht, eds., Mat. Res. Soc. Proc. Vol. 412, 257 – 264.

Ishidera, T., Ueno, K., Kurosawa, S. & Suyama, T. (2008): Investigation of montmorillonite alteration and form of iron corrosion products in compacted bentonite in contact with carbon steel for ten years. Physics and Chemistry of the Earth, 33, S269 – S275.

Janeczek, J. & Ewing, R.C. (1992): Coffinitization – a mechanism for the alteration of UO2 under reducing conditions. Mat. Res. Soc. Symp. Proc. 257, 497 – 504.

Jiang, W.-T., Peacor, D.R. & Slack, J.F. (1992): Microstructures, mixed layering, and polymorphism of chlorite and retrograde berthierine in the Kidd Creek massive sulfide deposit, Ontario. Clays and Clay Minerals, 40, 501 – 514.

Johnson, L.H. & King, F. (2003): Canister Options for the Disposal of Spent Fuel. Nagra Tech. Rep. NTB 02-11. Nagra, Wettingen, Switzerland.

Johnson, L.H. & McGinnes, D.F. (2002): Partitioning of radionuclides in Swiss power reactor fuels. Nagra Tech. Rep. NTB 02-07. Nagra, Wettingen, Switzerland.

Johnson, L.H. & Shoesmith, D.W. (1988): Spent Fuel. In: W. Lutze and R.C. Ewing, Eds.: Radioactive Waste Forms for the Future, North-Holland, pp. 635 – 698.

Johnson, L.H. (2014): A model for radionuclide release from spent UO_2 and MOX fuel. Arbeitsbericht NAB 13-37. Nagra, Wettingen, Switzerland.

Johnson, L.H., Ferry, C., Poinssot, Ch. & Lovera, P. (2005): Spent fuel radionuclide source-term model for assessing spent fuel performance in geological disposal. Part I: Assessment of the instant release fraction. J. Nucl. Mat. 346, 56 – 65.

Johnson, L.H., Ferry, C., Schumacher, S., Martin, A., Grambow, B., Martinez-Esparza Valiente, A. & Quinone, J. (2008b): Assessment of uncertainties associated with SF dissolution models from a performance assessment perspective. Deliverable 4.2, MICADO project, Sixth Framework Programme, European Commission, Brussels, Belgium (also available as Nagra report).

Johnson, L.H., Günther-Leopold, I., Kobler Waldis, J., Linder, H.P., Low, J., Cui, D., Ekeroth, E., Spahiu, K. & Evins L.Z. (2012): Rapid aqueous release of fission products from high burn-up LWR fuel: Experimental results and correlations with fission gas release. J. Nucl. Mat. 420, 54 – 62.

Johnson, L.H., Marschall, P., Wersin, P. & Gribi, P. (2008a): HMCBG processes related to the steel components in the KBS-3H disposal concept. SKB Rapport R-08-25, SKB, Stockholm, Sweden.

Johnson, L.H., Niemeyer, M., Klubertanz, G., Siegel, P., Gribi, P. (2002): Calculations of the temperature evolution of a repository for spent fuel, vitrified high-level waste and intermediate level waste in Opalinus Clay. Nagra Tech. Rep. NTB 01-04. Nagra Wettingen, Switzerland.

Jordan, N., Marmier, N., Lomenech, C., Giffaut, E., Ehrhardt, J.-J.(2007): Sorption of silicates on goethite, hematite, and magnetite: Experiments and modelling, J. Coll. Int. Sci. 312, 224 – 229.

Jougnot, D. & Revil, A. (2007): Diffusion of ions in unsaturated cla-rocks: Theory and application ot the Callovo-oxfordian argillite, in Proceedings of international meeting, September 17 – 18, 2007, Lille France: Clays in natural & engineered barriers for radioactive waste confinement, pp. P/MTPM/3, 427 – 428, Andra.

Jullien, M., Raynal, J., Kohler, E. & Bildstein, O. (2005): Physicochemical reactivity in clay-rich materials: Tools for safety assessment. Oil & Gas Science and Technology, 60, 107 – 120.

Kamei, G., Oda, C., Mitsui, S., Shibata, M. & Shinozaki, T. (1999): Fe(II)-Na ion exchange at interlayers of smectite: adsorption-desorption experiments and a natural analogue. Engineering Geology, 54, 15 – 20.

Karnland, O., Birgersson, M. (2006): Montmorillonite stability with special respect to KBS-3 conditions. SKB Technical Report TR-06-11. Stockholm, Sweden.

Karnland, O., Nilsson, U., Weber, H.P., Wersin, P. (2007): Sealing ability of Wyoming bentonite pellets foreseen as buffer material – Laboratory results. Nagra Working Report. NAB 07-023. Nagra, Wettingen.

Karpov, I.K., Chudnenko, K.V., Kulik, D.A., Avchenko, O.V. & Bychinskii, V.A. (2001): Minimization of Gibbs free energy in geochemical systems by convex programming. Geochem. Int. 39, 1108 – 1119.

KEG (2003): Kernenergiegesetz vom 21.03.2003 (KEG). Systematische Sammlung des Bundesrechts SR 732.1, Schweiz.

Keren, R. & Mezuman, U. (1981): Boron adsorption by clay minerals using a phenomenological equation. Clays Clay Miner. 29, 198 – 204.

Kohyama, N., Shimoda, S. & Sudo, T. (1973): Iron-rich saponite (ferrous and ferric forms). Clays and Clay Minerals, 21, 229 – 237.

Kolaříková, I., Švandová, J., Přikryl, R., Vinšová, H., Jedináková-Křížová, V., Zeman, J. (2010): Mineralogical changes in bentonite barrier within Mock-Up-Cz experiment. Applied Clay Science 47, 10 – 15.

Kosakowski G. & Berner U. (2011): Influence of a concrete liner on the evolution of the near field of a HLW repository. PSI Internal Report AN-44-10-09-Rev1. Paul Scherrer Institut, Villigen, Switzerland.

Kosakowski, G. & Berner U. (2013): The evolution of clay rock/cement interfaces in a cementitious repository for low- and intermediate level radioactive waste. Phys. Chem. Earth, Parts A/B/C, 64, 65 – 86. doi:10.1016/j.pce.2013.01.003.

Kosakowski, G., Berner, U., Wieland, E., Glaus, M. & Degueldre, C. (2014): Geochemical Evolution of the L/ILW Near-Field. Nagra Tech. Rep. NTB 14-11. Nagra, Wettingen, Switzerland.

Kosakowski, G., Blum, P., Kulik, D.A. & Pfingsten, W. (2009): Evolution of a generic clay/cement interface: First reactive transport calculations utilizing a Gibbs energy minimization based approach for geochemical calculations, Journal of Environmental Science for Sustainable Society, 3(March), 41 – 49.

Kulik, D.A. (2002): Gibbs energy minimization approach to modeling sorption equilibria at the mineral-water interface: Thermodynamic relations for multi-site-surface complexation. Am. J. Sci. 302, 227 – 279.

Kurashige, T., Fujisawa, R., Inagaki, Y. & Senoo, M. (1999): Gas generation behavior of Zircaloy -4 under waste disposal conditions. In: Proceedings of the 7th International Conference on Radioactive Waste Management and Environmental Remediation, September 26 – 30, 1999 Nagoya, Japan, ASME.

Kursten, B., Cornelis, B., Labat, S. & Van Iseghem, P. (1997): Completion of the corrosion programme in Boom Clay – in situ experiments. European Atomic Energy Community's shared cost programme (1990-94) on ‘Management and storage of radioactive waste' Task 3, EUR 17105 EN, European Commission.

Landolt, D., Davenport, A., Payer, J. & Shoesmith, D. (2009): A review of materials and corrosion issues regarding canisters for disposal of spent fuel and high-level waste in Opalinus clay. Nagra Tech. Rep. NTB 09-02. Nagra, Wettingen, Switzerland.

Lantenois, S., Lanson, B., Muller, F., Bauer, A., Julien, M. & Plançon, A. (2005): Experimental study of smectite interaction with metal Fe at low temperature: 1. Smectite destabilization. Clays and Clay Minerals, 53, 597 – 612.

Lee, J.O., Kang, I.M., Cho, W.J. (2010): Smectite alteration and its influence on the barrier properties of smectite clay for a repository. Applied Clay Science 47, 99 – 104.

Lemmens, K. (2001): The effect of clay on the dissolution of nuclear waste glass. J. Nucl. Mat. 298, 11 – 18.

Leupin, O. & Johnson, L. (2013): Buffer requirements for a SF/HLW Repository in Opalinus Clay. NAB 13-46, Nagra, Wettingen, Switzerland.

Loida, A., Metz, V., Kienzler, B. & Geckeis, H. (2005): Radionuclide release from high burnup spent fuel during corrosion in salt brine in the presence of hydrogen overpressure. J. Nucl. Mat. 346, 24 – 31.

Luna, M, Arcos, D, & Duro, L, (2006): Effects of grouting, shotcreting and concrete leachates on backfill geochemistry. SKB Report R-06-107. SKB, Stockholm.

Luo, J.S., Abrajano, T.A. & Ebert, W.L. (1998): Natural Analogues of Nuclear Waste Glass Corrosion. Argonne National Laboratory, ANL-98/22.

Lutze, W., Malow, G., Ewing, R.C., Jercinovic, M.J., Keil, K. (1985): Alteration of basalt glasses: implications for modelling the long-term stability of nuclear waste glasses. Nature, 314, 252 – 255.

Mäder, U. (2009): Reference pore water for the Opalinus Clay and "Brown Dogger" for the provisional safety-analysis in the framework of the sectoral plan – Interim results (SGT-ZE). Nagra Working Report NAB 09-14. Nagra, Wettingen, Switzerland.

Mäder, U.K., Fierz, T., Frieg, B., Eikenberg, J., Ruthi, M., Albinsson, Y., Moeri, A., Ekberg, S. & Stille, P. (2006): Interaction of hyperalkaline fluid with fractured rock: Field and laboratory experiments of the HPF project (Grimsel Test Site, Switzerland), Journal of Geochemical Exploration, 90(1-2), 68 – 94.

Madsen, F.T. (1998): Clay mineralogical investigations related to nuclear waste disposal. Clay Minerals, 33, 109 – 129.

Malow, G., Lutze, W., Ewing, R.C. (1984): Alteration effects and leach rates of basaltic glasses: Implications for the long-term stability of nuclear waste form borosilicate glasses. J. Non-Cryst. Solids 67, 305 – 321.

Martin, F.A., Bataillon, C. & Schlegel, M.L. (2008): Corrosion of iron and low alloyed steel within a water saturated brick of clay under anaerobic deep geological disposal conditions: An integrated experiment. Journal of Nuclear Materials, 379, 80 – 90.

Martin, G., Maillard, S., Van Brutzel, L., Garcia, P., Dorado, B. & Valot, C. (2009): A molecular dynamics study of radiation induced diffusion in uranium dioxide. J. Nucl. Mat. 385, 351 – 357.

Marty, N.C.M., Fritz, B., Clément, A. & Michau, N. (2010): Modelling the long term alteration of the engineered bentonite barrier in an underground radioactive waste repository, Applied Clay Science, 47(1-2), 82 – 90.

Marty, N.C.M., Tournassat, C., Burnol, A., Giffaut, E. & Gaucher, E.C. (2009): Influence of reaction kinetics and mesh refinement on the numerical modelling of concrete/clay interactions, Journal of Hydrology, 364(1-2), 58 – 72.

Matschei, T., Lothenbach, B. & Glasser, F.P. (2007): Thermodynamic properties of Portland cement hydrates in the system CaO-Al_2O_3-SiO_2-$CaSO_4$-$CaCO_3$-H_2O, Cement and Concrete Research, 37(10), 1379 – 1410.

Matzke, H. (1997): Alpha self-irradiation of waste glasses: state of the knowledge. In: Glass, Proceedings of the summer workshop held in Méjannes-Le-Clap, Aug. 31 – Sept. 7, 1997, Commissariat à l'Energie Atomique (CEA), France, 149 – 166.

McGinnes, D.F. (2002): Model Radioactive Waste Inventory for Reprocessing Waste and Spent Fuel. Nagra Tech. Rep. NTB 01-01. Nagra, Wettingen, Switzerland.

McGrail, B.P., Bacon, D.H., Icenhower, J.P., Mann, F.M., Puigh, R.J., Schaef, H.T. & Mattigod, S.V. (2001): Near-Field Performance Assessment for a Low-Activity Waste Glass Disposal System: Laboratory Testing to Modeling Results. J. Nucl. Mater. 298, 95-111.

McVay, G.L. & Buckwalter, G.Q. (1983): Effect of iron on waste glass leaching. J. Am. Ceram. Soc. 66, 170 – 174.

Metcalfe, R., & Walker, C. (2004). Proceedings of the International Workshop on Bentonite-Cement Interaction in Repository Environments, 14-16 April 2004, Tokyo, Japan. Technical Report NUMO-TR-04-05. p. 190, Nuclear Waste Management Organization of Japan (NUMO), Tokyo, Japan.

Milodowski, A.E., Cave, M.R., Kemp, S.J., Taylor, H., Green, K., Williams, C.L., Shaw, R.A., Gowing, C.J.B. & Eatherington, N.D. (2009a): Mineralogical investigations of the interaction between iron corrosion products and bentonite from the NF-PRO Experiments (Phase 2). SKB Technical Report TR-09-03. SKB, Svensk Kärnbränslehantering AB, Stockholm, Sweden.

Milodowski, A.E., Cave, M.R., Kemp, S.J., Taylor, H., Vickers, B.P., Green, K.A., Williams, C.L. & Shaw, R.A. (2009b): Mineralogical investigations of the interaction between iron corrosion products and bentonite from the NF-PRO Experiments (Phase 1). SKB Technical Report TR-09-02. SKB, Svensk Kärnbränslehantering AB, Stockholm, Sweden. 56 pp.

Minet, Y., Jollivet, P., Godon, N., Lartigue, J.E., Mestre, J.P., Petit, S. & Gin, S. (2008): Final activity report of CEA for WP1.2 (Joint modular integral material experiment) NF-PRO project, Deliverable 1.2.7 of RTD component 1, European Commission (Contract F16W-CT-2003-02389), 81 p.

Minne, J.B., Desgranges, L. Optasanu, V., Largenton, N., Raceanu, L. & Montesin, T. (2012): Specific Aspects of Internal Corrosion of Nuclear Clad made of Zircaloy, Defect and Diffusion Forum Vols. 323-325, 227-232.

Moench, R.H. (1962): Properties and paragenesis of coffinite from the Woodrow mine, New Mexico, Am. Min. 47, 26 – 33.

Molins, S. & Mayer, K.U. (2007): Coupling between geochemical reactions and multicomponent gas and solute transport in unsaturated media: A reactive transport modeling study, Water Resources Research, 43(5), 1 – 16.

Montes-Hernandez, G., Fritz, B., Clement, A. & Michau, N. (2005a): A simplified method to evaluate the swelling capacity evolution of a bentonite barrier related to geochemical transformations. Applied Geochemistry, 20, 409 – 422.

Montes-Hernandez, G., Marty, N., Fritz, B., Clement, A. & Michau, N. (2005b): Modelling of long-term diffusion-reaction in a bentonite barrier for radioactive waste confinement. Applied Clay Science, 30, 181 – 198.

Mosser-Ruck, R., Cathelineau, M., Guillaume, D., Charpentier, D., Rousset, D., Barres, O. & Michau, N. (2010): Effects of temperature, pH, and iron/clay and liquid/clay ratios on experimental conversion of dioctahedral smectite to berthierine, chlorite, vermiculite, or saponite. Clays and Clay Minerals, 58, 280 – 291.

Müller-Vonmoos, M. & Kahr, G. (1983): Mineralogische Untersuchungen von Wyoming Bentonite MX-80 und Montigel. Nagra Tech. Rep. NTB 83-12. Nagra, Wettingen, Switzerland.

Müller-Vonmoos, M., Kahr, G., Bucher, F., Madsen, F. & Mayor, P.-A. (1991): Untersuchungen zum Verhalten von Bentonit in Kontakt mit Magnetit und Eisen unter Endlagerbedingungen. Nagra Tech. Rep. NTB 91-14. Nagra, Wettingen, Switzerland.

Nagra (2002a): Project Opalinus Clay: Safety Report. Demonstration of disposal feasibility for spent fuel, vitrified high-level waste and long-lived intermediate-level waste (Entsorgungsnachweis). Nagra Tech. Rep. NTB 02-05. Nagra, Wettingen, Switzerland.

Nagra (2002b): Projekt Opalinuston: Synthese der geowissenschaftlichen Untersuchungsergebnisse. Nagra Tech. Rep. NTB 02-03. Nagra, Wettingen, Switzerland.

Nagra (2005): Spent Fuel Evolution under Disposal Conditions. Synthesis of Results from the EU Spent Fuel Stability (SFS) Project. Nagra Tech. Rep. NTB 04-09. Nagra, Wettingen, Switzerland.

Nagra (2008): Vorschlag geologischer Standortgebiete für das SMA- und das HAA-Lager. Darlegung der Anforderungen des Vorgehens und der Ergebnisse. Nagra Tech. Rep. NTB 08-03. Nagra, Wettingen, Switzerland.

Nagra (2010): Beurteilung der geologischen Unterlagen für die provisorische Sicherheitsanalyse in SGT Etappe 2 – Klärung der Notwendigkeit ergänzender geologischer Untersuchungen. Nagra Tech. Rep. NTB 10-01. Nagra Wettingen, Switzerland.

Nagra (2013): Modellhaftes Inventar für radioaktive Materialien – MIRAM 12. Nagra Working Report NAB 13-39. Nagra, Wettingen, Switzerland.

Nagra (2014a): SGT Etappe 2: Vorschlag weiter zu untersuchender geologischer Standortgebiete mit zugehörigen Standortarealen für die Oberflächenanlage. Charakteristische Dosisintervalle und Unterlagen zur Bewertung der Barrierensysteme. Nagra Tech. Ber. NTB 14-03. Nagra, Wettingen, Switzerland.

Nagra (2014b): Modellhaftes Inventar für radioaktive Materialien – MIRAM 14. Nagra Tech. Rep. NTB 14-04. Nagra Wettingen, Switzerland.

Nasrazadani, S. & Raman, A. (1993): Formation and transformation of magnetite (Fe_3O_4) on steel surfaces under continuous and cyclic water fog testing. Corrosion 49(4), 294 – 300.

Neff, D., Dillmann, P., Descostes, M. & Berger, G. (2006): Corrosion of iron archaeological artefacts in soil: Estimation of the average corrosion rates involving analytical techniques and thermodynamic calculations. Corrosion Science, 48, 2947 – 2970.

Neff, D., Saheb, M., Monnier, J., Perrin, S., Descostes, M., L'Hostis, V., Crusset, D., Millard, A. & Dillmann, P. (2010): A review of the archaeological analogue approaches to predict the long-term corrosion behaviour of carbon steel overpack and reinforced concrete structures in the French disposal systems. Journal of Nuclear Materials, 402, 196 – 205.

Odin, G.S. (1990): Clay mineral formation in the continent-ocean boundary: The verdine facies. Clay Minerals, 25, 477 – 483.

Olin, Å., Noläng, B., Osadchii, E.G., Öhman, L.-O. Rosén, E. (2005): Chemical Thermodynamics of Selenium. F.J. Mompean, J. Perrone and M. Illemassène (Eds.), Chemical Thermodynamics Vol. 7, NEA-OECD, Elsevier, Amsterdam.

Ollila, K. (2007): EU NF-PRO Project FI6W-CT-2003-02389. Deliverable 1.5.21, European Commission, Brussels, Belgium. NF-PRO FI6W-CT-2003-02389.

Ollila, K. (2008): Dissolution of Unirradiated UO_2 and UO_2 Doped with ^{233}U in Low- and High-Ionic-Strength NaCl under Anoxic and Reducing Conditions. Posiva working rep. 2008-50, POSIVA OY, Olkiluoto, Finnland.

Oscarson, D.W. & Heimann, R.B. (1988): The effect of an Fe(II)-silicate on selected properties of a montmorillonitic clay. Clay Minerals, 23, 81 – 90.

Palandri, J.L. & Kharaka, Y.K. (2004): A compilation of rate parameters of water-mineral interaction kinetics for application to geochemical modeling, Open File Report 2004-1068, U.S. Geological Survey, Menlo Park, California.

Papafotiou, A. & Senger, R. (2014): Sensitivity analyses of gas release from a SF/HLW repository in the Opalinus Clay in the candidate siting regions of Northern Switzerland. Nagra Working Report NAB 14-10. Nagra, Wettingen, Switzerland.

Papillon, F., Jullien, M. & Bataillon, C. (2003): Carbon steel behaviour in compacted clay: two long term tests for corrosion prediction. In: Féron, D. & MacDonald, D.D. (eds.): Prediction of the long-term corrosion behaviour in nuclear waste systems. European Federation of Corrosion Publications, 36, Maney Publishing, UK, 439 – 454.

Patel R., Punshon C., Nicholas J., Bastid P., Zhou R., Schneider C., Bagshaw N., Howse D., Hutchinson E., Asano R., King F. (2012): Canister Design Concepts for Disposal of Spent Fuel and High Level Waste. Nagra Tech. Rep. NTB 12-06. Nagra Wettingen, Switzerland.

Pearson, F.J., Arcos, D., Bath, A., Boisson, J.-Y., Fernandez, A.M., Gäbler, H.-E., Gaucher, E., Gautschi, A., Griffault, L., Hernan, P. & Waber, H.N. (2003): Mont Terri project – Geochemistry of water in the Opalinus Clay formation at the Mont Terri Rock Laboratory. In: F.O.W.G. (Ed.), Geology Series No. 5, Bern.

Pearson, F.J., Tournassat, C. & Gaucher, E.C. (2011): Biogeochemical processes in a clay formation in situ experiment: Part E – Equilibrium controls on chemistry of pore water from the Opalinus Clay, Mont Terri Underground Research Laboratory, Switzerland, Applied Geochemistry, 26(6), 990 – 1008.

Perronnet, M. (2004): Réactivité des matériaux argileux dans un contexte de corrosion métallique. Ph.D. Thesis, Institut National Polytechnique de Lorraine, Nancy, France, 280 pp.

Perronnet, M., Jullien, M., Villiéras, F., Raynal, J., Bonnin, D. & Bruno, G. (2008): Evidence of a critical content in Fe(O) on FoCa7 bentonite reactivity at 80 °C. Applied Clay Science, 38, 187 – 202.

Pfingsten, W., Bradbury, M.H. & Baeyens, B. (2011): The influence of Fe(II) competition on the sorption and migration of Ni(II) in MX-80 Bentonite. Applied Geochemistry, 26, 1414 – 1422.

Pieper, H., Bosbach, D., Panak, P.J., Rabung, T. & Fanghänel, T. (2006): Eu(III) coprecipitation with the trioctahedral clay mineral, hectorite. Clays Clay Min. 54,45 – 53.

Pierron, O.N., Koss, D.A., Motta, A.T. & Chan, K.S. (2003): The influence of hydride blisters on the fracture of Zircaloy-4. J. Nucl. Mat. 322, 21 – 35.

Pipon, Y., Toulhoat, N., Moncoffre, N., Bererd, N., Jaffrezic, H., Barthe, M-F., Desjardin, P., Raimbault, L., Scheidegger, A.M., Carlot, G. (2007b): Chlorine diffusion in uranium dioxide: Thermal effects versus radiation enhanced effects. Mat. Res. Soc. Symp. Proc. Vol. 985, 77 – 82.

Pipon, Y., Toulhoat, N., Moncoffre, N., Raimbault, L., Scheidegger, A.M., Farges, F., Carlot, G. (2007a): Thermal diffusion of chlorine in uranium dioxide studied by secondary ion mass spectrometry and X-ray absorption spectroscopy. J. Nucl. Mat. 362, 416 – 425.

Pistiner, J.S. & Henderson, G.M. (2003): Lithium isotope fractionation during continental weathering processes. Earth and Planetary Science Letters 214, 327 – 339.

Porrenga, D.H. (1967): Glauconite and chamosite as depth indicators in the marine environment. Marine Geology, 5, 495 – 501.

Pusch, R. & Yong, R.N. (2006): Microstructure of smectite clays and engineering performance. Taylor & Francis, Oxon and New York, 337 p.

Pusch, R., Bluemling, P., Johnson, L. (2003): Performance of strongly compressed MX-80 pellets under repository-like conditions. Applied Clay Science 23, 239 – 244.

Pusch, R., Karnland, O., Lajudie, A., Lechelle, J., Bouchet, A. (1992): Hydrothermal field test with French candidate clay embedding steel heater in the Stripa mine. SKB Technical Report TR-93-02, Stockholm, Sweden.

Pusch, R., Kasbohm, J., Thao, H.T.M. (2010): Chemical stability of montmorillonite buffer clay under repository-like conditions – A synthesis of relevant experimental data. Applied Clay Science 47, 113 – 119.

Putnis, A. & Putnis, Ch. V. (2007): The mechanism of reequilibration of solids in the presence of a fluid phase. J. Solid State Chem. 180, 1783 – 1786.

Putnis, A. (2009): Mineral Replacement Reactions. In Thermodynamics and Kinetics of Water-Rock Interaction. Reviews in Mineralogy & Geochemistry (eds. Oelkers, E.H. & Schott, J.), vol. 70, Min. Soc. Am., 87 – 124.

Rondinella, V.V., Cobos, J., Matzke, H.J., Wiss, T., Carbol, P. & Solatie, D. (2001): Leaching behaviour and α-decay damage accumulation of UO_2 containing short-lived actinides, Mat. Res. Soc. Symp. Proc., Vol. 663, 391 – 398.

Ryan, P.C. & Reynolds Jr., R.C. (1996): The origin and diagenesis of grain-coating serpentine-chlorite in Tuscaloosa Formation sandstone, U.S. Gulf Coast. American Mineralogist, 81, 213 – 225.

Saheb, M., Neff, D., Dillmann, P., Matthiesen, H. & Froy, E. (2008): Long-term corrosion behaviour of low-carbon steel in anoxic environment: Characterization of archaeological artefacts. Journal of Nuclear Materials, 379, 118 – 123.

Samper, J., Lu, C. & Montenegro, L. (2008): Reactive transport model of interactions of corrosion products and bentonite. Physics and Chemistry of the Earth, Vol.33 Suppl.1, S306-S316.

Saripalli, K., Meyer, P., Bacon, D. & Freedman, V. (2001): Changes in hydrologic properties of aquifer media due to chemical reactions: a review, Critical Reviews in Environmental Science and Technology, 31(4), 311 – 349.

Sauzéat, E., Guillaume, D., Neaman, A., Pfeiffert, C., Ruck, R., Dubessy, J., Cathelineau, M., Villiéras, F. & Yvon, J. (2002): Caractérisation minéralogique, cristallochimique et texturale de l'argile MX-80. Rapport ANDRA C. RP. 0LEM 01-001.

Savage, D. (2009): Forge(D3.1-R): A review of experimental evidence for the development and properties of cement-bentonite interfaces with implications for gas transport, Nagra Working Report NAB 09-30. Nagra, Wettingen, Switzerland.

Savage, D. (2011): A review of analogues of alkaline alteration with regard to long-term barrier performance, Mineralogical Magazine, 75(4), 2401 – 2418.

Savage, D., Benbow, S., Watson, C., Takase, H., Ono, K., Oda, C., & Honda, A. (2010b): Natural systems evidence for the alteration of clay under alkaline conditions: An example from Searles Lake, California. Applied Clay Science, 47, 72 – 81.

Savage, D., Noy, D. & Mihara, M. (2002): Modelling the interaction of bentonite with hyperalkaline fluids, Applied Geochemistry, 17, 207 – 223.

Savage, D., Walker, C. & Benbow, S. (2010a): An analysis of potential changes to barrier components due to interaction with a concrete liner in a repository for SF/HLW in Opalinus Clay, Nagra Working Report NAB 10-17. Nagra, Wettingen, Switzerland.

Savage, D., Walker, C., Arthur, R., Rochelle, C.A., Oda, C. & Takase, H. (2007): Alteration of bentonite by hyperalkaline fluids: A review of the role of secondary minerals, Physics and Chemistry of the Earth, Parts A/B/C, 32(1-7), 287 – 297.

Savage, D., Watson, C., Benbow, S. & Wilson, J. (2010c): Modelling iron-bentonite interactions. Applied Clay Science, 47, 91 – 98.

Schenk, R. (1988): Untersuchungen über die Wasserstoffbildung durch Eisenkorrosion unter Endlagerbedingungen. Nagra Tech. Rep. NTB 86-24. Nagra, Wettingen, Switzerland.

Schlegel, M.L., Bataillon, C., Benhamida, K., Blanc, C., Menut, D. & Lacour, J.-L. (2008): Metal corrosion and argillite transformation at the water-saturated, high-temperature iron-clay interface: A microscopic-scale study. Applied Geochemistry, 23, 2619 – 2633.

Schlegel, M.L., Bataillon, C., Blanc, C., Pret, D. & Foy, E. (2010): Anodic activation of iron corrosion in clay media under water-saturated conditions at 90 °C: Characterization of the corrosion interface. Environmental Science & Technology, 44, 1503 – 1508.

Senger, R., Ewing, J. (2008): Evolution of temperature and water content in the bentonite buffer: Detailed modelling of two-phase flow processes associated with the early closure period, Nagra Working Report NAB 08-32. Nagra, Wettingen, Switzerland.

Senger, R., Marschall, P. & Finsterle, S. (2008): Investigation of two-phase flow phenomena associated with corrosion in an SF/HLW repository in Opalinus Clay, Switzerland. Phys. Chem. Earth 33, S317 – S326.

Senger, R., Papafotiou, A. & Marschall, P. (2014): Thermo-hydraulic simulations of the near-field of a SF/HLW repository during early- and late-time post-closure period. Nagra Working Report NAB 14-11. Nagra, Wettingen, Switzerland.

Shao, H., Dmytrieva, S.V., Kolditz, O., Kulik, D.A., Pfingsten, W. & Kosakowski, G. (2009): Modeling reactive transport in non-ideal aqueous-solid solution system, Applied Geochemistry, 24(7), 1287 – 1300.

Shoesmith, D.W. (2000): Fuel corrosion processes under waste disposal conditions. J. Nucl. Mat. 282, 1 – 31.

Shoesmith, D.W. (2003): Used fuel and uranium dioxide dissolution studies – A review. Technical Report NWMO TR-2007-03. Nuclear Waste Management Organization, Toronto, Canada.

Shoesmith, D.W. (2008): The role of dissolved hydrogen on the corrosion/dissolution of spent fuel. Technical Report NWMO TR-2008-19. Nuclear Waste Management Organization, Toronto, Canada.

Shoesmith, D.W., Sunder, D. & Tait, J.C. (1998): Validation of an electrochemical model for the oxidative dissolution of used CANDU fuel. J. Nucl. Mat. 257, 89 – 98.

Simpson, J.P. & Wallotton, P.-H. (1986): Experiments on Container Materials for Swiss High-Level Waste Disposal Projects, Part III. Nagra Tech. Rep. NTB 86-25. Nagra, Wettingen, Switzerland.

Simpson, J.P. (1983): Experiments on Container Materials for Swiss High-Level Waste Disposal Projects, Part I. Nagra Tech. Rep. NTB 83-05. Nagra, Wettingen, Switzerland.

Simpson, J.P. (1984): Experiments on Container Materials for Swiss High-Level Waste Disposal Projects, Part II. Nagra Tech. Rep. NTB 84-01. Nagra, Wettingen, Switzerland.

Simpson, J.P. (1989): Experiments on Container Materials for Swiss High-Level Waste Disposal Projects, Part IV. Nagra Tech. Rep. NTB 89-19. Nagra, Wettingen, Switzerland.

SKB (2009): Long term test of buffer material at the Äspö Hard Rock Laboratory, LOT project. Final report on the A2 test parcel. SKB Technical Report TR-09-29. Stockholm, Sweden.

Smart, N.R., Blackwood, D.J. & Werme, L. (2001): The anaerobic corrosion of carbon steel and cast iron in artificial groundwaters. Technical Report TR-01-22. Swedish Nuclear Fueland Waste Management Co (SKB), Stockholm, Sweden, p. 26.

Smellie J. & Karlsson F. (1996): A reappraisal of some Cigar Lake issues of importance to performance assessment, SKB Technical Report TR-96-08. SKB, Stockholm, Sweden.

Smellie, J. (1998): Maqarin natural analogue study: Phase III, SKB Technical Report TR-98-04. SKB, Stockholm, Sweden.

Smith, R.M., Martell, A.E. (1989): Critical Stability Constants, Vol. 6, New York: Plenum Press.

Steefel, C. & Lichtner, P. (1994): Diffusion and reaction in rock matrix bordering a hyperalkaline fluid-filled fracture, Geochimica et Cosmochimica Acta, 58(17), 3595 – 3612.

Steefel, C. & Lichtner, P. (1998): Multicomponent reactive transport in discrete fractures – II: Infiltration of hyperalkaline groundwater at Maqarin, Jordan, a natural analogue site, Journal of Hydrology, 209(1-4), 200 – 224.

Stucki, J.W. (2006): Properties and behaviour of iron in clay minerals. In: Bergaya, F., Theng, B.K.G. & Lagaly, G. (eds.): Handbook of Clay Science. Developments in Clay Science, 1, Elsevier, 423 – 475.

Tagirov, B., Schott, J., Harrichoury & J.C., Escalier, J. (2004): Experimental study of the stability of aluminate-borate complexes in hydrothermal solutions. Geochim. Cosmochim. Acta 68, 1333 – 1345.

Tait, J.C., Cornett, R.J.J., Chant, L.A., Irovec, J.J., McConnell, J. & Wilkin, D.L. (1997): Determination of Cl impurities and 36Cl instant release from used CANDU fuels, in Mat. Res. Soc. Symp. Proc., 465, 503 – 510.

Taylor, H. F. W. (1997): Cement Chemistry (2nd. ed.). Thomas Telford, London, UK.

Taylor, K.G. (1990): Berthierine from the non-marine Wealden (Early Cretaceous) sediments of south-east England. Clay Minerals, 25, 391 – 399.

Techer, I., Advocat, T., Lancelot, J. & Liotard, J.M. (2000): Basaltic glass: alteration mechanisms and analogy with nuclear waste glasses, J. Nucl. Mat. 282, 40 – 46.

Techer, I., Bartier, D., Boulvais, P., Tinseau, E., Suchorski, K., Cabrera, J. & Dauzères, A. (2012): Tracing interactions between natural argillites and hyper-alkaline fluids from engineered cement paste and concrete: Chemical and isotopic monitoring of a 15-years old deep-disposal analogue, Applied Geochemistry, 27(7), 1384 – 1402.

Thien, B.M.J. (2010): Développement des bases théoriques nécessaires à la modélisation de la vitesse résiduelle d'altération en milieux aqueux des verres nucléaires AVM. Ph.D. Thesis, Univ. Montpellier II, France.

Thien, B.M.J., Godon, N., Ballestrero, A., Gin, S. & Ayral, A. (2012): The dual effect of Mg on the long-term alteration rate of AVM nuclear waste glasses, J. Nucl. Mat. 427, 297 – 310.

Thien, B.M.J., Godon, N., Hubert, F., Angeli, F., Gin, S. & Ayral, A. (2010): Structural identification of a trioctahedral smectite formed by the aqueous alteration of a nuclear glass, Applied Clay Science 49,135 – 141.

Thoenen, T., Berner, U., Hummel, W., Kulik, D. (2002): Equilibrium Constants at 50 °C for Species determining the solubility of Am, Pu, Np, U, Th and Tc in the reference Bentonite Porewater, PSI Technical Report, TM-44-02-05. Paul Scherrer Institut, Switzerland.

Thoenen, T., Hummel, W., Berner, U. & Curti, E. (2014): The PSI/Nagra Chemical Thermodynamic Database 12/07. Nagra Working Report NAB 14-49. Nagra, Wettingen, Switzerland.

Thompson, G.R. & Hower, J. (1975): The mineralogy of glauconite. Clays and Clay Minerals, 23, 289 – 300.

Tinseau, E., Bartier, D., Hassouta, L., Devol-Brown, I. & Stammose, D. (2006): Mineralogical characterization of the Tournemire argillite after in situ interaction with concretes., Waste management (New York, N.Y.), 26(7), 789 – 800.

Toth, T.A. & Fritz, S.J. (1997): An Fe-berthierine from a Cretaceous laterite: Part I. Characterization. Clays and Clay Minerals, 45, 564 – 579.

Tournassat, C., Greneche, J.-M., Tisserand, D. & Charlet, L. (2004): The titration of clay minerals. I. Discontinuous back titration technique combined with CEC measurements. Journal of Colloid and Interface Science 273, 224 – 233.

Traber, D. & Blaser, P. (2013): Gesteinsparameter der Wirtgesteine Opalinuston, 'Brauner Dogger', Effinger Schichten und Helvetische Mergel als Grundlage für die Sorptions-datenbank. Nagra Working Report NAB 12-39. Nagra, Wettingen, Switzerland.

Traber, D. & Mäder, U.K. (2006): Reactive transport modelling of the diffusive interaction between Opalinus Clay and concrete, Nagra Working Report NAB 05-06. Nagra, Wettingen, Switzerland.

Trotignon, L., Devallois, V., Peycelon, H., Tiffreau, C. & Bourbon, X. (2007): Predicting the long term durability of concrete engineered barriers in a geological repository for radioactive waste, Physics and Chemistry of the Earth, Parts A/B/C, 32(1-7), 259 – 274.

Trummer, M., Roth, O. & Jonsson, M. (2009): H_2 inhibition of radiation induced dissolution of spent nuclear fuel. J. Nucl. Mat. 383, 226 – 230.

Tumidajski, P., Schumacher, A., Perron, S., Gu, P. & Beaudoin, J. (1996): On the relationship between porosity and electrical resistivity in cementitious systems, Cement and concrete research, 26(4), 539 – 544.

Valcke, E. (2007): Integrated in situ corrosion test on α-active high-level waste (SF/HLW) glass – Phase 2 (CORALUS-2). European Commission, Contract No FIKW-CT-2000-0001. Final Report.

Van den Berg, C.M.G. (1984): Speciation of boron with Cu_2^+, Zn_2^+, Cd_2^+ and Pb_2^+. Geochim. Cosmochim. Acta 48, 2613 – 2617.

Van Loon, L.R. (2012): Estimation of anion accessible porosities of compacted bentonite to be used in performance assessment calculations. PSI Internal Report AN-44-12-01. Paul Scherrer Institut, Villigen, Switzerland.

Van Loon, L.R. (2014): Effective Diffusion Coefficients and Porosity Values for Argillaceous Rocks and Bentonite: Measured and Estimated Values for the Provisional Safety Analyses for SGT-E2. Nagra Tech. Rep. NTB 12-03. Nagra, Wettingen, Switzerland.

Van Loon, L.R., Mueller, W., Glaus, M.A. (2007): Anion exclusion effects in compacted bentonites: towards a better understanding of anion diffusion. Appl. Geochem. 22, 2536 – 2552.

Vernaz, E., Gin, S., Jégou, C. & Ribet, I. (2001): Present understanding of R7T7 glass alteration kinetics and their impact on long-term behavior modeling. J. Nucl. Mat. 298, 27 – 36.

Vernaz, E.Y. & Dussossoy, J.L. (1992): Current state of knowledge of nuclear waste glass corrosion mechanisms: the case of R7T7 glass, Appl. Geochem., Suppl. Issue No. 1, 13 – 22.

Verney-Carron, A., Gin, S. & Libourel, G. (2008): A fractured roman glass block altered for 1800 years in seawater: Analogy with nuclear waste glass in a deep geological repository. Geochim. Cosmochim. Acta 72, 5372 – 5385.

Waber, N., Schorscher, H.D. & Peters, T. (1990): Mineralogy, petrology and geochemistry of the Poços de Caldas analogue study sites, Minas Gerais, Brazil. I: Osamu Utsumi uranium mine. Nagra Tech. Rep. NTB 90-20, Nagra, Wettingen, Switzerland and TR-90-11, Swedish Nuclear Fuel, Waste Management Co (SKB), Stockholm, Sweden.

Watson, C., Benbow, S. & Savage, D. (2007): Modelling the Interaction of Low pH Cements and Bentonite Issues Affecting the Geochemical Evolution of Repositories for Radioactive Waste, SKI Report 2007:30, SKI, Stockholm, Sweden.

Watson, C., Hane, K., Savage, D., Benbow, S., Cuevas, J. & Fernandez, R. (2009): Reaction and diffusion of cementitious water in bentonite: Results of "blind" modelling, Applied Clay Science, 45(1-2), 54 – 69.

Wegen, D.H., Rondinella, V.V. et al. (2007): Deliverable 1.4.14, Final activity report, EU NF-PRO Project FI6W-CT-2003-02389. European Commission, Brussels, Belgium.

Weisberg, M.K., McCoy, T.J. & Krot, A.N. (2006): Systematics and evaluation of meteorite classification. In: Mc Sween Jr., H.Y. & Lauretta, D.S. (eds.): Meteorites and the early solar system I. The University of Arizona Press, Tucson, AZ, USA, 19 – 52.

Wellman, D.M., Parker, K.E., Powers, L., Whyatt, G.A., Clayton, L.N., Mattigod, S.V. & Wood, M.I. (2008): Effect of iron and carbonation on the diffusion of iodine and rhenium in waste encasement concrete and soil fill material under hydraulically unsaturated conditions, Applied Geochemistry, 23(8), 2256 – 2271.

Werme, L., Björner, I.K., Bart, G., Zwicky, H.U., Grambow, B., Lutze, W., Ewing, R.C. & Magrabi, C. (1990): Chemical corrosion of highly radioactive borosilicate nuclear waste glass under simulated repository conditions. J. Mater. Res. 5, 1130 – 1146.

Wersin, P., Birgersson, M., Olsson, S., Karnland, O. & Snellman, M. (2007b): Impact of corrosion-derived iron on the bentonite buffer within the KBS-3H disposal concept – the Olkiluoto site as case study. POSIVA 2007-11, Posiva Oy, Eurajoki, Finland. 69 pp.

Wersin, P., Curti, E., Appelo, C.A.J. (2004): Modelling bentonite–water interactions at high solid/liquid ratios: swelling and diffuse double layer effects. Applied Clay Science 26, 249 – 257.

Wersin, P., Johnson, L.H., McKinley, I.G. (2007a): Performance of the bentonite barrier at temperatures beyond 100 °C: A critical review. Physics and Chemistry of the Earth 32, 780 – 788.

West, J.M., Vialta, A. & McKinley, I.G. (1990): Microbiological analysis at the Osamu Utsumi mine and Morro do Ferro analogue study sites, Poços de Caldas, Brazil. Nagra Tech. Rep. NTB 90-28. Nagra, Wettingen, Switzerland.

Wilson, J., Cressey, G., Cressey, B., Cuadros, J., Ragnarsdottir, K.V., Savage, D. & Shibata, M. (2006a): The effect of iron on montmorillonite stability. (II) Experimental investigation. Geochimica et Cosmochimica Acta, 70, 323 – 336.

Wilson, J., Savage, D., Cuadros, J., Shibata, M. & Ragnarsdóttir, K.V. (2006b): The effect of iron on montmorillonite stability. (I) Background and thermodynamic considerations. Geochimica et Cosmochimica Acta, 70, 306 – 322.

Wolery, T.J. & Jove-Colon, C.F. (2004): Qualification of thermodynamic data for geochemical modeling of mineral-water interactions in dilute systems, Report ANL-WIS-GS-000003 REV 00, U.S. Department of Energy, Washington, USA.

Wu, L., Liu, N., Qin, Z. & Shoesmith, D. (2014): Modeling the Radiolytic Corrosion of Fractured Nuclear Fuel under Permanent Disposal Conditions. J. Electrochem. Soc., 161, E3259-E3266.

Xu, T. (2004): Reactive transport modeling of injection well scaling and acidizing at Tiwi field, Philippines, Geothermics, 33(4), 477 – 491.

Xu, T., Sonnenthal, E., Spycher, N. & Pruess, K. (2006): TOUGHREACT—A simulation program for non-isothermal multiphase reactive geochemical transport in variably saturated geologic media: Applications to geothermal injectivity and CO_2 geological sequestration. Computers & Geosciences, 32(2), 145 – 165.

Yamaguchi, T., Nakayama, S., Nagao, S. & Kizaki, M. (2007): Diffusive transport of neptunium and plutonium through compacted sand-bentonite mixtures under anaerobic conditions, Radiochimica Acta, 95(2), 115 – 125.

Yang, C., Samper, J. & Montenegro, L. (2008): A coupled non-isothermal reactive transport model for long-term geochemical evolution of a HLW repository in clay, Environmental Geology, 53(8), 1627 – 1638.

Zwicky, H.U., Grambow, B., Magrabi, C., Aerne, E.T., Bradley, R., Barnes, B., Graber, Th., Mohos, M. & Werme, L.O. (1989): Corrosion behaviour of British Magnox Waste Glass in pure water. Mat. Res. Soc. Proc. Vol.127, 129 – 136.

Appendix A: Conceptual setup and transport parameters for the numerical models

A1 Transport model

The reactive transport of chemical components is simulated with the multi-component reactive transport code OpenGeoSys-GEM. This code employs a sequential non-iterative approach to couple the mass transport code OpenGeoSys (http://www.ufz.de/index.php?en=18345) with the Gibbs Energy Minimization (GEM) code GEMS3K (http://gems.web.psi.ch/GEMS3K) for the thermodynamic modelling of aquatic geochemical systems. For each time step, the advection-dispersion equation is first solved for all dissolved species, and the changed composition of the phase assemblage is passed to the chemical solver which calculates the new local equilibrium at each grid node. The concentrations of dissolved chemical species are then taken as the result for this time step and used as the initial condition for the next transport step. Details regarding code development and verification can be found in Shao et al. (2009).

A2 Conceptual setup

Fig. A1 provides the model setup and dimensions. In order to minimize the code execution time, the 2D geometry of the nearfield was simplified into an axisymmetric 1D model. We did not model the full extension of the Opalinus Clay in order to minimize node numbers and calculation times. We found that positioning the right boundary at 5.6 m is enough to prevent the boundary condition influencing the system evolution near the interfaces.

In an interval of ±0.5 m around all interfaces, the distance between the finite element nodes was held constant at 0.01 m. This constant equidistant mesh makes it possible to compare the system evolution for the different cases near the interfaces. Towards the boundaries the node distance was gradually enlarged in order to minimize the number of calculation nodes. As the calculations are very time-consuming, and as the CPU time needed is linearly related to the number of nodes, the minimization of node numbers is an effective way to reduce calculation times.

All calculations were done at standard P-T conditions (1 bar, 25 ºC). The groundwater flow equation was solved at the beginning of the simulation, but only at the right boundary (Opalinus Clay). Hydraulic heads were set to a value of 10 m. The left boundary (canister) was assumed to be impermeable which causes the fluid velocities (and advective transport) to be zero. Constant concentration boundary conditions for the aqueous species were chosen for transport at the right boundary (Opalinus Clay). The left (canister) boundary was assumed to be impermeable. Initial porewater concentrations for dissolved species were in thermodynamic equilibrium with the solid phases. The corresponding systems for the three materials used in the calculations are given in Kosakowski & Berner (2013).

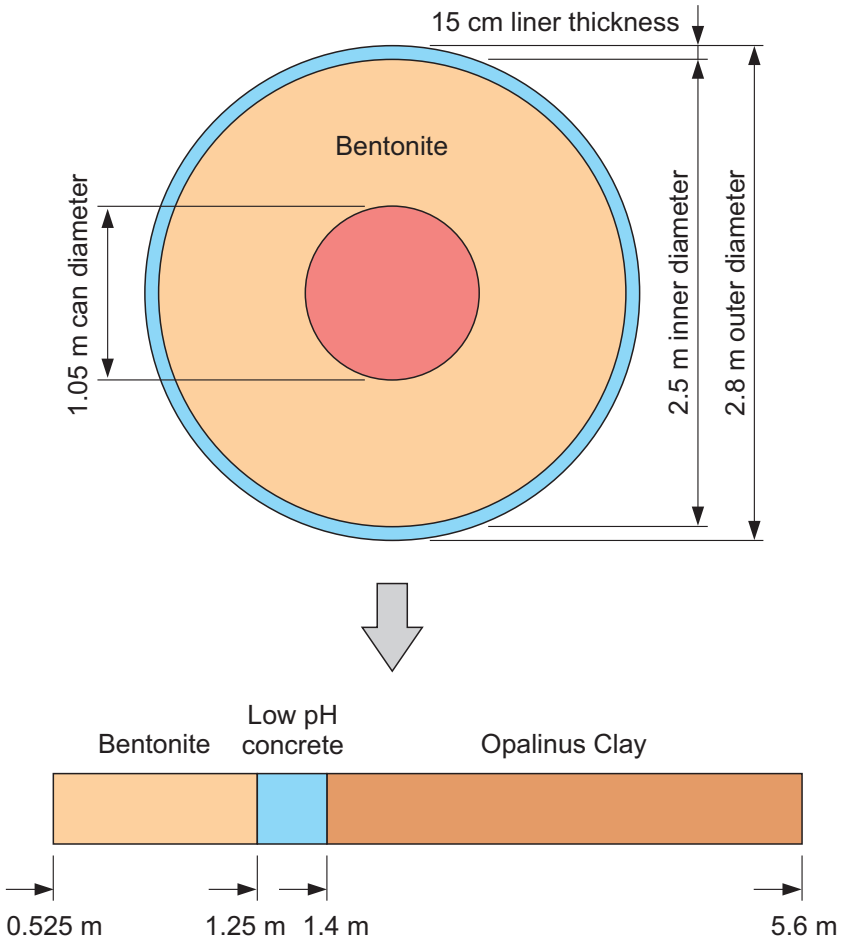

Fig. A1: Transformation of the two-dimensional near-field geometry into the axisymmetric one-dimensional conceptual model for reactive transport modeling.

The dimensions are in accordance with Nagra (2010).

A3 Porosities

Porosities of unaltered materials are given in Kosakowski & Berner (2013) for each material in accordance with Nagra (2010).

A4 Hydraulic conductivities

In these calculations we investigated cases where the transport of dissolved species is dominated by diffusion. Material parameters such as hydraulic conductivity and dispersion length were not needed since we set hydraulic heads to constant values in the whole domain which results in zero fluid velocities.

A5 Diffusion coefficients

A species independent effective diffusion coefficient D_e for all aqueous species was used for calculating the diffusive transport within OpenGeosys-GEM. It was calculated using Archie's relation from the porosity n and the free water diffusion coefficient D_0

$$D_e = D_0 n^m \quad \text{(A1)}$$

Here m is an exponent which can vary for different kinds of porous media (rock types) from 1.3 (unconsolidated sediments, e.g. sand) up to 2 in well cemented (clay-free) sediments and between 1.5 to 2.5 in cement pastes and mortars (Tumidajski et al. 1996). However, for clay rocks Van Loon (2014) estimated a mean value of m=2.4 and used the following modified relation:

$$D_e = 2 \times 10^{-9}\, n^m + 1 \times 10^{-11}\, n \quad \text{(A2)}$$

The diffusion coefficient in free water for electrolyte solutions varies between 1.1×10^{-9} m^2s^{-1} and 2.1×10^{-9} m^2s^{-1} (see Tab. 6.2-2 in Flury & Gimmi (2002)).

For our simulations we chose equation (A1) with the following parameters as "average" values for all the different materials: m = 2.0, $D_0 = 1.5 \times 10^{-9}$ m^2s^{-1} (value for 0.1 M to1.0 M NaCl, Tab. 6.2-2 in Flury & Gimmi (2002)).

The values for D_e from equation (A1) are within the lower and upper limits given in Nagra (2010) for materials that contain clays (Opalinus Clay, bentonite) and compare well with the harmonic mean of the anionic and cationic effective diffusion coefficients:

Bentonite: anion accessible porosity: 0.05,

D_e for cations in bentonite: 2.0×10^{-10} m^2s^{-1}

D_e for anions in bentonite: 2.0×10^{-12} m^2s^{-1}

Harmonic mean D_e of cations and anions in bentonite: 4.0×10^{-12} m^2s^{-1}

D_e from equation (A1): 3.75×10^{-12} m^2s^{-1}

The effective diffusion coefficient of 4.9×10^{-11} m^2s^{-1} for the low-pH concrete is in the range of 1×10^{-10} m^2s^{-1} – 1×10^{-11} m^2s^{-1} given in Section 5.2.2 of Luna et al. (2006) for similar concretes. For materials that do not contain clay (sand, mortars used for backfilling tunnels) the diffusion coefficients are too low by factors of 2-5 compared to the values given in Nagra (2010). This discrepancy cannot be avoided as we use only one porosity – diffusivity relationship to describe all the different materials in our setup. Porosity – diffusivity relationships are empirical laws that need to be tailored to each specific material. In addition, in the course of the simulations, material compositions and porosities near the interfaces may change completely. For the new material compositions, the compositional dependence of D_e on porosity is not known a priori.

A6 Geochemical setup

Our state-of-the-art geochemical model uses a single and unified thermodynamic setup for the consistent reactive modelling of mineral transformations and porosity evolution. A key feature of this geochemical setup is the fact that it simultaneously includes concretes, host rocks and tunnel backfill materials.

The geochemical setup for each material and the thermodynamic data are documented in (Berner et al. 2013, Kosakowski & Berner 2013, Tab. A1). Tab. A1 and A2 summarize the mineralogy, porosity and cation exchange properties of the bentonite, shotcrete and Opalinus Clay.

The mineral composition and the porewater chemistry of a low-pH shotcrete (ESDRED) recipe are described in detail in Kosakowski & Berner (2013). The setup is based on the most recent CEMDATA07 thermodynamic database which includes several ideal solid solutions for hydrated cement minerals consistent with the Nagra/PSI thermodynamic database 01/01.

The montmorillonite model representing MX-80 bentonite was calibrated based on the data of Bradbury & Baeyens (2002). The definition of montmorillonite, the main constituent of bentonite, includes cation exchange processes and amphoteric ≡SOH sites as described in Bradbury & Baeyens (2002). In other (common) reactive transport codes which are based on the Law of Mass Action (LMA) approach for solving geochemical equilibria, cation exchange processes are usually accounted for by assuming that the clay mineral is represented by an X^- "ligand" initially occupied with Na^+. We implemented a more chemically plausible solid solution model of ion exchange in clays which also considers the partitioning into interlayer water and free porewater.

The specifically developed host rock model for Opalinus Clay simultaneously reproduces the equilibrium porewater composition defined in Mäder (2009) and the mineralogical compositions and the water contents given in Nagra (2002b). The aim of the Opalinus Clay setup was to mimic the porewater composition in Mäder (2009), and simultaneously to reproduce the mineralogical composition as given in Tab. 5.3-1 in Nagra (2002b), and, in addition, to reproduce reasonable values for water content, anion accessible porosity and CEC. Our main assumption is that we can describe all cation exchange phases by the montmorillonite model we developed for the MX-80 bentonite. This montmorillonite should represent all the cation exchange capacity that is present in the Opalinus Clay.

In our present set-up the occupancies of the ion exchanger are linked to the montmorillonite solid solution phase. In the additional presence of illite and kaolinite (and the common phases quartz calcite, dolomite, siderite, celestite and barite) the Gibbs phase rule shows that there are only very few degrees of freedom in our system. Fixing total dissolved (Na)Cl and the ratio of SO_4/Cl in solution produces an invariant system where pCO_2 is, in principle, controlled by the relative occupancies of K^+, Ca^{2+}, Mg^{2+}, Sr^{2+}, Fe^{2+} and Ba^{2+}.

In addition, we inserted an illite phase with the composition $K_{0.6}Mg_{0.25}Al_{2.3}Si_{3.5}O_{10}(OH)_2$ into the database and took the thermodynamic properties from Wolery & Jove-Colon (2004). Mäder (2009) discusses a discrepancy between calculated and measured K^+ concentrations in the Opalinus Clay porewater. We also found this discrepancy and decided to adjust the stability of the illite phase (+3500 J/mol) to correct the K^+ concentrations. An alternative correction option would have been adjust the exchange constants of the montmorillonite phase. We however preferred not to do so because the montmorillonite phase had been calibrated with measured (in house) data.

Further, the setup includes a Ca, Na, K – phillipsite solid solution as an indicator for the occurrence of zeolite–type phases. Relative stabilities for the individual phillipsite end-members were taken from the THERMODEM DB (Blanc et al. 2012). The absolute stability of the Na-phillipsite end-member (and consequently the stabilities of the other two end-members) were adjusted to meet experimental observations, namely that zeolite phases are absent in Opalinus Clay and in bentonite systems, but may potentially be stabilized at slightly elevated pH (see also Traber and Mäder (2006).

Tab. A1: Mineralogy, cation exchange capacity and porosity values for the different clay based material models.

Phase weight fraction (based on dry weight)	**Opalinus Clay model**	**Opalinus Clay specifications** (Mazurek, M. Pers. Communication)[19]	**Bentonite model**	**Bentonite composition** (Bradbury & Baeyens 2002)	**Shotcrete model**
Illite	0.252	0.253	--	--	For mineral phases see Tab. A2
Kaolinite	0.187	0.188	--	--	
Montmorillonite	0.129	0.094 Illite/Smectite mixed layer	0.744	0.75	
Calcite	0.144	0.145	0.0068	0.007	
Dolomite	0.005	0.005	--	--	
Quartz	0.18	0.181	0.152	0.152	
Siderite	0.035	0.035	0.0072	0.007	
Pyrite	0.011	0.011	0.0029	0.003	
Barite	$1.24 \times 10^{--7}$	--	$4.9 \times 10^{--5}$	--	
Hydro-magnetite	--	--	0.0022	Total iron (hydro)oxide 0.0259 mol kg^{--1}	
Gypsum	--	--	0.004	--	
Inert	0.0824	Kalifeldspar 0.014 Plagioklas 0.011 C(org) 0.007 Chlorit 0.088	0.085	Feldspar 0.05 – 0.08 Organic carbon 0.004 Mica < 0.01	
CEC mol kg^{--1} (dry weight)	0.106	0.106	0.7547	0.787 ± 0.040	--
Porosity (total)	0.12	0.12	0.36	0.36	0.179
Porosity (anionic)	0.06	0.06	0.05	0.05	0.179

[19] A draft mineralogical composition of Opalinus Clay was defined in an earlier stage of the project. Later updates in Traber & Blaser (2013) as shown in Tab. 4-2 could not be considered in this model. Any differences are only marginal and do not affect the outcome of the modelling.

Tab. A2: Phase composition calculated for recommended low-pH ESDRED shotcrete bulk composition as given in Tab. 4-5.

From the total mass of 2.3884 kg, 0.1189 kg makes up the solution phase (temperature = 25 °C).

Phase	**Stoichiometry**	**[mol]**	**Composition if "Inert" is replaced by SiO_2** [mol]
Solid solution phases/endmembers			
Jennite	$(SiO_2)(CaO)_{1.667}(H_2O)_{2.1}$	20.92×10^{-3}	1.37×10^{-3}
Tobermorite_II	$(SiO_2)(CaO)_{0.833}(H_2O)_{1.333}$	2.4503	2.59
Al-ettringite	$Ca_6Al_2(SO_4)_3(OH)_{12}(H_2O)_{26}$	30.98×10^{-3}	--
Fe-ettringite	$Ca_6Fe_2(SO_4)_3(OH)_{12}(H_2O)_{26}$	6×10^{-11}	--
Hydrotalcite	$Mg_4Al_2(OH)_{14}(H_2O)_3$	25.47×10^{-3}	20.71×10^{-3}
Fe-hydrotalcite	$Mg_4Fe_2(OH)_{14}(H_2O)_3$	27×10^{-6}	1.21×10^{-3}
Phillipsite_Ca	$Ca(Al(SiO_2)_3O_2(H_2O)_3)_2$		0.69×10^{-3}
Phillipsite_K	$KAl(SiO_2)_3O_2(H_2O)_3$		23.2×10^{-6}
Phillipsite_Na	$NaAl(SiO_2)_3O_2(H_2O)_3$		1.49×10^{-3}
Ba-montmorillonite	$Ba(Si_{10.473}Al_{4.132}Mg_{0.737}Fe^{III}_{0.237}Fe^{II}_{0.211}O_{44.316}H_{30.737})_2$		25.68×10^{-9}
Ca- montmorillonite	$Ca(Si_{10.473}Al_{4.132}Mg_{0.737}Fe^{III}_{0.237}Fe^{II}_{0.211}O_{44.316}H_{30.737})_2$		6.34×10^{-3}
Fe- montmorillonite	$Fe^{II}(Si_{10.473}Al_{4.132}Mg_{0.737}Fe^{III}_{0.237}Fe^{II}_{0.211}O_{44.316}H_{30.737})_2$		1.28×10^{-25}
K- montmorillonite	$KSi_{10.473}Al_{4.132}Mg_{0.737}Fe^{III}_{0.237}Fe^{II}_{0.211}O_{44.316}H_{30.737}$		9.66×10^{-6}
Mg- montmorillonite	$Mg(Si_{10.473}Al_{4.132}Mg_{0.737}Fe^{III}_{0.237}Fe^{II}_{0.211}O_{44.316}H_{30.737})_2$		7.05×10^{-6}
Na- montmorillonite	$NaSi_{10.473}Al_{4.132}Mg_{0.737}Fe^{III}_{0.237}Fe^{II}_{0.211}O_{44.316}H_{30.737}$		3.89×10^{-3}
Sr- montmorillonite	$Sr(Si_{10.473}Al_{4.132}Mg_{0.737}Fe^{III}_{0.237}Fe^{II}_{0.211}O_{44.316}H_{30.737})_2$		46.05×10^{-6}
Single phases			
Gibbsite	$Al(OH)_3$	18.65×10^{-3}	--
Barite	$BaSO_4$	14×10^{-3}	14×10^{-3}
Calcite	$CaCO_3$	0.10	0.10
Gypsum	$CaSO_4.(H_2O)_2$(cr)	--	91.65×10^{-3}
Hydro-magnetite	$Fe_3O_4(H_2O)_2$	20×10^{-6}	--
Ferrihydrite	$Fe(OH)_3$	67.99×10^{-3}	58.20×10^{-3}
Illite	$K_{0.6}Mg_{0.25}Al_{2.3}Si_{3.5}O_{10}(OH)_2$	45.36×10^{-3}	53.32×10^{-3}
Celestite	$SrSO_4$	24×10^{-6}	--
Quartz	SiO_2	--	2.94
Inert (SiO_2)*	SiO_2	2.97025	1

* The term "Inert quartz" summarizes all entities not further specified, i.e. loss of ignition, minor oxides like TiO_2 etc. In order to keep mass and volume conservation the collectivity of these phases is operationally subsumed under the term inert (non-reactive) quartz.

Appendix B: Detailed information on the interaction of iron with bentonite in a SF/HLW repository

B1 Discussion of selected experimental studies

In a series of experiments Simpson (1983), Simpson (1984), Simpson & Wallotton (1986), and Simpson (1989) studied the corrosion behaviour of several canister materials (cast steel, nodular cast iron, copper, and the titanium-alloy Ti-Code 12) for the Swiss high-level waste disposal projects in crystalline bedrock. The main emphasis was put on corrosion tests in natural groundwaters. Some experiments also investigated the corrosion rates of the canister materials in contact with bentonite. In general, bentonite increased corrosion rates considerably, however, no information was given concerning the alteration of the bentonite itself.

Müller-Vonmoos et al. (1991) investigated powdered and compacted mixtures of 20 wt. % iron and 80 wt. % bentonite (MX-80 and Montigel) at 80 °C under an anoxic atmosphere of a mixture of hydrogen gas and water vapour. The duration of the experiment was 27 weeks. The observed reaction products were magnetite and hydrogen gas. No changes were observed for the interlayer charge of montmorillonite and for the CEC. Only a minor uptake of Fe (2 % of the CEC) by montmorillonite was observed. Similar experiments with mixtures of magnetite and bentonite that lasted for 29 weeks showed no appreciable changes in mineralogy, interlayer charge, CEC, and exchangeable cations.

The experiments by Müller-Vonmoos et al. (1991) were also reported by Madsen (1998).

Oscarson & Heimann (1988) studied the influence of an amorphous Fe(II)-silicate on bentonite. 5 g of each were suspended in 800 ml of a synthetic deep groundwater solution (containing no dissolved iron) and kept under oxic and anoxic conditions at 23 and 70 °C for 200 days. In contrast to the oxic experiments, detectable amounts of dissolved iron were found in the reacted anoxic systems at both temperatures, reflecting the higher solubility of iron phases at lower redox potential. The total iron content of the clay fraction in the anoxic experiments was increased by 7 wt. % at 23 °C and by 32 wt. % at 70 °C. The CEC in the anoxic experiments was reduced by 20 % at 23 °C and by 5 % at 70 °C. This reduction was explained by Oscarson & Heimann (1988) as being due to the precipitation of an Fe-hydroxide on the edges of clay particles, thereby blocking some of the cation-exchange sites. No mineralogical change in the clay fraction was detected by XRD.

Papillon et al. (2003) performed anoxic corrosion experiments with carbon steel and FoCa7 bentonite to study the corrosion behaviour of steel. Five metal sheets (50 × 20 × 2 mm) were placed into compacted bentonite in a corrosion cell, which was saturated and percolated with reducing natural granite groundwater at a pH of 8.0 at a hydrostatic pressure of 30 bar. Two experiments were made, one at 25 °C for 6 months and the other at 80 °C for 8 months. No significant mineralogical changes were detected in the bentonite at 25 °C, except in the immediate contact region with the steel, where the colour of the bentonite changed to green within a distance of, at most, 300 μm. In this homogeneous region, iron oxides (most likely magnetite) were formed in nanometric clusters, partially associated with micrometric calcite crystals (within 50 μm from the steel, a pure calcite layer was also partially formed directly on the steel surface). Nanometric crystals of goethite were preferentially dissolved within the first 100 μm of the bentonite, most likely due to reduction by the hydrogen produced during corrosion. The Fe(II) produced during this reductive dissolution could also explain the precipitation of magnetite. At 80 °C the texture of the bentonite near the steel surface was more heterogeneous and characterized by green and ochre coloured zones. The green zones were characterized by

the formation of calcite, siderite, and an iron rich 7Å-phyllosilicate analogous to berthierine, while in the ochre coloured zone only calcite was formed. Papillon et al. (2003) do not mention the dissolution of goethite, nor the formation of magnetite at 80 °C.

Guillaume et al. (2004) performed batch experiments with MX-80 bentonite and mixed hematite-magnetite powders in low salinity NaCl-$CaCl_2$ solutions at 80 and 300 °C under anoxic conditions. Bentonite was added to the solution with a liquid/solid mass ratio of 10. Equal masses of hematite and magnetite powders were then added to obtain an Fe/bentonite ratio of 0.1. The experiments were run for 1, 3, and 9 months. Control experiments with bentonite lacking the addition of hematite and magnetite were also made for the same duration and the same temperatures. Considering the minerals present in unreacted bentonite, there was evidence in all experiments (with or without hematite and magnetite) for the growth of quartz (or cristobalite), K-feldspar, and plagioclase. Carbonate, phosphate, pyrite, and mica were completely dissolved in all experiments with hematite and magnetite at 300 °C, but were largely unaffected at 80 °C, with the exception of mica, which disappeared after 9 months. Newly formed zeolite associated with clay particles was observed after 9 months at 300 °C in experiments with and without hematite and magnetite. The presence of hematite and magnetite at 80 °C did not change the crystal chemistry of montmorillonite significantly. At 300 °C, however, dioctahedral montmorillonite was partially converted to trioctahedral saponite-like smectite with a corresponding increase in Fe^{2+} content.

Charpentier et al. (2006) studied the anoxic interaction of iron with bentonite under alkaline conditions. MX-80 bentonite was mixed with an iron-magnetite powder at a mass ratio of 10, while the iron-magnetite ratio was 1. The mixture was added to an alkaline NaCl-$Ca(OH)_2$-SiO_2-$CaSO_4$-solution (pH = 12.35) with a liquid-solid mass ratio of 10. In addition, an iron plate was placed at the bottom of the vessel. Experiments were run at 80, 150, and 300 °C for 3, 6, and 9 months. Two types of newly formed minerals were found. At 80 °C and 6 months, and at 150 °C and 3 months, a magnesium-rich fibrous phase was found with a composition compatible with palygorskite, a clay mineral with ideal composition of $(Si,Al)_8(Mg,Al)_5O_{20}(OH)_2 \cdot 8H_2O$. However, this phase was not found in the experiments of longer duration, indicating that it is a transitory phase. Small laths of a zeolite mineral of mordenitic composition were found at 300 °C already after 3 months. The amount of mordenite increased with the duration of the experiments. Montmorillonite remained the predominant clay mineral at 80 and 150 °C although the crystal chemistry evolved with the duration of the experiments, notably by an enrichment in Fe and a depletion of Si near the iron plate. At 300 °C, however, the clay mineral composition was no longer that of the initially present montmorillonite already after 3 months. On the basal iron plate, an iron rich vermiculite was found. Further away from the plate, the clay minerals had intermediate compositions between montmorillonite and Mg-rich vermiculite. The Fe/Mg-ratio decreased with distance from the iron plate. In addition to the predominant vermiculite, a very small amount of an iron-rich trioctahedral smectite (saponite-type) was found.

Wilson et al. (2006a) studied the interaction between montmorillonite (Kunipia-F), native iron, and magnetite. Two series of experiments were performed. In the first series, a repository was simulated in which bentonite in contact with steel was altered as groundwater infiltrated into the bentonite. The experiments were carried out at 250 °C for 93 to 114 days with mixtures of fine grained starting materials and NaCl solutions. The initial stage was represented by mixtures of bentonite and pure Fe-metal. Additions of different quantities of magnetite simulated later stages of iron corrosion. The main reaction products in experiments with large initial amounts of Fe-metal were magnetite and altered smectites which were Fe(II)-rich resembling Fe(II)-saponite with some dispersed 7Å 1:1 layers. Solute activities were compatible with the stability field of hypothetical Fe(II)-saponite calculated by Wilson et al. (2006b). Experiments with

magnetite showed significantly less alteration of montmorillonite. In some experiments of the first series, calcite was added as an additional mineral likely to be present in bentonite. The addition of calcite resulted in the formation of analcime. The second series of experiments was performed at 80, 150, and 250 °C for 90 to 92 days under extreme Fe-rich conditions in order to promote bentonite alteration. Mixtures of powdered Fe-metal and bentonite were put into contact with $FeCl_2$-solutions. The main alteration products were magnetite and altered smectite. Significant montmorillonite alteration was only observed at 250 °C. The altered smectite contained only a small proportion of 7Å 1:1 layers. Solute activities were compatible with the stability field of berthierine calculated by Wilson et al. (2006b).

Carlson et al. (2007) and Carlson et al. (2008) performed experiments with carbon steel wires embedded in compacted MX-80 bentonite and similar experiments with coupons of cast iron and carbon steel, all in contact with artificial NaCl-Na_2CO_3 groundwaters with an initial pH of 10.4. Both series of experiments were run under anoxic conditions at 30 and 50 °C. The durations were 829 days at 30˚ and 911 days at 50 °C for the wire samples, and 900 days at 30˚ and 356 days at 50 °C for the coupon samples. The corrosion products were magnetite, hematite and goethite on the cast iron and carbon steel coupons. On the carbon steel wires, only magnetite was found. The total iron content in the reacted bentonite of the coupon samples was only slightly larger than in the initial bentonite. For the wire samples, however, the total Fe-content of the bentonite increased from 2.40 to 9.03 wt. % at 30 °C and to 11.1 wt. % at 50 °C. Local concentrations of Fe were highest near the wires (up to 20 wt. %) and decreased farther away. Still, there was no evidence for any iron corrosion products in the bentonite matrix and also no evidence for the formation of any secondary iron-rich clay minerals. The cation exchange capacity and the hydraulic conductivity of the bentonite containing wires were reduced with respect to the initial bentonite and the bentonite containing the coupons. The exact location of Fe(II) in the reacted bentonite remained uncertain.

De Combarieu et al. (2007) performed batch experiments of iron in contact with Callovo-Oxfordian clay and ultra pure water at 90 °C under anoxic conditions for durations between 1 to 6 months. Iron powders were mixed with clay powders in a mass ratio of 1 and suspended in ultra pure water with a mass ratio for solid/water of 4/10. In a second series of experiments iron foils were placed in contact with powdered clay and ultra pure water. Based on XRD, the main corrosion products observed were magnetite and iron-rich serpentine- or chlorite-like phases, but it was not possible to discriminate between the evolution of chlorite (also initially present) and the neoformation of the 7Å-phases greenalite, cronstedtite, berthierine, and odinite. The formation of these phases was associated with a decrease in quartz, illite, and illite-smectite. In order to interpret their experimental findings, de Combarieu et al. (2007) also performed a thermodynamic/kinetic modelling study, which is discussed in Section 7.3.6.

Ishidera et al. (2008) studied the interaction of carbon steel with Kunipia F and Kunigel V1 bentonite under anoxic conditions at 90 °C for 10 years. Carbon steel coupons were placed in the center of compacted bentonite in titanium columns which were immersed in three different solutions: simulated seawater, simulated seawater with a high concentration of carbonate, and a low-salinity solution. XRD-analysis revealed no alteration of montmorillonite and no formation of any secondary clay minerals. The CEC remained practically unchanged. Steel corrosion products in Kunipia F were mostly $Fe(OH)_2$, accompanied by green rust, GR1(Cl^-), and lepidocrocite. The iron corrosion products in Kunigel V1 could not be identified.

Martin et al. (2008) studied the corrosion behaviour of iron and low alloyed steel in compacted MX-80 bentonite and in Callovo-Oxfordian argillite saturated with a synthetic porewater at 90 °C and 50 bar during 8 months under anoxic conditions. The argillite and the compacted bentonite were machined into cubic blocks. Three different metal rods were inserted into each

block in vertical drill holes. The assembly was put into a confining cell consisting of a stainless steel cell with a pure nickel insert, so that the bentonite and argillite blocks were not in contact with the stainless steel. The assembly was set up as an electrochemical cell (for electrochemical monitoring of the iron corrosion process) with the nickel insert of the confining cell acting as a counter electrode. The central rod (nickel in the case of the argillite block, and pure iron in the case of the bentonite block) acted as reference electrode, and the lower and upper rods, consisting of a low alloyed steel, as working electrodes. The blocks were saturated and kept in contact with a synthetic solution representing the porewater of the Callovo-Oxfordian at Bure. In the bentonite experiment, the surfaces of the steel rods were covered by a thin layer of magnetite, covered by a thin homogeneous layer of Ca-containing siderite. Martin et al. (2008) suggested the following steel corrosion mechanism: As the steel is oxidized, a magnetite layer is formed with the oxidation of Fe taking place at the metal-magnetite interface. At the outer interface of magnetite, water is reduced and Fe(II) released, leading to the formation of siderite, which is progressively substituted with calcium cations. The argillite experiment showed a more complicated corrosion pattern with an additional intermediate layer containing Fe, O, Na, and Si, which was studied by Schlegel et al. (2008), albeit on the central iron rod. XANES-analyses suggested the formation of nontronite- or stevensite-like smectites, or possibly the formation of saponite-like smectites. The presence of magnetite relicts in the intermediate layer suggests the formation of the Fe-clay phases at least partly at the expense of magnetite, with Si provided from the destabilization and dissolution of clay minerals by dissolved Fe, which probably took place in the outer layer.

Using a similar experimental setup, Schlegel et al. (2010) investigated free and anodically activated corrosion of iron in a block of Callovo-Oxfordian argillite saturated with a synthetic Bure porewater at 90 °C for 4 months. A gold reference electrode was inserted into the lower drill hole, a massive iron rod in the upper drill hole (FCP, freely corroding probe) and an iron microcontainer in the central drill hole (APP, anodically polarized probe activated by a an anodic current). Free corrosion on the FCP produced similar reaction products as in the previous experiment with argillite, with an internal discontinuous magnetite layer, a central layer consisting of Fe-rich phyllosilicates and an outer layer consisting of siderite containing some Ca. Activated corrosion resulted in an inner magnetite layer, an intermediate layer with $Fe_2CO_3(OH)_2$ (chukanovite), an outer layer with a Fe-rich 7Å-phyllosilicate, and a transformed matrix layer containing siderite.

Perronnet et al. (2008) studied the oxic corrosion of iron in FoCa7 bentonite (mainly consisting of mixed-layer kaolinite/smectite) at 80 °C for 45 days. Batch experiments were performed with suspensions of iron and bentonite powders in Evian mineral water, with the iron/bentonite mass ratio (I/C) varying between 0 and 3. Kaolinite and smectite were altered into SiAlFe gels which were gradually converted into dioctahedral 7-Å phyllosilicates with compositions between odinite and greenalite.

Milodowski et al. (2009b) performed mineralogical investigations of experiments made in Phase 1 of the EU Framework 6 NF-PRO Project. The experimental setup consisted of a composite cylinder with a central section of compacted MX-80 bentonite containing carbon steel wires. The central section was bounded at either end by compacted MX-80 bentonite containing an iron coupon. The composite cylinder was loaded into a steel holder with porous metal filters, allowing the infiltration of a 1M NaCl solution and the escape of gas, and was placed in a stainless steel pressure vessel. The experiments were conducted in a reducing environment at 50 °C and pH 11 for 99 days, and at 50 °C and pH 8.4 for 193 and 198 days. After the experiments the central region displayed an obvious reddish-brown staining associated with the corrosion of the dispersed steel wires. In all three experiments, a poorly crystalline iron oxyhydroxide phase was found in the iron corrosion products directly on the steel wire surfaces. It was tentatively identi-

fied by XRD as åkagenite, Fe(O,OH,Cl). Magnetite was also identified on corrosion surfaces in one experiment. The fact that iron oxide corrosion products from all three experiments were magnetic indicated that magnetite was formed in all three experiments. Concentrations of Fe in alteration halos around the wires were enhanced by several weight %, decreasing to background levels at distances up to 1 mm from the wires. Greater penetration depths of Fe into the bentonite occurred along hairline fractures which radiated from the corroding wires. No discrete iron oxide phases could be detected in the bentonite matrix. Aragonite was formed immediately adjacent to the corroding iron and along the leading edge of the diffuse iron halos formed around the wires. The experimental pore fluid did not contain Ca, and there was no evidence for the dissolution of Ca minerals (calcite, apatite, feldspar), thus Milodowski et al. (2009b) suggested that the Ca must be derived from the exchangeable cation sites in the interlayer of montmorillonite, displaced by Fe produced by iron corrosion. Slightly increased d_{002}/d_{003} values (measured by XRD) of altered bentonite suggest an increase in the total number of electrons in the octahedral layers, possibly as a result of Fe substitution. According to Milodowski et al. (2009b), these alteration features might be an early stage in the transformation of montmorillonite into an Fe-rich smectite or reflect partial alteration of montmorillonite into berthierine, chlorite, or a mixed-layer chlorite-smectite.

For Phase 2 of the EU Framework 6 NF-PRO Project, Milodowski et al. (2009a) investigated 4 additional experiments at temperatures of 30 °C. The experiments were performed at 30 °C during 571-687 days with 0.01M NaCl (pH 8.4), with 1M NaCl (pH 8.4 and 11), and with "Allard" reference groundwater (pH 8.4). As in the Phase 1 experiments, narrow haloes of bentonite significantly enriched in Fe formed around the corroded steel wires and around the corroded iron coupons (less well developed than around the steel wires) and showed similar alteration features as in the Phase 1 experiments. However, the observed alteration zones were much thicker and more strongly developed. The main difference to the Phase 1 experiments was the formation of significant amounts of a Mg-Fe-rich aluminosilicate within the Fe-rich alteration haloes. This reaction product contained up to 20 wt. % of Mg and also considerable amounts of Si, Fe, and Al. Unfortunately, it was not possible to identify this alteration product. According to Milodowski et al. (2009a) the high Mg content is compatible with Mg-rich saponite, Mg-rich chlorite, kaolinite or with a mixture of these phases. With the exception of the "Allard" reference water, the experimental solutions did not contain any Mg, so the source of the Mg must have been the bentonite itself. This suggests that montmorillonite has been replaced by the Mg-Fe-rich aluminosilicate. The Mg-Fe-rich aluminosilicate appears to have formed early in the experiment and was later partially replaced by a Fe-rich aluminosilicate, which could also not be identified. Magnetite was the only iron-corrosion product, åkagenite or any other crystalline iron hydroxide phase could not be detected.

Mosser-Ruck et al. (2010) performed anoxic batch experiments of mixtures of Fe-metal and magnetite powders with MX-80 bentonite in dilute solutions of NaCl and $CaCl_2$ with different liquid-clay (L/C) and Fe-clay (F/C) mass ratios at temperatures of 80, 150, and 300 °C for durations of 3, 6, 9, and 12 months. In all experiments a small iron-metal plate was added. At 80 °C, with an L/C ratio of 10 and an Fe/C ratio of 0.1, the alteration products showed a slight decrease in Si content and interlayer charge and a slight increase in Fe, irrespective of the duration of the experiment. Clay particles in contact with the iron plate were richer in Fe than the bulk reaction products. Experiments at 80 °C with a larger Fe/C ratio of 0.5 and a smaller L/C ratio of 5 resulted in the formation of a phase rich in Fe and poor in Si and Ca which could be a mixture of a smectite and an Fe-rich 14 Å chlorite (chamosite-type) or an Fe-rich 7 Å clay (berthierine-type). The increase in temperature to 300 °C enhanced the depletion of Si and enrichment of Fe.

B2 Mass balance constraints for the conversion of montmorillonite to chlorite or berthierine

The mass balance calculations presented in this appendix are all based on the reference concept defined by Nagra (2002a) with the canister dimensions modified by Patel et al. (2012), see Fig. B1. Fig. B2 shows the reinforcement of the tunnel walls by a cement liner to ensure safety during the operational period. In order to prevent lateral fluid flow along the degrading cement liner over the entire length of the disposal tunnels, a hydraulic barrier is to be placed between every tenth canister (Leupin & Johnson 2013). As the open diameter of the emplacement tunnels will be maintained, the only difference between the reference and the alternative concept relevant for these mass balance consideration is the additional mass of bentonite used in the hydraulic barrier.

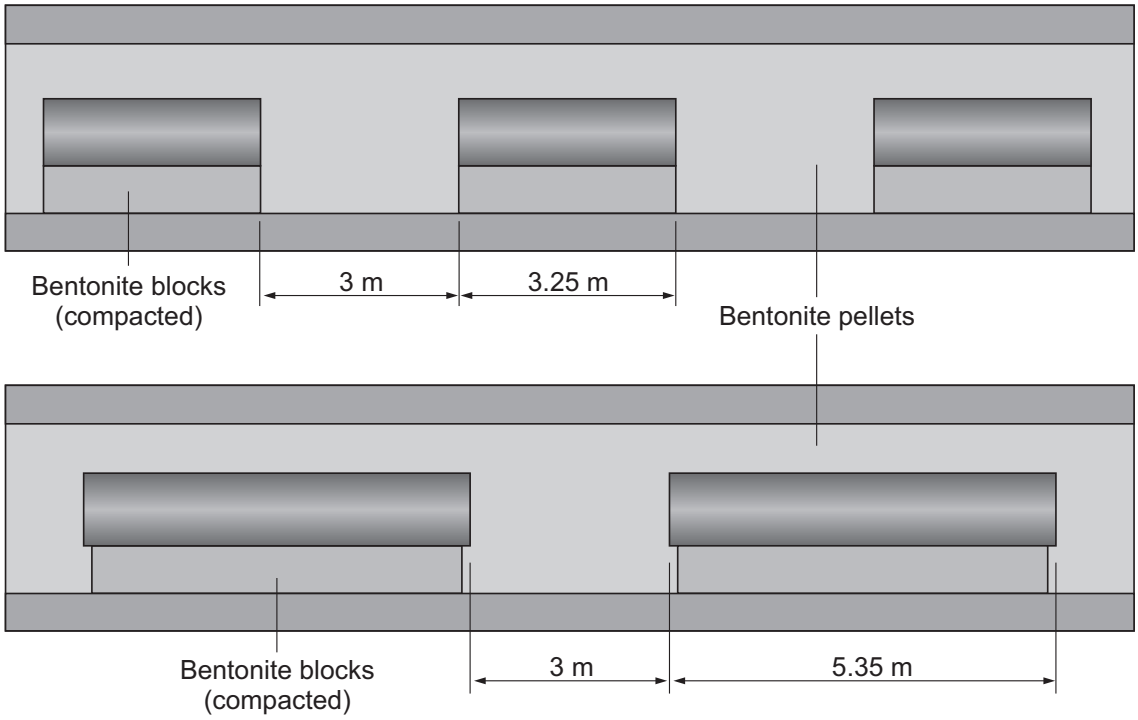

Fig. B1: Longitudinal section through disposal tunnels for HLW (top) and BWR SF (bottom) canisters according to the reference concept (Nagra 2002a, modified according to Patel et al. 2012).

Tunnel diameter is 2.5 m.

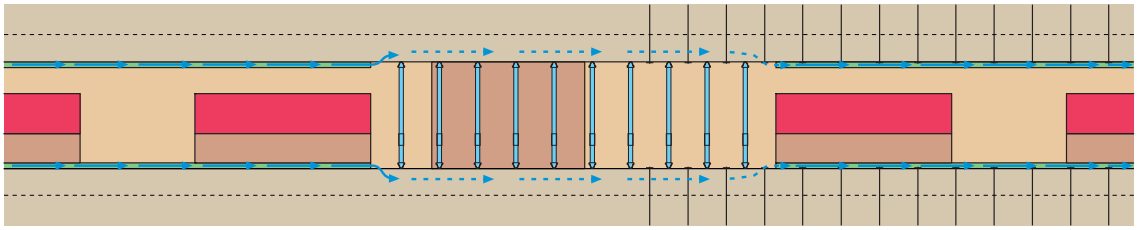

Fig. B2: Alternative concept for disposal tunnels. The tunnel walls are stabilized by a cement liner.

In order to prevent lateral fluid flow along the degrading cement liner over the entire length of the disposal tunnels, a hydraulic barrier is to be placed between every tenth canister (Leupin & Johnson 2013).

B2.1 Mass balance using total iron inventory

Following Wersin et al. (2007b) a simple mass balance calculation was used to assess the potential extent of the conversion of montmorillonite to chlorite or berthierine. This was done in the following steps:

1. **Volume of bentonite per canister**: According to Fig. B1 (Nagra 2002a, modified according to Patel et al. 2012) the diameter of the cylindrical disposal tunnels is 2.5 m. The cylindrical canisters have a length of 3.25 m (HLW) or 5.35 m (SF) and a diameter of 0.72 m (HLW) or 1.05 m (SF BWR). The canisters are lined up in the center of the tunnels (resting on compacted bentonite blocks) and are positioned 3 m apart. The void space around the canisters is filled with granular bentonite. The total length of a tunnel section containing a HLW canister is 6.25 m (length of canister plus distance between two canisters) and the total length of a tunnel section containing a SF canister is 8.35 m. Since the volume V of a cylinder is given by $V = \pi r^2 l$ (where r is its radius and l its length), the volume of a tunnel section is 30.68 m^3 for HLW and 40.99 m^3 for SF. The volume of a canister is 1.32 m^3 for HLW and 4.63 m^3 for SF. The volume of bentonite (compacted bentonite blocks plus granular bentonite backfill) per canister is given by the difference of the volume of a tunnel section and the volume of a canister, resulting in 29.36 m^3 bentonite per HLW canister and 36.36 m^3 bentonite per SF canister.

2. **Moles of montmorillonite per canister**: According to Berner (2010) in his report on setting up the conditionds for calculating a bentonite porewater, 1 dm^3 of completely dry bentonite saturated with in-diffusing Opalinus Clay porewater contains 3.56 mol montmorillonite of stoichiometry
$Na_{0.38}(Al_{1.55}Fe^{III}_{0.09}Fe^{II}_{0.08}Mg_{0.28})(Si_{3.98}Al_{0.02})O_{10}(OH)_2 \cdot 4.84H_2O$
(In order to simplify the calculations, the interlayer cations are represented by Na^+). Thus, there are 1.045×10^5 mol montmorillonite per HLW canister and 1.294×10^5 mol montmorillonite per SF canister.

3. **Moles of iron per canister**: In the following calculations the alloying constituents of steel are neglected and it is assumed that steel consists entirely of iron.
SF-waste sort BWR: The total unloaded canister mass is 17'100 kg, and the mass of the empty carbon steel basket 2314 kg (Patel et al. 2012), resulting in a total mass of steel of 19'414 kg per canister, which corresponds to 3.48×10^5 mol of iron per canister.
HLW-waste: The mass of the empty steel canister is 6400 kg (Patel et al. 2012), which corresponds to 1.15×10^5 mol of iron per canister.

4. **Mol % of montmorillonite converted to chlorite or berthierine by all of the iron of the canisters**: The conversion of montmorillonite (mont) $Na_{0.38}(Al_{1.55}Fe^{III}_{0.09}Fe^{II}_{0.08}Mg_{0.28})(Si_{3.98}Al_{0.02})O_{10}(OH)_2 \cdot 4.84H_2O$ to the Fe-chlorite chamosite (cham), $(Fe_5Al)(Si_3Al)O_{10}(OH)_8$, can be written as follows if it is balanced on Al:

$$\text{mont} + 3.755\ Fe^0 + 0.54\ H_2O(l) + 0.94\ H^+ \Leftrightarrow 0.785\ \text{cham} + 0.38\ Na^+ + 0.28\ Mg^{2+} + 1.625\ SiO_2(cr) + 3.71\ H_2(g)$$

The analogous reaction for the conversion to berthierine (berth), $(Fe_2Al)(SiAl)O_5(OH)_4$, is:

$$\text{mont} + 1.4\ Fe^0 + 0.94\ H^+ \Leftrightarrow 0.785\ \text{berth} + 0.38\ Na^+ + 0.28\ Mg^{2+} + 3.195\ SiO_2(cr) + 3.385\ H_2O(l) + 1.355\ H_2(g)$$

Therefore, 3.755 mol of iron are needed to convert one mol of montmorillonite to chlorite (chamosite) and 1.4 mol for the conversion to berthierine. Using the number of moles of Fe per canister determined above, this allows one to calculate the number of moles of montmorillonite that can be converted to chamosite by all of the iron contained in one canister: 3.05×10^4 mol for HLW and 9.26×10^4 mol for SF BWR. The corresponding numbers for the conversion to berthierine are: 8.19×10^4 mol for HLW and, 2.48×10^5 mol for SF BWR. These numbers and the number of moles of montmorillonite per canister calculated above lead to the mol % of montmorillonite that can be converted to chamosite by all of the iron contained in one canister: 29 mol % for HLW and 72 mol % for SF BWR. The corresponding numbers for the conversion to berthierine are: 78 mol % for HLW and 192 mol % for SF BWR.

B2.2 Mass balance considering corrosion rates

Given a constant corrosion rate of the iron canisters, the amount of montmorillonite converted to berthierine or chamosite as a function of time can be calculated as follows: It is assumed that the canisters are hollow cylinders with an even wall thickness, which is reduced by a constant corrosion rate c (1 μm/year[20]).

The initial volume V_0 of a cylinder is given by

$$V_0 = \pi l_0 r_0^2,$$

where r_0 is the initial radius and l_0 the initial length. At time t the volume of the canister is

$$V_t = \pi l_t r_t^2,$$

where the radius is

$$r_t = r_0 - ct$$

[20] The reference corrosion rates for Nagra's safety analyses have been reconsidered recently (Diomidis 2014). A statistical evaluation of experimental data resulted in a mean value of 0.43 μm/y. For the safety analyses, however, a higher reference value of 2 μm/y was selected. In this study, the earlier value of 1 μm/y was kept.

and the length is

$$l_t = l_0 - 2ct .$$

The corroded volume at time t (V_{corr}) is the difference between V_0 and V_t

$$V_{corr} = \pi l_0 r_0^2 - \pi(l_0 - 2ct)(r_0 - ct)^2 .$$

The mass of corroded iron is given by

$$m_{corr} = V_{corr}\rho_{Fe},$$

where ρ_{Fe} is the density of iron, and the number of moles of corroded iron is

$$n_{corr} = \frac{V_{corr}\rho_{Fe}}{M_{Fe}},$$

where M_{Fe} is the molar mass of iron. The percentage of corroded iron with respect to the uncorroded canister can be expressed as

$$\%_{corr} = \frac{m_{corr}}{m_0}100,$$

where m_0 is the mass of the uncorroded canister. Thus

$$\%_{corr} = \frac{\rho_{Fe}\left(\pi l_0 r_0^2 - \pi(l_0 - 2ct)(r_0 - ct)^2\right)100}{m_0}. \qquad \text{(B1)}$$

The number of moles of montmorillonite converted to berthierine or chamosite is

$$n_{conv} = \frac{n_{corr}}{n_{montfesi}},$$

where $n_{montfesi}$ is the number of moles of iron needed to convert one mole of montmorillonite. The percentage of initial montmorillonite converted to berthierine or chamosite is

$$\%_{conv} = \frac{n_{conv}}{n_{montpercan}}100$$

or

$$\%_{conv} = \frac{\rho_{Fe}\left(\pi l_0 r_0^2 - \pi(l_0 - 2ct)(r_0 - ct)^2\right)100}{M_{Fe} n_{montpercan} n_{montfesi}}. \qquad \text{(B2)}$$

Equations (B1) and (B2) with the parameters listed in Tab. B1 have been used to draw the diagrams given in Fig. 7-1 in the main text.

Tab. B1: Parameters used in mass balance calculations considering corrosion rates.

		SF BWR	HLW
Initial mass of canister [kg]	m_0	19'414	6'400
Initial length of canister [cm]	l_0	535	325
Initial radius of canister [cm]	r_0	50.025	36
Density of Fe [g cm^{-3}]	ρ_{Fe}	7.87	7.87
Molar mass of Fe [g mol^{-1}]	M_{Fe}	55.8457	55.8457
Corrosion rate [μm year^{-1}]	c	1	1
Number of moles of montmorillonite per canister	$n_{montpercan}$	1.294×10^5	1.045×10^5
Number of moles of iron needed to convert one mole of montmorillonite to **berthierine**	$n_{montfesi}$	1.4	1.4
Number of moles of iron needed to convert one mole of montmorillonite to **chamosite**	$n_{montfesi}$	3.755	3.755

B3 Effects of water depletion due to canister corrosion

An issue that has so far not received much attention is the impact of metal (steel/copper) canister degradation on the overall water mass balance in the HLW repository environment and the potential consequences on solute (salt) concentrations. Anaerobic corrosion of steel consumes considerable amounts of water, e.g. through the reaction

$$3\ Fe(cr) + 4\ H_2O(l) = Fe_3O_4(cr) + 4\ H_2(g)$$

Therefore, the region adjacent to the external canister surface could become water depleted and the residual water in this region would passively concentrate soluble salts (mainly NaCl), so that the ionic strength would increase if the excess dissolved salt were not transported away. The development of a high ionic strength porewater region at the canister-bentonite interface could have undesired consequences, e.g. an increased canister corrosion rate, modified bentonite swelling properties, and possibly also an increase in the solubility limits of radionuclides forming strong complexes with chloride (e.g. Ag, Pb, Pd, Co, and Ni).

Senger et al. (2008) performed two-phase flow calculations on gas and water transport in the near-field of a HLW repository in the Opalinus Clay. Their calculations explicitly took into account the production of gas and the consumption of water due to anaerobic canister corrosion. They found that "*For the case with water consumption, water flow converges toward the waste canister at a rate corresponding to the water consumption rate associated with the corrosion reaction. The water flow toward the canister is maintained even for very low permeabilities of the Opalinus clay sustaining the anaerobic corrosion of the steel canister.*" Thus, the conclusion drawn by these authors is that gas saturation in the bentonite remains low and that no local depletion of water (significant decrease in water saturation) in the bentonite is expected as a consequence of canister corrosion.

However, even for quasi-steady state equilibrium between water depletion and water inflow, the consumption of water at the corroding canister surface could still lead locally to an increase of porewater salinity. The relevant question is whether persistent high ionic-strength zones would

develop in the region adjacent to the external canister surface, or whether diffusion would be fast enough to transport away the excess salt. The simulations of Senger et al. (2008) cannot answer this question, as they include water consumption due to corrosion as a sink term in the hydraulic equations and do not explicitly consider solute transport or chemical reactions.

Even without taking into account solute transport processes, the quantification of solute concentration changes at the corroding interface is difficult. The concentration increase inversely depends on the volume of water equilibrated with the canister surface. Therefore, without experimental data to calibrate the averaging volume, quantitative values of the concentration increase cannot be provided.

Taking into account transport of solutes, two opposing transport mechanisms can be identified. Advective transport in the converging flow field drives solutes towards the canister surface. A realistic water consumption of 9 g/a/tm (tunnel meter) for 200'000 years (Senger et al. 2008) will result in relatively small flow velocities under conditions close to full water saturation, so that solute transport will be diffusion-dominated. On the other hand, diffusive transport of solutes will tend to reduce higher concentrations near the canister surface. Diffusion is most effective over short distances and will impose high mass fluxes if chemical gradients are high. From Fig. 5-11 (see Chapter 5) it can be deduced that for neutral or anionic species (which are not or only weakly influenced by sorption processes) enhanced near-field concentrations can be equilibrated within a few hundred years. Based on this finding, it may be expected by analogy that high concentration gradients of solutes due to water consumption will not persist for a long time between the inner and outer bentonite region.

The simulations by Senger et al. (2008) show a quasi-stationary state, where water consumption at the interface and resulting water flow towards the interface are in equilibrium for long times. Such a quasi-equilibrium state might also develop with respect to the transport of solutes under a constant rate of canister corrosion. However, quantitative predictions are possible only by applying state-of-the art coupled codes and, more importantly, provided that critical system parameters are known.

Appendix C: Derivation of bentonite porewater compositions used in the safety assessment

C1 Introduction

Knowledge of the porewater composition in equilibrium with compacted bentonite under repository conditions is a requirement for the calculation of solubility limits and sorption coefficients for safety assessment calculations. In recent years, there have been important improvements in the understanding of water-solid interaction and ionic diffusion in compacted clays (e.g. Wersin et al. 2004, Van Loon et al. 2007, Glaus et al. 2010, Pearson et al. 2011). Based on the new insights, improved thermodynamic data and refinements in the chemical codes, a novel approach is currently being developed in our laboratory to model the chemistry of aqueous solutions reacting with compacted bentonite in conjunction with diffusive transport (Berner 2010, Berner et al. 2013).

At the time of this reporting, such new developments are not complete and still under review. For this reason it was decided, in agreement with Nagra, to adapt the chemical model formerly applied to derive bentonite porewaters to the ongoing safety assessment. This transitional phase offers the opportunity to compare the "conventional" bentonite porewater model used for the "Opalinus Clay project" safety assessment (Curti & Wersin 2002, Wersin et al. 2004) with the novel model recently developed in our laboratory (Berner 2010, Berner et al. 2013) using a common set of boundary conditions and assumptions. The calculations carried out with both models, using as far as possible the same constraints (porosity, bentonite mineralogy and composition of Opalinus Clay porewater) led as expected to similar results in terms of pH, E_h, ionic strengths and solution composition.

In this Appendix, we briefly compare the two models and report the composition and characteristics of the six bentonite porewaters selected for the ongoing safety assessment calculations. All the calculations assumed a one-cycle reaction between a given amount of bentonite and a volume of Opalinus Clay water corresponding to the anion accessible porosity in the compacted bentonite. The six waters derived cover uncertainties in critical parameters such as pH, water salinity and degree of bentonite compaction.

C2 Models and constraints

Five of the six selected waters presented here were obtained using the conventional model approach. In the "Opalinus Clay project" safety assessment, two slightly different models were considered (Curti & Wersin 2002), termed "Model 1" and "Model 2". Besides using different sets of ion exchange constants, the two models relied on a different approach for the treatment of surface complexation. Both models included constants for the protonation/deprotonation of edge sites in montmorillonite, however in "Model 1" a one-site approach with a surface charge dependent electrostatic correction term was used (the classical constant capacitance model, see Dzombak & Morel 1990), whereas "Model 2" relied on the two-site model with no electrostatic correction developed by Bradbury & Baeyens (1995, 1997, 1998). "Model 2" was selected for the definition of bentonite porewaters in "Opalinus Clay project" based on its consistency with a large set of experimental data, and the results of "Model 1" were discarded.

Here, "Model 2" is used again to generate the five selected "conventional" bentonite porewaters, but we assumed updated Opalinus Clay water compositions (including a low salinity and a high salinity type, see Mäder 2009) and revised values for the volume of water reacting with bentonite (reactive porosity). This latter point is particularly important and represents the main

difference to the previous calculations. In the "Opalinus Clay project" calculations, all the water in bentonite (38 % by volume) was assumed to be available for reaction with the minor minerals as well as for ion exchange and surface complexation reactions. In the present update, the amount of reactive water corresponds to the anion accessible porosity (5 % to 14.5 %), not to the bulk porosity of the saturated bentonite (36 % to 48 %, respectively). This revised assumption is consistent with the current understanding on the behaviour of water in compacted bentonite, which is to a large extent displaced into the structural interlayers of montmorillonite. Interlayer and diffuse double layer water are not accessible to anions and probably do not have the same properties of free water. Only a minor fraction of the bentonite water is not subject to electrostatic forces and is equally accessible for dissolved anions, cations and neutral species. In the present calculations, we assumed therefore that only the volume of water corresponding to the anion accessible porosity interacts with reactive solids in bentonite (gypsum, calcite, siderite, kaolinite, quartz, pyrite, magnetite).

C3 Results

All calculations were carried out using the PSI/Nagra Chemical Thermodynamic Database 12/07 (Thoenen et al. 2014) and the chemical equilibrium codes PHREEQC ("conventional" model calculations) or the GEMS-PSI ("New model" calculations). It could be shown that, in spite of the large difference in the assumed reactive porosities, only small differences in solution composition result from the application of the old and updated "conventional" models (Curti 2011b, Curti 2012). This can be explained by the large buffering capacity of the system, which partly derive from the very high solid:liquid ratio and by internal buffering mechanisms of the water – compacted bentonite system (Curti & Wersin 2002).

The essential results obtained for the five updated "conventional" bentonite porewater calculations are listed in Tab. C1, together with the results obtained using the new model developed by Berner et al. (2013). The five "conventional" waters take into account current uncertainties in the composition of the reacting water (low and high salinity Opalinus Clay porewater variants) and of bulk porosity variations arising from different degrees of compaction of the initial bentonite. This parameter has a considerable influence on the anion accessible porosity and was calculated according to Eq. 2 in Van Loon (2012). An iterative procedure was necessary for the chemical calculations since the anion accessible porosity, which defines the volume of free water in bentonite, depends on ionic strength and the ionic strength is itself affected by changes in anion porosity via dissolution/precipitation of minor solids (Curti 2012).

The sixth bentonite porewater (denoted with the heading "New model" in Tab. C1) was derived by applying the new refined model for the interaction between aqueous solution and bentonite. Its derivation is described in detail as "Option 2" water in Berner (2010) and Berner & Kosakowski (2011). In order to allow for a comparison of the two model approaches, as far as possible the same boundary conditions were used in both types of calculations. The new approach differs from the "conventional" model as follows:

1. Montmorillonite is treated in the new model as a multicomponent, dissolving/precipitating reactive solid. This improvement was achieved by calibrating the thermodynamic properties of montmorillonite against in-house experimental data on aqueous solution-bentonite mixtures. Note that in the "conventional" model, montmorillonite is not treated as precipitating/dissolving solid. The only chemical processeses montmorillonite is involved with are ion exchange and protonation/deprotonation of surface sites at the edges of the clay plateletts.

2. No external pCO_2 constraint is applied in the new model, whereas in the "conventional" calculations the pCO_2 value was imposed externally. Imposing such a constraint implies that the bentonite is always in equilibrium with a large gas reservoir at the specified carbon dioxide partial pressure. Such an assumption is problematic since the near-field of a deep-seated repository is not obviously connected to a gas reservoir.
3. The new model simulates the diffuse double layer by defining fictive, high-stability Na^+ and Cl^- surface complexes ($Na\text{-}O_{0.5}$ and $Cl\text{-}H_2O_{0.5}$). These surface complexes exactly compensate the pH-dependent surface charge generated by the protonation/deprotonation of edge sites, yielding perfectly charge-balanced water. This procedure is necessary in order to couple the new model to diffusive transport (Kosakowski & Berner 2013). In "conventional" models, the excess of anions or cations compensating the surface charge is evenly distributed in the bulk solution. In order to obtain charge balanced solutions for the calculation of solubility limits and sorption coefficients, "conventional" waters must be subsequently balanced through addition/removal of major ions. Due to the high surface area: liquid ratios, such corrections are significant. We choose to balance the waters by subtracting appropriate amounts of Na^+ and then re-equilibrating the ion exchange populations and minor solids. Only such charge balanced waters are shown in Tab. C1. The effects of the charge-balancing procedure on pH, E_h, ionic strength and the calculated water compositions are minor (for details see Curti (2011b)).

In both "conventional" and "new model" calculations the montmorillonite interlayer space is assumed to be pre-saturated with water. Pre-saturation could take place for instance via uptake of in-diffusing water vapour prior to the infiltration of Opalinus Clay porewater. This means that the Opalinus Clay water itself is not used to "fill" the interlayers of dry (or partially dry) montmorillonite, which would considerably increase the salinity of the final bentonite porewater.

An inspection of Tab. C1 shows that variations in chemical composition, pH and ionic strength arising from the considered system uncertainties (porosity, Opalinus Clay water composition, bentonite compaction) are small and relatively insensitive to the choice of the model. The major system uncertainty, not considered in the calculations reported in Tab. 3-1, is probably the effect of the initial state of the bentonite (dry or wet initial state).

Tab. C1: Selected bentonite porewaters compositions for 36 % and 48 % bulk porosity obtained with the conventional "non-electrostatic" model ("Model 2") and the novel approach ("New model").

Model	**Model 2**	**Model 2**	**Model 2**	**Model 2**	**Model 2**	**New model**
Reacting OPA water	Low salinity	Low salinity	Low salinity	High salinity	High salinity	Low salinity
ID-code	CON-BPW-18lsa (neutral	CON-BPW-22lsa (neutral)	CON-BPW-22lsa-p48 (neutral)	CON-BPW-25hsa (neutral)	CON-BPW-25hsa-p48 (neutral)	NEW-BPW-opt2**
Bulk and anion accessible porosity						
ε_{bulk}	0.36	0.36	0.48	0.36	0.48	0.36
ε_{anion}	0.05	0.05	0.111	0.05	0.145	0.05
pH, ionic strength, redox potential, CO_2 partial pressure						
pH	7.07	7.27	7.28	7.08	7.10	7.79
I (m)	0.369	0.365	0.348	0.785	0.760	0.239
E_h (V)	-0.153	-0.167	-0.168	-0.158	-0.159	-0.204
Pe	-2.58	-2.84	-2.85	-2.68	-2.70	-3.44
Lg pco_2 (bar)	-1.8	-2.2	-2.2	-2.5	-2.5	(-3.20)*
***Total element concentrations** [molality]*						
[Na]	3.05×10^{-1}	3.01×10^{-1}	2.85×10^{-1}	6.24×10^{-1}	6.06×10^{-1}	1.92×10^{-1}
[Ca]	1.29×10^{-2}	1.30×10^{-2}	1.26×10^{-2}	3.67×10^{-2}	3.53×10^{-2}	9.11×10^{-3}
[Sr]	2.18×10^{-6}	2.10×10^{-6}	1.90×10^{-6}	1.24×10^{-5}	1.35×10^{-5}	5.63×10^{-5}
[Mg]	9.32×10^{-3}	9.07×10^{-3}	8.41×10^{-3}	2.63×10^{-2}	2.53×10^{-2}	5.15×10^{-3}
[Ba]	--	--	--	--	--	1.13×10^{-5}
[K]	1.58×10^{-3}	1.56×10^{-3}	1.49×10^{-3}	3.15×10^{-3}	3.06×10^{-3}	1.22×10^{-3}
[Fe]	4.96×10^{-5}	2.12×10^{-5}	2.04×10^{-5}	3.92×10^{-5}	3.72×10^{-5}	3.71×10^{-5}
[Al]	7.30×10^{-9}	1.08×10^{-8}	1.10×10^{-8}	7.04×10^{-9}	7.25×10^{-9}	1.47×10^{-8}
$[C]_{inorg}$	4.91×10^{-3}	2.96×10^{-3}	3.01×10^{-3}	1.17×10^{-3}	1.20×10^{-3}	8.98×10^{-4}
[S]	7.21×10^{-2}	7.08×10^{-2}	7.24×10^{-2}	2.63×10^{-2}	2.71×10^{-2}	3.01×10^{-2}
[Cl]	2.02×10^{-1}	2.02×10^{-1}	1.79×10^{-1}	6.99×10^{-1}	6.75×10^{-1}	1.61×10^{-1}
[Si]	1.76×10^{-4}	1.77×10^{-4}	1.77×10^{-4}	1.72×10^{-4}	1.72×10^{-4}	1.82×10^{-4}

* In this calculation the pCO_2 was unconstrained. The reported value is the hypothetical pCO_2 a gas phase should have to be in equilibrium with this solution composition. In the other calculations, the pCO_2 was imposed as a constraint.

** Taken from Berner & Kosakowski (2011), Tab. 1

Appendix D: Geochemical parameters and estimated porewater composition of bentonite altered due to iron corrosion

D1 Introduction

As described in Chapter 7, there are not enough unequivocal experimental, modelling or field data that allow a confident prediction of the geochemical parameters that influence the sorption and diffusion properties of bentonite altered due to iron corrosion. For this reason, Nagra decided to estimate the relevant parameters (mineralogy and porewater composition for sorption, porosity for diffusion) as follows:

- **Transformation of montmorillonite into Fe-rich smectite:**
  Mineralogy: Unspecific Fe-smectite, with sorption properties assumed to be similar to montmorillonite.
  Porewater composition: Same as the bentonite reference porewater, but with a pH increased to 10 to reflect the potential increase in pH due to iron corrosion.
  Porosity: The volume increase due to the conversion of iron metal into magnetite is assumed to be partly compensated by the cavities in the canister. It is further assumed that the transformation of montmorillonite into Fe-rich smectite does not change the porosity by very much. Thus, the porosity will hardly increase and is assumed to be equal to the reference value for bentonite (including the constraint of anion exclusion in the interlayer).
- **Transformation of montmorillonite into chlorite or 7Å-minerals:**
  Mineralogy: Unspecific chlorite or 7Å-mineral, with sorption properties described with a simplified structural model based on kaolinite and hydrous ferric oxides.
  Porewater composition: Same as the bentonite reference porewater, but with a pH increased to 10 to reflect the potential increase in pH due to iron corrosion.
  Porosity: The volume increase due to the conversion of iron metal into magnetite is assumed to be partly compensated by the cavities in the canister. It is further assumed that the transformation of montmorillonite into 7Å-minerals does not change the overall porosity by much. Since 7Å-minerals do not have an interlayer, all of the porosity is accessible to anions. The porosity of the altered bentonite is thus assumed to be equal to the reference value for bentonite with no distinction between anion accessible and anion excluding porosity.

D2 Estimated porewater composition of altered bentonite

The porewater composition of altered bentonite is based on the reference bentonite porewater CON-BPW-22lsA (neutral) (see Tab. C1). The only difference is that 4.008×10^{-3} m NaOH was added to the reference porewater in order to obtain a pH of 10, while the constraint of a fixed pCO_2 was removed. Saturation with calcite, gypsum, kaolinite, quartz, pyrite, and magnetite was maintained.

Tab. D1: Estimated porewater composition of bentonite altered due to iron corrosion.

This water is derived from the reference bentonite porewater CON-BPW-22lsA (neutral) (see Tab. C1) by adding an appropriate amount of NaOH to increase the pH to 10; and releasing the constraint of a fixed pCO_2. Saturation constraints (calcite, gypsum, kaolinite, quartz, pyrite, magnetite) were maintained.

pH, ionic strength, redox potential, CO_2 partial pressure	
pH	10.0
I (m)	0.37
pe	-6.307
E_h (V)	-0.373
log[pCO_2 (bar)]	-7.64
Total element concentrations [molality]	
[Na]	3.05×10^{-1}
[Ca]	1.26×10^{-2}
[Sr]	2.10×10^{-6}
[Mg]	9.07×10^{-3}
[K]	1.56×10^{-3}
[Fe]	3.87×10^{-10}
[Al]	5.18×10^{-6}
$[C]_{inorg}$	2.70×10^{-5}
[S]	7.34×10^{-2}
[Cl]	2.02×10^{-1}
[Si]	6.75×10^{-4}